Numerical simulation of multiquantum barriers in 630nm laser diodes.

Brown, Martyn Rowan

Numerical Simulation of Multiquantum Barriers in 630nm Laser Diodes

A thesis submitted for the degree of Doctor of Philosophy in the

School of Engineering,

University of Wales Swansea.

Martyn Rowan Brown (Mphys)

August 2004

Declaration

This work has not previously been accepted in substance for any degree and is not concurrently submitted in candidature for any degree.

Signed ... . (Candidate)

Date .....21/11/04.....

Statement 1

This thesis is the result of my own investigations, except where otherwise stated. Other sources are acknowledged by footnotes giving explicit references. A bibliography is appended.

Signed ..... (Candidate)

Date .....21/11/04.....

Statement 2

I hereby give consent for my thesis, if accepted, to be available for photocopying and inter-library loan, and for the title and summary to be made available to outside organisations.

Signed .. .. (Candidate)

Date .....21/11/04.....

Acknowledgements

I would like to thank my supervisor Professor Steve P. Wilks, for providing me with the opportunity to conduct my research studies within the semiconductor interface group at the University of Wales Swansea. Many thanks go to Professor Phil Mawby for his valuable advice throughout my studies.

I would also like to thank my housemates for they're friendship and support during the course of my PhD. I must also thank the guy's in the office for many long and fascinating coffee breaks.

I would also like to thank my parents and my fiancée Jessica Crossman for their unwavering patience and encouragement, which has meant so much to me over the last three years.

Abstract

Red-emitting quantum well (QW) 630nm laser diodes have many potential applications in industry and medicine. The main profiteers would be in areas such as the development of optical memory, barcode readers and in the treatment of cancer. The limitation of the low inherent band offsets of the materials used to create such devices, gives rise to a high percentage of electron leakage via thermal activation in the QW active region. However, implementation of Multiquantum Barrier (MQB) into the *p*-type cladding region of the device enhances the effective conduction band discontinuity, thus increasing the reflection probability of carriers back into the device active region, consequently elevating output power of the laser device.

A study of $(Al_{0.7}Ga_{0.3})_{0.5}In_{0.5}P/(Al_{0.3}Ga_{0.7})_{0.5}In_{0.5}P$ (barrier/well) MQB has been investigated as a feasible material structure to enhance electron confinement within laser diodes in the 630nm regime. The structure was optimised theoretically based on the Γ-X transport mechanisms, using an effective mass approximation and the transfer matrix technique.

To accurately model such structures it is important to include possible distortion to the conduction band profiles induced by the different positions of the Fermi level with respect to the vacuum level. Thus, a dual-band device simulator was developed to model the band bending features, of both the Γ and X minima. This novel simulator simultaneously solves the constituent expressions making up the drift-diffusion equation set, which is then solved iteratively with Schrödinger's equation to yield a self-consistent solution.

Using these two simulation models a novel MQB structure is proposed which inhibits electron transmission across it in both the Γ and X bands. Subsequently, this MQB structure predicts a theoretical effective enhancements of 50% the height of the intrinsic conduction band offset.

Table Of Contents

Chapter 1

Introduction

1.1 Preamble

Semiconductor devices form the foundation of modern electronics, being used in applications extending from computers to satellite communication systems. A wide variety of devices are available, fabricated from a range of semiconductor materials. In order to characterise a semiconductor device it is necessary to obtain a suitable representation of the electrical and physical processes involved. It is also necessary to develop a description for the processes that cannot be directly observed. This is often achieved by implementing some form of analogy, which follows the behaviour of the device as closely as possible within the constraints of the defined operating environment. This process is termed numerical simulation or modelling.

There are currently a multitude of semiconductor devices under development and this research project will focus upon the numerical simulation of light emitting laser diodes, specifically, quantum well laser diodes in the 630nm wavelength regime, fabricated from the quaternary semiconductor material aluminium gallium indium phosphide (AlGaInP) and the ternary material gallium indium phosphide (GaInP).

Short-wavelength (600-700nm) visible laser diodes are of considerable technological interest. Lasers of this ilk have potential applications in consumer and professional markets, ranging from optical storage, bar-code readers, short-haul communication networks, laser printers and photodynamic therapy (PDT) treatment for cancer patients. Although the production of reliable lasers at wavelengths as short as 650nm is almost routine, it is found that as the emission wavelength is reduced

further, lasers increasingly suffer from high-threshold current densities, low power output and low characteristic temperatures. This behaviour is caused by small conduction and valence band-edge discontinuities between the $Ga_xIn_{1-x}P$ and $(Al_xGa_{1-x})_yIn_{1-y}P$ alloys used in these visible lasers (predominantly the latter). The small band-edge discontinuities allow a significant portion of the injected electrons to leak over the cladding-waveguide hetero-barrier, a problem that is exacerbated as the operating wavelength is decreased [1,2,3,4].

Several techniques are used to minimize this problem such as increasing the level of *p*-doping in the cladding region [1,2] and using highly disordered alloys to achieve the largest possible band offsets [5]. An alternative technique to inhibit electron leakage first proposed by Iga *et al* [6] in 1986, was to include a multi-layered structure called a multiquantum barrier (MQB) [7] into the *p*-doped cladding region of the laser. A MQB consists of alternating periods of wide and narrow band-gap semiconductor material. By judicious choice of the superlattice period widths, inclusion of such structures can instigate a quantum mechanical interference effect, which sets up a high reflection coefficient for the implemented structure, i.e. the interference effect effectively enhances the intrinsic conduction band barrier height, culminating in reduced electron leakage from the vicinity of the active region and hence improved device performance [8,9]. Initial studies by Iga *et al* [6] predicted theoretical effective enhancements in excess of 50% of the intrinsic conduction band offset, this makes MQB's an attractive stratagem to improve carrier confinement in the active region of AlGaInP laser diodes. In fact, MQB structures are regularly placed within infrared laser diodes composed from GaInAsP/InP material systems [10,11,12], to improve their operating range and performance.

Recent investigations conducted by Morrison *et al.* [13] and Raisch *et al.* [14] to determine how theoretically predicted effective enhancements associated with AlGaInP MQB's correlate with those measured experimentally, revealed a big inconsistency between the two results. Hitherto, MQB structures have been optimised on the assumption that electron transport is only evident via the direct Γ-valley, however, at high aluminium compositions the $(Al_xGa_{1-x})_yIn_{1-y}P$ semiconductor alloy becomes indirect as the X-valley lies at a lower energy position, this detail is not accounted for in single-valley models, and it is this fact that is gives rise to the aforementioned disparity.

To construct a MQB structure out of AlGaInP, it is the usual convention to have a low aluminium content within the well regions and conversely a high content in the barrier regions. Hence, from the previous statement, it is apparent that across the MQB the lowest lying conduction band minima switches between the direct Γ-band and the indirect X-band. This behaviour initiates inter-valley transport between these two minima and could theoretically destroy the enhancement effect associated with an optimised single-band MQB structure. This characteristic leads to an increased number of electron transport mechanisms, i.e. an additional loss mechanism which might involve the non-radiative loss of electrons via the X-minimum [15], such a mechanism would give rise to a significant proportion of the large excess currents measured in AlGaInP laser diodes. Recent experimental work by Blood *et al.* [16] found that this transport route was in fact the dominant contributor to the observed leakage currents in visible 630nm laser diodes.

Therefore, to theoretically model electron transport across AlGaInP MQB structures via the Γ-minimum only, appears to be a drastic oversimplification, implying that greater attention should be paid to other possible loss mechanisms. One of the focal points of this thesis is to address the above issues, by developing a numerical model that allows for the possibility of inter-valley scattering events to occur between the Γ and X conduction band minima across a MQB structure. Furthermore, the majority of authors in this field, work on the assumption that at the operating voltage of the laser diode, flatband conditions are evident across the active and immediately surrounding cladding regions, that is, there is negligible distortion to the energy band structure in these regions due to non-linear charge distribution initiated by charge injection. Although, this is a very good first approximation the effects of band bending and their subsequent effect on the reflective nature of the MQB should be taken in to account. Hence, a numerical routine has also been developed to theoretically optimise a MQB structure under lasing conditions of the device in order to acquire a maximum confining potential when there is the maximum amount of injected carriers within the active region. This was done in two stages; firstly, Poisson's equation was solved across the active region and a linear bias applied across the simulation area to mimic working condition of the device. Secondly, a complete coupled general steady-state device simulator was developed, which allows prediction of the energy band structure across the whole laser device under a user-defined bias. This simulator was then adapted specifically for imitation of 630nm

laser diodes and its associated dual-band nature. The development of this simulator enveloped the majority of my time during my PhD studies.

1.2 Thesis Content

The initial Sections of Chapter 2, give a brief account of the solid-state physics required to obtain an understanding of the band nature of electrons in a periodic crystal and how these bands may be arranged to form metals, insulators and semiconductors. This is followed by a short interlude into some of the physical properties of semiconductors, pertinent to this thesis. These are semiconductor band structure, carrier recombination mechanisms, the phenomenon of effective mass, doping, alloy compositions and the formation of hetero-structures. This sub-section is followed by a brief description of the structure and operation of a general laser diode. The Chapter concludes with a material list, which presents all the physical parameters of the GaInP and AlGaInP semiconductor alloys used in the remainder of the thesis.

The analogous miniband effect present in semiconductor superlattices, to that of the allowed and non-allowed electron states within a periodic lattice is the main focus of Chapter 3. The initial Sections of this chapter deal with eigensolutions of confined particles in both the infinite and finite quantum well systems. This discussion is then moved on to specifically look at semiconductor quantum wells and the solution of Schrödinger's equation. Utilising a simplified tight-binding approximation the occurrence of coupling of electronic states in closely positioned quantum well structures is deduced. This taken a step further by considering a collection of like structures closely positioned to form a superlattice structure; from this scenario the miniband effect is inferred. The final Section of this Chapter is devoted to the application of such superlattice structures within laser diodes. It is shown schematically how inclusion of such multi-layered structures, may improve the lasing efficiency of the device at elevated temperatures by judicious placement of the non-allowed electron states emerging from wavefunction coupling in the superlattice.

Within Chapter 4, a mathematical model that is capable of predicteding the theoretical extent of the confining potential associated with the multiquantum barriers

is developed. Following this, the issue of conduction band crossover is investigated as a possible electron leakage source in AlGaInP laser devices. The existing numerical model is refined to account for inter-valley transport and tested against a more sophisticated psuedo-potential models of Marsh [17]. Chapter 4 finishes by firstly, detailing the optimisation procedure used to find the best enhancement properties of the superlattice structures, and secondly, a novel optimised MQB structure and its corresponding reflectivity spectra are deduced and displayed.

In Chapter 5, a multiquantum barrier structure is designed to give optimum performance under lasing conditions. To achieve this Poisson's equation is solved through an explicit integration method, in order to account for the effects of non-linear charge distribution. This method is applied to the Γ and X conduction band minima. To model the structure under working conditions a linear bias, which is doping and width dependent is dropped across the structure as a whole. Under these conditions a novel MQB structure is proposed that blocks transmission of electrons across the superlattice in both the Γ and X minima. This structure is compared with a previously designed single band structure and the results displayed.

Chapter 6 considers the numerical methods behind the steady-state simulation of general hetero-structure devices. The fundamental device equations, namely, Poisson's equation, and the two carrier continuity equations are presented and their one-dimensional solution is developed. Particular attention is paid to the Schafetter-Gummel discretisation scheme [18] for calculating the current density within heterogeneous semiconductor materials.

This Chapter also details the fundamental physical models required for the simulation of AlGaInP heterogeneous devices, i.e. the models that are required for the most basic simulation. To incorporate the changes in material composition (e.g. bandgap, effective masses etc.) two band parameters, θ_n and θ_p [19] are developed and are used as an additional parameter in the Maxwell-Boltzmann exponential. Models are also given for the different recombination mechanisms and composition dependent low field mobilities used in the simulator.

This is followed by the extension of the model to degenerate statistics. To do this, two additional parameters are derived, namely, V_n and V_p. Employing these extra

terms within the carrier concentrations terms, enables Fermi-Dirac statistics to be used within the Maxwell-Boltzmann statistics framework. This is essential as the discretisation scheme is founded upon Maxwell-Boltzmann statistics. The use of the Maxwell-Boltzmann expression in the Newton-Raphson non-linear algebra scheme is complicated by the fact that the Fermi-Dirac parameters V_n and V_p depend on the potential. This therefore requires alteration of the Jacobian entries in the non-linear algebra scheme and this is discussed in detail with reference to Poisson's equation.

In the final Section of this Chapter the numerical simulation of quantised two-dimensionally confined electrons is considered. A model is developed for quantum transport, which employs a coupled solution to Schrödinger's equation and the conventional device equations. To illustrate the effect that two-dimensionally confined carriers have on the carrier concentration, the solution of this improved numerical model to a quantum well structure under a forward bias is analysed and presented.

Chapter 7 gives a brief account of how the existing numerical model may be adapted to allow simulation of a second conduction band. Here, the recombination mechanisms are altered slightly to allow for recombination from both minima. Also, detailed is the method used to populate the conduction band minima, via an extra exponent in the Maxwell-Boltzmann formalism.

Utilising this new solution procedure, an investigation of the reflectivity spectra of previously designed multiquantum barriers is considered, and the results shown. The final Section of this Chapter details a novel multiquantum barrier structure that predicts high and stable reflection probabilities [20].

Finally Chapter 8 gives some conclusion of the work carried out in this thesis, and suggests a few ideas as to how this work may be taken forward to enable future research.

1.3 References

[1] A. T. Meney, A. D. Prins, A. F. Phillips, J. L. Sly, E. P. O'Reilly, D. J. Dunstun, A. R. Adams, and A. Vaster, 'Determination of the band structure of disordered AlGaInP and its

influence on visible-laser characteristics', IEEE J. Select. Quantum Electron., **1**, pp.697-706, (1995).

[2] D. P. Bour, D. W. Treat, R. L. Thornton, R. S. Geels, and D. F. Welch, 'Drift leakage in AlGaInP quantum well lasers', IEEE J. Quantum Electron., **29**, pp.1337-1342, (1993).

[3] G. Hatakoshi, K. Itaya, M. Ishikawa, M. Okajima and Y. Uematsu, *IEEE J. Quantum Electron.*, **27**, pp.1476-1482, (1991).

[4] P. J .A Thijs, IEEE Int. Semiconductor Laser Conference, 1992, p.2.

[5] T. Suzuki, A. Gomyo, S. Iijima, K. Kobayashi, S. Kawata, I. Hino, and T. Yuasa, 'Band-gap energy anomaly and sublattice ordering in GaInP and AlGaInP grown by metalorganic vapour phase epitaxy',*Jpn. J. Appl. Phys.*, **27**, pp. 2098-2102, (1988).

[6] K.Iga, H. Uenohara, and F. Koyama, 'Electron Reflectance of Multiquantum Barrier (MQB)', *Electron. Lett.*, **22**, pp. 1008, (1986).

[7] R. Tsu, and L. Esaki, 'Tunnelling in a finite superlattice', *Appl. Phys. Lett.*, **22**, pp. 562-564, (1973).

[8] K. Kishino, A. Kikuchi, Y. Kaneko and I. Nomura, 'Enhanced carrier confinement by the multiquantum barrier in 660nm GaInP/AlInP visible lasers', *Appl. Phys. Lett.*, **58**, pp. 1822-1824, (1991).

[9] T. Takagi, F. Koyama and K. Iga, *Electron Lett.*, 27(12), pp.1081-1082, (1991).

[10] Koyama, K.Y. Liou, A.G. Dentai, T. Tanbun-ek and C.A. Burrus, 'Multiple-quantum well GaInAs/GaInAsP tapered broad-area amplifiers with monolithically integrated waveguidelayers for high-power applications', *IEEE Photonic Tech. Lett.*, **5**, pp. 916, (1993).

[11] H. Lee, P. K. York, R. J. Menna, R. V. Martinelli, D. Z. Garbuzov, S. Y. Narayon and J. C. Connelly, 'Room-temperature 2.78 μm AlGaAsSb/InGaAsSb quantum-well lasers', *Appl. Phys. Lett.* **66**(15), p.1942, (1995).

[12] M. Irikawa, H. Shimizu, T. Fukushima, K. Nishikata and Y. Hirayama, 'Strained GaInAs-AlGaInAs 1.5mm-wavelength MQW laser loaded with GaInAs-AlInAs MQB's at the p-type optical confinement layer', *IEEE J. Selected topics in Quantum. Electron.*, **1**, pp. 285, (1995).

[13] A. P. Morrison, L. Considine, S. Walsh, N. Cordero, J. D. Lambkin, G. M. O'Connor, E. M. Daly, T. J. Glynn, and, C. J. van der Poel, 'Photoluminescence investigation of the carrier confining properties of multiquantum barriers', *IEEE J. Quantum. Electron.*, **33**(8), (1997).

[14] P. Raisch, R. Winterhoff, W. Wagner, M. Kessler, H. Schweizer, T. Riedl, R. Wirth, A. Hangleiter, and F. Scholz, 'Investigations on the performance of multiquantum barriers in short wavelength (630nm) AlGaInP laser diodes', *Appl. Phys. Lett.*, **74**(15), (1999).

[15] S.T. Yen, C.P Lee, C.M. Tsai and H. R. Chen, 'Influence of X-valley superlattice on electron blocking by multiquantum barriers', *Appl. Phys. Lett.*, **65**(21), pp.2720, (1994).

[16] S. A. Wood,C. H. Molloy, P. M. Smowton, P. Blood C. C. Button, 'Minority Carrier Effects in GaInP Laser Dioides', *IEEE J. Quantum. Electron.*, **36**, pp. 742-750, (2000).

[17] A. C. Marsh and J. C. Inkson, 'An empirical pseudopotential analysis of (100) and (110) GaAs-$Al_xGa_{1-x}As$ heterostructures' *J. Phys.C: Solid-State Phys.*, **17**, pp. 6561-6571, (1984).

[18] H. K. Gummel, 'A Self-Consistent Iterative Scheme for One-Dimensional Steady-State Transistor Calculations', *IEEE Trans. Electron. Devices*, No. **ED-27**, pp. 455-465, (1964).

[19] J. E. Sutherland and J. R. Hauser, 'A computer analysis of heterojunction and graded composition solar cells', *IEEE Trans. Electron. Devices*, Vol. **ED-24**, pp.363-372, (1977).

[20] M. R. Brown, K. S. Teng, and S. P. Wilks, 'AlGaInP Multiquantum Barriers Designed and Optimised Using a Novel Dual-Band Drift-Diffusion Simulator', Submitted to *Journal of Quantum Electonics* June (2004).

Chapter 2

Semiconductor Physics, Laser Diodes and AlGaInP Material Issues

2.1 Introduction

The aim of this Chapter is to give a brief account of all the relevant solid-state and semiconductor physics needed to give a foundation to the numerical simulation routines developed in later chapters.

Section 2.2, begins by introducing the concept of $\boldsymbol{k}$-space as a tool for presenting the electronic energies of a solid. This concept is illustrated, by considering two primary cases, namely, the Free Electron Model [1,2] and the Kronig-Penney Model [1,3]. The Kronig-Penney Model is included to demonstrate how electrons in solids exist in allowed energy bands subdivided by forbidden energy regions, and give an analogy to a similar effect induced by a multiquantum barrier in the following chapter. From this model, the energy band structures of insulators, metals and semiconductors is deduced in Section 2.3.

In Section 2.4, some intrinsic properties of semiconductors relevant to this thesis are outlined. Firstly, a brief discussion focusing on the lowest conduction band minima of some popular semiconductors used in device design is given. This is followed by overview of the direct and indirect recombination mechanisms. In sub-section 2.4.3 the concept of an effective mass is outlined. The effect of doping intrinsic semiconductors to n and p-type semiconductors is next described. Sub-section 2.4.5 details how semiconductor alloys may be formed and highlights their importance in semiconductor device design. The final topic in this Section gives a

short account of semiconductor hetero-structures, detailing the ways in which two semiconductor materials of differing band-gap physically line-up.

In Section 2.5, a brief account of the construction of a general semiconductor quantum well laser device is given; this subject matter is followed by a basic interpretation of the operation of such quantum device.

In the penultimate Section of this Chapter, a short investigation focusing on the origin of the two main issues hindering development of 630nm laser diodes is presented. This is followed by a list of the material parameter used for simulation of laser diodes fabricated from the GaInP and AlGaInP alloys.

The Chapter concludes with Sections 2.7 and 2.8, where a brief summary of the main issues discussed within in the chapter and all referenced articles are listed respectively.

2.2 Electronic Energies of a Solid

The energy band structure of a crystal is usually presented by plotting the allowed energy values of the electron E, for different values of the wave vector $\boldsymbol{k}$, in the first Brillouin zone [1,2,4] where the value of E depends both on the magnitude and direction of $\boldsymbol{k}$. In this section, the relationship between E and $\boldsymbol{k}$ is derived, by solving Schrödinger's time independent equation, which may be given by

$$\nabla^2\zeta + \frac{2m}{\hbar^2}(E-V)\zeta = 0, \tag{2.1}$$

here E is the electron energies, ζ the wavefunction, V the electrostatic potential, m the electron mass, and $\hbar$ the reduced Plank constant.

Calculation of energy bands in real materials is a very complex mathematical process. At this stage two approximations are introduced, firstly the free electron model [1,2], which neglects any electron-ion core interaction, but provides an initial solution to the problem. Secondly, the Kronig-Penney Model [1,3], which treats the electron-core interactions and shows, qualitatively how electrons exist in allowed energy states subdivided by bands of excluded electron energies within crystalline materials.

2.2.1 The Free Electron Model

The simplest approach is to assume that the electrons in a crystal behave in a similar manner to a gas of free particles. Removing the valence electrons from an atom leaves a positively charged ion core. The model ignores the repulsive interaction between the conduction electrons, and assumes that the charge density associated with the core is spread uniformly throughout the crystal so that the electrons move in a constant electrostatic potential.

By considering a cubic crystal of side L with faces perpendicular to the x, y and z-axes, without loss of generality, the crystal potential may be taken to be zero and thus Schrödinger's one-dimensional time independent equation may be expressed as

$$\frac{\partial^2 \zeta}{\partial x^2} + \frac{2m}{\hbar^2} E\zeta = 0, \tag{2.2}$$

under the above assumptions. If a periodic boundary condition of the form $\zeta(x + L) = \zeta(x)$ is imposed then the solutions of equation (2.2) are Bloch waves [1,2] of the form

$$\zeta(x) = \frac{1}{\sqrt{C}} e^{ikx} \qquad \text{where} \qquad k = \frac{2\pi n}{L} \tag{2.3}$$

n is any integer value and C is introduced as a normalising factor. The corresponding electron eigenenergies of equation (2.2) are given by

$$E = \frac{\hbar^2 k^2}{2m}. \tag{2.4}$$

In three dimensions, the corresponding wavefunctions and electron energies are given by

$$\zeta(x,y,z) = \frac{1}{\sqrt{C}} e^{i\mathbf{k}.\mathbf{r}}, \qquad \text{and} \qquad E = \frac{\hbar^2}{2m}\left(k_x^2 + k_y^2 + k_z^2\right). \tag{2.5}$$

Therefore, from this model the allowed electron states are quadratic functions of k, and their energies are distributed continuously from zero to infinity.

2.2.2 The Kronig-Penney Model.

The Kronig-Penney Model assumes a periodic array of square potential wells and barriers as shown in Figure 2.1 where E represents the energy of an electron and is an eigenvalue of the solution of the wave equation. The potential $V(x)$, to be used in Schrödinger's equation is shown, and its periodicity is that of a lattice with period l representing the unit cell length, which implies the following relation

$$V(x+nl) = V(x) \quad \text{where } n = 0, 1,2,\ldots . \tag{2.6}$$

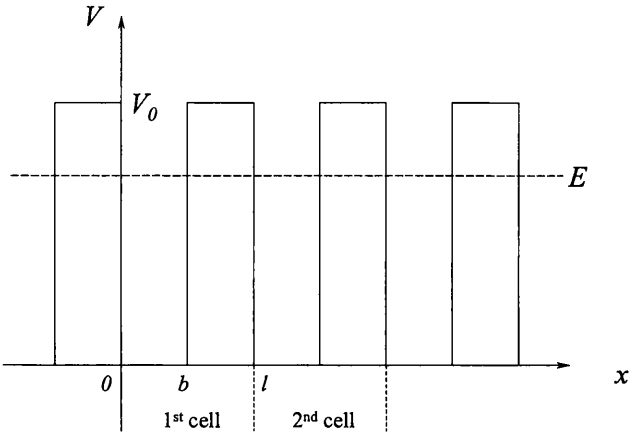

Figure 2.1: The Kronig-Penney periodic potential model.

In order to obtain a solution it is assumed that the one-dimensional crystal takes the form of a circular ring. Therefore, the wavefunction ζ must repeat itself after a distance Nl. Where N is the number of atoms in the crystal, such that

$$\zeta(x+Nl) = \zeta(x) . \tag{2.7}$$

With the use of Floquet's theorem [5], the solutions to Schrödinger's one-dimensional equation that also satisfy equations (2.6) and (2.7) have the form

$$\zeta(x) = V(x)e^{ikx} \tag{2.8}$$

where

$$k = \frac{2n\pi}{Nl} \tag{2.9}$$

and $V(x)$ is itself periodic with period l, and could be complex. Here, the solution for the wavefunction of the 1st cell shown in Figure 2.1 is in two parts, the left-hand and right-hand sides of the cell respectively. By defining the electron energies on the left-hand part of the first cell as $E = \hbar^2 k_1^2 / 2m$, where $k_1 \neq k$, the wave equation for the left-hand part of the first cell is reduced to

$$\frac{\partial^2 \zeta}{\partial x^2} + k_1^2 \psi = 0, \quad 0 \leq x \leq b. \tag{2.10}$$

If the difference between the maximum potential V_0 and E in Figure 2.1 is given by $V_0 - E = \hbar^2 K_2^2 / 2m$, the wave equation for the right-hand part of the first cell maybe written as

$$\frac{\partial^2 \zeta}{\partial x^2} - K_2^2 \psi = 0, \qquad b \leq x \leq l \tag{2.11}$$

Solutions to equations (2.10) and (2.11) may be given by

$$\zeta(x) = A\exp(ik_1 x) + B\exp(-ik_1 x) \qquad 0 \leq x \leq b \tag{2.12}$$

and

$$\zeta(x) = C\exp(-K_2 x) + D\exp(K_2 x) \qquad b \leq x \leq l \tag{2.13}$$

respectively. The dependency of the solution for the left-hand part of the second cell must be the same as for the left-hand part of the first cell, with x replaced by $(x - l)$. Furthermore, it must fulfil the periodicity condition given in equation (2.8), which implies

$$\zeta(x + l) = U(x + l)\exp(ik(x + l)) = U(x)\exp(ikx)\exp(ikl). \tag{2.14}$$

Therefore, the solution for the left-hand part of the second cell contains a phase shift of exp(*ikl*), given by

$$\zeta(x) = \left[A\exp(ik_1(x-l)) + B\exp(-ik_1(x-l))\right]\exp(ikl), \quad l \le x \le l+b \qquad (2.15)$$

By insuring that both ζ and its derivative $d\zeta/dx$, are continuous at the finite discontinuities in the potential at $x = b$, and $x = l$, a set of four homogeneous equations can be obtained for the constants A, B, C and D, through the use of equations (2.10) through to (2.13). This will have a non-trivial solution when the determinant of coefficients is exactly zero, given by the condition

$$\cos k_1 b \cosh(K_2(l-b)) - \frac{k_1^2 - K_2^2}{2k_1K_2}\sin k_1 b \sinh(K_2(l-b)) = \cos kl, \quad E < V_0 \quad (2.16)$$

Equation (2.16) is an implicit expression for the allowed energies E determined by the values of k_1 and K_2. Due to the magnitude of the right-hand side being bounded by unity, not every arbitrary value of E can satisfy the equation for a given V_0, which implies that the electrons cannot have these energies. The energy ranges for which solutions do not exist are thus termed 'forbidden' energy bands. For values of $E > V_0$, equation (2.16) remains essentially the same, but here K_2 is purely imaginary, and is replaced by ik_2 for simplicity, thus yielding

$$\cos k_1 b \cos(k_2(l-b)) - \frac{k_1^2 - k_2^2}{2k_1k_2}\sin k_1 b \sin(k_2(l-b)) = \cos kl, \quad E > V_0. \qquad (2.17)$$

Forbidden energy bands also arise in this energy range, along with allowed energy bands. The right-hand sides of equations (2.16) and (2.17) are both periodic, and rewriting k as $2n\pi/Nl$ (by equation (2.9)) the cosine terms go through a whole cycle as n changes by N in very small discrete steps, which can be regarded as a continuum as the steps are so close together. The band boundaries occur at points where $coskl = \pm 1$, or $k = \pm 2\pi/l$ for $n = 1, 2, \ldots$.

Taking the lowest possible energy band for each value of E, a corresponding value of k can be found from equation (2.17). A plot of E verses the corresponding k

value called the dispersion curve can thus be derived and is shown in Figure 2.2(a). The first band, covering the ranges $-\pi/l < k < \pi/l$ is called the first Brillouin zone; the second, covering the ranges $-\pi/l < |k| < 2\pi/l$ forms the second Brillouin zone, and so on and so forth.

It is conventional to shift the second and higher Brillouin zones to the first zone along the k-axis by multiples of $2\pi/l$, since the left-hand sides of equations (2.16) and (2.17) are unchanged when kl changes by $\pm 2n\pi$. This yields Figure 2.2(b) and is called the reduced-zone representation in k-space.

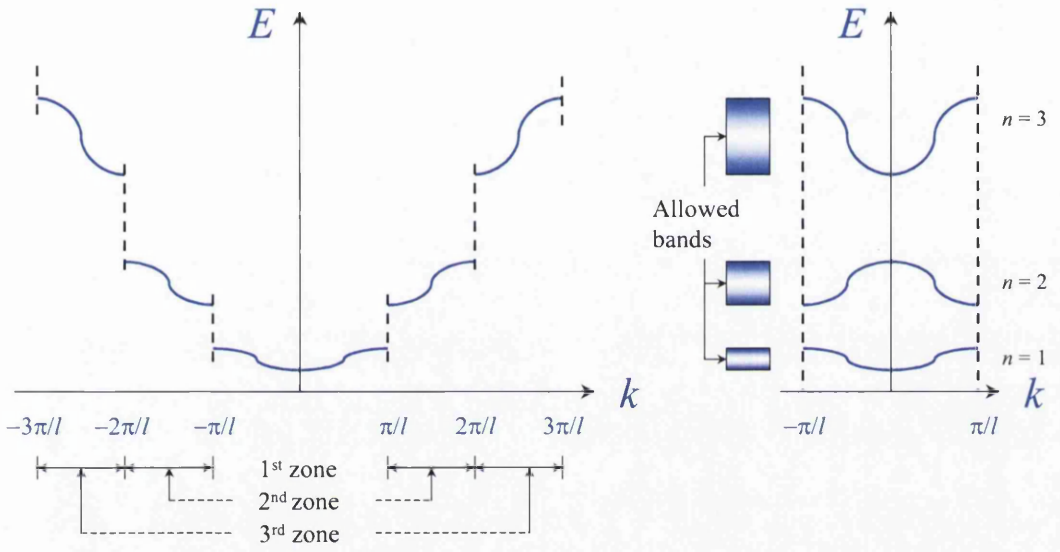

Figure 2.2 (a) The *E-k* dependence of the Kronig-Penney Model, (b) The reduced-zone representation of the Kronig-Penney Model.

Each Brillouin zone consists of N distinct values of k, each corresponding to a different energy state. Because each energy state can be populated by at most two electrons with opposite spin, each zone can therefore contain $2N$ electrons. At the absolute zero of temperature, the electrons fill the lowest possible energy states, and so all states are filled from zero up to an energy E_f, known as the Fermi-energy. The energy band structure derived above is used in the following section to classify crystalline solids.

2.3 Metals, Insulators and Semiconductors

The difference in energy between the highest energy level in the valence band (the highest completely full energy band at absolute zero) and the lowest energy level in the conduction band (the next lowest energy band) is known as the forbidden energy gap, E_g, and is of great importance in determining the conduction properties of the crystal. Each solid has its own characteristic energy band structure, which can be evaluated by solving equation (2.1) with the inclusion of the relevant electrostatic potentials. Solids can then be further subdivided into insulators, metals and semiconductors.

The trait that defines an *insulator* is that, as Figure 2.3(a) shows, the highest occupied level coincides with the top of a band. In addition, this band must be separated from the unoccupied region above it by a substantial energy gap. By definition, an insulator is a solid through which electrons cannot flow as a directed drift current. If an electric field is applied to an insulator it will exert a force, eE, on each electron. Classically, this force will induce an increase to the electrons velocity in the direction of the field, subsequently altering its kinetic energy. In quantum terms, if the energy of an electron changes, the electron must move to a different energy level within the solid. However, in an insulator the Pauli principle prevents the electron from doing so because all other levels within the band are already occupied.

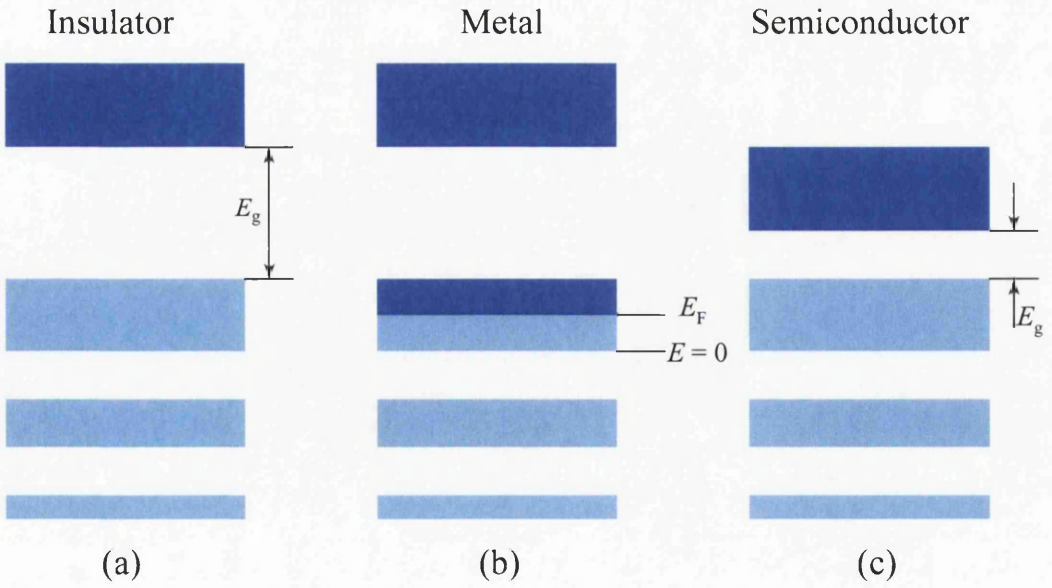

Figure 2.3: Simplified representation of the energy band structures of (a) an insulator, (b) a metal and (c) a semiconductor.

Figure 2.3(b) indicates the idealised representation of the band-gap pattern of a metal at absolute zero. The highest occupied level falls approximately in the middle of a band. Electrons that occupy this partially filled band are the valence electrons of the atoms, which, being free to move throughout the solid, become the *conduction electrons* of the solid. At the absolute zero of temperature, thermal agitation plays no role and all electrons occupy states of the lowest possible energy. Thus, it is plausible to suggest with little error that the potential energy of conduction electrons remains constant as they move within the solid. This constant is set equal to zero; hence, the total energy E associated with any level is equal to the kinetic energy of the electron that occupies that level.

The level at the bottom of the partially filled band corresponds to $E = 0$. The highest occupied level in this band (at absolute zero) is referred to as the *Fermi level* and the energy corresponding to it is the *Fermi energy*, E_F.

Comparison between Figure 2.3(a) and (c) shows that a semiconductor is like an insulator in that its upper most filled level (at absolute zero) lies on top of a band. A semiconductor differs from an insulator, however, in that the gap between this filled band and the next vacant band above it is much smaller than for an insulator, which vastly increases the probability that electrons will negotiate the forbidden band by thermal agitation.

2.4 Semiconductors

In this Section a brief summary of the major semiconductor properties that need to be considered for design and numerical simulation of laser diodes. Of particular interest are the band-edge properties since they dominate the transport and optical properties of most devices. Thus, in sub-section 2.4.1, the simplified energy band structures of two semiconductors, commonly used in device design are illustrated and discussed. From this discussion the concept of direct and indirect semiconductors is shown, also, the phenomenon of carrier recombination is mentioned.

Sub-section 2.4.2, briefly highlights why the mass of an electron within a solid i.e. semiconductor in this case, must be considered to have an effective mass as

opposed to using the free-electron mass, which is some cases the magnitudes deviate quite strongly from the electron mass in vacuum.

In sub-section 2.4.3, it is detailed how the addition of impurities to a semiconductor crystal may result in an increase to electron or hole concentration, giving rise to *n*-type or *p*-type semiconductor material.

The following sub-section is extremely pertinent to semiconductor device design, i.e. the topic of potential barrier formation. Within this sub-section the properties of bulk semiconductors will be briefly analysed before moving on to discuss semiconductor alloys. The sub-section finishes with a short discussion of hetero-junctions and the way energy levels either side of these junction line-up.

2.4.1 Energy Band Structure

In Section 2.2, the concept of $\boldsymbol{k}$-space was introduced to enable a means to represent the electronic energy band structure of a crystal, where the electron energies E depend both on the magnitude and their orientation in $\boldsymbol{k}$-space. The characteristic features of the energy band are displayed by plotting E versus $\boldsymbol{k}$ (i.e. dispersion relation) at points of high symmetry and along the directions of high symmetry, usually given by the zone centre, and along the $\langle 100 \rangle$ and $\langle 111 \rangle$ crystallographic directions.

A simplified picture of the energy band structure for two of the more popular semiconductors used in device design, namely, silicon (Si), and gallium arsenide (GaAs) are presented below in Figure 2.4. These energy band diagrams can be calculated using non-local empirical pseudopotential methods similar to that detailed in [6,7,8,9], although the curves shown here are adapted from [10].

It can be seen from the *E-k* curves that for each semiconductor there is an energy gap, E_g, separating the conduction and valence bands; at 300K [10] these have been experimentally verified to be at 1.11eV for Si and 1.424eV for GaAs. The tops of the valence bands are situated at the zone centre (Γ-point), whereas the bottom of the conduction bands are located at different points along different directions for each of the two semiconductors. In the case of Si Figure 2.4(a) the conduction band minima occur along the $\langle 100 \rangle$ (X-point) direction, however for GaAs semiconductor, the conduction band minimum occurs at the zone centre (Γ-point), directly above the

valence band maximum. Gallium Arsenide is therefore, referred to as a direct band gap semiconductor, whereas silicon is referred to as an indirect band-gap semiconductor.

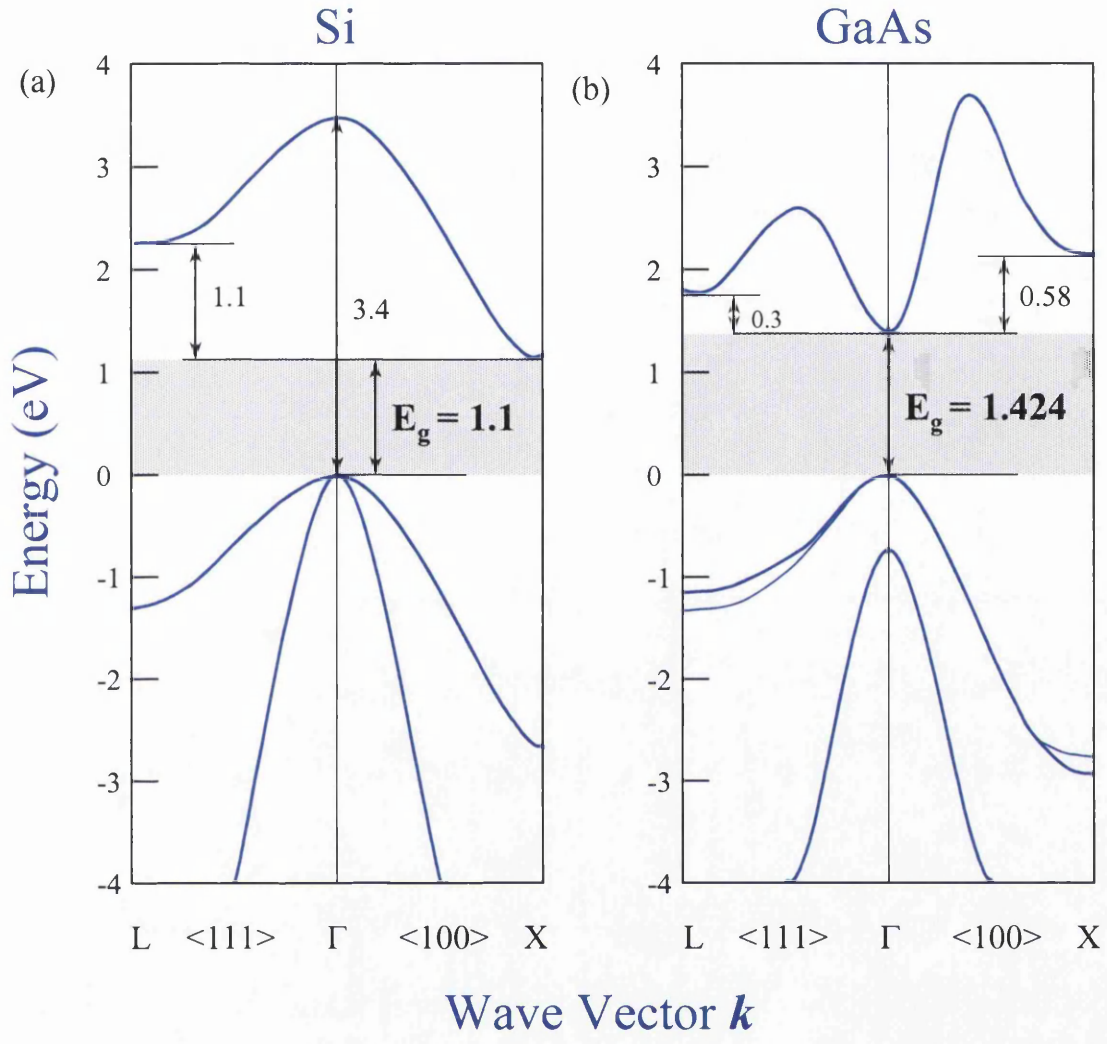

Figure 2.4: Dispersion relations of (a) Si and (b) GaAs. Adapted from [10]

As noted earlier in sub-section 2.2.2, all the *E-k* curves like the ones presented in Figure 2.4(a) and (b) and in the aforementioned sub-section, consist of many discrete points, each corresponding to a possible electron or hole state, i.e. wavefunction, that is allowed to exist in the crystal. The points are so close together that it is normal practice to link the points in a continuous curve. Also, present in the above *E-k* curves are the forbidden energy ranges predicted by the Kronig-Penney Model in Section 2.2. It is also important to note that the minima and maxima of the conduction and valence band respectively, although look almost parabolic, they are not, this fact has important implications when attempting to determine the electron

and hole effective masses (see sub-section 2.4.3). Above absolute zero of temperature, due to thermal excitation some of the electrons from the top of the valence band can be excited to the bottom of the conduction band. When the electron reverts to its initial state it recombines with a hole and a quanta of energy is emitted. The way in which the process occurs differs between direct and indirect semiconductors and is the topic of the following sub-section.

2.4.2 Direct and Indirect Recombination

When an electron in the conduction band loses its energy and subsequently transfers to the valence band, it will be captured by a hole therein, this process is known as recombination. Since the electron and the hole are in two separate energy bands, it is possible that there are different recombination processes. In this sub-section, two of these processes are highlighted, namely, direct and indirect recombination.

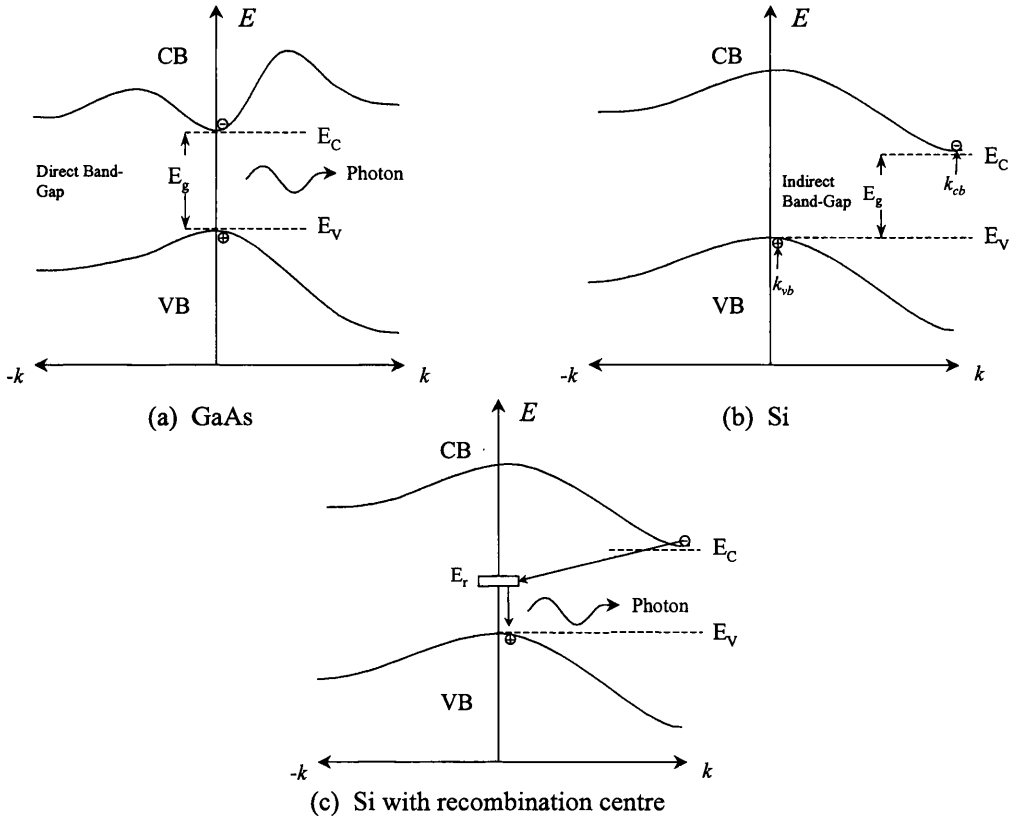

Figure 2.5: Schematic diagram of the recombination processes that occur in both direct and indirect semiconductors. (a) The direct band-gap semiconductor GaAs showing direct recombination of a electron and hole pair. (b) Si the indirect band-gap semiconductor. (c) Recombination of an electron and a hole in Si involves a recombination centre (i.e. phonon).

When an electron makes a transition from the conduction band to the valence band via the Γ-point (see Figure 2.5(a)), it is known as direct recombination, i.e. it occurs in a direct band-gap semiconductor material (e.g. GaAs), where the minimum of the conduction band aligns with the maximum of the valence band in k-space. Under this condition, an electron in the conduction band can simply recombine with a hole in the valence band without a change in momentum. When this happens, the energy given up by the electron will be emitted as a photon. Hence, the radiative recombination process in a direct band-gap semiconductor can be harnessed to produce light emitting diodes and lasers.

In an indirect semiconductor such as Si, the minimum of the conduction band and the maximum of the valence band are separated in momentum space (see Figure 2.5(b) above). Therefore, in order for an electron to transit to the valence band via the X-point, requires a change in momentum as well as energy to satisfy the law of conservation. The most likely route for indirect recombination would be an electron travelling to a trap (assuming the state is initially vacant) and residing there before recombining with a hole in the valence band (see Figure 2.5(c) above) via a phonon interacrion. This form of non-radiative process can also occur in direct band-gap materials if impurity atoms and defects are present in the crystal structure. These imperfections in the structure introduce electronic states, which are localised energy levels near the centre of the forbidden band-gap, acting as traps of recombination centres.

2.4.3 Effective Mass

In the introductory paragraph of this Section, it was mentioned that the shape of the conduction and valence bands near the minimum and maximum respectively, determines the motion of the electrons and holes under an applied field. Under the influence of such an electric field, an electron and hole in a semiconductor are found to possess an effective mass, m^*, which can differ substantially, from the mass of an electron in a vacuum. In the following discussion, an expression for the effective mass of an electron is derived which is dependent upon the curvature of the minima shown in the above dispersion relations.

The velocity and acceleration of an electron in the conduction band under the influence of a electric field acting in the one-dimensional negative x-direction,

imposes an external force $F_{ext} = qE_x$ in the positive x-direction. As the electron in this scenario is pictured to be a wave, it is necessary to evaluate its group velocity v_g, which by definition is given by $v_g = d\omega/dk$.

The time dependence of the electron wavefunction is given by $\exp(-iEt/\hbar)$ where the energy E is equal to the product of the angular frequency, ω, associated with the wave motion of the electron and the reduced Plank constant, $\hbar$. Both E and ω depend on k. Thus, the group velocity is

$$v_g = \frac{d\omega}{dk} = \frac{1}{\hbar}\frac{dE}{dk}. \tag{2.18}$$

Hence, the group velocity is determined by the gradient of the E-k curve. In the presence of an electric field, the electron experiences a force $F_{ext} = qE_x$, from which energy is gained. This increase in energy results in the electron moving to a higher position in the E-k curve, this motion is continued until the electron is scattered to a different position by a lattice vibration (i.e. phonon). During the time interval between collisions, the electron moves a distance equal to $v_g \delta t$ and hence gains an energy, δE, which may be expressed as

$$\delta E = F_{ext} v_g \delta t. \tag{2.19}$$

By substitution of equation (2.18) in equation (2.19) the relationship between the external force and the energy may be given as

$$F_{ext} = \frac{1}{v_g}\frac{dE}{dt} = \hbar\frac{dk}{dt} \tag{2.20}$$

This equation is a re-statement of Newton's second law of motion. Here, the change in momentum cannot be attributed to the electron only, but associated with the crystal lattice as a whole [11]. For this reason, the quantity $\hbar k$ is referred to as the crystal momentum of the electron.

Using this formalism the acceleration of an electron may be expressed as

$$a = \frac{dv_g}{dt} = \frac{d}{dt}\left(\frac{1}{\hbar}\frac{dE}{dk}\right) = \frac{1}{\hbar}\frac{d^2E}{dk^2}\frac{dk}{dt} \tag{2.21}$$

dk/dt may be substituted for a rearrangement of equation (2.20) in equation (2.21), which reveals a relationship between F_{ext} and a, the electron acceleration of the form

$$F_{ext} = \frac{\hbar^2}{\left[\frac{d^2E}{dk^2}\right]} a . \tag{2.22}$$

Comparison of equation (2.22) with the more familiar expression of Newton's second law of motion, namely

$$F_{ext} = m_e a \tag{2.23}$$

where m_e is the mass of a free electron in a vacuum, suggests the following expression for the effective mass, m^*, in a crystal

$$m^* = \hbar^2\left(\frac{d^2E}{dk^2}\right)^{-1} . \tag{2.24}$$

Thus, the electron responds to an external force and moves as if its mass were given by equation (2.23). The effective mass obviously depends on the *E-k* relationship, which in turn depends upon crystal symmetry and the nature of atom bonding. Its value is different for electrons in the conduction band and for those in the valence band, and moreover, it depends on the energy of the electron since it is related to the curvature of the *E-k* behaviour by the second differential d^2E/dk^2. This behaviour can distort the magnitude of the effective mass to be substantially smaller than the free electron mass, e.g. the effective mass of GaAs is $0.067m_e$ for a electron residing in the parabolic part of the conduction band minimum.

A high majority of device modellers use the magnitude of the electron and hole effective masses when they exist within the parabolic region of the corresponding minima or maxima of the conduction and valence bands. Such values

have been repeatedly refined over the years and their magnitudes are now well established for the more prominent semiconductor materials. To a first approximation this is a very good assumption, however, as highlighted above, as the energy of the electron or hole increases they move out of these parabolic regions and the assumption that their effective masses remains at the magnitude of that measured in the parabolic regions becomes increasingly invalid. In an attempt to achieve a more accurate determination of the electron and hole effective masses, many researchers are turning to very complex ***k.p*** models [12,13]. Such theoretical models are capable of predicting energy dependent electron and hole effective masses, $m^*(E)$. However, these methods are very intricate and their application to ternary and quaternary semiconductors like those used in this dissertation are at present not well founded, subsequently, all values of effective mass used in the following discussion use the parabolic approximation.

Another very important issue in semiconductor device physics is the process of doping. This procedure is of great importance when fabricating laser diodes due to the fact that, the laser diode is essentially two differently doped regions, i.e. a *p* and *n*-doped region, separated by a thin intrinsically doped region within which resides a quantum well hetero-structure (see sub-section 2.4.6).

2.4.4 Doping

As the temperature of a semiconductor is raised, some of the valence band electrons acquire sufficient energy to be excited across the band-gap to the conduction band. This excitation leaves a hole in the valence band and thus creates an electron-hole pair. The electron in the conduction band and the hole in the valence band can both move under the influence of an electric field. The number of electron-hole pairs created in this manner is strongly dependent on temperature, and the semiconductor in which the electrons and holes are as a result of the creation of electron-hole pairs alone is called an intrinsic semiconductor [14]. The intrinsic carrier concentration is defined as the electron concentration in the conduction band, which is thus also equal to the hole concentration in the valence band and may be mathematically expressed by the mass-action law [15]

$$pn = n_i^2 = N_C N_V e^{-E_g / k_B T} \tag{2.25}$$

where p and n are the electron and hole concentrations, n_i is the intrinsic carrier concentration, N_C and N_V are the are the effective density of states in the conduction and valence bands, E_g is the semiconductor band-gap, k_B is the Boltzmann constant and T the temperature of the semiconductor. A simplified energy band diagram for an intrinsic semiconductor is illustrated in Figure 2.6(a). Here, E_{Fi} refers to the Fermi-level in the intrinsic semiconductor, which lies approximately midway between the conduction and valence band-edges in this case.

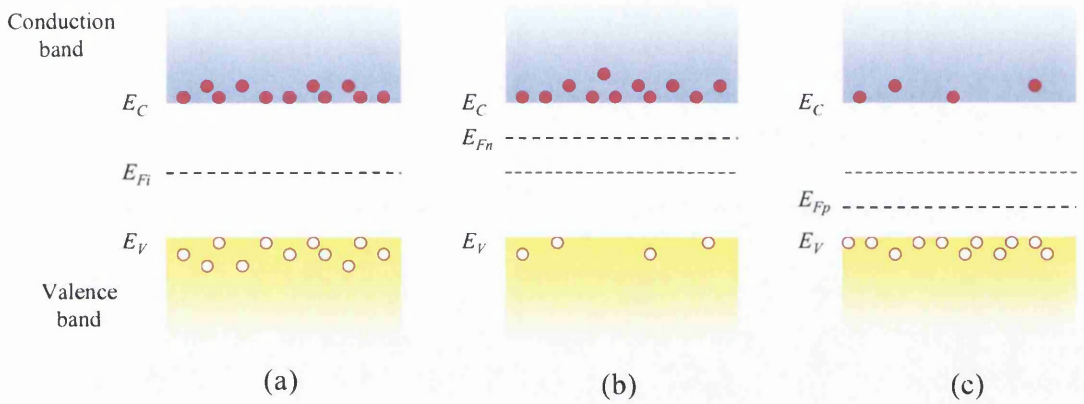

Figure 2.6: A simplified energy band schematic showing allowed states created by the addition of impurity atoms. (a) An intrinsic semiconductor, (b) a *n-type* semiconductor. (c) a *p-type* semiconductor. In all cases $np = n_i^2$.

In practice doping with impurity atoms increases the conductivity of intrinsic semiconductors. If a dopant is added to the intrinsic semiconductor, an extrinsic semiconductor is formed, and doping serves to increase the conductivity of the material. If the added impurity donates excess electrons to the semiconductor, they are called donors, and the semiconductor is termed *n-type* as the majority of carriers are electrons. Suitable donors for silicon are the *group V* atoms phosphorus and arsenic, which fit into the crystal lattice in the place of silicon atoms. Four of the valence electrons will form covalent bonds with neighbouring silicon atoms, while the other valence electron remains weakly attached to the donor atom. Similarly, if a concentration of *group III* atoms (or acceptors), such as boron or gallium is introduced to an intrinsic silicon crystal a *p-type* material is formed, and holes are the

predominant carriers. In this case the acceptor atom gains a valence electron from one of the original covalent bonds, thus producing an extra hole in the valence band.

The addition of dopants actually adds allowed energy states in the forbidden energy gap, slightly below the conduction band E_C at the electron quasi-Fermi level, E_{Fn}, in the case of donors, and slightly above the valence band E_V at thr hole quasi_Fermi level, E_{Fp}, in the case of acceptors. A schematic representation of this is shown above in Figure 2.6(b) and (c).

In the case of low and moderately doped *n-type* semiconductors at low temperatures, the extra donor electrons are still attached to their atoms and occupy the E_{Fn} levels (stable energy state of an electron) and it can be assumed that the impurity atoms are relatively far apart so that their effect on each other is negligible. As temperature increases to about 100K the thermal energy available enables the impurity electrons to shift into one of the many nearby conduction band states. Similarly in the case of low and moderately doped *p-type* semiconductors after an increase of thermal energy, electrons from the originally full valence band with energies E_V will transfer into the higher states E_{Fp} (stable energy state of a hole), thus leaving holes. In both cases the effect is a significant increase in electrical conductivity. It is noteworthy that in an extrinsic semiconductor even though the equilibrium electron and hole concentrations are different their product is constant, and is thus the same as the intrinsic semiconductor [4,14] as depicted in the equation (2.25).

In the following sub-section a brief discussion on semiconductor alloys is presented. This topic has particular relevance in the simulation of red emitting laser diodes, as they are themselves fabricated from ternary and quaternary semiconductor alloys.

2.4.5 Semiconductor Alloys

The individual properties of binary compound semiconductors, of the form AC and BC where A and B are group III elements and C is a group V element, for example, can be combined by coupling an x fraction of one with a $(1 - x)$ fraction of the other. This method naturally produces an alloy, or ternary compound, of the form $A_xB_{1-x}C$, where the lattice spacing, $\mathring{a}$, of the ternary material can be obtained by applying Vegards law [15].

$$\mathring{a}(A_xB_{1-x}C) = \mathring{a}ACx + \mathring{a}BC(1-x) = c_1 + c_2x \qquad (2.26)$$

where c_1 and c_2 are constants. Many other properties of the ternary compound semiconductor are also determined using this approximation, for example the energy band-gaps, effective masses and the elastic coefficients. However, experimental evidence has shown that for some systems, such as the gallium indium phosphide, $Ga_xIn_{1-x}P$, a more correct approximation for the band gap (direct Γ-band) variation with x is quadratic, and may be given by the following expression [16]

$$E_g(Ga_xIn_{1-x}P) = 1.34 + 0.69x + 0.48x^2 . \qquad (2.27)$$

This idea can be taken a step further when considering quaternary materials such as aluminium gallium indium phosphide, $(Al_xGa_{1-x})_yIn_{1-y}P$, which is used in conjunction with $Ga_xIn_{1-x}P$ to produce laser diodes in the 630nm wavelength regime. Here, the y composition is chosen to be lattice matched with that of a GaAs substrate, and the x composition chosen to provide the desired band-gap. The relationship between band-gap and aluminium content in lattice matched AlGaInP has been experimentally deduced by Bour *et al.* [17] to be

$$E_g = 1.91 + 0.61x \qquad (2.28)$$

at 300K for the direct Γ-band. In Section 2.6

In Section 2.6, a closer look at the direct and indirect band-gap parameters for the AlGaInP material system is taken. It becomes evident at high aluminium contents the material becomes indirect as opposed to direct at low contents. This feature has important implications to the design of laser diodes fabricated from this alloy. Also listed within this Section, are all the relevant semiconductor parameters of GaInP and AlGaInP used in the forthcoming Chapters of this thesis.

The following sub-section deals with semiconductor hetero-structures. Within this discussion, a brief look at semiconductor alloys is taken before detailing how the energy bands of two different semiconductor alloys might line-up in a useful way to produce semiconductor devices such as quantum well laser diodes. A short dialogue

highlighting present band line-up models used in theoretical and experimental research follows this.

2.4.6 Hetero-Structures

Nearly all important semiconductor hetero-structures arise when two or more semiconductor materials of differing band-gap are brought together in intimate contact. As a consequence of this situation a potential barrier may be formed at the interface; this is usually referred to as a conduction or valence band discontinuity. The band alignment that results from this scenario is unique for a particular material pair and may depend on both the bulk and surface contributions from the materials involved. Any attempt to manipulate the magnitude of the potential barrier, of fundamental concern to band structure engineering, thus requires a understanding of the factors that dominate the manner of band alignment for the material pair in question.

In sub-section 2.4.6.1, three different ways in which semiconductor band alignment can occur to yield the aforementioned conduction and valence band discontinuities are shown and discussed. A brief overview of the microscopic and macroscopic methods used at present to determine the magnitudes of conduction band discontinuities are reviewed in sub-section 2.4.6.2.

2.4.6.1 Hetero-junctions

A hetero-junction is formed at the interface between two differently terminated semiconductor materials. Figure 2.7 is a schematic of the energy band line-up for a hypothetical hetero-junction. When two crystals are brought together into intimate contact charge will flow until the equilibrium condition is reached, at which point the Fermi-levels of both materials are coincident. The amount of charge transfer required to achieve this depends on the doping levels employed within each layer and may be so large that a region on either side of the interface may become depleted of electrons over a significant distance. This will cause the bands to bend upwards within this region towards the interface. On the other side of the interface, due to an excess of electrons, the bands bend downwards. If two semiconductors have different band

gaps, i.e. E_{gA} and E_{gB}, then the difference in the band gap between these two materials can be written

$$\Delta E_g = E_{gB} - E_{gA}. \tag{2.29}$$

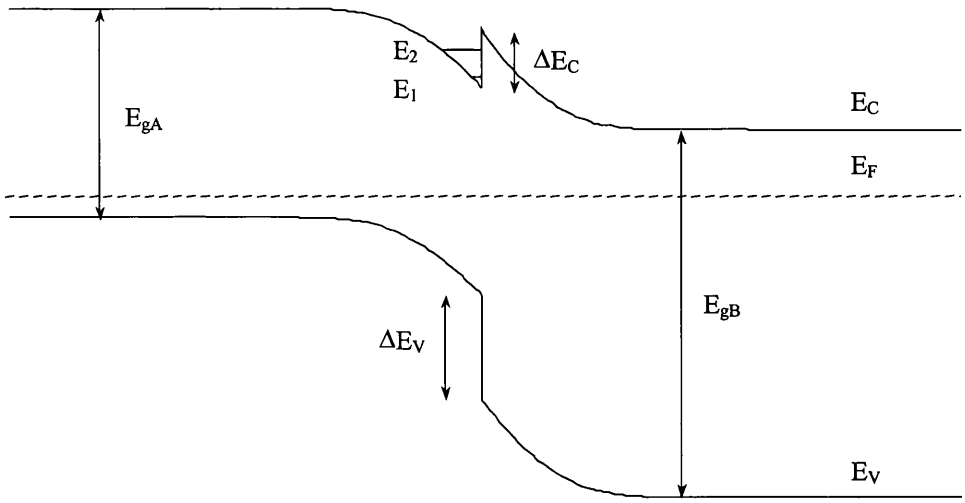

Figure 2.7: Diagram to show the band line-up across a typical hetero-junction. The materials involved have different band-gaps, E_{gA} and E_{gB}, where $E_{gB} > E_{gA}$. Due to the charge transfer required to bring the hetero-junction into equilibrium, a triangular potential well is formed within the accumulation layer at the interface. Electrons contained within this well are quantised.

This magnitude is shared between the valence band discontinuity and the conduction band discontinuity such that

$$\Delta E_g = \Delta E_C + \Delta E_V. \tag{2.30}$$

The electrical and optical behaviour of a hetero-junction is effectively dictated by the magnitudes of ΔE_C and ΔE_V. Therefore determining how the difference in the band-gap is shared between the conduction and valence band discontinuities is of great importance for semiconductor device design.

Three types of band alignment can be defined for the semiconductor hetero-junction (see Figure 2.8 below). Type I occurs when the band gap of material B is nested within the band gap of material A. In this instance, both ΔE_C and ΔE_V are conventionally taken to be positive values. Type II occurs either when the conduction and valence band of A is below the conduction band and valence band of B, referred to as a *staggered* junction, or when the conduction band of A occurs at an energy

below the valence band of material B. This is called a *misaligned* junction. Type III occurs when one of the semiconductors is, in fact, a semi-metal. It is the type I alignment that is used within devices where carrier confinement is important.

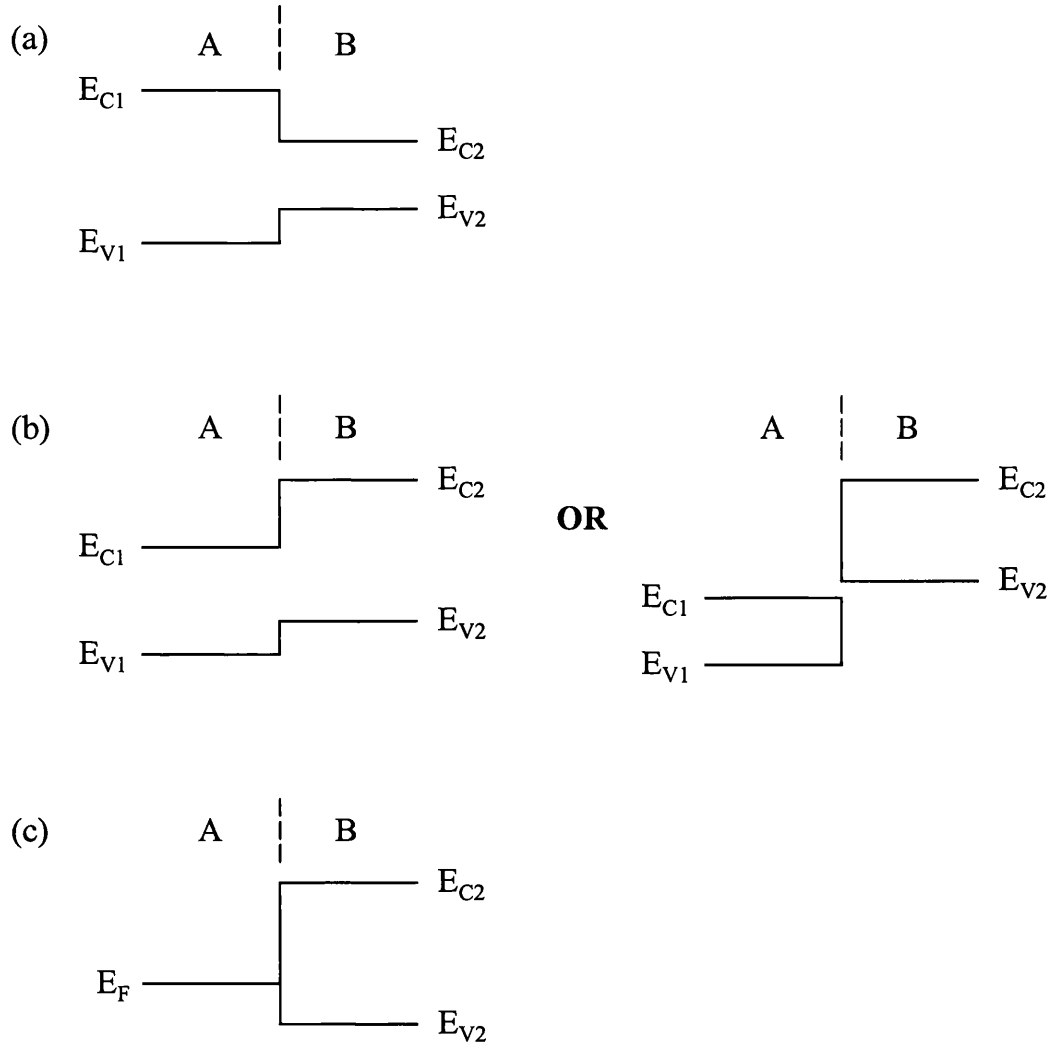

Figure 2.8:Energy band diagrams for (a) a Type I, (b) a Type II and (c) a Type III band discontinuity.

2.4.6.2 Hetero-junction Models

Various models have been proposed which predict the band line-ups of hetero-junctions. In general, the models, which are based on some energy reference level upon which all semiconductors can line-up, are applicable to several material systems. However, none can be universally used with the same degree of success. The basis upon which the models are founded can be separated into two categories:

(i) Macroscopic: these rely on the bulk properties of the materials. Models include the Electron Affinity Rule developed by Anderson [18], the empirical Deep Level model [19] and the Common Anion model [20].

(ii) Microscopic: these include interface details of the materials. Models include Frensley and Kroemers dipole reference potential [21], Harrisons theory of band line-ups [22] and the Charge Neutrality model developed jointly by Tejedor and Flores [23], and Tersoff [24].

A full discussion of the advantages and disadvantages of these models can be found in Chapter 1 of [5].

An alternative approach is to use self-consistent interface calculations (SCIC) [2]. In these calculations the values of the band offsets obtained are determined uniquely by the mathematical approached used. Generally, the principle upon which models are based is that the charge distribution for a particular interface is dependent on the potential at that interface, and vice-versa. This leads to the requirement that the calculations be performed in a self-consistent manner. This enables the charge distribution and any dipole effects occurring at the interface to be automatically included within the calculations. In order to establish the actual physical mechanisms that cause the predicted alignment it is then necessary to compare the theory with experimental results. From such comparisons over a wide range of material conditions, trends can be extracted to determine fundamental factors dominating band alignment for particular systems.

Comparison of macroscopic and microscopic models with experimental results generally gives good agreement. However, the agreement is consistently better for materials where interface effects and charge transfer are small and have little effect on the alignment. This is due to the use of bulk values for material parameters within the models. If the density of the interface states is large then the charge transfer across the interface to bring the system into equilibrium may be dominated by interface states and agreement between 'bulk-based' theory and experiment may be poor.

In the next Section, the previously discussed issues will be combined to explain the structure and basic operation of a general quantum well laser diode.

2.5 Quantum Well Laser Diodes

One of the major objectives of this thesis is to appropriately model the behaviour of 630nm visible laser diodes, details of which are presented in later Chapters. In this Section however, the basic physical idea behind such semiconductor devices is presented. Firstly, the main physical attributes of a general laser diode are reviewed and secondly its mode of operation.

2.5.1 Laser Diode Structure

Quantum-well laser diodes can be thought of as modified versions of the very important solid-state electronic semiconductor *pn*-junction device. These are modified in the sense that, they have a very thin additional intrinsically doped semiconductor layer sandwiched between both the *p*-doped and *n*-doped regions, which comprise the so-called *p-i-n* junction. The semiconductor material or alloy within this intrinsic region has a smaller band-gap than that of the surrounding *p* and *n*-doped layers constituting the formation of a quantum-well by the type I band line-up mechanism as illustrated above in Figure 2.8(a).

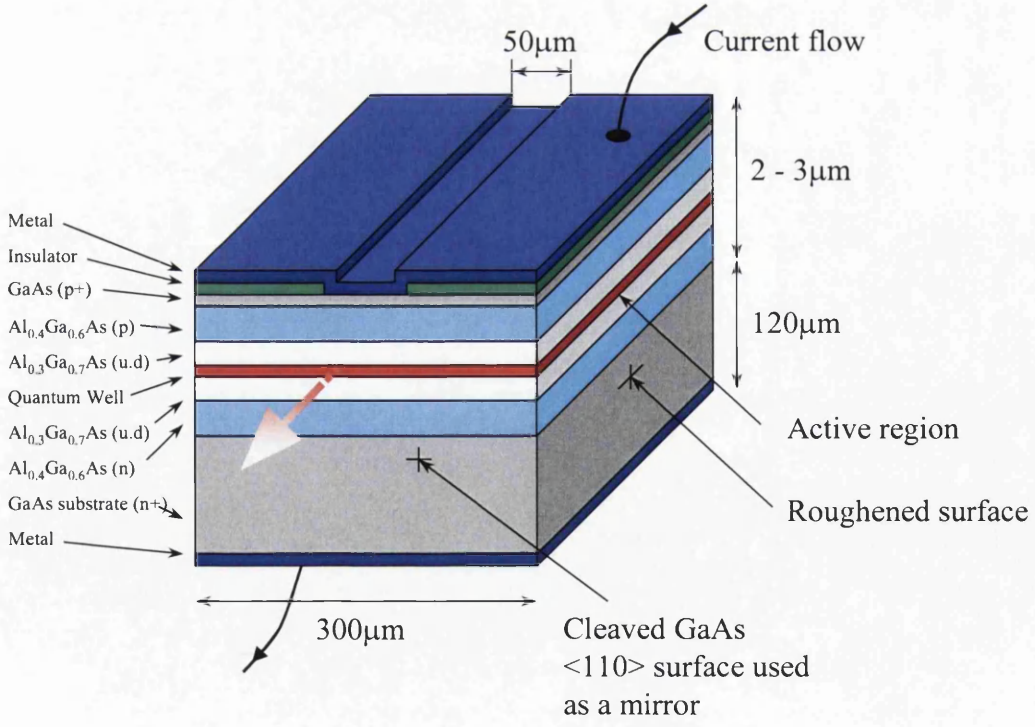

Figure 2.9: A typical AlGaAs semiconductor quantum well laser device.

In practice however, there are many more semiconductor layers than the three suggested above, each of which is specifically chosen to enhance the lasing efficiency of the device. For instance immediately surrounding either side of the quantum well layer there are so-called waveguide regions. These regions serve to guide the light within the active layer, maximising the interaction between the optical field and gain. In Figure 2.9 above, a typical AlGaAs quantum well laser device is illustrated in which the many different material layers of various thickness and doping content are shown. Immediately below and above the metal contacts on the top and bottom of the laser device respectively, are two highly doped GaAs cladding layers. As illustrated in Figure 2.9, the *p*-doped (p+) GaAs layer is relatively thin, whereas *n*-doped (n+) GaAs substrate layer is very thick at approximately 120 microns. Within these two layers exist two $Al_{0.4}Ga_{0.6}As$ layer each moderately *p* or *n*-doped. These layers have a larger band-gap than the surrounding GaAs layers and are used primarily for charge injection into the active region of the device. Contained by these moderately doped AlGaAs alloys are the active regions of the laser diode. This region is undoped (ud) and consists of a GaAs quantum well surrounded by two waveguide regions constructed from the $Al_{0.3}Ga_{0.7}As$ alloy. The $Al_{0.3}Ga_{0.7}As$ alloy has a larger band-gap than GaAs but less than $Al_{0.4}Ga_{0.6}As$ semiconductor. The energy band structure under flatband conditions is schematically illustrated in Figure 2.10 below.

2.5.2 Laser Diode Operation

When a forward bias is applied across a laser diode, electrons and holes are injected into the active region of the device, as illustrated schematically in the band diagram shown in Figure 2.10.

The electrons in the conduction band of the quantum well make a direct transition to valence band where they recombine with holes. Such recombination is radiative and energy quanta in the form of photons are emitted during the process. In order to achieve stimulated emission, the emitted photons must be kept within the active region to activate subsequent emission. This process can be accomplished by using a resonant cavity consisting of two parallel mirrors, known as the *Fabry-Perot resonantor*. The stimulated photons are allowed to bounce back and forth within the cavity, creating an avalanche of photons until lasing threshold is reached and light is then emitted from the barrier. The resonant cavity is usually obtained by cleaving

along the $\langle 110 \rangle$ plane, which is a natural cleaving plane for the GaAs semiconductor. Ideally, the two cleaved $\langle 110 \rangle$ surfaces would be optically flat, forming a pair of parallel mirrors at the two ends of the laser device normal to the active region (shown in Figure 2.9).

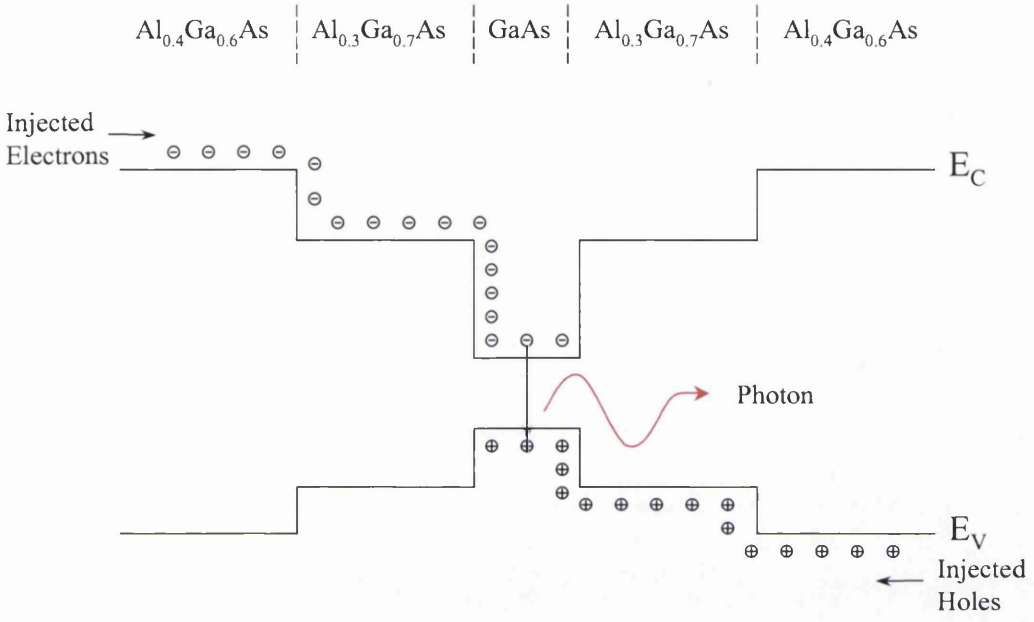

Figure 2.10: Band diagram of the active region in a typical AlGaAs quantum well laser diode. Band diagram illustrates the injection of carriers into the active region of the device under biased conditions (Diagram not drawn to scale).

In the final Section of this Chapter some of the idiosyncrasies associated with the semiconductor materials used to construct 630nm visible laser diodes in particular are illustrated and discussed.

2.6 AlGaInP Material Issues and Parameter List

In Chapter 1 of this thesis, it was highlighted that there are two predominant issues delaying full exploitation of AlGaInP red emitting laser diodes. Both these issues relate back to the fact that such diodes are constructed from the quaternary semiconductor alloy AlGaInP. In sub-section 2.6.1 these issues are inferred from a plot indicating the variation of energy band-gap of both the Γ and X minima as a function of aluminium content. The final sub-section of this Section lists all the

semiconductor parameters for the GaInP and AlGaInP material systems pertinent for laser diode simulation.

2.6.1 AlGaInP Band-Gap Variation

As mentioned previously, the two major idiosyncrasies that at present hinder development of 630nm laser diodes are associated with the AlGaInP semiconductor material used to construct them. These may be summarised as (i) small intrinsic conduction band discontinuities and (ii) the occurrence of inter-valley transport due to elastic scattering between conduction band minima. Both of these issues can be deduced from the variation of energy band-gap of both the Γ and X minima, which are plotted in Figure 2.11 below, as a function of aluminium content.

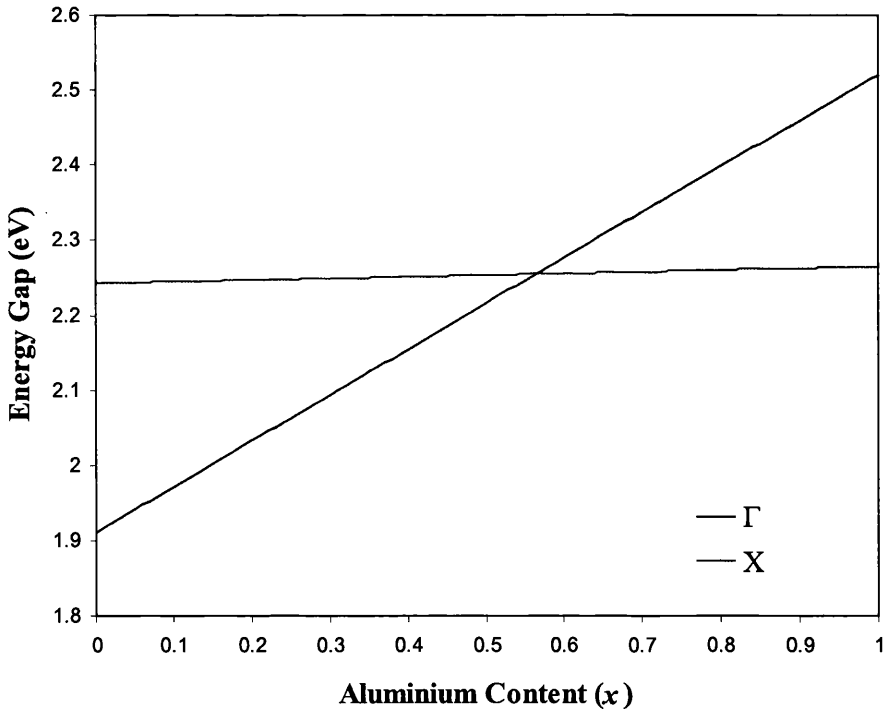

Figure 2.11: Direct and nearest indirect energy gaps of $(Al_xGa_{1-x})_yIn_{1-y}P$ as a function of aluminium content *x*. the smaller energy range covered by AlGaInP makes designing devices with good electrical confinement more difficult.

In sub-section 2.4.5, the variation of direct band-gap of the $(Al_xGa_{1-x})_yIn_{1-y}P$ alloy lattice matched to GaAs (i.e. index *y* is in the range 0.49 to 0.51) was given by the following expression experimentally determined by Bour *et al.* [18]:

$$E_{g\Gamma} = 1.91 + 0.61x. \tag{2.31}$$

where x is the aluminium content in the lattice matched $(Al_xGa_{1-x})_yIn_{1-y}P$ alloy. A stronger aluminium content dependence has been reported at low temperatures by [25,26], but for the laser diode device ultimately under consideration in this thesis, low temperature considerations are for the most part irrelevant. Thus, the weight of evidence supports equation (2.31).

A variety of values have been reported for an expression describing the correlation of the aluminium content and the energy gap of the indirect X-minimum [17,26], in this study, an aluminium dependent expression determined from recent photoluminescence excitation measurements conducted by Krijn *et al.* [27], has been employed, namely

$$E_{gX} = 2.242 + 0.022x. \tag{2.32}$$

Here again, x refers to the aluminium content present within the AlGaInP alloy. As stated earlier, equations (2.31) and (2.32) have been plotted as the aluminium content is increased from 0 to 1 in Figure 2.11 above. It can be deduced from Figure 2.11, that the maximum difference in Γ-point energy across the full range of aluminium content is approximately 0.6eV, this magnitude is relatively small when compared with maximum difference of approximately 1.3eV for a corresponding band in the AlGaAs material system. Consequently, when a hetero-structure is formed by whatever band line-up mechanism, it is an inevitable result that the structure will exhibit small conduction and valence band offsets in comparison with other materials used to fabricate laser diodes. The method used to deduce the band line-ups to produce hetero-structure is presented in Chapter 4.

Figure 2.11 also indicates that there is a conduction band crossover point occurs at an aluminium content of approximately 0.56. Above this value the AlGaInP semiconductor switches from a direct to an indirect semiconductor. To produce hetero-structures such as a simple potential barrier in the AlGaInP material system, typically a low aluminium content such as 0.3 is used to define a well region and a high aluminium content of 0.7 is used to create the barrier. From Figure 2.11, it is evident that the lowest minima in the well regions is the Γ-point and the X-point in

the barrier region, this fact gives rise to the possibility of elastic electron scattering events taking place between the two minima. Suggesting an incident Γ-electron on the aforementioned potential barrier may traverse it by means of switching to the lowest lying minima in each material region. A full account of the transmission routes available to an incident Γ-electron on a similar potential barrier constructed from AlGaInP alloys is discussed in more depth in Chapter 4 of this thesis.

The next sub-section details the expressions used in the remainder of this thesis to determine all the relevant material parameters for the GaInP and AlGaInP alloys.

2.6.2 Material Parameter List

Below is a list of all the material parameters used throughout the following discussion for the GaInP and AlGaInP semiconductor alloys. All the values shown are at present the best estimates for the particular material parameter and if possible a relevant reference is also given.

GaInP

The material parameters for the $Ga_xIn_{1-x}P$ semiconductor alloy are as follows where x refers to the gallium content:

Energy Band-Gaps (eV)

$$E_{g_\Gamma} = 1.34 + 0.69x + 0.48x^2 \text{ [17]} \tag{2.33}$$

$$E_{g_X} = 2.26 \text{ [17]} \tag{2.34}$$

Effective Masses

$$m^*_{e\Gamma} = 0.064 + 0.086x \text{ [17]} \tag{2.35}$$

$$m^*_{eX} = 0.6 \text{ [17]} \tag{2.36}$$

$$m^*_h = 0.6 + 0.19x \text{ [17]} \tag{2.37}$$

Bulk Mobility ($cm^2V^{-1}s^{-1}$)

$$\mu_{e\Gamma} = 600 \text{ [17]} \tag{2.38}$$

$$\mu_{eX} = 100 \text{ [17]} \tag{2.39}$$

$$\mu_h = 170 \text{ [17]} \tag{2.40}$$

Relative Permittivity (Fm^{-1})

$$\varepsilon_r = \varepsilon_0(12.5 - 1.4x) \text{ [17]} \tag{2.41}$$

where ε_0 is the permittivity in a vacuum.

Electron Affinity (eV)

$$\chi = 4.38 - 0.58x \text{ [28]} \tag{2.42}$$

AlGaInP

The material parameters for the $(Al_xGa_{1-x})_yIn_{1-y}P$ semiconductor alloy lattice matched to GaAs are as follows where x refers to the aluminium content:

Energy Band-Gaps (eV)

$$E_{g\Gamma} = 1.91 + 0.61x \text{ [18]} \tag{2.43}$$

$$E_{gX} = 2.242 + 0.022x \text{ [28]} \tag{2.44}$$

Effective Masses

$$m^*_{e\Gamma} = 0.1079 + 0.036x \text{ [28]} \tag{2.45}$$

$$m^*_{eX} = 0.35 \text{ [28]} \tag{2.46}$$

$$m^*_h = 0.4443 + 0.015x \text{ [28]} \tag{2.47}$$

Bulk Mobility ($cm^2V^{-1}s^{-1}$)

$$\mu_{e\Gamma} = 525 - 100x \text{ [28]} \tag{2.48}$$

$$\mu_{eX} = 170 \text{ [29]} \tag{2.49}$$

$$\mu_h = 7 \text{ [29]} \tag{2.50}$$

Relative Permittivity (Fm^{-1})

$$\varepsilon_r = \varepsilon_0(11.76 - 0.954x) \text{ [4]} \tag{2.51}$$

where ε_0 is the permittivity in a vacuum (i.e. $8.854187817\times10^{-12}Fm^{-1}$)

Electron Affinity (eV)

$$\chi = 4.07 + 1.424 + 7.2 + 0.25x - 6.92 - E_{g\Gamma} \text{ [28]} \tag{2.52}$$

2.7 Summary

This Chapter starts with a review of electronic energies of a crystal. A mathematical formalism was derived that revealed electrons within a periodic crystal exist in bands of allowed and forbidden states. This idea is extended in the following Chapter to specifically look at analogous bands that exist in periodic semiconductor hetero-structures. From the existence of such allowed and forbidden bands, crystals were categorised into three main groups namely, metals, insulators and semiconductors. The following Section briefly described some fundamental semiconductor properties such as, energy band structures in which a distinction was made between direct and indirect band-gap semiconductors. Also, touched upon were semiconductor recombination, effective masses, doping of semiconductors and semiconductor alloys and hetero-structures.

In Section 2.5, a brief overview of the construction and operation of a general quantum well laser diode was given. Within this Section it was highlighted that such devices are constructed from many different material layers, each of which as a specific task to ensure optimum performance.

The final Section of this Chapter, briefly commented upon two of the main issues surrounding red emitting laser diodes, namely, inherently small conduction band discontinuities and the possibility of inter-valley transport due conduction band crossover between the Γ and X minima. It was established by means of an energy band-gap diagram, that both these problems are intrinsically associated with the semiconductor material used to construct such devices. The latter part of this Section all relevant material parameters of the AlGaInP and GaInP semiconductors used to simulate red emitting were listed and references to their origin given.

In the following Chapter a step back is taken in order to build-up an understanding of the origin of coupled electron states emerging from closely positioned quantum well systems. The coupling effect initiates minibands of allowed and non-allowed electron states across the multi-layered structure in a similar manner to that predicted in a crystal as shown in Section 2.2 of this Chapter. Chapter 3, goes on to look at implementing such a multi-layered structure within a 630nm laser device to increase carrier confinement within the active region and hence address the issue of small conduction band offsets evident in AlGaInP hetero-structures. The issue of multi-valley transport is addressed in Chapter 4.

2.8 References

[1] C. Kittel., 'Introduction to Solid State Physics', *Wiley*, 7th Edition, (1996).

[2] N.W. Ashcroft and M.D. Mermin, "Solid State Physics", *Holt-Saunders International*, (1976).

[3] R. de L Kronig and W.J. Penney, 'Quantum mechanics of electrons in crystal lattices', *Proc. Roy. Sic.*, Vol. A130, pp. 499-513, (1930).

[4] S.M. Sze. 'Physics of Semiconductor Devices', *Wiley*, 2nd Edition, (1981).

[5] A. Bar-Lev., 'Semiconductors and Electronic Devices', *Prentice Hall International,* 2nd Edition, (1984).

[6] A. C. Marsh and J. C. Inkson, 'An empirical pseudopotential analysis of (100) and (110) GaAs-$Al_xGa_{1-x}As$ heterostructures' *J. Phys.C: Solid-State Phys.*, **17**, pp. 6561-6571, (1984).

[7]A. C. Marsh, 'Indirect band-gap tunnelling through a <100> GaAs/AlAs/GaAs heterostructure', *Semicond. Sci. Technol.*, **1**, pp. 320-326, (1986).

[8] A. C. Marsh, 'Electron tunnelling in GaAs/A/GaAs heterostructures', *IEEE J. Quantum. Electron.*, **23**, pp. 371-375, (1987).

[9] J. R. Chelikowski and M. L. Cohen, *Phys. Rev. B*, **14**, p. 556, (1976).

[10] M. Levinshtein, S. Rumyantsev, and M. Shur, 'Handbook Series On Semiconductor Parameters-Volume 1', *World Scientific*, (1999).

[11] J. R. Hook and H. E. Hall, 'Solid-State Physics', *John Wiley and Sons*, 2nd Edition, (1991).

[12] S. Colak, R. Eppenga, and, M. F. Schuurmans, *IEEE J. Quantum. Electron.*, **23**, pp. 960-967, (1987).

[13] E. O. Kane, Handbook on Semiconductors Vol. 1, *North-Holland,* Amsterdam, (1982).

[14] S.O. Kasap, 'Principals of Electrical and Engineering Materials and Devices', *McGraw-Hill*, (1997).

[15] S. Adachi, *J. Appl. Phys.*, **58** R1-R29, (1985) and references 1-8 therein.

[16] M. Levinshtein, S. Rumyantsev, and M. Shur, 'Handbook Series On Semiconductor Parameters-Volume 2', *World Scientific*, (1999).

[17] D. P. Bour, Chapter 9 in 'Quantum Well Lasers', P. S. Zory, Jr., *Ed. Academic Press*, New York, (1993).

[18] R. L. Anderson, 'Experiments of Ge-GaAs heterojunctions', *Solid-State Electron.*, Vol. **30**, p. 341, (1962).

[19] J. M. Langer and H. Heinrich, *Phys. Rev. Lett.*, **55**, p. 1414, (1985).

[20] J. Tersoff, *Phys. Rev. Lett.*, **56**, p. 2755, (1986).

[21] W. R. Frensley and H. Kroemer, *Phys. Rev. B*, **16**, p. 26421414, (1977).

[22] W. A. Harrison, *J. Vac. Sci and Tech.*, **14**, p. 1016, (1977).

[23] C. Tejeder and, F. Flores, *J. Phys. B.*, **11**, p. L19, (1978).

[24] J. Tersoff, *Phys. Rev. B*, p. 4875, (1984).

[25] M. D. Dawson, G. Duggan and D. J. Arent, *Physical Review B*, **51**, pp. 17660, (1995).

[26] D. J. Mowbray, O. P. Kowalski, M. Hopkinson, M. S. Skolnick, and J. P. R. David, *Appl. Phys. Lett.*, **65**, pp. 213, (1994).

[27] M. P. C. M. Krijn, 'Heterojunction band offsets and effective masses in III-V quarternary alloys', *Semicond. Sci. Tech.*, Vol 6, pp. 27-31, (1991).

[28] Y. Ohba, 'Growth of high-quality InGaAlP epilayers by MOVCD using methyl metaorganics and their applications to visible semiconductor lasers', *J. Crystal Growth*, 77, pp. 374-379, (1986).

[29] S. A. Wood, C. H. Molloy, P. M. Smowton, P. Blood, and C. C. Button, 'Minority Carrier Effects in GaInP Laser Diodes', *J. Quant. Elec.*, Vol. 36(6), (2000).

Chapter 3

Quantum Structures

3.1 Introduction

In the preceding Chapter an analytical model was presented that predicted bands of allowed and forbidden electron energy regions present in a periodic crystal lattice. A similar effect is present in periodic semiconductor hetero-structures, or so-called superlattices. Introduction of a superlattice potential perturbs the band structure of the host material, since the superlattice period is much longer than the original lattice constant. Consequently, the Brillouin zone is divided into a series of minizones, giving rise to narrow subbands, separated by forbidden regions analogous to the Kronig-Penny band model [1,2] for the conduction or valence band of the host crystal.

Also, previously discussed, was the fact that laser diodes constructed from the AlGaInP alloy suffer from small conduction band offsets. These confining potentials offer little hindrance to electrons injected into the active region of the device, and as a result a vast majority escape into the cladding regions of the device to produce high leakage currents.

It was postulated by Iga *et al.* [3] that implementation of a superlattice structure into the *p*-doped cladding region immediately adjacent to the active region, might increase carrier confinement if a miniband of non-allowed electron states could be placed upon the intrinsic barrier height, which may be achieved by tuning the superlattice parameters. This situation would result in an effective increase to the

height of the conduction band offset, thus amplifying the confinement characteristics and giving rise to an improved lasing action.

Thus, the aims of this Chapter are to firstly show, how the minibands of allowed and forbidden energy states arise from coupling of electron wavefunctions between closely positioned quantum wells. And secondly, indicate why embedding a superlattice structure within a laser diode may enable improved lasing performance at elevated temperatures.

Therefore, the structure of the following chapter is as follows; in Section 3.2, a brief introduction to quantum wells is given. Next, solutions to the infinite and finite quantum well systems in Sections 3.3 and 3.4 respectively are described. Additionally, Section 3.4 introduces the reduced electron wavefunction traditionally employed in quantum well analysis, namely, the mass-envelope wavefunction [4]. Furthermore, the boundary conditions needed to evaluate the mass-envelope wavefunction across a hetero-interface are discussed.

The issue of wavefunction coupling between closely positioned wells is discussed in Section 3.5 using a simplified tight binding approximation. The idea of coupled wells is extended to a multi-layered structure (i.e. the multi-quantum barrier (MQB)) in sub-section 3.5.2, from which it is possible to infer the existence of discrete bands of allowed and forbidden eigenenergies stretching across the superlattice.

Section 3.6, discusses how such multi-layered structures embedded within the active region of a laser diode may generate increased carrier confinement, as a direct consequence of fortuitous positioning of the forbidden electron states. Theoretical work already conducted is also acknowledged within this Section. The Chapter closes with a summary and a list of all referenced articles in Section 3.7 and 3.8 respectively.

3.2 Quantum Wells

The single most useful quantum-confined structure in opto-electronics is arguably the quantum well. The quantum well is a sandwich made of a thin (~7nm) layer of a narrower band gap semiconductor, surrounded by two wider band gap semiconductor layers, showing type-I band line up [5,6] (i.e., with the energy minimum for electrons and holes occurring in the narrower band gap semiconductor).

The conduction and valence band profile of a quantum well structure are shown schematically in Figure 3.1 where the effects of band bending have been ignored. The conduction and valence band discontinuities between the two semiconductors provide the quantum well.

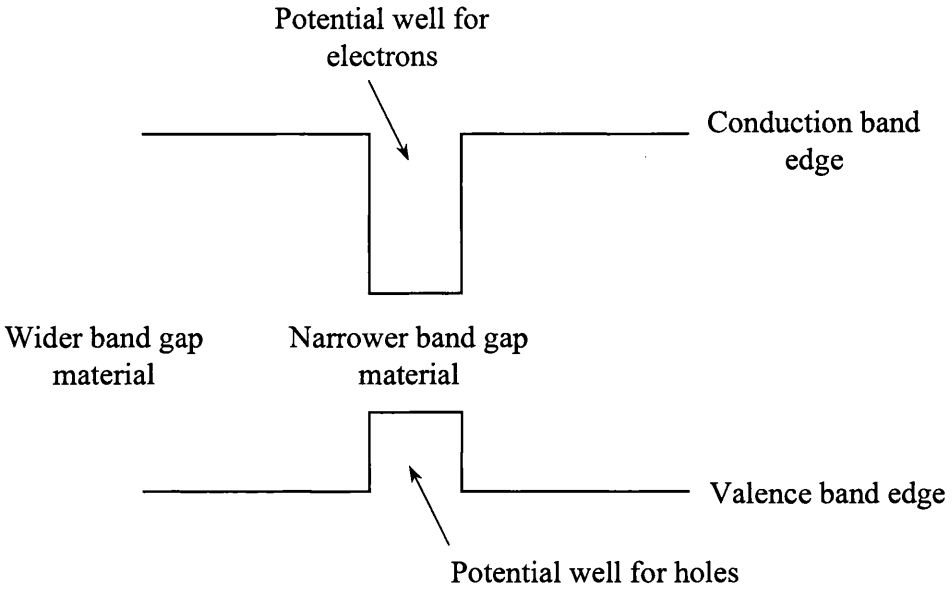

Figure 3.1: Schematic diagram of a quantum well structure, illustrating the formation of the well, by enclosing a narrow band gap semiconductor material by two wider semiconductor materials.

Hence, the narrower band gap layer in the above structure is a potential well for both electrons and holes, both of which will find lower energy in that layer. If the layer is made sufficiently thin, quantum effects also become apparent. For layers of thickness ~10nm, for example, these quantum effects are very obvious even at room temperature in typical semiconductors. The essence of the quantum effects can be understood qualitatively, and approximately quantitatively, through the simple infinitely deep quantum well model (see Section 3.3).

Quantum wells and related structures have a broad range of uses [7,8,9,10]. The use of quantum wells in some existing devices, such as laser diodes and some kinds of photodetectors, can lead to improved device performance. In other cases, such as quantum well modulators, inter-subband detectors, and quantum-cascade lasers, they make possible devices without analogs in bulk materials. They also can be used simply to adjust the effective band gap of materials without changing the underlying material compositions, an option that is useful especially when the material growth is constrained by lattice matching requirements [11].

Because quantum-confined structures can be made relatively easily when one is growing hetero-structures using modern growth techniques [12], they have become a routine part of many advanced opto-electronic device structures, and they can be combined with mirrors, waveguides, transistors, and other optical and electronic structures. They have arguably revolutionised the opportunities for opto-electronics devices and systems. Figure 3.2 shows a scanning tunnelling microscopy (STM) image of an InP/InGaAs/InP quantum well structure published previously by Mitchell *et al.* [13].

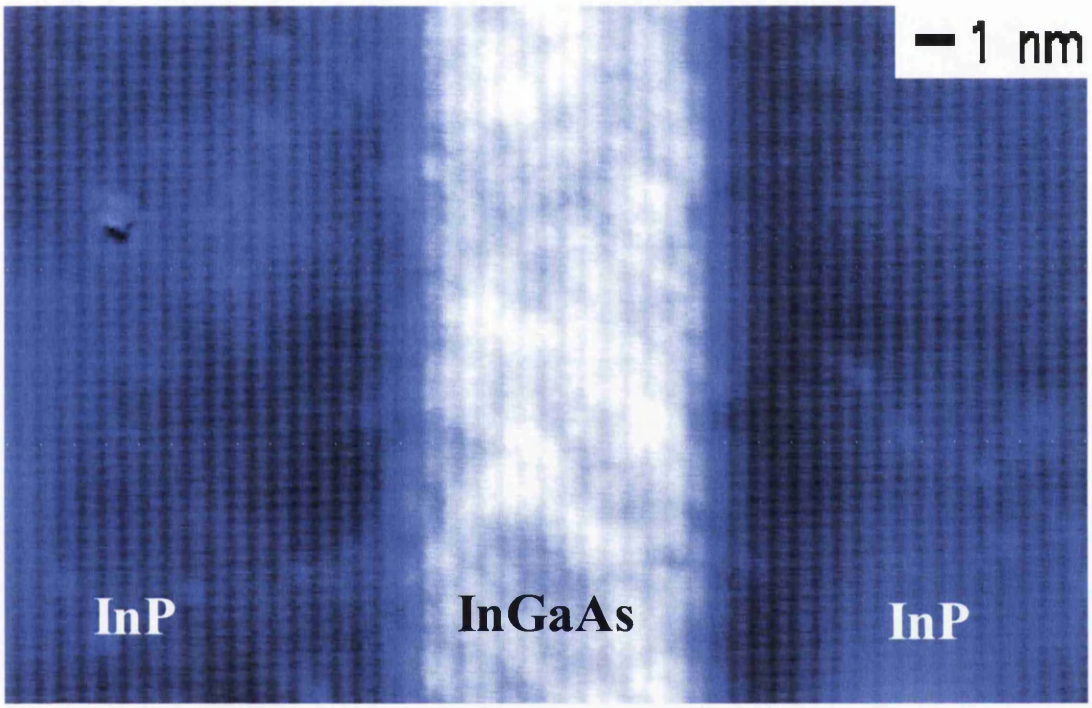

Figure 3.2: Atomically sharp STM image of a quantum well, published by Mitchell *et al.* [13].

3.3 The Infinite Quantum Well

To understand the infinite quantum well model, it is convenient to consider the simplest case i.e. that of a particle, of mass m, in a spatially varying potential $V(x)$ in the x direction. For this discussion it is not essential to consider the fact that in a real structure the particle may also be free to move in the y and z directions. In fact, that motion can be considered separately and its consequences added in later, strictly, the quantum-mechanical problem is separable mathematically in the three dimensions.

Thus, the (time independent) Schrödinger's equation for the particle's motion in the x direction is

$$-\frac{\hbar^2}{2m}\frac{\partial^2\zeta(x)}{\partial x^2}+V(x)\zeta(x)=E\zeta(x) \tag{3.1}$$

where E is the energy of the particle and $\zeta(x)$ is the wavefunction.

In this particular case, the thickness of the well and the value of V in the well are chosen to be L_x and zero respectively. On the either side of the well (i.e. for $x < 0$ or $x > L_x$), the potential, V, is presumed infinitely high. Because these potentials are infinitely high, although the particles energy E is finite, there can be no possibility of finding the particle outside the well; if this case were true, there would be a finite probability of the particle being in a region of infinite energy, which would mean the particle would have infinite energy. Hence, the wavefunction, ζ, of the particle must be zero at the walls of the well. Formally putting the infinite potential into equation (3.1), gives

$$-\frac{\hbar^2}{2m}\frac{\partial^2\zeta(x)}{\partial x^2}=E\zeta(x) \tag{3.2}$$

within the well, subject to the boundary conditions

$$\zeta=0 \quad \text{at} \quad x=0,L_x \tag{3.3}$$

The solution to equation (3.2) is very simple. Explicitly, the eigenfunctions are

$$\zeta_n(x)=A_n\sin\left(\frac{n\pi x}{L_x}\right) \tag{3.4}$$

where A_n is a normalisation constant and the associated eigenenergies are

$$E_n=\frac{\hbar^2}{2m}\left(\frac{n\pi}{L_x}\right)^2. \tag{3.5}$$

The index n is a positive integer, i.e. $n = 1, 2, \ldots$.

The first three energy levels and wavefunctions are calculated and shown below

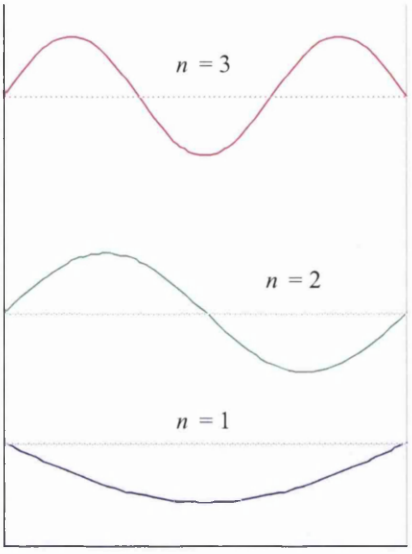

Figure 3.3: Infinite quantum well, which shows the calculated eigenvalues (dotted lines) and their corresponding eigenfunctions (full line) for a well width of 50Å.

There are several basic points about quantum confinement that emerge from this classic particle-in-a-box behaviour characteristic of such quantum-confined systems. First, there is a minimum possible energy for the particle that is above the classical energy associated with the bottom of the well, i.e. corresponding to $n = 1$. (One might think that n = 0 would have zero energy, but since the wavefunction has to be zero at the well walls, the corresponding wavefunction will be zero everywhere, so this is not a physically meaningful state). States corresponding to negative n are not distinct from their positive counterpart, and hence do not need to be considered. The zero-point energy leads to one of the simple uses of quantum wells and related quantum-confined structures, i.e. it is possible to change the effective position of the band edge or the effective size of the band gap by alteration of the layer thickness, without changing material composition.

Secondly, the quantum-confinement energies, E_n, grow quite rapidly (quadratically in this case) as the thickness, L_x, is reduced. In practice this means that the quantum confinement tends to become important at a particular size scale, with a relatively abrupt onset; in semiconductors, this size scale for strong effects at room temperature tends to be around 10nm.

A third point is that, in quantum-confined semiconductors structures, the quantum mechanical properties has to be somewhat different compared to bulk crystalline semiconductors. In the bulk materials, there are $\boldsymbol{k}$-states as the eigenstates, which are momentum eigenstates corresponding to travelling waves going in particular directions. In the quantum-confined system, the eigenstates are generally standing waves, and the quantum number describing this behaviour in the quantum-confined direction is now n, where as before it was k_x.

Another very important point about quantum-confinement effects is that the eigenenergies become larger as the mass of the particle is reduced, a fact that is particularly important for semiconductors where exploitation of small effective masses to get large quantum confinement effects is envisaged. In semiconductors, the quantum confinement can act on the 'envelope function' (see Section 3.4.1) and be based on the effective mass rather than the electron mass. Because, in particular, the electron effective mass can be relatively quite small, and subsequently the quantum confinement effect can be a particularly strong.

3.4 Semiconductor Quantum Wells

There are several differences in the semiconductor quantum well compared to the idealised 'particle-in-a-box' scenario. Firstly, the wavefunction of the particle in question is described by an envelope wavefunction, which is an approximation to the particles full wavefunction. Secondly, the quantum well will have only a finite depth.

3.4.1 Envelope functions

When considering wavefunctions in bulk semiconductors, it is standard to employ the Bloch formalism [14], i.e.:

$$\zeta_{\mathbf{k}}(\mathbf{r}) = u_{\mathbf{k}}(\mathbf{r})\exp(i\mathbf{k}\cdot\mathbf{r}). \tag{3.6}$$

This follows from the fact that the semiconductor is a non-uniform crystal. When the only potential of interest or importance is strictly a periodic potential from the perfectly crystalline structure of the material, this Bloch form is correct, and is a

rigorous solution to Schrödinger's equation in the crystal. In many situations of interest, there are other potentials that are not necessarily completely periodic throughout the crystal. It is obvious in the case of a simple quantum well heterostructure, for example, that the potential does not repeat exactly every unit cell; some of the unit cells are different from the others because they are made of differing materials.

In general, it is possible to consider $u_{\mathbf{k}}(\mathbf{r})$ as being the unit cell part of the wavefunction, and $\exp(i\mathbf{k}\cdot\mathbf{r})$ as being one example of an envelope function. In addition to the case of hetero-structures, there are several other situations where interest lies not simply in the perfect empty crystal, but in additional perturbations to the crystal by way of excitons for example, which lead to other forms of wavefunction [2]. In many cases, however, the resulting wavefunctions can still be approximately, but usefully, written in similar form, especially where the perturbation is not large over a unit cell. Then it is possible to approximately separate the wavefunction into some envelope that is slowly varying over the unit cell, and that multiplies a unit cell function. Such an approach is labelled a 'slowly-varying envelope function approximation'.

In this approximation, the wavefunction is written in the form

$$\mathrm{Z}(\mathbf{r}) = u(\mathbf{r})\zeta_{env}(\mathbf{r}) \tag{3.7}$$

where $\mathbf{Z}(\mathbf{r})$ represents the actual electron or hole wavefunction, $u(\mathbf{r})$ is an appropriate unit cell function, and $\zeta_{env}(\mathbf{r})$ is the envelope function. In quantum wells and similar structures, it is a valid assumption to work with such envelope functions rather than the full wavefunctions, and also to treat the particles as having effective masses. In the case of hetero-structures, the potential perturbation can be non-trivial at the interface between materials, but, with suitable boundary conditions, the envelope function approximation is still applicable. These presumptions can be justified to some extent by the effective mass approximation [15,16,17], which is detailed below. In the case of hetero-structures, the envelope function approach works much better than perhaps first envisaged; it is an effective and relatively accurate model, even in quite extreme situations where it might be expected to fail completely (e.g., for layers only a few unit cells thick inside a hetero-structure).

3.4.2 The Finite Quantum Well

In practice, the barriers on either side of a quantum well are finite. In the semiconductor, they are generally as high as the appropriate band discontinuity between well and barrier material. This finite height introduces one other very important phenomenon, which is tunnelling of the wavefunction into the barrier material.

Returning to equation (3.1), and considering the situation where the eigenenergy, E, is less than the potential energy, V, in some region (as will be the case in the barrier on either side of the quantum well if an allowed state lies within the quantum well), then, in that region, the Schrödinger's equation becomes

$$-\frac{\hbar^2}{2m}\frac{\partial^2\zeta(x)}{\partial x^2}+=-(V(x)-E)\zeta(x) \tag{3.8}$$

where $(V(x)-E)$ is positive. Rather than being sinusoidal, the solutions to this equation are exponentially varying, i.e.,

$$\zeta = A\exp\left(\sqrt{\frac{2m^*(V-E)}{\hbar^2}}x\right)+B\exp\left(-\sqrt{\frac{2m^*(V-E)}{\hbar^2}}x\right) \tag{3.9}$$

where A and B are constants determined by appropriate boundary conditions and normalisation procedures. In general, for a finite quantum well, sinusoidal wavefunctions in the well are expected (for states with energies inside the well), and exponentially decaying wavefunctions into the barrier regions. Though the solutions for the wavefunctions inside the well are still sinusoidal, the wavefunctions now do not, in general, reach zero at the walls of the well and, in general, do not have complete sinusoidal periods or half periods in the well.

At this point it would be straightforward to calculate the actual solution for a hypothetical quantum well that confines a real electron, by matching boundary conditions between the different regions of the quantum well. In the semiconductor case, however, it is important to examine the appropriate boundary conditions more carefully.

3.4.3 Boundary Conditions

In the envelope function case, the electrons generally have different effective masses in the different materials that make up the structure. This means the boundary conditions needed to evolve the wavefunctions across a material interface need to be chosen very carefully. In the case of a simple 'real' electron, continuity is satisfied across a hetero-junction by matching the particular wavefunction, ζ, and its corresponding derivative, $d\zeta/dx$ at either side of the hetero-interface. If the mass is not the same on the two sides, however, these boundary conditions cause problems. In particular, particle current is not conserved. The choice of boundary conditions is still a subject of some debate and there are several conditions that will satisfy conservation of particle current [17,18].

The difficulty of deciding the correct boundary conditions arises because the wavefunctions proper are not dealt with, but their corresponding envelope functions. The envelope functions themselves are approximations, which are derived for slowly varying conditions, making it difficult to deduce what the boundary conditions should be.

Despite these formal complexities, very reasonable practical results, in good agreement with experiment, can be attained with the simple envelope function boundary conditions. Hence, the envelope function approach is used in the spirit of a model rather than the total rigorous theory. In practice, it is quite a reliable model, and is very useful for describing many kinds of properties in semiconductor structures, including electronic states and optical properties of quantum wells and superlattices [19].

The most commonly used envelope boundary conditions are:

$$\zeta(x)^{-} = \zeta(x)^{+}$$

$$\frac{1}{m^{*}(x)}\frac{\partial\zeta(x)}{\partial x}\bigg|^{-} = \frac{1}{m^{*}(x)}\frac{\partial\zeta(x)}{\partial x}\bigg|^{+} \tag{3.10}$$

where $m^{*}(x)$ is the effective mass either side of the material boundary. Presuming in the finite quantum well of interest, there are one or more bound states, there exist two distinct kinds of regions. In the well material, where $E > V$ a sinusoidal solution is

found. In the barrier material where $E < V$, an exponentially decaying solution into each wall on either side is supposed. Applying the above boundary conditions (equation (3.10)), after some algebra, the solutions for the energies of the states, j, of a finite quantum well, may be given by

$$E_j^{1/2} \tan\left[\frac{\pi}{2}\left(\frac{E_j}{E_1^{\infty}}\right)^{1/2}\right] = \left[\frac{m_w}{m_b}(V_b - E_j)\right]^{1/2}$$
$$E_j^{1/2} \cot\left[\frac{\pi}{2}\left(\frac{E_j}{E_1^{\infty}}\right)^{1/2}\right] = \left[\frac{m_w}{m_b}(V_b - E_j)\right]^{1/2} \qquad (3.11)$$

where E_1^{∞} is the energy of the lowest state in an infinite well of the same width, V_b is the height of the barrier relative to the well, and m_w and m_b are the effective masses of the well and barrier materials respectively.

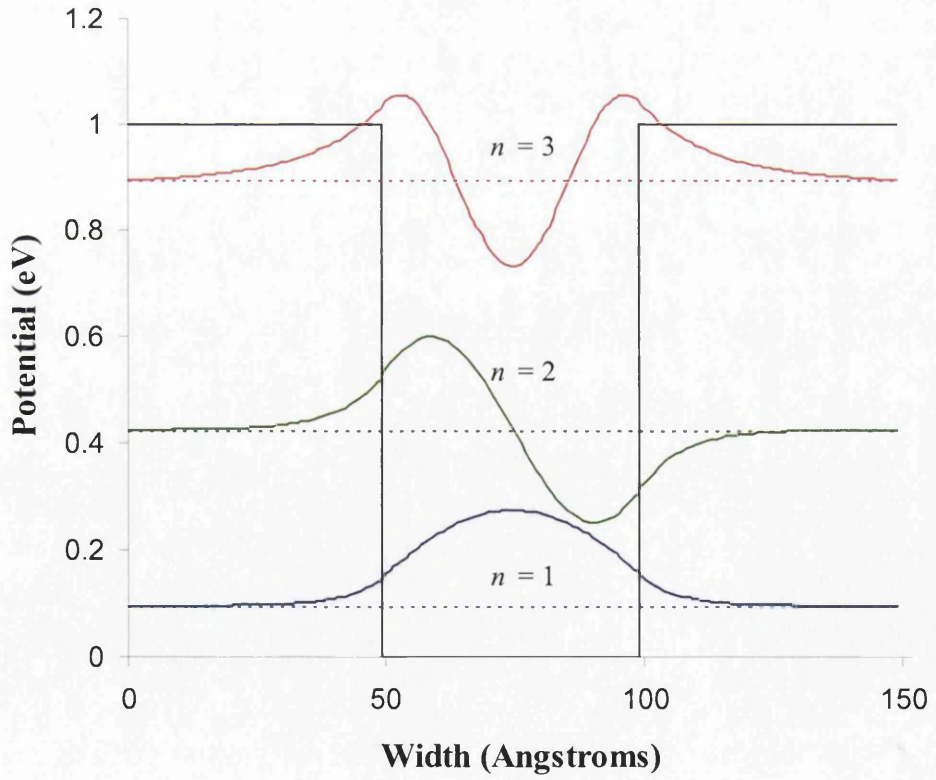

Figure 3.4: Graph showing the three lowest eigenenergy solutions to a 1eV deep, 50Å wide quantum well. The eigenenergies are shown as the dotted lines, whereas full lines denote their corresponding wavefunctions.

The *tan* equation refers to even wavefunctions and the *co-tan* equation refers to odd wavefunctions [20,21]. These solutions are not in closed form; the equations (3.11) have to be solved numerically to find the eigenenergies, E_j. They do illustrate, however, that this finite well problem does have an exact solution. Once the energies of the state are known, it is a simple matter to calculate the sinusoidal and exponential wavefunctions in the well and barrier, respectively. The result of this analysis is illustrated in Figure 3.4 above. Here, the energy eigenvalues (intermittent lines) and their corresponding eigenvectors (solid lines) are shown for the three confined electron states in a 1eV potential well of width 50Å.

3.5 Coupling between Quantum Wells

Hitherto, an isolation quantum well has only been considered. One of the focal points of this dissertation as a whole is to examine the consequences arising from the implementation of a multi-layered quantum well structure within a *p-i-n* laser device. Thus, in the following sub-sections, the coupling effect that occurs between two closely positioned quantum wells is outlined. Following this, the miniband effect (comprising of allowed and non-allowed electron states [22]), which arises from close positioning of many quantum well structures is discussed.

Quantum wells are frequently positioned quite close together [23,24]. If the barrier between two adjacent wells is sufficiently thin that there is significant tunnelling penetration between wells, then quantum mechanically it is necessary to consider them as a coupled system. As a very rough guideline, in most quantum well systems used practically, barriers of ~10nm or thicker have little coupling (at least in the sense of influencing the energy levels), whereas a barrier thickness of ~1nm will probably have very strong coupling between adjacent wells.

Two examples of such coupled systems are the coupled quantum well (a pair of quantum wells separated by a thin potential barrier) and the superlattice (multiple repetitive layers of adjacently positioned quantum wells and barriers e.g. the MQB or the MQW).

3.5.1 Symmetric Coupled Quantum Well

A particularly simple case to analyse, and one that introduces many of the consequences of electronic coupling in quantum well systems, is the symmetric coupled quantum well, illustrated below in Figure 3.5(a). Here, the consequences of coupling between the two lowest lying energy states are illustrated. If the potentials illustrated were considered as, V_{left} and V_{right}, separately (Figures 3.5(b) and (c) respectively), each of the quantum wells would have essentially identical wavefunctions in the lowest energy level. However, if the two wells are positioned less than 100Å apart, a composite potential V is formed. By choosing the potential to be zero within the barrier material, the expression $V = V_{left} + V_{right}$ may be obtained, though the final result does not depend on the location of zero energy.

To illustrate the origin of the coupling behaviour a relatively simple approach may be utilised, whereby the coupling between the adjacent wells is not too strong. This approach is referred to as the Tight-Binding Model, so-called because its validity is most potent, when there is little coupling between adjacent wells, with the electrons then being viewed as being *tightly bound* within a quantum well. Thus, with aforementioned choice of energy origin, the Hamiltonian for this system may be given by the expression

$$H = \frac{-\hbar^2}{2m}\frac{d^2}{dx^2} + V_1 + V_2 . \tag{3.12}$$

The wavefunctions in the isolated wells, ζ_{left} and ζ_{right}, are chosen to be the basis state, on the presumption that all other states are at such different energies and have such different forms of wavefunction that there will be negligible blends of them in the final results, at least approximately. Hence the wavefunction in this problem may be written approximately in the form

$$\zeta = a\zeta_{left} + b\zeta_{right} \tag{3.13}$$

This yields the following form of Schrödinger's equation

$$\left[-\frac{\hbar^2}{2m^*}\frac{\partial^2}{\partial x^2} + V_1 + V_2\right](a\zeta_{left} + b\zeta_{right}) = E(a\zeta_{left} + b\zeta_{right}) . \tag{3.14}$$

Equation (3.14) may be recast in matrix form by pre-multiplying each side by the appropriate basis functions and integrating over distance, to obtain

$$\begin{bmatrix} E_1 & -\Delta E \\ -\Delta E & E_1 \end{bmatrix} \begin{bmatrix} a \\ b \end{bmatrix} = E \begin{bmatrix} a \\ b \end{bmatrix}. \tag{3.15}$$

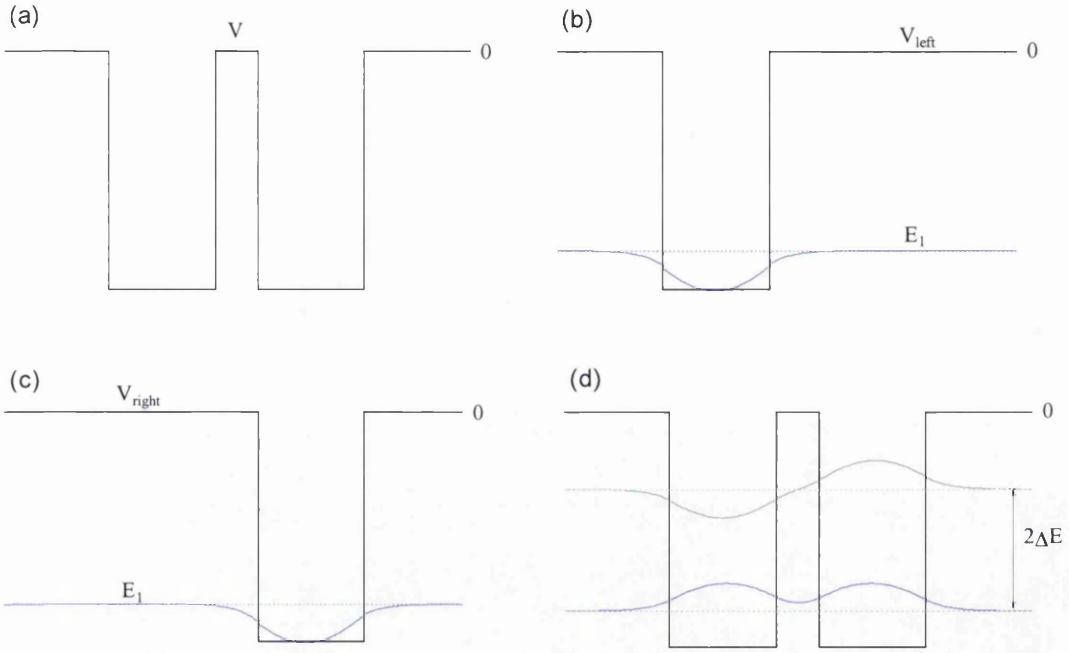

Figure 3.5: Schematic illustration of a coupled quantum well, showing the two-coupled states formed from the lowest states isolated wells. The lower state is symmetric, and the upper state is anti-symmetric.

Here, E_1 is the energy of the first state in the isolated well, and explicitly

$$\Delta E = -\int \zeta^*_{left} H \zeta_{right} dx \tag{3.16}$$

where x, is the horizontal distance coordinate in Figure 3.5. (For simplicity, the wavefunctions are assumed to be real-valued). The minus sign is used in the definition of equation (3.16) because the result of the integral itself will be negative, given the choice of energy origin. In this approximation the following terms have been neglected

$$\int \zeta_{right} V_1 \zeta_{left} dx \quad \text{and} \quad \int \zeta_{left} V_2 \zeta_{right} dx . \tag{3.17}$$

At the positions where V_2 is non-zero, the first integrand is proportional to the square of the amplitude of the tail of the ζ_{left} wavefunction, which is very weak, and similarly for the second integral.

The energy eigenvalues of equation (3.15) are deduced by setting

$$\det\begin{vmatrix} E_1 - E & -\Delta E \\ -\Delta E & E_1 - E \end{vmatrix} = 0 \tag{3.18}$$

to obtain

$$E = E_1 \pm \Delta E\,. \tag{3.19}$$

Within the above approximations, the coupling between the wells splits the energy levels, approximately symmetrically about the original single well energy E_1. By substituting the eigenvalues back into equation (3.15) it is possible to deduce their associated normalised wavefunctions

$$\zeta = \frac{1}{\sqrt{2}}(\zeta_{left} + \zeta_{right}) \text{ and } \zeta = \frac{1}{\sqrt{2}}(\zeta_{left} - \zeta_{right})\,. \tag{3.20}$$

These wavefunctions are calculated and shown in Figure 3.5(d). The lower energy state is associated with a symmetric linear combination of the single well eigenfunctions (i.e. the wavefunction has the same sign in both wells), and the upper state is associated with the anti-symmetric combination (i.e., the wavefunction has the opposite sign in the two wells). Thus, it is not a valid assumption now to view the states as corresponding to an electron in the left or an electron in the right well; in both states the electron is equally in both wells.

3.5.2 Superlattices

If multiple quantum well systems are placed adjacently in a periodic manner, this gives rise to a so-called superlattice structure. Semiconductor superlattice structures can have two different definitions. Crystallographically, a superlattice would be any lattice of lattices. Any periodic arrangement of semiconductor layers

would then be a superlattice. If a large number of quantum wells were evenly spaced with thick barriers, the structure would be crystallographically a superlattice, but, because of the thick barriers, the electronic states would be essentially those of many isolated quantum wells, and this is referred as a multiquantum well (MQW) structure.

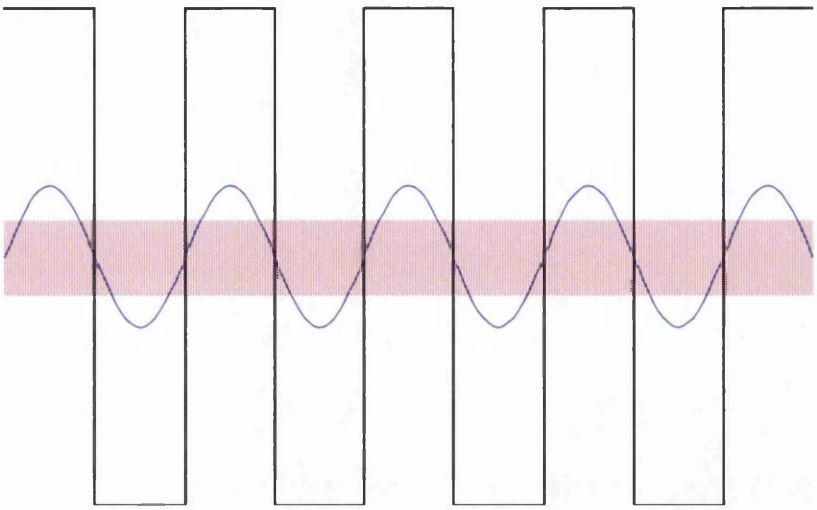

Figure 3.6: Schematic illustration of a superlattice. The red mesh region indicates the miniband of allowed energy states. One of the possible MQB wavefunctions is shown.

Alternatively, if the potential barriers separating the quantum well layers were sufficiently thin, strong quantum mechanical coupling between the layers would be evident (just as in the coupled quantum well system above), subsequently the electronic states would be substantially different. In fact, such a structure, known as a multiquantum barrier (MQB), gives rise to minibands of allowed and forbidden coupled states, analogous to that which arise when considering a regular arrangement of atoms or molecules in crystals [1,2].

As previously stated the multi-quantum barrier is the one of the major focal points of this dissertation; hence, in the following sub-section a detailed analysis of this type of superlattice is considered, rather than the crystallographic one. A MQB superlattice is illustrated above in Figure 3.6, illustrating the position of a miniband of allowed energy levels, and one representative wavefunction. There is a clear link in the properties of superlattices and those of coupled quantum wells, this can be made explicit by constructing a tight-binding model of a superlattice.

3.5.3 Superlattices – Tight-Binding Model

As mentioned earlier, the tight-binding model works well as long as the coupling is not too strong between adjacent wells. The treatment for analysis of a superlattice follows exactly the approach of the tight-binding model sometimes used to analyse electron states and bands in crystals [1,2]. The only difference being in this case the envelope function is considered rather than the true wavefunction itself.

Elementary solid-state physics predicts that the allowed wavefunctions in a periodic potential take on the Bloch form, which for the true wavefunction in a crystal can be written as

$$\zeta_{\mathbf{k}}(\mathbf{r}) = u_{\mathbf{k}}(\mathbf{r})\exp(i\mathbf{k}\cdot\mathbf{r}) \tag{3.21}$$

where $u_{\mathbf{k}}(\mathbf{r})$ has the periodicity of the crystal lattice. In other words, the electron wavefunction $\zeta_{\mathbf{k}}(\mathbf{r})$, is the product of a unit cell wavefunction, $u_{\mathbf{k}}(\mathbf{r})$, that is the same in every unit cell, repeating throughout the entire crystal, and a plane wave $\exp(i\mathbf{k}\cdot\mathbf{r})$. The Bloch theorem comes from the presumption that the wave in a crystal must obey periodic boundary conditions. In the case of the superlattice, the envelope function must have a Bloch form because it must be a solution in this periodic superlattice potential. The approach of the tight-binding model is to assert that, because the coupling is presumed weak between adjacent wells (or unit cells), the unit cell function will be taken to be the unperturbed atomic function. In the superlattice case, the equivalent statement is that the unit cell function will be at the isolated well (i.e., one of the wells from the set of wells that make up the superlattice, considered on its own). This is equivalent to the statement that all other states are at different energies and have different forms of wavefunction, such that there will be negligible admixtures of them in the final results. Hence, these are omitted from the basis set of functions used to address this problem; thus, the basis set will be the isolated well functions for each of the wells in the superlattice. Thus, this is an analogous but extended procedure, to that followed in sub-section 3.5.1 when the coupled quantum well case was considered.

For notational purposes, it is presumed there are N periods within the superlattice, where the envelope function in the Bloch formalism is given by

$$\zeta_k(x) = \frac{1}{\sqrt{N}} \sum \exp(iKx_j)\zeta_{iw}(x - x_j)\,. \tag{3.22}$$

Here, x_j is the position of the centre of a given well in the superlattice, and $\zeta_{iw}(x)$ is the wavefunction in the isolated well. K can take on the values

$$K = \frac{2m\pi}{Na_{sl}}, \quad m = 0, \pm 1, \pm 2, \ldots \pm N \tag{3.23}$$

where a_{sl} is the superlattice period or repeat distance. Equation (3.22) is in a slightly different form from equation (3.21) above, because the unit cell function is not periodic throughout the crystal, but still satisfies the fundamental Bloch condition

$$\zeta_k(x + T) = \exp(iKT)\zeta_k(x) \tag{3.24}$$

for any translation T, of an integer number of superlattice periods, as is easily confirmed by direct substitution into equation (3.22).

Given the above assumptions, it is apparent that these Bloch functions must be energy eigenfunctions of the problem, within the approximations. The energy eigenfunctions have to be in Bloch form as the potential is periodic, also, it has been explicitly presumed that none of the other possible single well basis functions matter (e.g., the second level of a given quantum well is not important here for calculating these properties associated with the first quantum level). Furthermore, a linear combination of the single well basis functions has been constructed using the Bloch formalism.

The Hamiltonian for this problem is a simple extension of the Hamiltonian for the previous scenario, except now the potentials corresponding to each individual well in the superlattice are added in (as before, the top of the barriers is referenced to zero energy). Therefore, the following Hamiltonian may describe the N well superlattice

$$H = \frac{-\hbar^2}{2m}\frac{d^2}{dx^2} + V_1 + V_2 + \ldots + V_N\,. \tag{3.25}$$

It is now possible to evaluate the energy of any of these Bloch functions. where there are E_k energy states, i.e.

$$E_k = \int \zeta_k^*(x) H \zeta_k(x) dx \,. \tag{3.26}$$

Here, it is presumed that the wavefunctions are normalised (which will be the case if the single well wavefunction is normalised). Substituting the wavefunction from equation (3.22) into equation (3.26), gives

$$E_k = \frac{1}{N} \sum_j \sum_p \exp(iK(x_j - x_p)) \int \zeta_{iw}(x - x_p) H \zeta_{iw}(x - x_j) dx \tag{3.27}$$

where for simplicity, the isolated wavefunction ζ_{iw}, is chosen to be real. Taking a nearest neighbour approximation, for any given lattice period j (i.e. centered on x_j), the only integrals that survive will be those where $x_p = x_j$ (i.e. same well terms) or those with $x_p = x_j \pm a_{sl}$ (adjacent well terms). Since, by assumption, the isolated well wavefunctions ψ_{iw} are too small to give any significant contributions once a well more than one period away is considered.

Summing over j simply reduces to a factor N if all of the integrals are assumed the same regardless of the initial superlattice period position, yielding

$$\begin{aligned} E_k = {} & \exp(-iKa_{sl}) \int \zeta_{iw}(x + a_{sl}) H \zeta_{iw}(x) dx \\ & + \int \zeta_{iw}(x) H \zeta_{iw}(x) dx \\ & + \exp(iKa_{sl}) \int \zeta_{iw}(x - a_{sl}) H \zeta_{iw}(x) dx \end{aligned} \tag{3.28}$$

The individual integrals are now the same as the ones dealt with for the coupled quantum well system earlier in Section 3.5.1. Utilising the same approximations, gives

$$\Delta E = -\int \zeta_{iw}(x + a_{sl}) H \zeta_{iw}(x) dx = -\int \zeta_{iw}(x - a_{sl}) H \zeta_{iw}(x) dx \tag{3.29}$$

as previously calculated in equation (3.17), and

$$\int \zeta_{iw}(x) H \zeta_{iw}(x) dx = E_1 \tag{3.30}$$

for the first energy level in the isolated well. Evaluating equation (3.28) yields

$$E_k = E_1 - 2\Delta E \cos(K a_{sl}). \tag{3.31}$$

Equation (3.31) predicts a miniband of states, of total width $4\Delta E$. The lowest energy value for $K = 0$, at $E_1 - 2\Delta E$, corresponds to the wavefunctions in the adjacent wells having the same sign, where the highest value occurs for $K = \pm \pi / a_{sl}$, which corresponds to the wavefunctions in adjacent wells having opposite signs. The superlattice miniband width is twice the separation of the levels in the coupled quantum well, since in the superlattice case it is possible to couple both to a well on the left and right-hand sides.

3.6 Embedded MQB Applications

In the preceding Section, a physical understanding that permits an approximate mathematical description, of the allowed and non-allowed electron energy states apparent across a MQB superlattice was presented. In the following sub-sections it is highlighted why implementation of such structures are able to improve carrier confinement in laser diodes, subsequently increasing device performance at elevated temperatures. Also, theoretical and experimental work previously achieved by other authors in the AlGaInP diode lasers research field is reviewed.

3.6.1 MQB Application to a Laser Diodes

In Section 2.6 of the previous Chapter, it was highlighted that visible 630nm laser diodes comprised of the AlGaInP material system have intrinsically low confining potential barriers [25,26,27,28]. The efficiency of these barriers to retain electrons has increasingly little impact as the temperature of the device is increased (i.e. at applied bias) as lattice vibrations impart a supplementary thermal energy to the electrons entering the active region for recombination. The additional energy gain allows a high percentage of *hot* electrons to overcome the small inherent confining

potential and escape into the cladding regions of the device, subsequently giving rise to high leakage currents [29,30] and breakdown of the laser diode.

This process is illustrated schematically in Figure 3.7(a). Here, a conduction band profile of the active region and immediate surrounding cladding regions of a laser device are shown under flatband conditions. An electron injected from the *n*-type cladding region into the active region is depicted. The incident electron has an energy slightly greater in magnitude than the confining potential barrier, U, in the *p*-type cladding region. Hence, the electron surmounts the barrier and passes into the *p*-doped region of the device adding to a thermal leakage current.

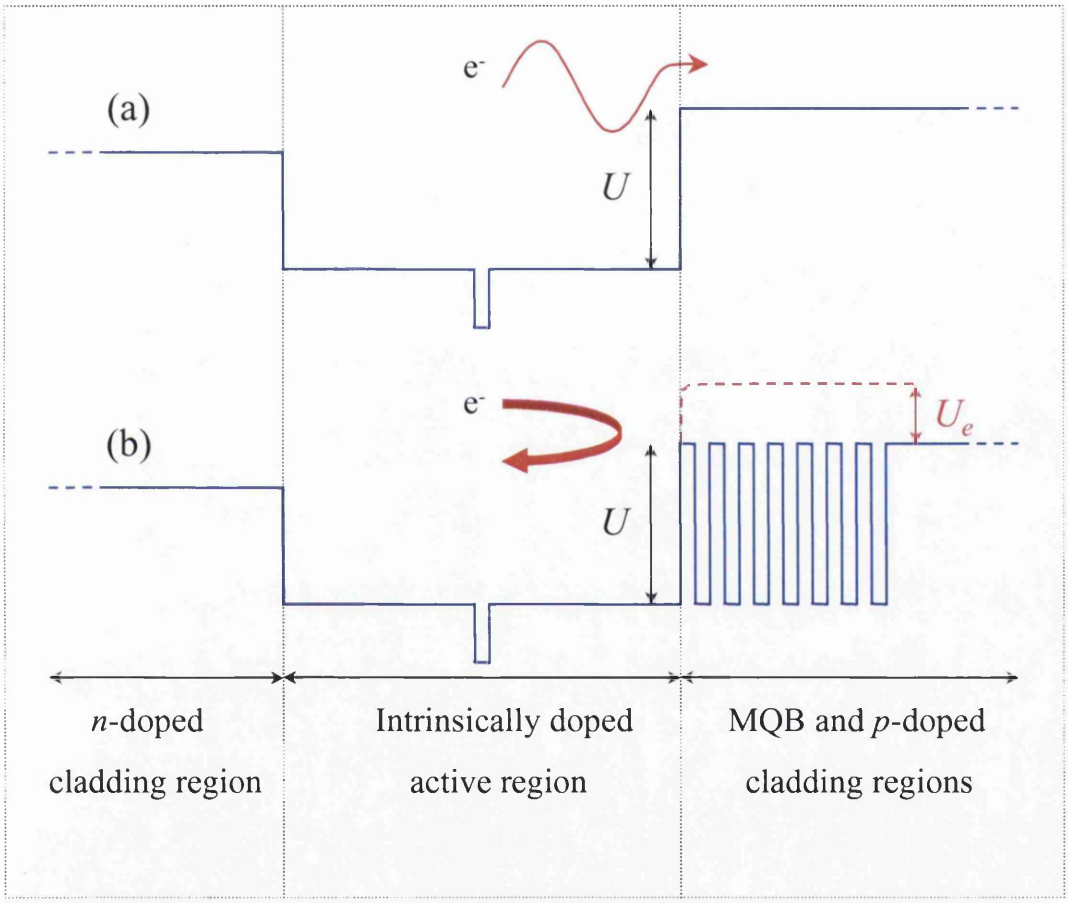

Figure 3.7: Illustration of the MQB effect on an electron injected from *n*-type cladding region. In (a) the electron has sufficient energy to escape from the active region by overcoming the inherently low conduction band barrier. (b) Implementation of a MQB into the *p*-doped cladding region through a quantum mechanical interference effect effectively enhances the conduction band offset such that the incident electron is now reflected back into the active region of the device.

However, in 1986 Iga *et al.* [3] envisaged that MQB superlattices could be implemented within the active regions of light-emitting devices to enhance carrier and optical confinement. The physical idea behind this proposal was that through astute

tuning of the superlattice periods, it would be possible position a band of non-allowed electron energy states upon the existing intrinsic barrier maximum, U, (as illustrated in Figure 3.7(b)). This subsequently results in an effective increase, U_e, to the intrinsic barrier height. This suggests classically, that any incident electron must possess at least an energy greater then $U+U_e$ to negotiate its way over the augmented confining barrier as apposed to U previously. Theoretical enhancements of this nature have been reported to be in excess of 30% the original barrier height [3,31], indicating why implementation of superlattice structures into AlGaInP laser diodes is such an attractive prospect.

The effective enhancement to the intrinsic barrier height can most easily be theoretically determined by calculation of the quantum mechanical reflection probability of the structure; this process is discussed in the following Chapter. The outcome of this numerical analysis is a reflectivity plot similar to the one shown below in Figure 3.8.

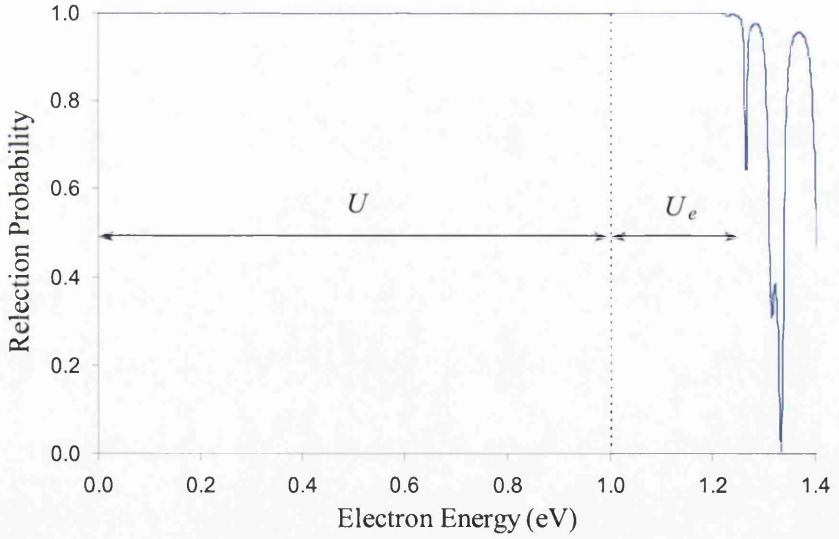

Figure 3.8: An example of a reflection probability plot indicating an enhancement, U_e to the natural barrier height, U.

The reflectivity spectra displayed in Figure 3.8 shows the extent of the effective enhancement, U_e, resulting from a band of non-allowed electron states being positioned directly upon the intrinsic barrier height, U.

3.6.2 Previous Work

Hitherto, there has been much theoretical and experimental work regarding the implementation of superlattice structures within laser devices. Initially, the majority of work has focused on GaInAsP/InP and GaAs/AlGaAs material systems [23,32,33], which are capable of dispensing wavelengths in the infrared regime. Theoretical work in this field has predicted high effective enhancements to the intrinsic barrier heights consequently reducing thermionic leakage currents. Experimental work by Takagi *et al.* and Kishino *et al.* when attempting to verify theoretical predictions found fruitful evidence when analysing comparisons between the reflectivity of a bulk barrier and a MQB were investigated [34,35]. Takagi found that the effective enhancement of the MQB almost matched that predicted by theory in devices comprised of the aforemented materials.

The increasing complexity of devices has developed in parallel with the improved sophistication of the growth techniques available to produce the structures. It is now routine for multi quantum wells (MQW's) and MQB's to be included within the active region of a laser in addition to the MQB contained within the *p*-type cladding layer [24] in GaAs/AlGaAs laser devices.

Within the last decade or so, authors in this field have reverted to the quaternary AlGaInP semiconductor alloy in a bid to produce laser diodes of even shorter wavelength, i.e. in the range 600nm to 700nm. If devices of this nature could be realised they would have a myriad of potential applications open to them spanning both the professional and consumer markets for example, optical memory, laser printers and bar code readers.

However, as previously acknowledged in sub-section 3.6.1, the confining potentials of AlGaInP barriers are relatively small and consequently laser devices constructed of this material suffer from a low characteristic temperatures and high threshold currents, making it difficult to operate them at high temperatures. Thus embedded MQB structures like that in the GaAs/AlGaAs material system seemed the perfect candidate to enhance carrier confinement and improve lasing efficiency of such AlGaInP devices.

Most theoretical work looking at the reflective properties of AlGaInP MQB structures have focused solely on transport via the direct Γ-minimum only [16,36,37], and have shown that theoretically predicted effective enhancements do not coincide

favourably with that found experimentally [38,39]. The candidate most authors attribute to this discrepancy is elastic inter-valley scattering between the lowest lying conduction band minima [36,40]. Scattering of this nature introduces further transport mechanisms other than single Γ-valley transport (see sub-section 4.3.1 in the following Chapter).

Experimental work by Bour [9] and Krijn *et al.* [41] have shown that for low aluminium contents the $(Al_xGa_{1-x})_yIn_{1-y}P$ material is direct, however, as the aluminium content is increased beyond 0.56 the material becomes indirect. This factor is important when constructing an AlGaInP superlattice, where typically the constituent potential barriers and wells are constructed from aluminium contents of 0.6-1 and 0.4-0 respectively. As illustrated in Figure 2.11 of Section 2.6 in the previous Chapter, Γ-point potential barriers will have a lower lying X-point well within them, and similarly, a Γ-point well will have a X-point barrier situated above it at a higher energy. This situation gives rise to the possibility of inter-valley transfer of electrons between the two conduction band minima. Hence, there exists a possibility that an incident electron will pass through the MQB via the Γ-band, or the X-band or a combination of both these transport modes. Recent experimental evidence reported by Blood *et al.* [**Error! Bookmark not defined.**] confirmed that the dominant leakage currents in visible 630nm laser diodes are associated with X-band electrons. Thus, it is crucial to include scattering mechanisms that take account of inter-valley transport when considering the reflective nature of material systems that exhibit conduction band crossover.

3.7 Summary

In the opening Sections of the Chapter, a brief discussion highlighting of the continuing importance of quantum well structures to the welfare of the semiconductor device industry was presented. In Sections 3.3 and 3.4.2, the eigensolutions to the infinite and finite quantum well systems where considered respectively.

Using a simplified tight-binding approximation, the phenomenon of wavefunction coupling between adjacently positioned quantum wells, separated by a small (less than 100Å) potential barrier was investigated. It was deduced that for structures of the aforementioned dimension, it is imperative to recognise that

wavefunctions are strongly coupled, and consequently, they should not be considered as an individual electron residing in one well or the other, but as a superposition of states residing within both.

The idea of a superlattice structure was considered in sub-section 3.5.2. Superlattice structures were categorised into two main genuses; firstly, the multiquantum well, which consists of regular quantum well structures isolated from each other by thick potential barriers, implying no coupling of states. Secondly, the multiquantum barrier or MQB, this consists of quantum wells separated by very narrow layers of barrier material. As a consequence of the small widths of the potential barriers strong coupling between adjacent quantum wells throughout the MQB superlattice is observed. Hence, it was inferred that: (i) there are extended states, i.e., states that in principle extend throughout the entire structure rather than being confined to individual quantum wells; (ii) there are minibands, ranges of energy in which there are allowed states, with mini-bandgaps between them; (iii) the width of the minibands depends very much on the coupling between adjacent wells.

The final issue was discussed in Section 3.6, where it was demonstrated how application of a judiciously designed MQB, may result in placement of a forbidden energy band directly on top of the natural barrier height, which may be viewed sas effectively enhancing the intrinsic barrier height. This situation will result in amplified carrier confinement, giving increased device performance. Further to this, it was suggested that MQB structures would be an ideal candidate to help prevent electron loss in AlGaInP visible 630nm laser diodes where huge leakage currents are evident due to inherently low conduction band offsets.

However, in sub-section 3.6.2 it was emphasised to numerical model the reflectivity probabilities and design MQB structures constructed from the AlGaInP alloy, it is essential that elastic scattering processes between the Γ and X conduction band minima are taken into account.

In the following Chapter, a numerical model is presented which determines the reflectivity profile of a user-defined MQB structure. The model is built-up in stages; firstly, a step back is taken and a single-band Schrödinger solver based on the aforementioned mass-envelope function approximation is established. Following this, the model is extended to allow inter-valley across material hetero-interfaces. These first two stages consider MQB structures in the flatband zero-biased regime, which for

a first approximation is adequate. However, real MQB structures are to be correctly modelled the effects of band bending which occur at applied biases need also be accounted for. This matter is dealt with in Chapter 5.

3.8 References

[1] R. de L Kronig and W.J. Penney, 'Quantum mechanics of electrons in crystal lattices', *Proc. Roy. Sic.*, Vol. A130, pp. 499-513, 1930.

[2] C. Kittel., 'Introduction to Solid State Physics', *Wiley*, 7th Edition, (1996).

[3] K. Iga, H. Uenohara and F. Koyama, 'Electron Reflectance of Multiquantum Barrier', *IEEE Electron. Lett.*, **22**(19), pp.1008, (1986).

[4] R. Tsu, and L. Esaki, 'Tunnelling in a finite superlattice', *Appl. Phys. Lett.*, **22**, pp. 562-564, (1973).

[5] J. Singh, 'Semiconductor Optoelectronics Physics and Technology', *McGraw Hill*, (1995).

[6] J. Batey, S. L. Wright, and D. J. Dimaria, 'Energy bandgap discontinuities in GaAs: (Al)GaAs heterojunctions', *Appl. Phys. Lett.*, **57**, pp. 484-487, (1985).

[7] H. C. JR. Casey, and M. B. Panish, 'Heterostructure lasers, part A, fundamental principles', *Academic Press*, pp. 192, (1978).

[8] P. Blood, 'Heterostructures in semiconductor lasers', in: D. V. Morgan and R. H. Williams (Eds.), 'Physics and Technology of Heterostructure Devices', *Perigrinus*, London, (1990).

[9] D. P. Bour, Chapter 9 in 'Quantum Well Lasers', P. S. Zory, Jr., *Ed. Academic Press*, New York, (1993).

[10] C. H. Henry, 'The Origin of Quantum Wells and the Quantum Well laser',in: P. S. Zory, Jr (Ed.), 'Quantum Well Lasers', *Academic Press*, San Diego, pp. 1-16, (1993).

[11] P.M. Smowton and P. Blood, 'Visible emitting (AlGa)InP laser diodes', in: M. O. Manasreh (Ed.), 'Strained-layer Quantum Wells and their applications', *Gordon and Breach*, pp. 431-487, (1997).

[12] M. Razeghi, 'The MOVCD challenge: Vol. 1; 'A Survey of AsGaInP-InP for Photonic and Electronic Applications', *Adam Hilger Press*, (1989).

[13] H. J. Chen, H. A. McKay, R. M. Feenstra, G. C. Aers, P. J. Poole, R. L. Williams, S. Charbonneau, P. G. Piva, T. W. Simpson, I. V. Mitchell, 'InGaAs/InP quantum well intermixing studied by cross-sectional scanning tunnelling microscopy'. *J. Appl. Phys.*, **89**(9), pp. 4815-4823, (2001).

[14] N.W. Ashcroft and M.D. Mermin., 'Solid State Physics', *Holt-Saunders International*, (1976).

[15] K. Iga, H. Uenohara, and F. Koyama, 'Electron Reflectance of Multiquantum Barrier (MQB)', *Electron. Lett.*, **22**, pp. 1008, (1986).

[16] H. Uenohara, K.Iga, and F. Koyama, 'Analysis of electron reflectivity and leakage current of multiquantum barrier, (MQB)', *Trans. IEICE Japan*, **J70-C**, pp. 851-857, (1987).

[17] Y. Seko, S. Fukatsu and Y. Shiraki, 'Optical transition energies of GaInP quantum wells with GaInP/AlInP superlattice barriers', *J. Appl. Phys.*, **72**, pp. 1355-1357, (1994).

[18] M. G. Burt, 'The Justification for Applying the Effective-Mass Approximation to Microstructures', *J. Phys: Condens, Matter*, **4**, pp.6651-6690, (1992).

[19] W. A. Harrison and A. Kozlov, 'Matching Conditions in Effective Mass Theory', *Proc. 21st Int. Conf. Phys. Semiconductors*, Beijing, China, (1992).

[20] P. C. W. Davies, 'Quantum Mechanics', Chapman and Hall, (1989).

[21] F. Mandel, 'Quantum Mechanics', John Wiley & Sons, (1996).

[22] Y. Huang, C. Wang and, C. Lien, 'Electric-field enhancement and extinguishment of optical second-harmonic generation in asymmetric coupled quantum wells', *IEEE J. Quant. Electron.*, **31**(10), pp. 1717-1725, (1995).

[23] Koyama, K.Y. Liou, A.G. Dentai, T. Tanbun-ek and C.A. Burrus, 'Multiple-quantum well GaInAs/GaInAsP tapered broad-area amplifiers with monolithically integrated waveguidelayers for high-power applications', *IEEE Photonic Tech. Lett.*, **5**, pp. 916, (1993).

[24] D.H. Chow, R.H. Miles, T.C. Hasenburg, A.R. Kost, Y.H. Zhang, H.L. Dunlao and L. West, 'Mid-wave infrared diode lasers based on GaInSb/InAs and InAs/AlSb superlattices' *Appl. Phys. Lett.*, **67**(25), p.3700, (1995).

[25] A. Valster, C. T. H. F. Liedenbaum, M. M. v.d.Heijden, G. Finke, A. L. G. Severens, and M. J. B. Borrmans, '633 operation of GaInP/AlGaInP laser-diodes', *In Proc. 12th IEEE Semiconductor Laser Conf.*, pp.28-29, (1990).

[26] H. Hamada, M. Shono, S. Honda, R. Hiroyama, K. Yodoshi, and Y. Yamaguchi, '*AlGaInP visible laser diodes grown on misordered substrates*', *In Proc. 12th IEEE Semiconductor Laser Conf.*, pp.174-175, (1990).

[27] A. T. Meney, A. D. Prins, A. F. Phillips, J. L. Sly, E. P. O'Reilly, D. J. Dunstun, A. R. Adams, and A. Vaster, 'Determination of the band structure of disordered AlGaInP and its influence on visible-laser characteristics', *IEEE J. Select. Quantum Electron.*, **1**, pp.697-706, (1995).

[28] D. P. Bour, D. W. Treat, R. L. Thornton, R. S. Geels, and D. F. Welch, 'Drift leakage in AlGaInP quantum well lasers', *IEEE J. Quantum Electron.*, **29**, pp.1337-1342, (1993).

[29] D. P. Bour, D. W. Treat, K. J. Beernine, B. S. Krusor, R. S. Geels, and D. F. Welch, '', *IEEE Photonic Tech. Lett.*, **6**, pp. 128-131, (1994).

[30] S. A. Wood,C. H. Molloy, P. M. Smowton, P. Blood C. C. Button, 'Minority Carrier Effects in GaInP Laser Dioides', *IEEE J. Quantum. Electron.*, **36**, pp. 742-750, (2000).

[31] H. Uenohara, K.Iga, and F. Koyama, 'Analysis of electron reflectivity and leakage current of multiquantum barrier, (MQB)', *Trans. IEICE Japan*, **J70-C**, pp. 851-857, (1987).

[32] H. Lee, P. K. York, R. J. Menna, R. V. Martinelli, D. Z. Garbuzov, S. Y. Narayon and J. C. Connelly, 'Room-temperature 2.78 μm AlGaAsSb/InGaAsSb quantum-well lasers', *Appl. Phys. Lett.* **66**(15), p.1942, (1995).

[33] M. Irikawa, H. Shimizu, T. Fukushima, K. Nishikata and Y. Hirayama, 'Strained GaInAs-AlGaInAs 1.5mm-wavelength MQW laser loaded with GaInAs-AlInAs MQB's at the p-type optical confinement layer', *J. Selected topics in Quantum. Elec.*, **1**, pp. 285, (1995).

[34] T. Takagi, F. Koyama and K. Iga, 'Design and Photoluminescence Study on a Multiquantum Barrier ', *Electron Lett.*, **27**, pp.1511-1518, (1991).

[35] K. Kishino, A. Kikuchi, Y. Kaneko and I. Nomura, 'Enhanced carrier confinement by the multiquantum barrier in 660nm GaInP/AlInP visible lasers', *Appl. Phys. Lett.*, **58**, pp. 1822-1824, (1991).

[36] T. Takagi, F. Koyama and K. Iga, 'Modified multiquantum barrier for 600nm range AlGaInP lasers', *Electronic Lett.*, **27**(12), pp. 1081-1082, (1991).

[37] C. S. Chang, Y. K. Su, S. J. Chang, P. T. Chang, Y. R. Wu, K. H. Huang, and T. P. Chen, 'High-Brightness AlGaInP 573nm Light-Emitting Diode with A Chirped Multiquantum Barrier', *IEEE J. Quantum. Electron.*, **34**(1), pp. 77-82, (1998).

[38] P. Raisch, R. Winterhoff, W. Wagner, M. Kessler, H. Schweizer, T. Riedl, R. Wirth, A. Hangleiter, and F. Scholz, 'Investigations on the performance of multiquantum barriers in short wavelength (630nm) AlGaInP laser diodes', *Appl. Phys. Lett.*, **74**(15), (1999).

[39] A. P. Morrison, J. D. Lambkin, C. J. van der Poel, and A. Valster, 'Evaluation of Multiquantum Barriers in Bulk Double Heterostructure Visible Laser Diodes', *IEEE Photon. Tech. Lett.*, **8**(7), (1996).

[40] P. M. Smowton and P. Blood, 'GaInP $(Al_xGa_{1-x})_yIn_{1-y}P$ 670nm quantum well lasers for high-temperature operation', *IEEE J. Quantum. Electron.*, **31**, pp. 2159-2164, (1995).

[41] M. P. C. M. Krijn, 'Heterojunction band offsets and effective masses in III-V quaternary alloys', *Semicond. Sci. Tech.*, Vol 6, pp. 27-31, (1991).

Chapter 4

Multiquantum Barrier Numerical Model

4.1 Introduction

The premise of this Chapter is to develop a numerical simulation package able to calculate the quantum mechanical reflection probability associated with a user defined multiquantum barrier (MQB) reflector. This subsequently will allow any effective enhancement to the natural stopping potential barrier arising from extended non-allowed electron states (minibands) within the structure to be determined. To achieve this task the numerical model describing the path of the electron across the MQB reflector has been assembled in stages.

Firstly, transport across the MQB is considered initially to take place via the direct Γ-point alone, consistent with calculations presented by the majority of authors in this field. However, in Chapter 2 it was highlighted that the AlGaInP material system needed to produce visible wavelengths in the 600 to 700nm regime is subject to a conduction band crossover at aluminium contents of 0.56 and above, whereby the lowest conduction band minima reverts from the direct Γ-minimum to the indirect X-minimum. Thus, in the second instance the numerical model is adapted to consider the possibility of inter-valley transport from the Γ to the X-valley and visa-versa. To simplify the initial analysis all MQB structures in this Chapter are considered under flatband zero-biased conditions. In the following Chapters a more realistic conduction band is presented where Poisson's equation is solved across the simulation region to imitate the effects of band bending present in laser diodes under applied bias.

Therefore, the structure of this chapter is as follows; in Section 4.2, the transfer matrix method (TMM) employed to evolve the wavefunction and its derivative of an incident electron in the mass-envelope function approximation and solve Schrödinger's equation across a MQB structure is summarised. This procedure is presented for electrons in the direct Γ-valley only. The TMM is illustrated by calculating and comparing the reflection spectra associated with a classical potential step, a single potential barrier and a theoretical MQB reflector.

The numerical model is evolved in Section 4.3, to include the additional electron transport mechanisms that arise if inter-valley transport between the Γ and X conduction band minima is considered. These transport modes are illustrated across a single AlGaInP hetero-barrier structure. To verify the applicability of the improved simulation package, the calculated the reflectivity spectra across a single aluminium arsenide potential barrier is compared with a more sophisticated psuedo-potential technique used on this material system.

Section 4.4 of this Chapter outlines the optimisation procedure utilised throughout this investigation to achieve the greatest barrier enhancement through astute tuning of the MQB's periodicity. An additional physical problem associated with the AlGaInP material system used to develop 630nm laser diodes is also discussed here. This primarily is a growth issue concerning superlattice hetero-interface roughness.

Using the optimisation procedure a single Γ-band and a novel dual Γ-X band MQB reflector is presented in Section 4.5. Comparison of the reflectivity spectra from both MQBs is displayed and some remarks concerning the impact of inter-valley transfer on these structures is given.

The Chapter concludes with a summary of the main aspects encountered within the above Sections and all cited articles are referenced in Sections 4.6 and 4.7 respectively.

4.2 Single-Valley Reflectivity Model

In the preceding chapter, it was mathematically deduced that within the multiquantum barrier there exist allowed and forbidden energy regions (i.e., minibands), analogous to those found in a periodic crystal lattice [1,2]. It was

established that these minibands originate from wavefunction coupling between adjacent well layers, and may extend across the whole superlattice structure. By a judicious choice of the superlattice parameters (i.e. material, widths and doping values), a miniband of non-allowed energy states may be placed directly upon the barrier height maximum enhancing its effective height. As briefly discussed in Chapter 3 sub-section 3.6.1, a simple way to determine the effective enhancement associated with a particular MQB arrangement is to calculate the reflection and transmission probabilities across it for a specified energy spectrum. The reflectivity of a MQB is most easily ascertained by utilising the mass-envelope function approach [3,4,5] introduced in the previous chapter, in conjunction with the transfer matrix method (TMM) [3,4,5], which is briefly outlined in the following Section.

4.2.1 Transfer Matrix Method

In this investigation the electron reflectivity only is evaluated, although the following method is equally valid for the calculation of the reflection spectra of holes with only one additional requirement concerning the average value of the effective mass due the three different valence band maximums. However, very good quantitative results can be obtain by considering just the heavy hole mass [2].

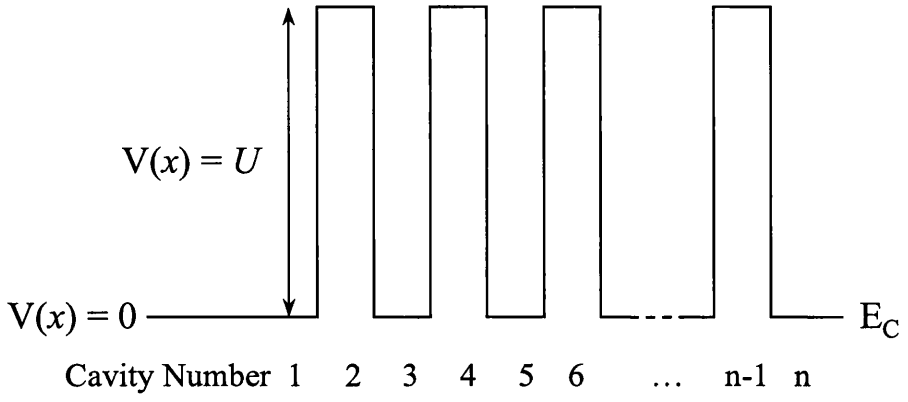

Figure 4.1: Schematic diagram indicating the conduction band of superlattice structure comprising of n material layers. The potential of the quantum wells is referenced to zero for simplicity and the height of the potential barriers is given by the value *U*.

To evaluate the reflection probability the one-electron Schrödinger equation (equation (4.1)) needs to be solved to determine the wavefunction, ζ, of the electron.

$$-\frac{\hbar^2}{2}\frac{\partial}{\partial x}\frac{1}{m(x)}\frac{\partial\zeta(x)}{\partial x}+V(x)\zeta(x)=E\zeta(x) \tag{4.1}$$

here $\hbar$ is Plank's reduced constant, $V(x)$ is piecewise constant potential and has a value $V(x) = U$ if the layer number is even and zero otherwise (see Figure 4.1), $m^*(x)$ is the position dependent effective mass and E is the total energy of the electron. Solution of equation (4.1) may be written as a plane wave and subsequently the wavefunctions of the first and second cavities may be expressed as

$$\zeta_1 = A_1 e^{ik_1 x} + B_1 e^{-ik_1 x} \tag{4.2}$$

$$\zeta_2 = A_2 e^{ik_2 x} + B_2 e^{-ik_2 x} \tag{4.3}$$

where A and B are the amplitudes of the incident and reflected waves respectively. The wavevector, k, in first cavity can be given by

$$k_1 = \sqrt{\frac{2m_1^* E}{\hbar^2}} \tag{4.4}$$

and by

$$k_2 = \sqrt{\frac{2m_2^* (E-U)}{\hbar^2}} \tag{4.5}$$

in the second cavity.

The problem is set-up such that the energy of the electron impinging on the MQB structure is always greater than zero. Subsequently, k_1 will always be real and the wavefunction will be propagating, whilst k_2 will be imaginary for electron energies less than U and real otherwise resulting in wavefunctions that will be evanescent and propagating respectively in these energy ranges.

Previously in Chapter 3 Section 3.4, equation (4.1) was applied to a quantum well hetero-structure to yield the energy eigenfunctions and eigenvectors of the confined electron states within. In this scenario, continuity of the wavefunction and its

derivative multiplied by the reciprocal effective mass across a material interface was upheld. The same continuity scheme is also adhered to when calculating the quantum mechanical reflection probabilities of a particular structure in the mass-envelope approximation. Equation (4.6) below gives the continuity condition across the first hetero-interface sandwiched between the first and second material layers.

$$\begin{gathered}\zeta_1 = \zeta_2 \\ \frac{-\hbar^2}{2}\left(\frac{1}{m_1^*(x)}\frac{\partial\zeta_1}{\partial x} - \frac{1}{m_2^*(x)}\frac{\partial\zeta_2}{\partial x}\right) = 0\end{gathered} \tag{4.6}$$

Expressing the wavefunctions and their corresponding derivatives fully across the first material interface the matching conditions above may be given by the following matrix equation

$$\begin{pmatrix} e^{ik_1 z} & e^{-ik_1 z} \\ \frac{ik_1}{m_1^*}e^{ik_1 z} & \frac{-ik_1}{m_1^*}e^{ik_1 z} \end{pmatrix}\begin{pmatrix} A_1 \\ B_1 \end{pmatrix} = \begin{pmatrix} e^{ik_2 z} & e^{-ik_2 z} \\ \frac{ik_1}{m_1^*}e^{ik_2 z} & \frac{-ik_2}{m_2^*}e^{ik_2 z} \end{pmatrix}\begin{pmatrix} A_2 \\ B_2 \end{pmatrix}. \tag{4.7}$$

Equation (4.7) may be rewritten more compactly as

$$M_1\begin{pmatrix} A_1 \\ B_1 \end{pmatrix} = M_2\begin{pmatrix} A_2 \\ B_2 \end{pmatrix}. \tag{4.8}$$

Similar matrix equations may be determined for the material interface between layers 2 and 3, i.e.,

$$M_2\begin{pmatrix} A_2 \\ B_2 \end{pmatrix} = M_3\begin{pmatrix} A_3 \\ B_3 \end{pmatrix}. \tag{4.9}$$

Eliminating the coefficients A_2 and B_2 from equations (4.8) and (4.9) yields

$$\begin{pmatrix} A_1 \\ B_1 \end{pmatrix} = M_1^{-1}M_2M_3^{-1}\begin{pmatrix} A_3 \\ B_3 \end{pmatrix} \tag{4.10}$$

By continuing on in this manner the coefficients of the nth layer can be related to those of the first via the M matrices, which transfer information about the wavefunction and its derivative at each of the material interfaces across the whole MQB structure. It is assumed in this case and all others in this investigation that the outgoing (transmitted) wave has no reflected component, which allows the matrix equation (equation (4.10)) to be written as

$$\begin{pmatrix} A_1 \\ B_1 \end{pmatrix} = M_1^{-1} M_2 M_3^{-1} M_4 \ldots \quad \ldots M_n^{-1} M_{n+1} \begin{pmatrix} 1 \\ 0 \end{pmatrix}$$

$$\begin{pmatrix} A_1 \\ B_1 \end{pmatrix} = M \begin{pmatrix} 1 \\ 0 \end{pmatrix} \tag{4.11}$$

and the reflection and transmission coefficients R and T respectively are given by the squared modulus of the amplitude coefficients B_1 and A_1 respectively, i.e.

$$R = |B_1|^2 \equiv \left| \frac{M_{21}}{M_{11}} \right|^2 \tag{4.12}$$

$$T = |A_1|^2 \equiv \left| \frac{1}{M_{11}} \right|^2 . \tag{4.13}$$

4.2.2 Reflective Nature of Quantum Structures

To illustrate the above numerical model the reflection probabilities for three gallium-arsenide/aluminium-arsnide (GaAs/AlAs) quantum structures under flatband zero-biased conditions as shown in Figure 4.2 are analysed. Here, the AlAs semiconductor generates the barrier structures and GaAs the quantum wells. There exists a conduction band discontinuity, U, of 0.96eV between the GaAs wells and AlAs barriers, corresponding to 60% the difference between their respective energy gaps [6,7]. The effective electron masses for GaAs and AlAs are taken as $0.063m_0$ [8] and $0.15m_0$ [9] respectively, where m_0 is the rest mass of an electron. Figure 4.2 schematically illustrates (a) a classical potential barrier, (b) a single potential barrier

of width 17Å and finally, (c) a MQB structure. The individual layer widths of the MQB reflector are displayed below in Table 4.1.

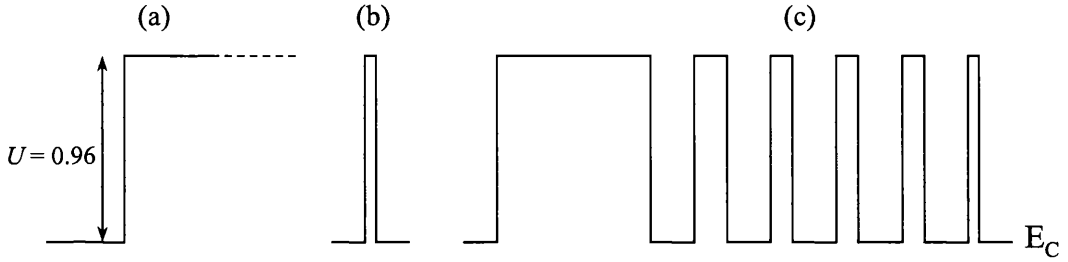

Figure 4.2: Schematic diagrams of three GaAs/AlAs quantum structures, namely, (a) a potential step, (b) a single potential barrier of width 17Å and (c) a MQB. In each case the barrier and wells are constructed from the AlAs and GaAs semiconductor. The height of the conduction band offset between these two materials is taken to be 0.96eV [7,8].

For an infinitely thick potential step, classically all electrons with energy below that of the conduction band offset, U, are reflected and conversely electrons with an energy greater then U are transmitted over the barrier. This behaviour is confirmed numerically in Figure 4.3 where the calculated reflectivity profile is given by the black vertical dotted line (here the actual width of the potential step was taken to be 3000Å).

Layer No.	1	2	3	4	5	6	7	8	9	10	11
Width (Å)	56	200	56	28	56	23	56	23	56	17	56

Table 4.1: Individual material layer widths of the MQB reflector displayed in Figure 4.2.

However, for a potential barrier of finite thickness electrons have a finite probability traversing the barrier due to quantum mechanical tunnelling through the barrier, which can be quite significant at layer widths considered in the next example, a barrier of width 17Å. The corresponding reflectivity profile of the single potential barrier (solid blue line in Figure 4.3) shows an almost immediate drop in reflectivity probability as a consequence of the onset of electron transmission across the thin barrier layer.

Finally, the third reflection spectra (solid red line in Figure 4.3) calculated for the MQB reflector detailed in Table 4.1 indicates an effective potential barrier height enhancement, U_e, of approximately 25% to the classical barrier height U. This illustrates, why MQB structures are such an attractive solution to the carrier leakage problem apparent in many laser diode devices as the discontinuity is effectively

increased. However, this can only be achieved by astute tuning of the MQB periodicity.

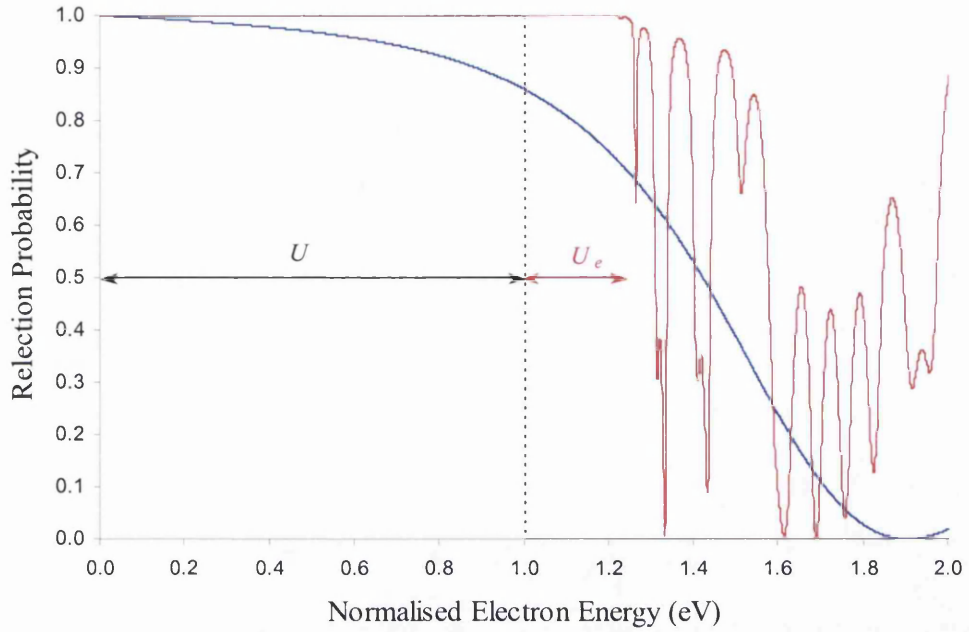

Figure 4.3: Reflection probability profile indicating the reflection spectra of an incident electron impinging on a classical potential step (black dotted line), a potential barrier (blue solid line) and a MQB (red solid line). Each reflectivity profile is normalised with respect to the barrier height *U*.

It is important to note in this example and for reflectivity profiles analysed in the remainder of this thesis, the enhancement effect is deduced by finding the difference between the leading edge of the reflection probability and the intrinsic barrier height, *U*. The leading edge of the reflectivity spectra refers to the point where the reflection probability first falls below a value of 0.99.

4.3 Inter-Valley Transport Model

In Section 2.6 of Chapter 2 the occurrence of conduction band crossover between the direct Γ and indirect X-bands in the AlGaInP material system was discussed. This phenomenon arises as a consequence of varying aluminium content in the AlGaInP semiconductor, which is necessary to construct the barrier and well layers within MQB superlattice. Figure 2.11 illustrated how the magnitude of the energy gaps of the Γ and X-bands varied as a function of aluminium content. At

aluminium contents of 0.56 or above the AlGaInP material reverts from a direct (Γ-band) semiconductor to an indirect (X-band) one. This fact strongly suggests the possibility of carrier exchange between the two conduction band minima at hetero-interfaces. Such inter-valley transport can in principle completely negate the enhancement effect posed by the periodicity of the MQB superlattice and is presently the overriding favourite to explain the discrepancy in the numerically predicted and experimentally observed barrier height enhancements [10,11,12]. Hitherto, a very high percentage of authors attempting to model the enhancing effects of MQBs constructed from the AlGaInP material system have considered electron transport across the superlattice via the direct Γ-band only [13,14,15]. This presumption has recently been proved experimentally to be inaccurate, analysis of the leakage current from 630nm laser diode devices by Blood *et al.* [16] found that the magnitude of the electrons mobility corresponds with that of electrons present in the indirect X-minimum as opposed to the direct Γ-minimum as is previously supposed.

In sub-section 4.3.1, analysis a single AlGaInP hetero-barrier structure is discussed. This, investigation uncovers two additional modes of transport available to an incident electron when elastic inter-valley scattering is considered. Hence, it is essential to include these extra transport routes when numerically simulating and designing AlGaInP MQB structures for operation in 630nm laser diodes. Therefore, sub-section 4.3.2 discusses the necessary modifications to the previously presented single band reflectivity model to allow for possible inter-valley scatterings at hetero-junctions in the mass-envelope function approximation. The predicted reflectivity profiles from the improved numerical model is compared with that calculated via a more sophisticated psuedo-potential technique of Marsh and Inkson [17,18,19] across a single aluminium arsnide (AlAs barrier) sandwiched between two gallium arsnide (GaAs well) layers in sub-section 4.3.3.

4.3.1 Inter-Valley Transport Modes

Below a $(Al_xGa_{1-x})_yIn_{1-y}P$ potential barrier is presented where the well and barrier regions are constructed using aluminium contents of 0.3 and 0.7 respectively. Using the appropriate energy gap equations [20,21] and the two-thirds conduction band offset approximation [22,23,24] the potential barrier height with respect to the Γ-band is 0.163eV higher than that of the well energy position, which for convenience

is set to 0eV. The positions of the X-minimum with respect to these energies are deduced by finding the difference of the Γ and X energy gaps in each of the respective layers. These positions are 0.156eV and 0.083eV in the well and barrier layers respectively. This structure is presented below in Figure 4.4(a). Here, the solid dark blue line and the red intermittent line denote the Γ and X conduction band minima respectively.

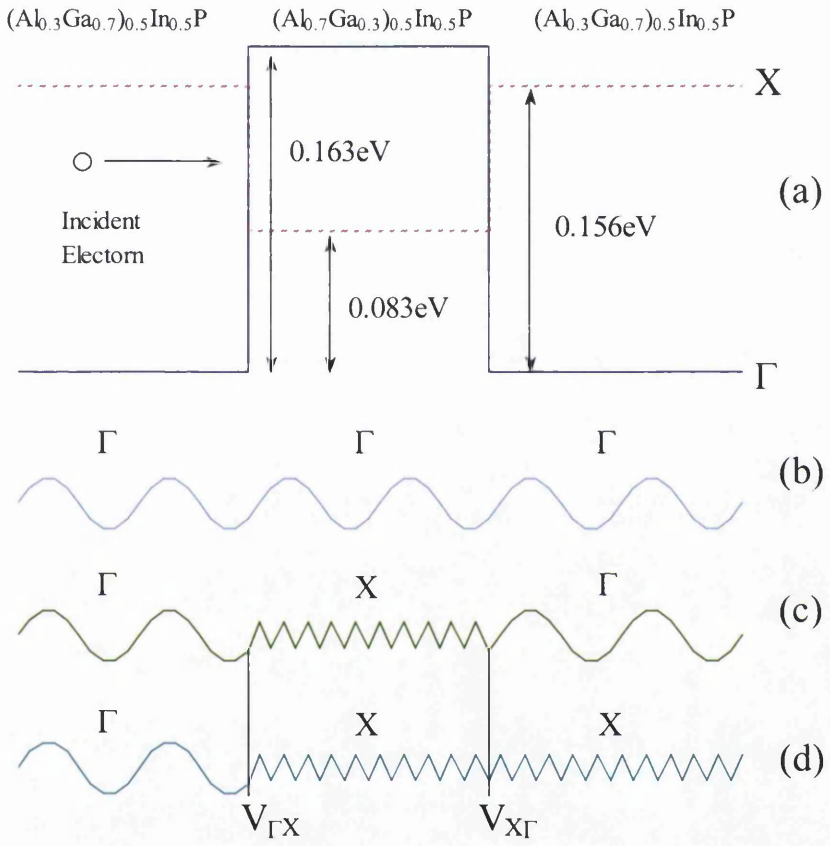

Figure 4.4: (a) conduction band edge profiles for both the Γ and X minima (solid navy and dashed red lines respectively). (b), (c) and (d) representations of the direct Γ and indirect Γ-X transfer tunnelling processes available to an incident electron. Scattering events occur only at the hetero-interfaces represented by the vertices $V_{\Gamma X}$ and $V_{X\Gamma}$.

The lower parts of Figure 4.4, i.e. plots (b), (c) and (d) schematically illustrate the physical transport mechanisms available to an incident electron. The propagations of the Γ and X electrons are represented by wavy and zig-zag lines respectively in all three transfer processes and inter-valley elastic scatterings at material boundaries are represented by the two vertices $V_{\Gamma X}$ and $V_{X\Gamma}$.

The first transfer mechanism Figure 4.4(b) represents an incident Γ electron traversing the potential barrier, solely within the Γ-valley (equivalent to the single-band model encountered in sub-section 4.2.2). Hence, no change in the propagation

line shape is observed. Electrons with energy less than the X-well minimum in the $(Al_{0.7}Ga_{0.3})_{0.5}In_{0.5}P$ alloy can only exist within their original Γ-state. In this energy interval incident electrons have only two transport options open to them, either they penetrate the barrier by quantum mechanical tunnelling or they are reflected, there is no chance for these electrons to scatter to the X-minimum as it lies at an energy higher than they posses.

However, a second mode of transport becomes apparent within the energy interval between the bottom of the X-well and the top of the X-barrier (i.e. in the energy range $0.083 < E < 0.156$ eV). Electrons with energies in this range may experience two elastic inter-valley scattering events, firstly, at the $V_{\Gamma X}$ potential vertex, where an electron may transfer to the lower X conduction band minimum and exist as a quasi-bound state, due to the fact that it is situated with in a well region but is still propagating. A second scattering event may occur at the $V_{X\Gamma}$ potential vertex, the electron may again revert to the Γ minimum, which in the Γ well region has the lower energy minimum. Electron transport of this type gives rise to very sharp resonant tunnelling spikes as a consequence of the presence of the quasi-bound states in the X-well (see sub-section 4.3.3); these have been experimentally verified in single hetero-layered structures of the GaAs/AlAs/GaAs material system where conduction band crossover between the Γ and X minima is also evident [25,26,27,28]. This transport process is illustrated in Figure 4.4(c).

The final possible mode of transport illustrated in Figure 4.4(d) is similar to the previous mechanism shown in Figure 4.4 (c), in that the incident Γ electron reverts to the lower lying energy X-valley at the first material interface (i.e. the $V_{\Gamma X}$ potential vertex), however, at the second potential vertex, the electron remains within the X-band minimum. This transport mechanism is reported to be the dominant mode at applied biases in 630nm laser diodes [29], culminating in the previously mentioned X-band leakage currents [38].

4.3.2 Dual-Band Schrödinger Numerical Model

There have been various investigations into electron transport across a single hetero-barrier structure in an attempt to model or to experimental verify the resonant tunnelling mechanism predicted by [17-19,23-26] like that illustrated in Figure 4.4(c). Most authors in this field have concentrated their efforts on the GaAs/AlAs/GaAs

structure shown schematically below in Figure 4.5. This material structure exhibits a similar conduction band crossover between the Γ and X minima like the AlGaInP semiconductor. Therefore, the improved numerical model developed in this sub-section is based on a numerical model developed by Lui [30], which originally described electron transport across a single GaAs/AlAs/GaAs hetero-barrier taking account of inter-valley scatterings.

This model is based on a similar mass-envelope function approximation as that of the previously described single-band model (see Section 4.2). This fact minimised the numerical algorithm building, as the foundations were previously laid. However, this technique is not as physically rigorous as the pusedo-potential method proposed by Marsh and Inkson [17-19], but as shown in the following sub-section, the calculated reflection spectra correlates very well with that predicted by Marsh and Inkson.

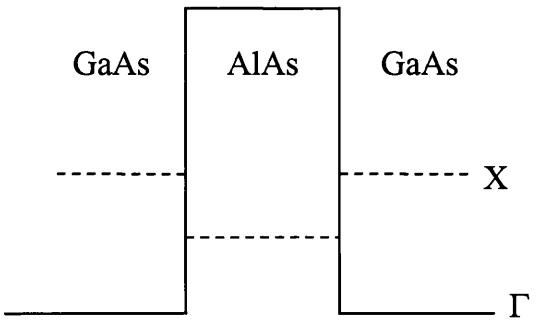

Figure 4.5: Schematic diagram of a single AlAs hetero-barrier structure embedded between two GaAs well layers. The diagram indicates the relative position of the direct Γ and indirect X-bands in all three material layers.

Thus, to account for potential electron band-to-band transfer at the material boundaries an extended effective mass-envelope model has been employed. This model amounts to the solution of a coupled set of time-independent Schrödinger equations, where transfer between the Γ and X conduction band minima is mediated by off-diagonal elements in a potential energy matrix, and is allowed to occur only across material interfaces, whereas the diagonal terms represent pure Γ and X conduction band discontinuities. By employing a spinor like matrix notation the Γ-wavefunction may be described by the upper component, while the lower component describes the X-wavefunction. Therefore, for a single heterointerface located at $x = 0$, it is possible to define a 2×2 potential energy matrix of the form

$$\hat{V}(x)=\begin{pmatrix} V_{\Gamma}(x) & \alpha\delta(x) \\ \alpha\delta(x) & V_{X}(x) \end{pmatrix}, \tag{4.14}$$

for a two-component (Γ-X) wavefunction

$$\mathrm{Z}(x)=\begin{pmatrix} \zeta_{\Gamma}(x) \\ \zeta_{X}(x) \end{pmatrix}, \tag{4.15}$$

where α is the inter-valley mixing parameter, $\delta(x)$ is the Dirac-delta function, V_Γ and V_X are the band offset discontinuities for the Γ and X minima (unless otherwise stated, these magnitudes are determined via the method discussed previously in sub-section 2.4.6 of Chapter 2). The off-diagonal terms $\alpha\delta(x)$ quantify the inter-valley transfer potentials ($V_{\Gamma X}$ and $V_{X\Gamma}$). In this discussion, the inter-valley mixing parameter was positive and real-valued, but in general it could be complex.

Due to the nature of the effective mass envelope approximation the detailed shape of the inter-valley transfer potential in the neighbourhood of the heterojunction is not important, and hence, a delta-function approach is adequate to describe the inter-valley transfers. The coupled Schrödinger's equation set then reads:

$$\hat{T}\mathrm{Z}+\hat{V}\mathrm{Z}=E\mathrm{Z} \tag{4.16}$$

where E is the eigenenergy of the system, $\hat{T}$ is the kinetic energy operator, and is defined to be

$$\hat{T}=\begin{pmatrix} -\frac{\hbar^2}{2}\frac{\partial}{\partial x}\frac{1}{m_{\Gamma}(x)}\frac{\partial}{\partial z} & 0 \\ 0 & -\frac{\hbar^2}{2}\frac{\partial}{\partial x}\frac{1}{m_{X}(x)}\frac{\partial}{\partial x} \end{pmatrix}, \tag{4.17}$$

here, $\hbar$ is the reduced Plank's constant and $m_{\Gamma,X}$ are the effective electron masses corresponding to the Γ and X conduction bands. Matching conditions for the wave

function and its derivative across a material interface ($x = 0$) may be given by the following expressions:

$$\begin{pmatrix} \zeta_\Gamma \\ \zeta_X \end{pmatrix}_{x=+0} = \begin{pmatrix} \zeta_\Gamma \\ \zeta_X \end{pmatrix}_{x=-0} \tag{4.18}$$

$$\begin{aligned} &\frac{-\hbar^2}{2}\left(\frac{1}{m_\Gamma(x)} \frac{\partial \zeta_\Gamma}{\partial x}\bigg|_{x=+0} - \frac{1}{m_\Gamma(x)} \frac{\partial \zeta_\Gamma}{\partial x}\bigg|_{x=-0} \right) + \alpha \zeta_X\big|_{x=0} = 0 \\ &\frac{-\hbar^2}{2}\left(\frac{1}{m_X(x)} \frac{\partial \zeta_X}{\partial x}\bigg|_{x=+0} - \frac{1}{m_X(x)} \frac{\partial \zeta_X}{\partial x}\bigg|_{x=-0} \right) + \alpha \zeta_\Gamma\big|_{x=0} = 0 \end{aligned} \tag{4.19}$$

where equation (4.18) is the wavefunction continuity condition, and equation (4.19) is obtained by integrating the two Schrödinger equations across the material interface. Equations (4.18) and (4.19) are the two-valley equivalent of the single-valley continuity conditions given in equation (4.6). To evaluate the above matrix formalism, the transfer matrix approach was implemented in a similar fashion to that detailed in sub-section 4.2.1.

4.3.3 Verification of Dual-Band Schrödinger Algorithm

To validate the above extended mass-envelope function model, the transmission spectra determined from analysis of the electron transport across a single GaAs/AlAs/GaAs potential barrier (illustrated below in Figure 4.6) with that of Marsh and Inkson [17-19], who investigated the structure using an empirical many band psuedo-potential technique.

To be definite, the exact material parameters and conduction band offsets for both the Γ and X bands as used in Marsh and Inkson's paper [17-19] have been adhered to, although these values have since been updated through more sophisticated experimental techniques.

The material parameters used in the numerical calculation are the magnitudes of the conduction band offsets and effective electron masses for both the Γ and X minima; these values are displayed below in Table 4.2.

Parameter	GaAs		AlAs	
	Γ	X	Γ	X
Conduction Band Offset, ΔE_C (eV)	0	0.365	0.88	0.195
Effective Masses (m_e/m)	0.069	0.169	0.124	0.224

Table 4.2: Material parameters for the GaAs/AlAs/GaAs potential barrier.

Using the above material parameters the total electron transmission spectra (i.e. the sum of the Γ and X band transmission probabilities) has been calculated for two potential barrier widths, namely 5.64Å and 14.1Å (i.e. 2 and 5 monolayers (1 monolayer ~ 2.83Å)) in conjunction with that presented by Marsh and Inkson [17-19]. Furthermore, in these simulations the magnitude of the mixing parameter α was set to a value of 0.155eVÅ in accordance with experimentally determined value reported by Stoner *et al* [31] for the GaAs/AlAs/GaAs material system.

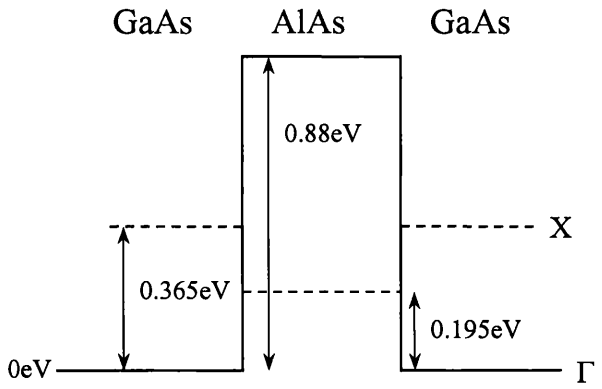

Figure 4.6: Schematic diagram indicating the relative conduction band offsets of the Γ and X minima. All positions of the band edges are referenced with respect to the bottom of the GaAs Γ band.

The first transmission profile associated with the very thin AlAs material layer of 5.64Å is displayed in Figure 4.7(a). Here, as expected there is a high probability of electron transfer across such a thin layer, which sharply increases from the origin as the energy of the incident electron energy is increased until an energy equivalent to approximately half the barrier height is reached whereby the transmission probability plateaus. This general trend would be evident if the transmission spectra were calculated using single Γ-valley model. Actually this behaviour has already been indicated in sub-section 4.2.2 in Figure 4.3 where the inverted transmission spectra (the reflectivity probability) is displayed by a blue solid line calculated from a single thin barrier schematically shown in Figure 4.2(b). However, there are additional

componenst in the transmission spectra associated in the dual-band Schrödinger model, namely the resonant tunnelling spike centred about an electron energy of 0.34eV.

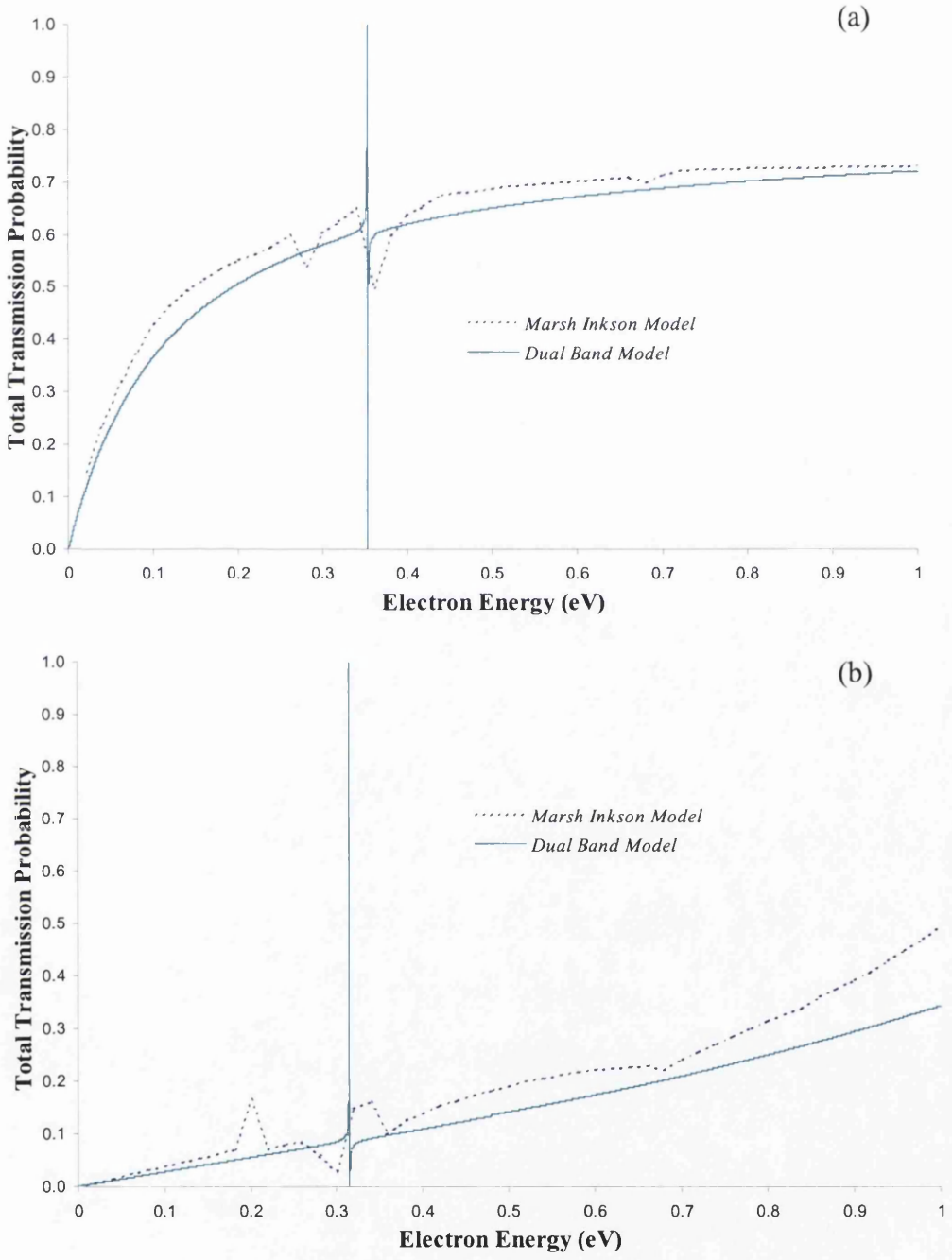

Figure 4.7: Comparison of the extended effective mass model with the empirical pseudo-potential model of Marsh [17-19] for single GaAs/AlAs potential barrier of thickness (a) 5.64Å and (b) 14.1Å.

This sharp transmission feature is a consequence of inter-valley transport across the thin AlAs layer, where an incident electron in the Γ-minimum is elastically scattered

to the lower lying X-band at the first material interface where it exists as a quasi-bound state in the X-well and is scattered back to the initial Γ-band at the second hetero-interface.

Independent work by Mendez *et al.* [23,24] and Bonnefoi *et al.* [25,26] have experimentally verified the presence of such resonant peaks for single tunnelling layer GaAs\AlAs\GaAs structures validating this theoretical data. Figure 4.7(b) indicates similar transmission traits to that of the Figure 4.7(a), but in this case the tunnelling probability is less severe due to the increased thickness of the potential barrier. On both Figure 4.7(a) and (b) the transmission probability data obtained from Marsh and Inkson's [17-19] theoretical results have been superimposed on the transmission data collected from the dual-band Schrödinger model. In general, the extended effective mass-envelope approximation demonstrates very good quantitative information in the transmission spectra when compared to that of the many band pusedo-potential model of Marsh and Inkson. There is however, an underestimation of the predicted transmission probability associated with the two differing potential barrier widths particularly at higher incident electron energies. This is primarily due to the fact that in the author's calculations, contribution from the two lowest conduction band minima is considered only, whereas the model proposed by Marsh and Inkson sums over all such minima. Additionally, as a first approximation it has been assumed that the shape of the two conduction band minima employed within the model exhibit a parabolic behaviour, but in reality the shape of these are different and fairly complex.

Therefore, from the above analysis, it is possible to conclude that the extended effective mass-envelope model presented can give very good quantitative information of the tunnelling processes present when two conduction band minima overlap.

In the following Section, the optimisation process utilised to design a MQB reflector to subsequently give maximum enhancements to the intrinsic conduction band offset is discussed.

4.4 MQB Design and Optimisation

In order to achieve optimum reflection of electrons back into the active region by means of an embedded MQB structure, it is essential that all the constituent MQB parameters be chosen in a methodical way. This systematic process should yield

maximum effective enhancement to the existing conduction band offset when these parameters are combined to form a MQB. Furthermore, for the particular case in question, namely, development of a MQB structure via the AlGaInP material system it is essential to seek also a 'stable' greatest enhancement. Stable in this sense refers to the widths of the elemental layers of the MQB. Growth techniques at present are unable to repeatedly grow the thin layers of the superlattice with sufficient accuracy to fully exploit the reflective nature of the theoretically designed structures. Hence, it is imperative that allowances are made when designing such structures and that some leeway is made for inaccuracies in experimental layer width. Thus, all optimised structures are designed with a layer width tolerance of ±1 monolayer, that is, the optimum MQB structures retain their fruitful effective enhancements if their superlattice periods are altered either way by a width of one monolayer.

Another growth related problem associated with the AlGaInP material system is that concerning the aluminium content in the constituent barrier and well layers of MQB. The magnitude of the aluminium content determines the intrinsic height and depth of these layers respectively. Hence, it is intuitive to choose a scenario whereby the conduction band offset is at the greatest magnitude it can be, however due to inter-diffusion of zinc between the barrier and well layers this is not physically a great idea. In sub-section 4.4.4 this issue is discussed in greater detail. First the optimisation procedure used to design each MQB structure in this thesis is discussed.

The MQB structure has the following variable parameters:

(i) First barrier thickness
(ii) Widths of wells and barriers
(iii) Number of periods

Understanding how the magnitude of the barrier enhancement depends on these parameters, is fundamental to the effective and controlled use of a MQB in the modification of a conduction band offsets. For simplicity, the following analysis considers a MQB structure constructed solely from the Γ-minimum of the AlGaInP material system, and in the flatband zero-bias regime.

4.4.1 Variation in first barrier width

To prevent low energy electrons from tunnelling through the thin material layers of the MQB superlattice, a thick barrier is employed, typically of width several times that of the constituent barriers within the superlattice [32]. To assess how the probability of electron reflection changes by varying the width of the initial barrier, a single $(Al_{0.3}Ga_{0.7})_{0.5}In_{0.5}P/(Al_{0.7}Ga_{0.3})_{0.5}In_{0.5}P/(Al_{0.3}Ga_{0.7})_{0.5}In_{0.5}P$ potential barrier was investigated, by altering its width from 20Å to 200Å (see sub-section 4.4.4 for choice of aluminium content in these layers). The results are shown by means of reflectivity plots in Figure 4.8. In each of the four reflectivity profiles presented here the incident electron energy has been normalised with respect to the height of the potential barrier, which in this material set-up has a magnitude of 0.163eV. Hence, a value of one on the *x*-axis in Figure 4.8 is equivalent to the height of the potential barrier in question (also, marked by the black intermittent line).

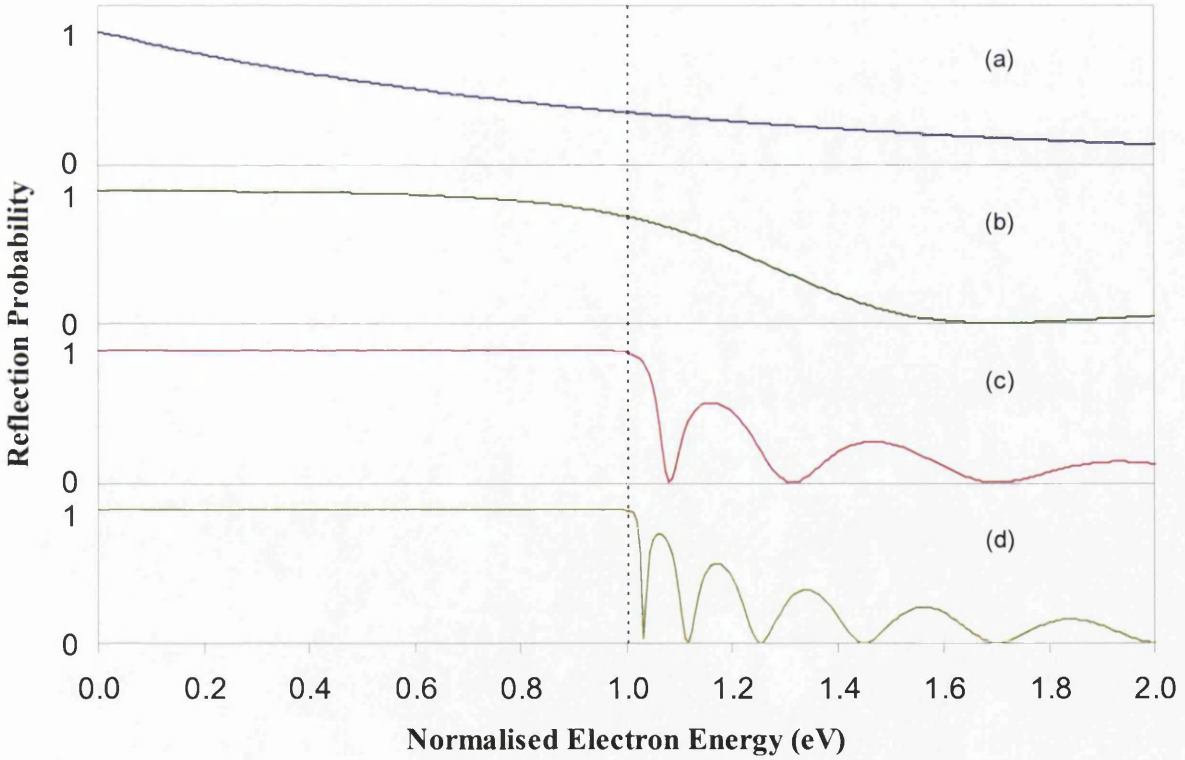

Figure 4.8: Reflectivity plots for an $(Al_{0.3}Ga_{0.7})_{0.5}In_{0.5}P/(Al_{0.7}Ga_{0.3})_{0.5}In_{0.5}P/(Al_{0.3}Ga_{0.7})_{0.5}In_{0.5}P$ single potential barrier of width (a) 20Å, (b) 50Å, (c) 150Å and (d) 200Å. As the barrier width is increased further beyond 200Å, the reflectivity plot remains unchanged, indicating that the maximum barrier to electron transport has been attained.

As established earlier in sub-sections 4.2.2 and 4.3.2, thin material layers less than approximately 100Å provide no significant impediment to the electron transfer

through it. This fact is emphasised in Figures 4.8(a) and (b), where the reflectivity profiles corresponding to the $(Al_{0.7}Ga_{0.3})_{0.5}In_{0.5}P$ potential barrier of widths 20Å and 50Å are displayed respectively. However, as the barrier is increased further to 150Å and then to 200Å, (Figures 4.8(c) and (d) respectively), the effective barrier height is increased as the probability of transmission is reduced due to increased barrier thickness (i.e. the leading edge of the reflectivity probability remains at unity for a wider energy spectrum). With an initial thick barrier of 150Å Figure 4.8(c), the energy range of total reflection extends up to the intrinsic barrier height, i.e. unity in the normalised representation. However, as the width of the barrier is increased further to 200Å (Figure 4.8(d)) and beyond, the probability of reflection remains fixed at a position equivalent to the intrinsic conduction band offset.

The only observable difference between the last two reflectivity profiles Figures 4.8(c) and (d), is that the leading edge of the reflection probability becomes increasingly defined as the width of the potential barrier is increased, which again is a feature previously noted in sub-section 4.2.2 when considering the reflection probability of a classical potential step.

4.4.2 Variation of Superlattice Barrier and Well Width

Altering the widths of the wells and barriers induces an energy shift in the position of the allowed and forbidden minibands. If the widths of the barrier and well layers are reduced, the positions of the minibands are shifted upward in energy and vice-versa. From comparing the condition for interference within both well and barrier layers with the solution of a particle in an infinite well [33], the relationship between band position and width of well and barrier regions was established to be an inverse square law (when considering the Γ-band only). Hence, it is advantageous to have these layers as thin as possible. However, this condition is limited by the accuracy and consistency of the growth techniques employed to deliver these material layers at present. Thus, in this study a minimum layer width of 42Å (15ML) has been employed in an attempt to balance the beneficial shifting of the forbidden minibands with layer widths that modern growth techniques can reliably produce.

4.4.3 Variation of Superlattice Periods

In this sub-section the reflection probability is examined as the number of superlattice periods varied from two to eight (Figure 4.9). This investigation at first is undertaken with no initial thick stopping potential like that previously discussed in sub-section 4.4.2. However, at the end of this sub-section an ideal reflectivity profile is displayed which is calculated from a MQB structure that incorporates a thick stopping potential and an optimum superlattice period number (see Figure 4.10 later).

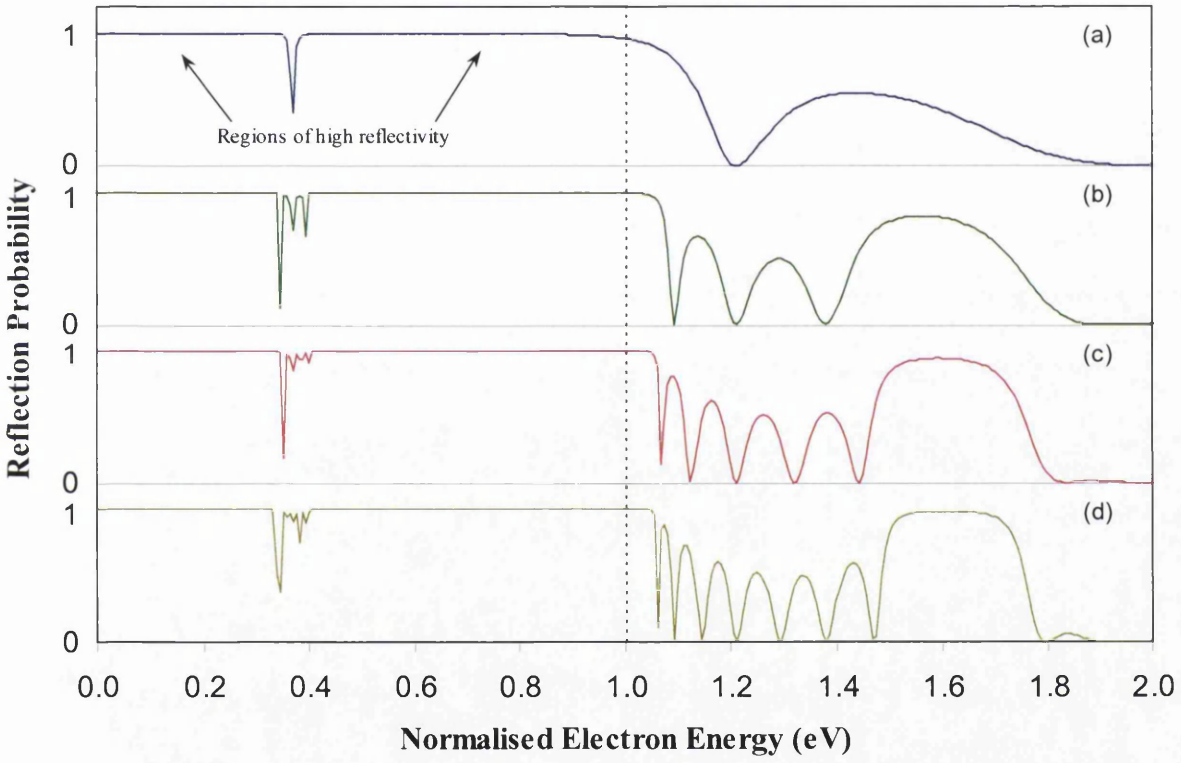

Figure 4.9: Reflectivity plots for an $(Al_{0.3}Ga_{0.7})_{0.5}In_{0.5}P/(Al_{0.7}Ga_{0.3})_{0.5}In_{0.5}P/(Al_{0.3}Ga_{0.7})_{0.5}In_{0.5}P$ MQB structure consisting of (a) 2, (b) 4, (c) 6 and (d) 8 superlattice periods. The width of the wells and barriers within the superlattice were 15ML. The maximum number of periods was restricted to 8, for this study, in accordance with the coherence limits reported by Mendez *et al.* [34].

In practice, it is important to maintain electron coherence across the MQB structure to ensure that the allowed and forbidden miniband effect arising form coupled electron states do not diverge from what is theoretically assumed. Any deviation by off-axis scattering would render the optimised MQB structure ineffective. It has been reported by Mendez *et al.* [34] that electron coherence can be maintained at room temperature, through a MQB of total width 1000Å obtained for

the GaAs/AlGaAs material system. However, to the author's knowledge, no experimental data for the electron coherence length in an AlGaInP superlattice is currently available. Therefore, for a first approximation an upper limit of eight superlattice periods at a total width of no more than 900Å (here one period comprises a barrier and well layer) was adhered to when designing the superlattice in order to maintain electron coherence throughout and avoid losses due to scattering.

Figure 4.9 above, indicates the reflection probabilities calculated by solving the one-electron Schrödinger equation across the four superlattice structures, where the electron coherence restriction was upheld. Widths of both the constituent superlattice wells and barriers are set to an optimum value of 42Å (see sub-section 4.4.2). Superlattice layers thicker than this become increasingly susceptible to X-band transfer. Figure 4.9 (a) illustrates the reflection spectra of a double barrier system. This single band material system displays an analogous behaviour to that of the resonant dual-band single barrier layer presented in sub-section 4.2.2. In both cases a sharp resonant transmission peak is evident separating two regions of high reflectivity. In the dual-band case this emerges from quasi-bound states in the X-well, whereas in the single band case under consideration here, results from a bound state present between the two Γ-band potential barriers.

As the superlattice period number is increased to four, six and eight as shown in Figures 4.9(b), (c) and (d) respectively, the regions of high reflectivity are separated further by fine tunnelling spikes. Also the position of the observed transmission features is shifted toward the origin as layer number is increased. It is also noticeable that the leading edge of the reflectivity profile above the intrinsic conduction band offset becomes increasingly more defined as the period number is increased in a similar fashion to that observed in sub-section 4.4.1.

The most important feature of all four reflectivity plots shown in Figure 4.9 is the fact that the periodicity of the superlattice periods has produced an effective enhancement, (i.e. the leading edge of the reflectivity extends beyond the classical barrier height, marked by the black intermittent line) if the obvious low energy transmission spikes are ignored. Thus, by combining the low energy reflectivity and the effective enhancement characteristics associated with the stopping potential barrier and the superlattice period width and number, it is possible to obtain a reflectivity profile exhibiting high effective enhancement with no transmission features present below the leading edge of the reflectivity spectrum. This concept is

illustrated in Figure 4.10 below, which displays the reflectivity spectra associated with a 200Å thick initial barrier, i.e. plot (a), an eight period superlattice structure where each individual material layer is 42Å thick, in plot(b) and a composite structure combining the stopping potential and the superlattice structure described previously in plot (c). The reflection probability of the thick barrier exhibits no transmission features up to the normalised barrier height, U, as previously seen.

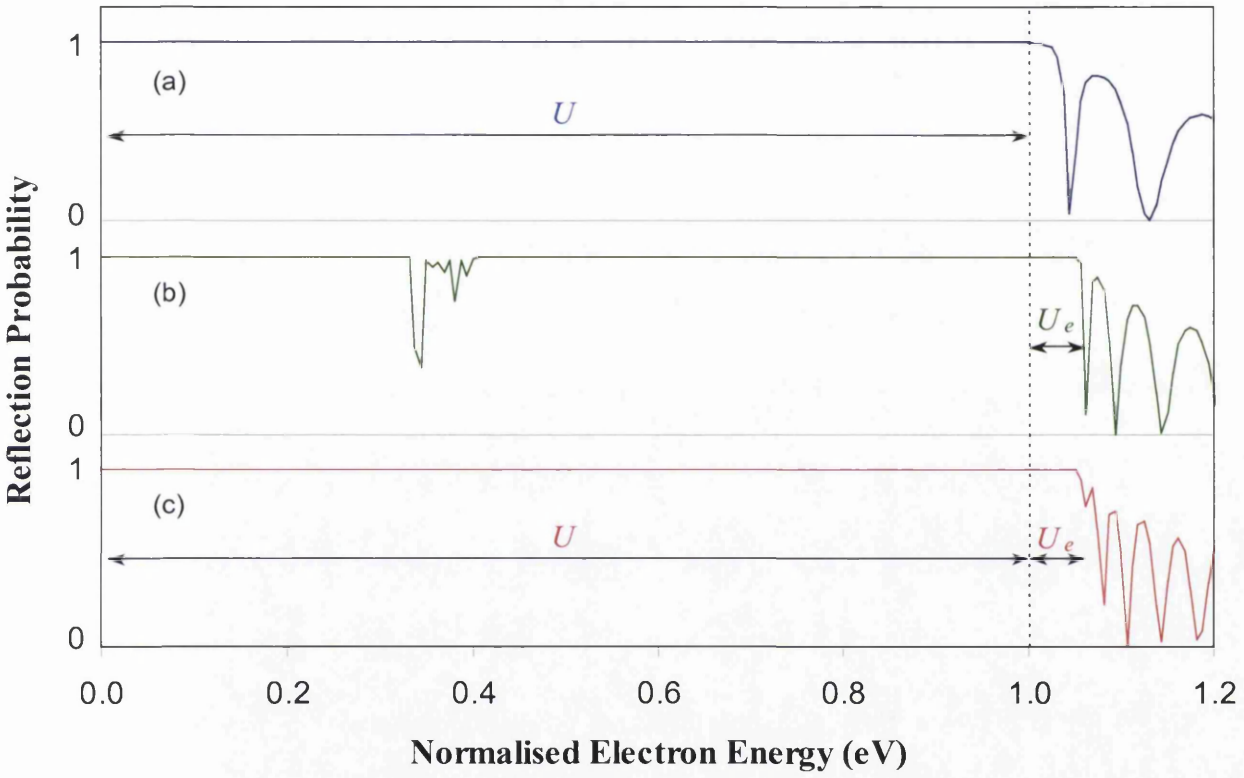

Figure 4.10: Reflectivity plots for an $(Al_{0.3}Ga_{0.7})_{0.5}In_{0.5}P/(Al_{0.7}Ga_{0.3})_{0.5}In_{0.5}P/(Al_{0.3}Ga_{0.7})_{0.5}In_{0.5}P$ MQB structure illustrating the benefit to the magnitude of the barrier height enhancement by inclusion of a first thick barrier within the MQB design. Cases shown are (a) a single barrier of width 200Å, (b) a MQB consisting of 8 barrier-well periods of width 15ML and (c) a compound structure containing both structures described in (a) and (b) in series. The enhanced barrier height is approximately 5% of the intrinsic barrier height.

The reflectivity spectrum of the superlattice structure indicates that it is susceptible to low electron tunnelling, but importantly produces an enhancement feature, U_e, if this is ignored. The reflectivity associated with the composite material possesses an effective enhancement, U_e in excess of five percent of the intrinsic barrier height, U, similar to that of the superlattice reflectivity (when ignoring the low-energy transmission spikes). In addition, there are no transmission features evident at all below the leading edge of the reflectivity spectrum like that of the thick

barrier reflection probability. Thus, it is reflectivity probabilities with the same characteristics like that displayed by the composite MQB structure, which are most beneficial to augmented carrier confinement in laser diode devices, and it is these the above optimisation procedure is designed to uncover.

4.4.4 Superlattice interface diffusion

As mentioned in the introductory paragraphs of this section, the optimum theoretical choice of aluminium content used in the AlGaInP semiconductor material was not employed in this investigation due to growth issues, reasons for which are summarised below.

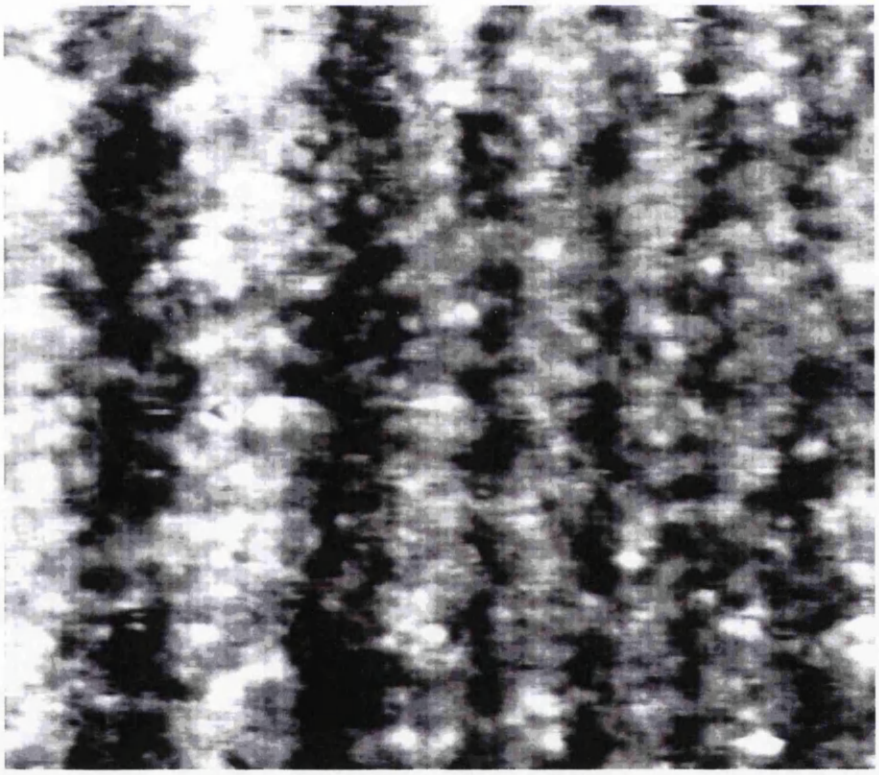

Figure 4.11: STM image depicting the extent of interface roughness in the AlInP/GaInP barrier well superlattice.

The intrinsic barrier discontinuity between the constituent ternary materials of AlGaInP (i.e. GaInP and AlInP) is relatively small, thus, it is intuitive to implement the material composition where the barrier discontinuity is maximum. This choice corresponds to an aluminium content of zero and unity in the well and barrier regions respectively, resulting in a GaInP/AlInP superlattice structure [35,36]. However, recent experiments conducted by Teng *et al.* [37], which investigated superlattices of

this material type, using cross-sectional scanning tunnelling microscopy (XSTM), have shown the interfaces between such material layers to be non-abrupt, and the layer widths to be non-uniform; a XSTM image of an AlInP/GaInP superlattice is shown above in Figure 4.11. Teng *et al.* postulated that these effects might be attributed to inter-diffusion of the aluminium and gallium atoms across the superlattice structure. Vacant gallium atoms within the GaInP (well) layers giving rise to preferential aluminium-gallium bonding at the hetero-interfaces are thought to promote this process. Thus a graded AlGaInP alloy is generated across the original AlInP/GaInP interfaces. This gives the impression of larger than prescribed well regions, evident in Figure 4.11. Interface roughness and non-prescribed layer widths both contribute to loss of superlattice periodicity, subsequently altering the location of the theoretically predicted forbidden energy minibands predicted by the theoretical model.

To limit the above behaviour, the barrier and well regions have been constructed of AlGaInP with aluminium contents 0.7 and 0.3 respectively. Due to a reduced number of gallium vacancies, the migration of aluminium atoms toward the well layers should be reduced, lessening the influence of the grading and alloy-clustering mechanisms mentioned above. Furthermore, as mentioned in sub-section 4.4.2 the optimisation process involves altering all the constituent material layer widths of the MQB by one monolayer in an attempt to find a reasonably stable effective enhancement to reduce the need for an idealised MQB structure to be grown.

Section 4.4, is of the utmost important to the whole design and numerical simulation of the novel MQB structures presented in this thesis. To stress this significance and to further underline the volume of work needed to realize the optimisation process, a small summary is given below before some new MQB structures are presented in the following Section.

Each MQB structure presented in the remainder of this thesis has undergone the above optimisation process, whereby the main parameters of the MQB i.e. the initial thick stopping potential and the superlattice are optimised as described in sub-sections 4.4.1 and 4.4.3 respectively. All MQBs are constructed from aluminium contents of 0.7 and 0.3 for barriers and wells respectively to reduce the effect of

interface roughness and alloying. Also, the overall width of the MQB was set to a limit of 900Å to diminish losses resulting from lack of electron coherence.

The optimium initial thick barrier and superlattice structures are combined to yield a composite structure and the corresponding reflection probability noted. The magnitude of the layer widths are increased and decreased by one monolayer and the reflection probabilities compared to determine if a stable enhancement has been established. Here, each reflection spectra should exhibit the characteristics displayed in Figure 4.10(c), namely, high effective enhancements with no evidence of electron transmission below the leading edge of the reflection probability. If these criteria are not met the process is repeated until a MQB structure that exhibits the aforementioned qualities is found.

In the following Section, a typical AlGaInP MQB structure designed for operation in 630nm laser diodes is analysed. Initially, this structure is optimised considering single Γ-band transport only and its reflection spectra determined. This structure is then evaluated using the dual-band Schrödinger solver, a reflection probability generated, and the two compared. Using the above optimisation procedure the structure is re-designed to take account of the additional transport mechanisms present in the inter-valley numerical model.

4.5 Single and Dual-Band models: Application to MQB

Previously, it was postulated that the predominant factor initiating the apparent rift between experimentally measured and theoretically predicted barrier height enhancements arising from the periodicity of a AlGaInP MQB was due to X-valley electrons propagating through the structure into the cladding regions resulting in high leakage currents [11,12,38,39]. In sub-section 4.5.1 this proposition is investigated, using the optimisation technique detailed in Section 4.4 a MQB structure is designed based solely on single Γ-band transport in the flatband zero biased regime. The reflective nature of this structure is deduced using both previously presented single-valley and inter-valley transport models and the results compared.

To inhibit the proposed transfer of X-band electrons across the single-band MQB structure, its periodicity is again re-optimised in conjunction with the dual-band

inter-valley transport model (see Section 4.3) and its improved reflection probability presented in below sub-section 4.5.2.

4.5.1 Optimised Γ-Band MQB Structure

After following the aforementioned optimisation process the Γ-band MQB reflector comprises of an initial thick barrier of 150Å. The superlattice itself consists of eight well barrier pairs, each of which is 42Å in width, consistent with the total width limit set previously to retain electron coherence [32]; the structure is illustrated below in Figure 4.12 and all layer widths and alloy compositions displayed in Table 4.3.

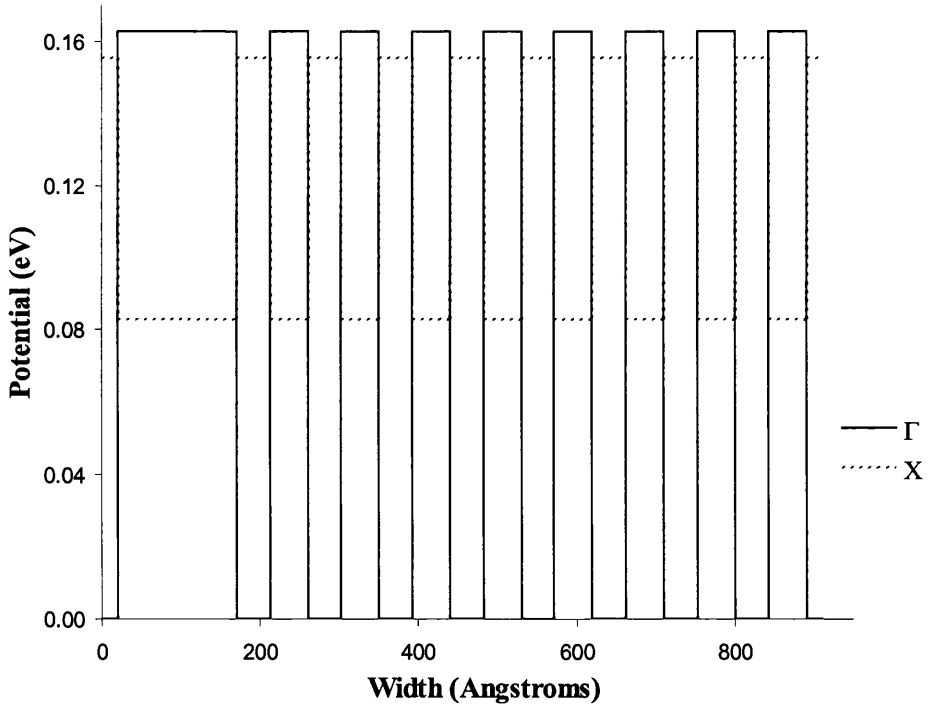

Figure 4.12: Schematic diagram of the optimised single-valley MQB structure.

The reflection probability calculated from this structure is displayed in Figure 4.13 below. Here, the incident electron energy has been normalised to the Γ-band maximum, which from Figure 4.12 can be seen to be 0.163eV. The reflection spectra associated with the single-band MQB structure predicts an effective enhancement of approximately 5% the intrinsic conduction band offset. Although, this enhancement is not as great in magnitude as that predicted by [13-15] due to reasons outlined in

Section 4.4 it is still remains non-trivial for the AlGaInP material system, which suffer from small conduction band offsets.

However, if this structure is solved with dual-band Schrödinger solver detailed in Section 4.3 the observed reflection probability breaks down due to the onset of sharp resonant tunnelling modes and electron leakage across the structure via the X-band minimum. The reflection and transmission probabilities associated with this structure are displayed below in Figures 4.14(a) and (b) respectively.

Layer Number	AlGaInP Alloy	Layer Type (w.r.t. Γ-band)	Structure Widths (Å)
1	$(Al_{0.7}Ga_{0.3})_{0.5}In_{0.5}P$	barrier	200
2	$(Al_{0.3}Ga_{0.7})_{0.5}In_{0.5}P$	well	42
3	$(Al_{0.7}Ga_{0.3})_{0.5}In_{0.5}P$	barrier	42
4	$(Al_{0.3}Ga_{0.7})_{0.5}In_{0.5}P$	well	42
5	$(Al_{0.7}Ga_{0.3})_{0.5}In_{0.5}P$	barrier	42
6	$(Al_{0.3}Ga_{0.7})_{0.5}In_{0.5}P$	well	42
7	$(Al_{0.7}Ga_{0.3})_{0.5}In_{0.5}P$	barrier	42
8	$(Al_{0.3}Ga_{0.7})_{0.5}In_{0.5}P$	well	42
9	$(Al_{0.7}Ga_{0.3})_{0.5}In_{0.5}P$	barrier	42
10	$(Al_{0.3}Ga_{0.7})_{0.5}In_{0.5}P$	well	42
11	$(Al_{0.7}Ga_{0.3})_{0.5}In_{0.5}P$	barrier	42
12	$(Al_{0.3}Ga_{0.7})_{0.5}In_{0.5}P$	well	42
13	$(Al_{0.7}Ga_{0.3})_{0.5}In_{0.5}P$	barrier	42
14	$(Al_{0.3}Ga_{0.7})_{0.5}In_{0.5}P$	well	42
15	$(Al_{0.7}Ga_{0.3})_{0.5}In_{0.5}P$	barrier	42
16	$(Al_{0.3}Ga_{0.7})_{0.5}In_{0.5}P$	well	42
17	$(Al_{0.7}Ga_{0.3})_{0.5}In_{0.5}P$	barrier	42

Table 4.3: AlGaInP layer width and composition for the MQB structure displayed in Figure 4.12.

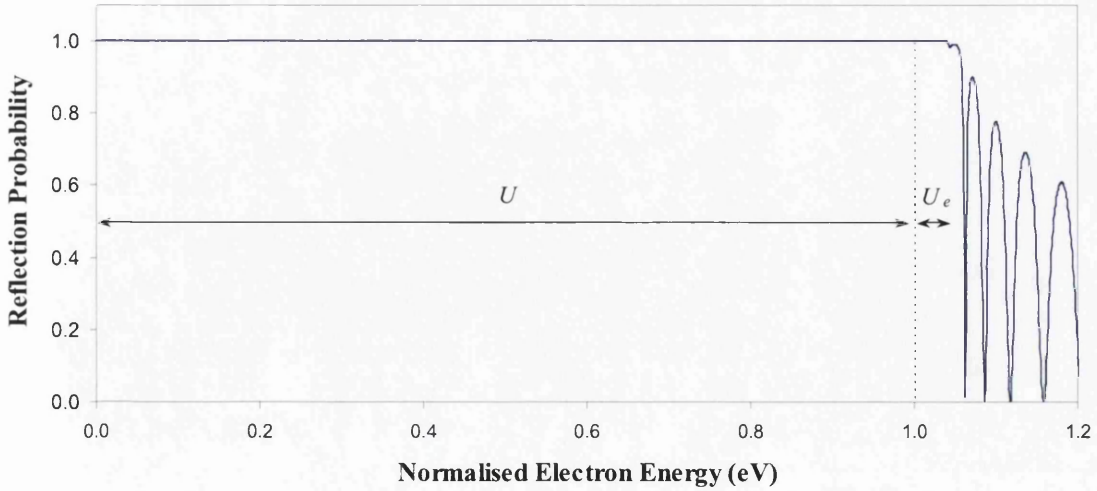

Figure 4.13: Two normalised Reflectivity plots, calculated from the proposed optimised single-band MQB structure, considering single band transfer via the Γ minimum only.

The first plot in Figure 4.14(a) indicates the normalised total reflection spectrum (i.e. sum of the Γ and X reflection probabilities) for the single-band MQB structure. Here, there is an apparent loss of reflection probability at an energy of approximately 65% of the normalised barrier height (marked by the pink intermittent line). This corresponds to the presence resonant tunnelling modes at electron energies of approximately 0.1eV. As discussed earlier, these energy modes are associated with quasi-bound states present within the X-well in the $(Al_{0.7}Ga_{0.3})_{0.5}In_{0.5}P$ material layers. Electron transmission of this type is associated with the transport mechanism illustrated in Figure 4.4(c). Modes associated with this resonant behaviour can also be identified at higher energies particularly in the normalised energy range 0.9eV to 0.95eV. Both these resonant features are more easily identified in Figure 4.14(b) where the transmission probabilities for the Γ and X bands are shown (green and red solid lines respectively). The transmission associated with Γ-band resonant modes mirror that present in the total reflectivity shown in Figure 4.14(a).

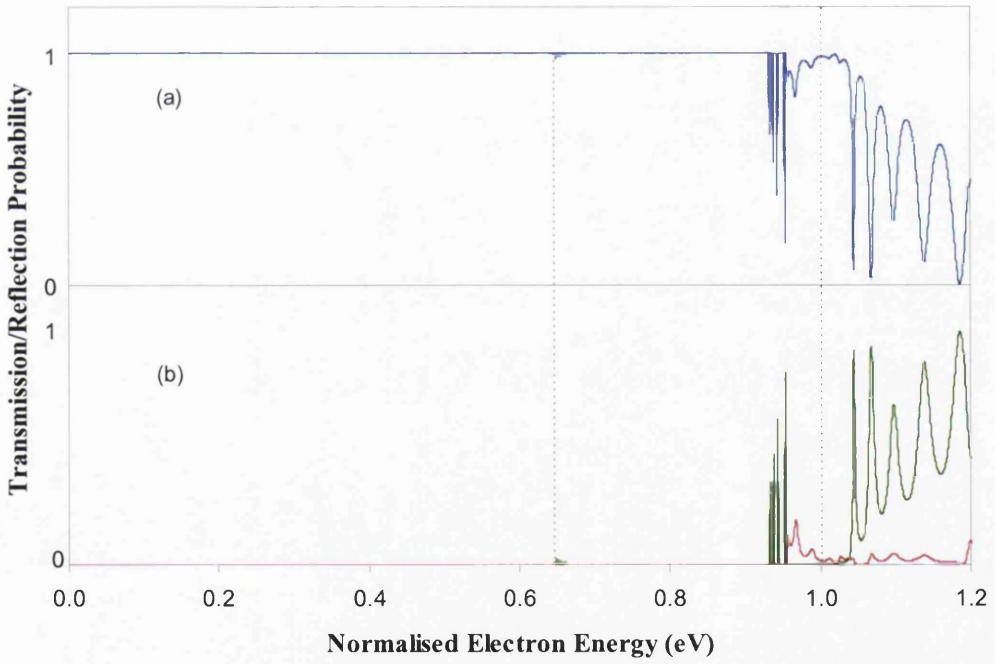

Figure 4.14: (a) illustrating inter-valley transfer of the electrons via the Γ and X minima. (c) Indicates the transmission spectra of electrons via the Γ and X conduction minima (green and red lines respectively).

Figure 4.14 (b) also indicates total transmission via the X-band state, (solid red line) this corresponds to the final transport mechanism displayed previously in Figure 4.4(d). In this case electrons do not revert back to the initial Γ-state at the end of the

MQB structure but remain in the X-minimum, consequently, giving rise to X-band leakage current. Both the transmission features present in Figure 4.14 suggest a high probability of substantial leakage currents if the above single-band MQB structure was to be embedded within a laser diode.

Comparison of the predicted total reflectivity profiles by the dual-band Schrödinger model and the more simplistic single-band Schrödinger model differ quite considerably. This fact adds weight to the previously proposed argument that current single-band models are inadequate when modelling structures where inter-valley transport is probable and furthermore, details one factor that may influence the disagreement btw experimentally determined effective enhancements and that predicted theoretically.

4.5.2 Optimised Γ and X Band MQB Reflector

To combat transmission via the X-minimum and the piercing resonant tunnelling spikes, a novel MQB superlattice structure [40] is proposed below. A flatband zero-biased representation of this structure is displayed below in Figure 4.15. The material layer widths are displayed below in Table 4.4.

Layer Number	AlGaInP Alloy	Layer Type (w.r.t. □Γ-band)	Structure Widths (Å)
1	$(Al_{0.7}Ga_{0.3})_{0.5}In_{0.5}P$	barrier	90
2	$(Al_{0.3}Ga_{0.7})_{0.5}In_{0.5}P$	well	60
3	$(Al_{0.7}Ga_{0.3})_{0.5}In_{0.5}P$	barrier	90
4	$(Al_{0.3}Ga_{0.7})_{0.5}In_{0.5}P$	well	42
5	$(Al_{0.7}Ga_{0.3})_{0.5}In_{0.5}P$	barrier	42
6	$(Al_{0.3}Ga_{0.7})_{0.5}In_{0.5}P$	well	42
7	$(Al_{0.7}Ga_{0.3})_{0.5}In_{0.5}P$	barrier	42
8	$(Al_{0.3}Ga_{0.7})_{0.5}In_{0.5}P$	well	42
9	$(Al_{0.7}Ga_{0.3})_{0.5}In_{0.5}P$	barrier	42
10	$(Al_{0.3}Ga_{0.7})_{0.5}In_{0.5}P$	well	42
11	$(Al_{0.7}Ga_{0.3})_{0.5}In_{0.5}P$	barrier	42
12	$(Al_{0.3}Ga_{0.7})_{0.5}In_{0.5}P$	well	42
13	$(Al_{0.7}Ga_{0.3})_{0.5}In_{0.5}P$	barrier	42
14	$(Al_{0.3}Ga_{0.7})_{0.5}In_{0.5}P$	well	42
15	$(Al_{0.7}Ga_{0.3})_{0.5}In_{0.5}P$	barrier	42
16	$(Al_{0.3}Ga_{0.7})_{0.5}In_{0.5}P$	well	42
17	$(Al_{0.7}Ga_{0.3})_{0.5}In_{0.5}P$	barrier	42

Table 4.4: Layer widths of the optimised MQB structure displayed in Figure 4.15.

The dimensions of the MQB structure after the re-optimisation process comprises of two initial thick barrier-well systems of 90-60 angstroms and 90-42

angstroms in width respectively, followed by seven barrier-well periods of 42Å each, which comprise the superlattice.

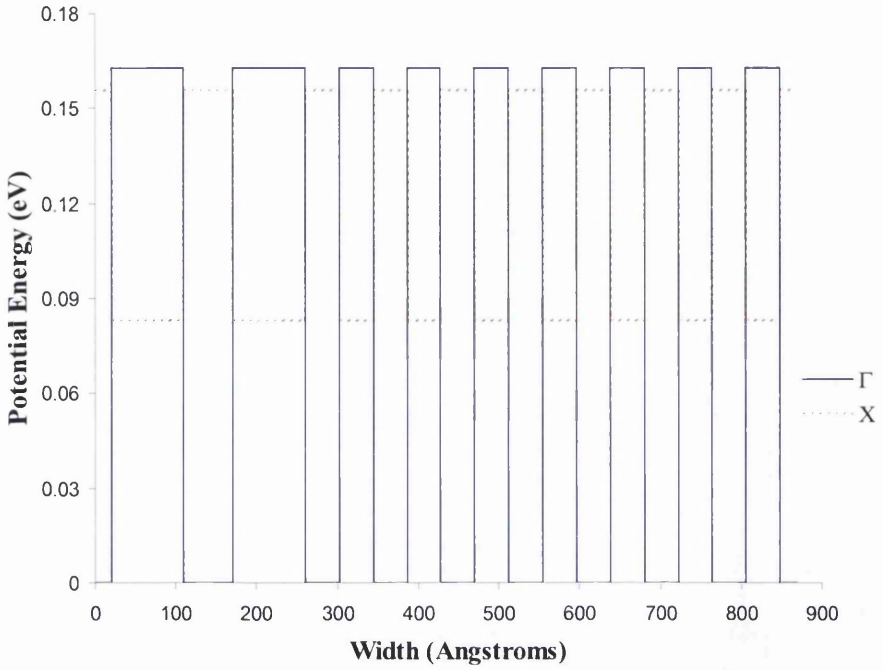

Figure 4.15: Schematic diagram of proposed AlGaInP Γ-X MQB reflector.

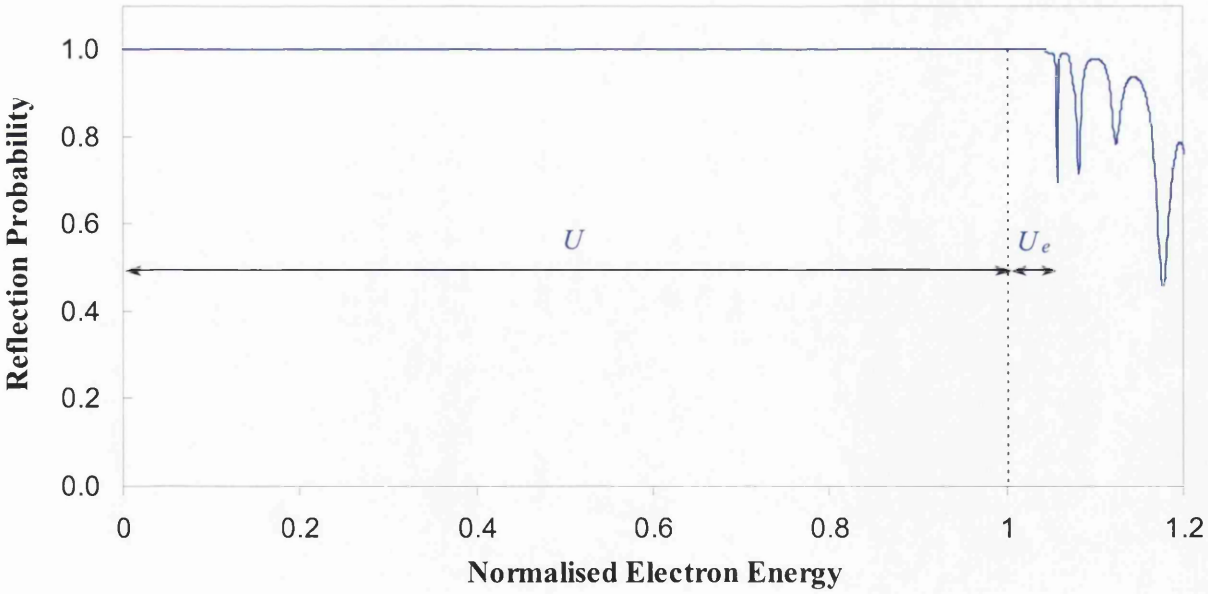

Figure 4.16: Reflection and transmission probability plots indicating the total reflectivity (i.e. the sum of the Γ and X reflectivity's)

Here, three thick initial material layers have been employed. This idea is simply an extension of the thick initial barrier in the single-band regime, utilised to inhibit low energy tunnelling. However, in this case a supplementary thick X-band barrier (i.e. a $(Al_{0.3}Ga_{0.7})_{0.5}In_{0.5}P$ material layer) has been added to suppress X-valley transportation. In addition, the number of superlattice periods has been reduced from eight to seven, to hinder the onset of resonant tunnelling modes.

Figure 4.16 above displays the calculated total reflectivity of the novel MQB structure displayed in Figure 4.15. In this simulation the magnitude of the inter-valley mixing parameter was held constant at a magnitude of 0.155ÅeV [27]. At this magnitude no visible resonant tunnelling modes or direct X-band leakage is evident and the size of the effective enhancement is approximately 5% the intrinsic Γ-band maximum. Hence, the effective enhancement of the single-band MQB analysed via the single-band Schrödinger solver has been regained.

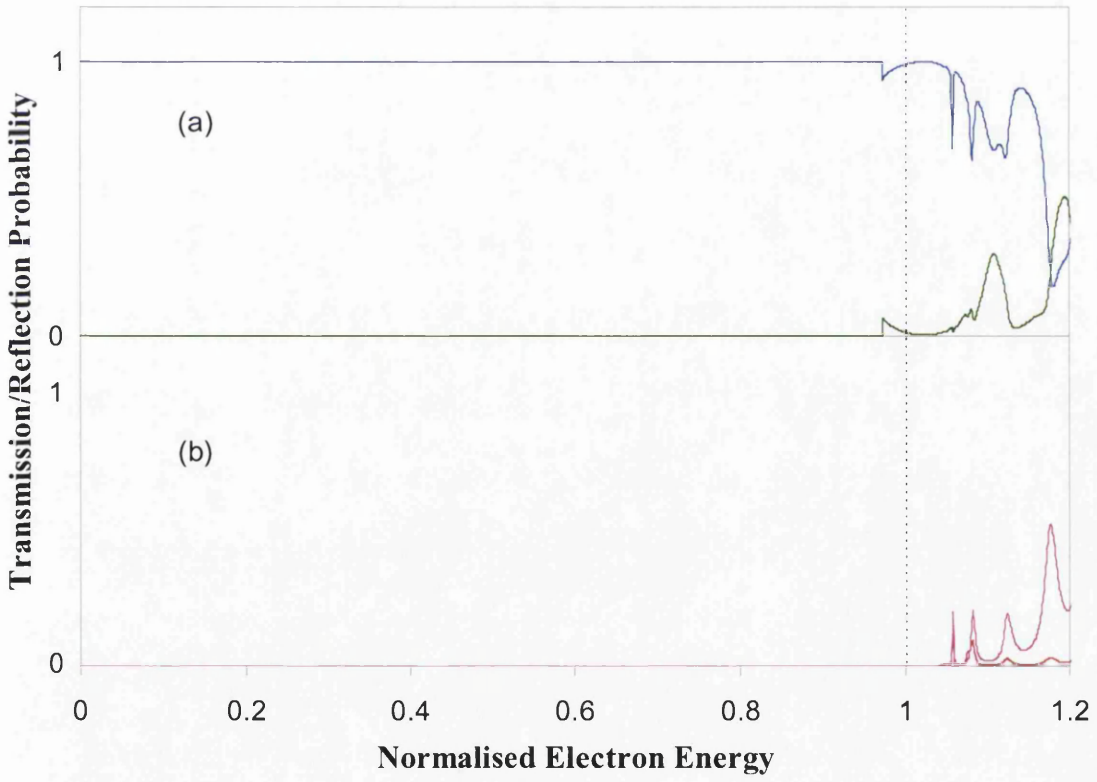

Figure 4.17: Calculated Γ and X-band reflection and transmission probabilities, plot(a) and (b) respectively.

In Figures 4.17(a) and (b) above, the reflection and transmission probabilities are displayed for the individual Γ and X conduction band minima respectively. From

Figure 4.17(a) it is easy to see that the sum of the Γ and X reflection probabilities (blue and green solid lines respectively) approximately results in the total reflectivity profile shown in Figure 4.16. The missing transmission features can be envisaged by addition of the transmission profiles shown in Figure 4.17(b). Here, the magenta coloured line corresponds to Γ-band tunnelling and the red to X-band. No transmission processes are evident for energies equivalent to 5% the intrinsic barrier height.

Thus, from this initial results section, it has been demonstrated that the popular single-band effective mass-envelope model is inadequate when considering the reflectivity properties of multi-layered structures where conduction band crossover is apparent. The oversimplification of the transport mechanisms in the AlGaInP material under the single-band method, reveals one factor to explain the degree of difference seen between theoretically predicted effective enhancements and of those determined experimentally.

4.6 Summary

In Section 4.2 of this Chapter a mechanism to theoretically deduce the reflection properties of a multi-layered structure has been detailed. To do this a numerical routine was developed that via the transfer matrix method solved Schrödinger's equation across the structure in question, yielding the transmission and reflection probabilities of an incident electron. Furthermore, by way of an example, the routine was applied to three quantum structures, namely, an infinite step potential, a potential barrier and a MQB structure, and their corresponding reflection profiles displayed.

It was discussed in Section 4.3, that to accurately model the reflection spectra calculated from multi-layered structures comprised of the AlGaInP semiconductor, it was important to include the possibility of elastic inter-valley transport of electrons between the Γ and X conduction band minima at material interfaces. The additional transfer possibilities arising from elastic scattering events were then subsequently discussed.

To allow for these additional transfer mechanisms to occur, the simple effective mass-envelope model was extended to solve simultaneously two Schrödinger equations, one for each conduction band minimum. Here, inter-valley transport of electrons was mediated by a mixing parameter added into each Hamiltonian.

This model was then verified quantitatively, by comparison of the transmission spectra acquired from a single layer GaAs/AlAs/GaAs potential barrier at various widths, with that of more complex psuedopotential models of Marsh and Inkson [17-19]. It was shown that each of the two models predicted the presence of resonant tunnelling modes present within the X-band well in the AlAs material layer, signifying the dual-band Schrödinger solver fairs favourably with the more complicated model.

Section 4.4 of this Chapter dealt with the important issue of MQB design and optimisation. It was established here that there were physical limitations to the choice of individual AlGaInP material layer thickness, overall MQB thickness and choice of aluminium content in the AlGaInP alloy used to comprise the constituent barriers and wells. This first limitation is imposed by modern growth techniques, to have any confidence applying the numerical model to a physical structure, the dimensions of the physical structure should be as near as possible to those used in the numerical model. From STM experiments it was established that a material layer minimum of 15 monolayers should be adhered to. As seen in Chapter 3, the thinner the well layers the more the forbidden minibands get pushed above the intrinsic barrier height. Hence, the optimisation procedure always started with superlattice layer widths of 15 monolayers. Also, a limit to the overall width of the MQB was instigated; this was set at a maximum of 900Å in order to retain electron coherence throughout the structure.

The final physical restriction was set on the composition of the barrier and well layers. In sub-section 4.4.4, STM images looking at a MQB structure composed of the ternary semiconductors AlInP (barriers) and GaInP (wells), evidence of alloy intermixing gave rise to graded regions of the quaternary semiconductor AlGaInP. By using AlGaInP material with aluminium contents of 0.7 and 0.3 for the barriers and wells respectively, the detrimental effects of alloy clustering and grading are kept to a minimum.

The optimisation process itself detailed how variation of the width of an initial thick barrier can alter the reflection probability to leave no low energy electron

tunnelling features below the intrinsic barrier height. Also, it was shown that by varying the number of superlattice periods an effective enhancement might be achieved if the low energy electron tunnelling is ignored. Finally, it was shown that a composite of the aforementioned structures predict high reflectivity with no low energy transmission features.

Using the optimisation procedure, a single band MQB structure was optimised for single-valley transport in Section 4.5; this yielded an effective enhancement of 5% to the conduction band maximum. However, re-solving this structure with the dual-band Schrödinger solver resulted in the intrinsic barrier height being reduced to approximately 65% of its initial Γ-band barrier height maximum. Here, sharp resonant transmission peaks were evident at energies equivalent to the well regions of the X-minimum; also, direct X-transmission across the structure was observed, implying a X-band leakage current. However, these effects were negated by the proposal of a novel MQB design, consisting of a double Γ and X barrier. The corresponding reflectivity plots gained from the analysis of this structure, found that transmission via both conduction band minima was subdued, regaining the effective enhancement of 5% predicted by the single-band model.

Thus, from this initial study it has been shown that it is possible to consider inter-valley elastic scatterings, and still theoretically predict effective enhancements equivalent to that of the popular single-band model.

In addition to the above comments, it was mentioned that the majority of authors in this field tend to use the flatband zero biased approximation, to construct the conduction band profiles of their MQB structures. This standard approximation may be superseded, by consideration of the distribution charge across the active region of the device, as a consequence of differently doped regions.

As the structure designed in this thesis are to be grown and experimentally examined, it is of utmost importance to be able to mimic the physical behaviour of the bands within a PIN junction. To tackle this issue, in the next chapter Poisson's equation is numerically solved across the active region of the device to approximate the conduction band profile in a more physically correct manner, and by recalibrating the dual-band MQB structure favourable enhancements to the intrinsic conduction band potential barrier are produced.

4.7 References

[1] R. de L Kronig and W.J. Penney, 'Quantum mechanics of electrons in crystal lattices', *Proc. Roy. Sic.*, Vol. A130, pp. 499-513, 1930.

[2] C. Kittel., 'Introduction to Solid State Physics', *Wiley*, 7th Edition, (1996).

[3] R. Tsu, and L. Esaki, 'Tunnelling in a finite superlattice', *Appl. Phys. Lett.*, **22**, pp. 562-564, (1973).

[4] K.Iga, H. Uenohara, and F. Koyama, 'Electron Reflectance of Multiquantum Barrier (MQB)', *Electron. Lett.*, **22**, pp. 1008, (1986).

[5] H. Uenohara, K.Iga, and F. Koyama, 'Analysis of electron reflectivity and leakage current of multiquantum barrier, (MQB)', *Trans. IEICE Japan, **J70-C***, pp. 851-857, (1987).

[6] J. Batey, S. L. Wright, and D. J. Dimaria, 'Energy bandgap discontinuities in GaAs: (Al, Ga)As heterojunctions', *Appl. Phys. Lett.*, **57**, pp. 484-487, (1985).

[7] H. C. JR. Casey, and M. B. Panish, 'Heterostructure lasers, part A, fundamental principles', *(Academic Press)*, pp. 192, (1978).

[8] M. Levinshtein, S. Rumyantsev, and M. Shur, 'Handbook Series On Semiconductor Parameters Volume 1', *World Scientific*, (1999).

[9] M. Asada, A. Kameyama, and Y. Suematsu, 'Gain and intervalence band absorption in quantum-well lasers', *IEEE J. Quantum. Electron.*, **20**, pp. 745-753, (1984).

[10] P. Raisch, R. Winterhoff, W. Wagner, M. Kessler, H. Schweizer, T. Riedl, R. Wirth, A. Hangleiter, and F. Scholz, 'Investigations on the performance of multiquantum barriers in short wavelength (630nm) AlGaInP laser diodes', *Appl. Phys. Lett.*, **74**(15), (1999)>

[11] A. P. Morrison, J. D. Lambkin, C. J. van der Poel, and A. Vaslster, 'Evaluation of Multiquantum Barriers in Bulk Double Heterostructure Visible Laser Diodes', *IEEE Photon. Tech. Lett.*, **8**(7), (1996).

[12] P. M. Smowton and P. Blood, 'GaInP $(Al_xGa_{1-x})_yIn_{1-y}P$ 670nm quantum well lasers for high-temperature operation', *IEEE J. Quantum. Electron.*, **31**, pp. 2159-2164, (1995).

[13] T. Takagi, F. Koyama and K. Iga, 'Design and Photoluminescence Study on a Multiquantum Barrier ', *Electron Lett.* **27**, pp.1511-1518, (1991).

[14] T. Takagi, F. Koyama and K. Iga, 'Modified multiquantum barrier for 600nm range AlGaInP lasers', *Electronic Lett.*, **27**(12), pp. 1081-1082, (1991).

[15] C. S. Chang, Y. K. Su, S. J. Chang, P. T. Chang, Y. R. Wu, K. H. Huang, and T. P. Chen, 'High-Brightness AlGaInP 573nm Light-Emitting Diode with A Chirped Multiquantum Barrier', *IEEE J. Quantum. Electron.*, **34**(1), pp. 77-82, (1998).

[16] S. A. Wood,C. H. Molloy, P. M. Smowton, P. Blood C. C. Button, 'Minority Carrier Effects in GaInP Laser Dioides', *IEEE J. Quantum. Electron.*, **36**, pp. 742-750, (2000).

[17] A. C. Marsh, 'Indirect bandgap tunnelling through a (100) GaAs/AlAs/GaAs heterostructure', *Semicond. Sci. Technol.*, **1**, pp. 320-326, (1986).

[18] A. C. Marsh, 'Electron tunnelling in GaAs/A/GaAs heterostructures' *IEEE J. Quantum. Electron.*, **23**, pp. 371-375, (1987).

[19] A. C. Marsh and J. C. Inkson, 'An empirical pseudopotential analysis of (100) and (110) GaAs-$Al_xGa_{1-x}As$ heterostructures' *J. Phys.C: Solid-State Phys.*, **17**, pp. 6561-6571, (1984).

[20] D. P. Bour, Chapter 9 in 'Quantum Well Lasers', P. S. Zory, Jr., *Ed. Academic Press*, New York, (1993).

[21] M. P. C. M. Krijn, 'Heterojunction band offsets and effective masses in III-V quarternary alloys', *Semicond. Sci. Tech.*, Vol 6, pp. 27-31, (1991).

[22] H. Tanaka, Y. Kawamura, S. Nojima, K. Wakita, and H. Asahi, 'InGaP/InGaAlP double-heterostructure and multiquantum-well laser diodes grown by molecular-beam epitaxy', *J. Appl. Phys.*, Vol **61**, pp. 1713-1719, (1987).

[23] R. P. Schnieder, Jr., R. P. Bryan, E. D. Jones, and J. A. Lott, 'Excitonic transitions in InGaP/InAlGaP strained quantum wells', *Appl. Phys. Lett.*, Vol **63**, pp. 1240, (1993).

[24] X. H. Zhang, S. J. Chua, and W. J. Fan, 'Band offsets at GaInP/AlGaInP (001) heterostructures Lattice matched to GaAs', *Appl. Phys. Lett.*, **73**(8), pp. 1098-1100, (1998).

[25] E. E. Mendez, E. Calleja, C. E. T. Gonclaves da Silva, L. L. Chang, and W. I. Wand, 'Observation by resonant tunnelling of high-energy states in GaAs-$Ga_{1-x}Al_xAs$ quantum wells', *Phys. Rev. B*, **33**, p.7368, (1986).

[26] E. E. Mendez, E. Calleja, and W. I. Wand, 'Tunneling through indirect-gap semiconductor barriers', *Phys. Rev. B*, **34**, pp. 6026, (1986).

[27] A Bonnefoi, R. Collins, T. C. McGill, R. Burnham and F. Ponce, 'Resonant tunnelling in GaAs/AlAs heterostructures grown by metalorganic chemical vapor deposition', *Appl. Phys. Lett.*, **46**, pp. 285-287, (1985).

[28] A. Bonnefoi, T. C. McGill, R. D. Blurnham, 'Resonant tunneling through GaAs quantum-well energy levels confined by $Al_xGa_{1-x}As$ Gamma - and X-point barriers', *Phys. Rev. B*, **37**, pp. 8754, (1988).

[29] D. Landheer, H.C. Lui, M. Buchanan and R. Stoner, 'Tunneling through AlAs barriers:Γ–X transfer current', *Appl. Phys. Lett.* **54**(18), pp. 1784-1786, (1989).

[30] H. C. Lui, 'Resonant tunnelling through single layer heterostructures', *Appl. Phys. Lett.* Vol.51, No.13, (1987).

[31] D. Landheer, H.C. Lui, M. Buchanan and R. Stoner, 'Tunneling through AlAs barriers:Γ–X transfer current', *Appl. Phys. Lett.* **54**(18), pp. 1784-1786, (1989).

[32] T. Takagi, F. Koyama, and K. Iga, 'Potential barrier height analysis of AlGaInP multiquantum barrier', *Jpn. J. Appl. Phys.*, Part 2 **29**, L1977, (1990).

[33] Chapter 3 this thesis.

[34] E. E. Mendez, F. Agulló-Rueda, and J. M. Hong, 'Temperature dependence of the electronic coherence of GaAs-GaAlAs superlattices', *Appl. Phys. Lett.* **56**, pp. 2545, (1990).

[35] K. Kishino, A. Kikuchi, Y. Kaneko and I. Nomura, 'Enhanced carrier confinement by the multiquantum barrier in 660nm GaInP/AlInP visible lasers', *Appl. Phys. Lett.* **58**, pp. 1822-1824, (1991).

[36] Y. Seko, S. Fukatsu and Y. Shiraki, 'Optical transition energies of GaInP quantum wells with GaInP/AlInP superlattice barriers', *J. Appl. Phys.* **72**, pp. 1355-1357, (1994).

[37] K. S. Teng, M. R. Brown, A.Kestle, P. Smowton, P. Blood, S. Pinches, P. A. Mawby and S. P. Wilks, 'An investigation of multiquantum barriers for band offset engineering in AlGaInP/GaInP lasers', *Appl. Surf. Sci.*, **190**, p. 284, (2001).

[38] P. Raisch, R. Winterhoff, W. Wagner, M. Kessler, H. Schweizer, T. Riedl, R. Wirth, A. Hangleiter, and F. Scholz, 'Investigations on the performance of multiquantum barriers in short wavelength (630nm) AlGaInP laser diodes', *Appl. Phys. Lett.*, **74**(15), (1999).

[39] A. P. Morrison, J. D. Lambkin, C. J. van der Poel, and A. Valster, 'Electron Transport Across Bulk $(Al_xGa_{1-x})_{0.5}In_{0.5}P$ Barriers Determined from the I-V Characteristics of n-I-n Diodes Measured between 60 and 310K', *IEEE J. Quantum. Electron.*, **36**(11), (2000).

[40] M. R. Brown, K. S. Teng, A.Kestle, and S. P. Wilks, 'Theoretical investigation of the role of inter-valley transport in AlGaInP MQB structures', Submitted to *Applied Surface Science* June (2004).

Chapter 5

Effects of Non-Linear Charge Distribution

5.1 Introduction

The main focus of this chapter is the design and optimisation of a novel dual-band (i.e. Γ and X) MQB reflector that predicts good enhancements to the intrinsic conduction band offsets, when evaluated at the working bias of a visible 630nm laser diode. To achieve this goal, it is necessary to employ Poisson's equation to predict the band bending effects emerging from the non-linear doping concentrations across the device. To imitate approximate lasing conditions a doping and dimension dependent bias is dropped linearly across the simulation region. Under these biased conditions the MQB barrier and well periods are optimised to achieve a high and stable effective enhancement.

Therefore this Chapter is structured in the following manner; in Section 5.2 Poisson's equation is derived from Maxwell's equations and arranged into an appropriate form that can be of functional use in semiconductor analysis.

An explicit integration method is developed in Section 5.3 to numerically solve Poisson's equation across the active and MQB regions of the laser device. In addition to this, a simple linear bias method is detailed, which allows the Poisson solved structure to be adjusted to mimic the laser diode when lasing.

The single Γ-band and the dual-band (Γ and X) MQB reflectors detailed previously in Chapter 4 sub-sections 4.5.1 and 4.5.2 respectively, are re-optimised in Section 5.4 under applied bias to achieve a good effective enhancement whilst taking

account of the increase in transmission modes attributed to band bending features. The reflectivity of both these structures are analysed and a comparison made, where it becomes apparent that once more that the inter-valley transport mechanism is the dominant issue in the simulation.

Sections 5.5 and 5.6 give some conclusions on the theoretical work carried out in this chapter and all referenced articles and books are listed respectively.

5.2 Poisson's equation

In this section, a viable form of Poisson's equation applicable specifically for the analysis of semiconductor devices is derived, by means of Maxwell's equations. The section concludes with an explanation of the constituent terms within the derived Poisson equation necessary to initiate its solution.

5.2.1 Derivation of Poisson's equation

Poisson's equation is essentially a limiting case of the Gauss-Maxwell equation (equation (5.1)). However, to make this equation directly applicable to this semiconductor problem, some manipulations have to be undertaken.

$$\nabla.\mathbf{D} = \rho, \tag{5.1}$$

Firstly, the electric displacement vector **D** may be related to the electric field vector **E** by the following expression

$$\mathbf{D} = \varepsilon \cdot \mathbf{E} \tag{5.2}$$

where ε denotes the permittivity tensor. This relation is valid for all materials, which have time independent permittivity. Furthermore, polarisation by mechanical forces is ignored [1]. Both assumptions hold reasonably well for the intended semiconductor application.

The electric field vector is related to the electrostatic potential, ψ, by invoking Maxwell's magnetic flux equation:

$$\nabla.\mathbf{B} = 0 \tag{5.3}$$

and introducing a vector field **A**, and the following identity

$$\nabla.\nabla \wedge \mathbf{A} = 0 \tag{5.4}$$

to propose

$$\mathbf{B} = \nabla \wedge \mathbf{A}\,. \tag{5.5}$$

Substituting equation (5.5) into the Faraday-Maxwell equation yields

$$\nabla \wedge \mathbf{E} = -\frac{\partial(\nabla \wedge \mathbf{A})}{\partial t} \tag{5.6}$$

which maybe rearranged to give

$$\nabla \wedge \left(\mathbf{E} + \frac{\partial(\nabla \wedge \mathbf{A})}{\partial t}\right) = 0\,. \tag{5.7}$$

Using the vector identity

$$\nabla \wedge \nabla\psi = 0\,, \tag{5.8}$$

the gradient scalar field $\nabla\psi$, may be related to the bracketed expression in equation (5.7) (in this particular circumstance a more physical interpretation is gained by choosing the negative gradient of the scalar potential), hence

$$\boldsymbol{E} = -\frac{\partial \boldsymbol{A}}{\partial t} - \nabla\psi\,. \tag{5.9}$$

Substituting for the electric field **E**, in equation (5.2) via equation (5.9) yields,

$$\boldsymbol{D} = -\varepsilon \frac{\partial \boldsymbol{A}}{\partial t} - \varepsilon \nabla \psi \tag{5.10}$$

Exchanging the electric displacement vector **D** in equation (5.1) by the relation derived in equation (5.10) gives,

$$\nabla . \left(\varepsilon \frac{\partial \boldsymbol{A}}{\partial t} + \varepsilon \nabla \psi \right) = -\rho \tag{5.11}$$

Here, the first term is zero if the permittivity ε can be considered to be homogeneous. Thus, equation (5.11) finally reduces to the well-known form of Poisson's equation applicable semiconductor device analysis.

$$\nabla . \varepsilon \nabla \psi = -\rho \tag{5.12}$$

From herein the permittivity, ε, will be considered a scalar constant within a particular semiconductor material. Thus, Poisson's equation in one-dimension may be expressed in the following form:

$$\frac{\partial^2 \psi}{\partial x^2} = -\frac{\rho}{\varepsilon}, \tag{5.13}$$

where the space charge density ρ, can be broken down into the product of the elementary charge q times the sum of the positively charged hole concentration p, the negatively charged electron concentration n, and the ionised donor and acceptor concentrations N_D and N_A respectively, i.e.

$$\rho = q\left(p - n + N_D - N_A\right). \tag{5.14}$$

5.2.2 Analysis of Constituent Parameters in Poisson's Equation

To solve equation (5.13) for the electrostatic potential, ψ, requires evaluation of each individual term within the expression. Firstly, the electron density n maybe determined from the following integral

$$n = \int_{E_c}^{\infty} N(E)F(E)dE \tag{5.15}$$

where $N(E)$ is the density of states, and may be approximated to

$$N(E) = \frac{M_C}{2\pi^2}\left(\frac{2m_{de}}{\hbar^2}\right)^{3/2}(E - E_c)^{1/2} \tag{5.16}$$

where M_C is the number of equivalent conduction band minima and m_{de} is the density of states effective mass for the electrons and is given by:

$$m_{de} = \sqrt[3]{m_1^* m_2^* m_3^*} \tag{5.17}$$

where m_i^* (i = 1, 2, 3) are the anisotropic components of the effective mass tensor [2]. $F(E)$ is the standard Fermi-Dirac distribution function given by

$$F(E) = \frac{1}{1 + \exp\left(\frac{E - E_F}{k_B T}\right)} \tag{5.18}$$

Substituting this into equation (5.15) and using the relation

$$F_{1/2}(\eta_F) = \int_0^{\infty} \frac{\sqrt{\eta}\,d\eta}{1 + \exp(\eta - \eta_F)} \tag{5.19}$$

with

$$\eta_F = \left(\frac{E_C - E_F}{k_B T}\right) \quad \text{and} \quad \eta = \left(\frac{E - E_C}{k_B T}\right), \tag{5.20}$$

yields

$$n = N_C \frac{2}{\sqrt{\pi}} F_{1/2}\left(\frac{E_C - E_F}{k_B T}\right)_C \quad \text{where} \quad N_C = 2\left(\frac{2\pi m_{de} k_B T}{h^3}\right)^{3/2} M_C \tag{5.21}$$

where N_C is the effective density of states in the conduction band and $F_{1/2}(\eta)$ is the Fermi Integral of order ½ which, unfortunately does not have a closed form solution. Due to the complexity involved in calculating the $F_{1/2}(\eta)$ analytically, a set of approximations proposed by various authors has been employed to evaluate the integral over the entire real number range of η. In the two extreme cases, i.e. $\eta << -1$ and $\eta >> +1$ the integral can be expressed in the form of a rapidly converging series. For $\eta << -1$ the Fermi-Dirac integral reduces to the following form

$$F_{1/2}(\eta) = \int_0^\infty \frac{x^{1/2}\exp(\eta - x)}{1+\exp(\eta - x)}dx \tag{5.22}$$

and hence, may be expressed as follows

$$F_{1/2}(\eta) = \frac{1}{2}\sqrt{\pi}\exp(\eta)(1 - 2^{-2/3}\exp(\eta) + ...) \tag{5.23}$$

For $\eta >> +1$ the Fermi-Dirac integral can be presented in the form of a series [3]

$$F_{1/2}(\eta) = \frac{3}{2}\eta^{3/2}\left[1 + \frac{1}{8}\pi^2\eta^{-2} + 0.267\eta^{-4} + ...\right]. \tag{5.1}$$

In the transitory interval $-4 < \eta < +10$ the Fermi-Dirac integral is approximated by the function [4]

$$F_{1/2}(\eta) = \frac{1}{2}\sqrt{\pi}\left(\frac{3}{4}\sqrt{\pi a(\eta)}^{-3/8} + \exp(-\eta)\right)^{-1} \tag{5.24}$$

where

$$a(\eta) = \eta^4 + 33.6\eta\left(1 - 0.68\exp\left(-0.17(\eta+1)^2\right)\right) + 50$$

The relative error of the above expressions is less than 0.4% and is not a major factor with respect to numerical convergence of the simulation program detailed in the following sections, due to the error incurred by the overall solution process.

Utilising a similar argument to the one presented above for electrons, the following expressions for the hole concentration p and the density of states in the valence band N_V may be deduced to be

$$p = N_V \frac{2}{\sqrt{\pi}} F_{1/2}\left(\frac{E_V - E_F}{k_B T}\right) \tag{5.25}$$

$$N_V = 2\left(\frac{2\pi m_{dh} k_B T}{h^3}\right)^{3/2} \tag{5.26}$$

where m_{dh} is the density of states effective mass for holes given by

$$m_{dh} = \left(m_{lh}^{*3/2} + m_{hh}^{*3/2}\right)^{2/3} \tag{5.2}$$

and m_{lh} and m_{hh} are the effective masses for the light and heavy holes respectively.

Finally, the ionised donor and acceptor impurities are evaluated by invoking the following expressions.

$$N_{D^+} = N_D\left(1 - \frac{1}{1 + \frac{1}{g}\exp\left(\frac{E_D - E_F}{k_B T}\right)}\right) \tag{5.27}$$

where k_B is the Boltzmann constant, T is the lattice temperature (unless otherwise stated assumed to be 300K), g is the degeneracy of the donor level, E_D is the energy level of the donors below the conduction band edge and N_D is the total density of donor atoms in the semiconductor.

$$N_{A^-} = \frac{N_A}{1 + \frac{1}{g}\exp\left(\frac{E_A - E_F}{k_B T}\right)} \tag{5.28}$$

Similarly, E_A is the energy level of the acceptors above the valence band edge and N_A is the total density of acceptor atoms in the semiconductor.

5.3 Poisson Solution Procedure

Having ascertained expressions for the constituent parameters in the space charge density ρ, the explicit integration method used to evaluate the variation of electrostatic potential, ψ, across the active and MQB regions of the laser device is next reviewed.

5.3.1 Numerical Algorithm

Numeric solution of Poisson's equation is initiated firstly, by approximating the electrostatic potential between adjacent nodes by the following truncated Taylor series expansion

$$\psi_{i+1} = \psi_i + \Delta\psi_i' + \frac{\Delta^2}{2!}\psi_i'' + \frac{\Delta^3}{3!}\psi_i''' + \vartheta(\Delta^4) \tag{5.29}$$

where i denotes the i^{th} node along the simulation area, and Δ is the magnitude of the step-size between adjacent nodes. Secondly, the second order derivatives present in the truncated series are exchanged for their corresponding charge densities, ρ_i, on the corresponding node. The third order derivative of the electrostatic potential in equation (5.29), is approximated by the following backward difference relation

$$\psi_i''' \cong \frac{1}{\Delta}\left(\psi_i'' - \psi_{i-1}''\right). \tag{5.30}$$

Substitution of equation (5.30) and the aforementioned charge densities in equation (5.29) yields

$$\psi_{i+1} = \psi_i + \Delta\psi_i' + \Delta^2\left(\frac{2\rho_i}{3} - \frac{\rho_{i-1}}{6}\right). \tag{5.31}$$

Equation (5.31) with the addition of suitable initial conditions is now able to predict the variation of the electrostatic potential ψ, across a desired semiconductor interval.

However, due to the explicit nature of the above discretisation technique an associated error of the order Δ^2 is endowed upon the value of the electrostatic potential on each subsequent node calculated from a prior node. To reduce this cumulative error, which is an unfortunate artefact of this type of solution procedure, the node spacing has been maintained at a magnitude of 1Å and the Richardson improvement formula [5] has been implemented into above numerical routine. This formula amounts to a more accurate way of discretising the third order derivatives present in equation (5.29). Using Richardson improvement formula the third order derivatives may be approximated by the following expression

$$\psi_i''' = \frac{2\psi_i'' - \psi_{i-1}''}{\Delta}. \tag{5.32}$$

Substitution of equation (5.32) into equation (5.29) yields the following improved estimate for the calculated electrostatic potential on the $(i + 1)$ node

$$\psi_{i+1} = \psi_i + \delta\psi_i' + \frac{\Delta^2}{6}\left(5\rho_i - \rho_{i-2}\right). \tag{5.33}$$

In Figure 5.1, a flow chart is presented depicting all the major steps of the solution procedure used to solve Poisson's equation for both the Γ and X conduction band across the active and MQB regions of the laser diode.

The preliminary step of the program ascertains the basic structure of the simulation region of interest. Wherein, each individual semiconductor material or alloy layer is given a particular spatial width and doping magnitude. Utilising this information a flat-band zero biased conduction band approximation is determined. In this idealised conduction band profile the two-thirds approximation was used to determine the conduction band offsets. From this the magnitude of the energy separation between the Fermi-level and the conduction band minima at the beginning and end of the structure is determined. It is not necessary to evaluate the Fermi-level at each node, as by definition it is constant across the structure under zero bias conditions. The Fermi-level is always referenced to zero unless otherwise stated. Three trial values of the Fermi-level are needed to initiate to calculation of true self-consistent energy separation. These initial guesses assume that the aforementioned

energy differences be bounded within the energy interval $\pm 2E_g$, This approximation allows the charge density to be deduced through equation (5.14). Under flatband zero biased conditions, the charge density should be zero. Therefore, a comparison of the three trial values may be conducted to test if they are within a set tolerance from zero. If this test is found to be true the simulation procedure moves on to the main part of the program where the conduction band profiles are determined, if not, a simple bisection algorithm adjusts the starting values of the Fermi-level separation and the procedure repeated until convergence is obtained.

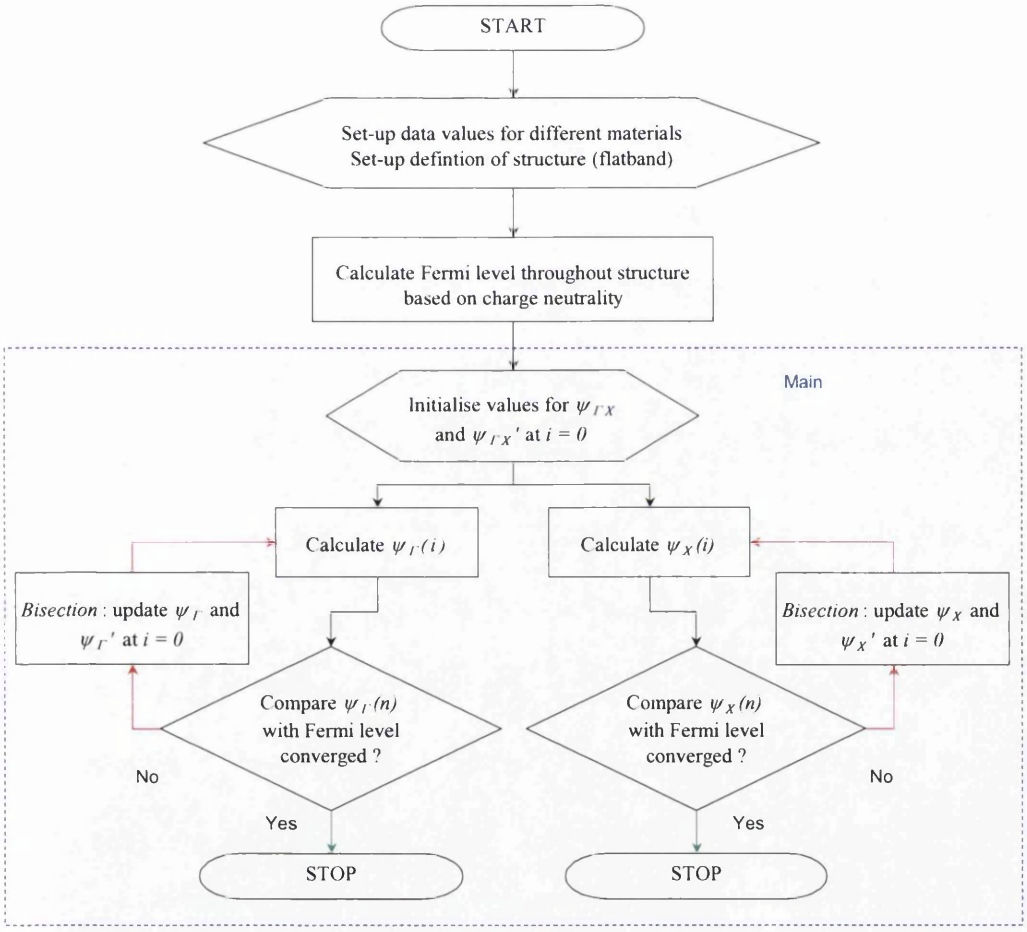

Figure 5.1: Flow chart illustrating the main steps involved in the explicit integration method used to determine the conduction band profiles by solution of Poisson's equation.

To commence the main part of the program initial values for the electrostatic potential ψ and the electric field at the first node ($i = 1$) are required. Subsequent values of ψ are determined via equations (5.29) or (5.33) depending on node position. The conduction band minimum is calculated via the following expression

$$E_C(i) = -\psi(i) + E_{Cfb}(i) + E_f(i) \tag{5.34}$$

where E_{Cfb} is the conduction band in the flat-band approximation, which essentially is required to add in the predetermined conduction band offsets, and E_f if the calculated Fermi-level separation. Convergence of the solution is determined, when direct comparison between the conduction bands minus the Fermi-level separation on the last node is below a set tolerance. If this criterion is not met, a bisection algorithm amends the initial starting values of the electric field until convergence is achieved.

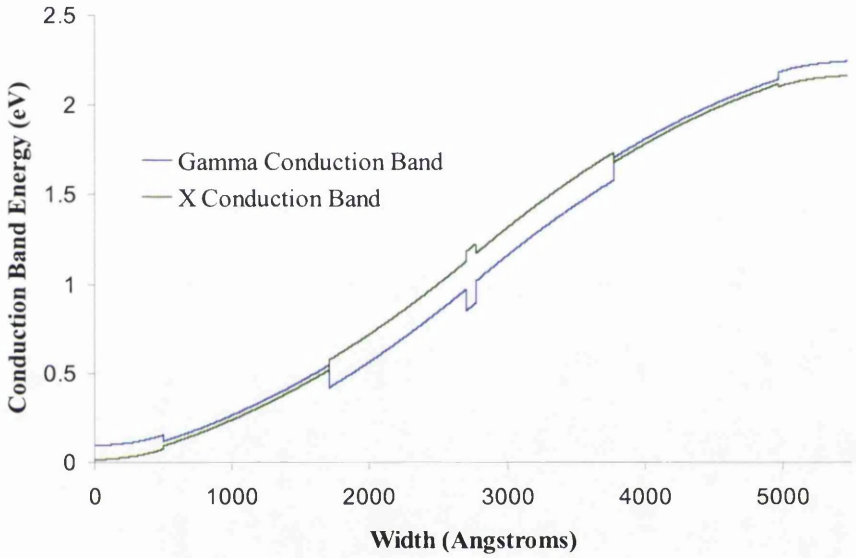

Figure 5.2: Calculated conduction band profile of the Γ and X minima.

Figure 5.2 above shows the numerically determined Γ and X conduction band profiles across the active region of a AlGaInP laser device.

5.3.2 Linear bias

To achieve the conduction band profile at a working voltage, a simple linear voltage drop across the device has been employed. It was assumed that the resistance across a particular semiconductor layer was uniform and varied proportionally as a function of layer width and reciprocal doping:

$$R(j) \propto \frac{L(j)}{N_t(j)} \tag{5.35}$$

where N_t is the sum of the donor and acceptor concentrations and j is an index to the j^{th} layer. From this expression, a proportionality constant may be calculated to enable the effective resistance of each individually doped layer to be determined. By multiplying the required applied bias voltage V_A, by the individual layer resistances, the voltage drop across each semiconductor layer can be deduced; it is then a simple case to divide each layer by its corresponding width, to determine the voltage drop per unit length ($Å^{-1}$) across the laser device

$$V/L = \frac{R(j)V_A}{L(j)}. \tag{5.36}$$

Examples of the active region and surrounding cladding region under the aforementioned linear bias are shown in the following sub-sections.

5.4 Simulation of the Active Region

In this Section, the above solution procedure is implemented in conjunction with the linear bias approximation, to obtain a more realistic approximation of the conduction band profile within the active and MQB regions of the laser diode under operating conditions.

Firstly, in sub-section 5.4.1 the single-band MQB structure designed previously under flatband conditions (sub-section 4.5.1) is placed adjacent to the active region of the device and the aforementioned simulation routine is utilised to approximate the conduction band profile across these regions under lasing conditions of the laser device. This MQB structure is then re-optimised via the procedure detailed in Chapter 4, Section 4.4 to achieve a stable maximum enhancement. In addition to this simulation, the newly optimised single-band MQB structure is then solved using the dual-band Schrödinger solver developed in Section 4.3 of the last Chapter. This analysis is performed to re-emphasise the importance of taking into account inter-valley transport within the numerical model where appropriate and its ability to destroy the effective conduction band offset enhancements predicted by the single-band theoretical model.

In a similar manner, sub-section 5.4.2 takes the optimised flatband dual-band (Γ and X) MQB reflector presented in sub-section 4.5.2 of Chapter 4. Again this structure is placed next to the active region of the device, and then the conduction band in this area is Poisson solved and a linear bias dropped across it to imitate the conduction band under operating conditions. The structure is re-optimised to null any resonant tunnelling or X-band transmission features via the optimisation process presented previously to thus exhibit high reflective enhancements. Additionally, the magnitude of the mixing parameter is varied to investigate if the predicted reflection probabilities behave in a similar manner.

5.4.1 Optimised Single-Band MQB Structure

The individual layer alloy compositions, doping and widths for the single-band MQB structure after the re-optimisation process are shown below in Table 5.1.

Material	Layer Type w.r.t. □Γ-band	Doping (cm^{-3})	Layer Width (Å) Optimised Γ-band Structure
$(Al_{0.7}Ga_{0.3})_{0.5}In_{0.5}P$	cladding	5e17 (*n*+)	50
$(Al_{0.51}Ga_{0.49})_{0.5}In_{0.5}P$	cladding	5e17 (*n*+)	945
$(Al_{0.3}Ga_{0.7})_{0.5}In_{0.5}P$	waveguide	Undoped (*p*+)	900
$Ga_{0.49}In_{0.51}P$	quantum well	Undoped (*p*+)	68
$(Al_{0.3}Ga_{0.7})_{0.5}In_{0.5}P$	Waveguide	Undoped (*p*+)	900
$(Al_{0.7}Ga_{0.3})_{0.5}In_{0.5}P$	barrier	5e17 (*p*+)	200
$(Al_{0.3}Ga_{0.7})_{0.5}In_{0.5}P$	well	5e17 (*p*+)	42
$(Al_{0.7}Ga_{0.3})_{0.5}In_{0.5}P$	barrier	5e17 (*p*+)	42
$(Al_{0.3}Ga_{0.7})_{0.5}In_{0.5}P$	well	5e17 (*p*+)	42
$(Al_{0.7}Ga_{0.3})_{0.5}In_{0.5}P$	barrier	5e17 (*p*+)	42
$(Al_{0.3}Ga_{0.7})_{0.5}In_{0.5}P$	well	5e17 (*p*+)	42
$(Al_{0.7}Ga_{0.3})_{0.5}In_{0.5}P$	barrier	5e17 (*p*+)	42
$(Al_{0.3}Ga_{0.7})_{0.5}In_{0.5}P$	well	5e17 (*p*+)	42
$(Al_{0.7}Ga_{0.3})_{0.5}In_{0.5}P$	barrier	5e17 (*p*+)	42
$(Al_{0.3}Ga_{0.7})_{0.5}In_{0.5}P$	well	5e17 (*p*+)	42
$(Al_{0.7}Ga_{0.3})_{0.5}In_{0.5}P$	barrier	5e17 (*p*+)	42
$(Al_{0.3}Ga_{0.7})_{0.5}In_{0.5}P$	well	5e17 (*p*+)	42
$(Al_{0.7}Ga_{0.3})_{0.5}In_{0.5}P$	barrier	5e17 (*p*+)	42
$(Al_{0.3}Ga_{0.7})_{0.5}In_{0.5}P$	well	5e17 (*p*+)	42
$(Al_{0.7}Ga_{0.3})_{0.5}In_{0.5}P$	barrier	5e17 (*p*+)	42
$(Al_{0.3}Ga_{0.7})_{0.5}In_{0.5}P$	well	5e17 (*p*+)	42
$(Al_{0.7}Ga_{0.3})_{0.5}In_{0.5}P$	barrier	5e17 (*p*+)	42
$(Al_{0.3}Ga_{0.7})_{0.5}In_{0.5}P$	well	5e17 (*p*+)	42
$(Al_{0.7}Ga_{0.3})_{0.5}In_{0.5}P$	barrier	5e17 (*p*+)	42
$(Al_{0.3}Ga_{0.7})_{0.5}In_{0.5}P$	well	5e17 (*p*+)	42
$(Al_{0.7}Ga_{0.3})_{0.5}In_{0.5}P$	barrier	5e17 (*p*+)	42
$(Al_{0.3}Ga_{0.7})_{0.5}In_{0.5}P$	well	5e17 (*p*+)	45
$(Al_{0.7}Ga_{0.3})_{0.5}In_{0.5}P$	cladding	5e17 (*p*+)	200

Table 5.1: List of physical parameters of the Γ-band MQB.

From the above physical parameters, it can be seen that the dimensions of the single-band MQB reflector have retained their original form, to that described

previously in sub-section 4.5.1 except that the thick initial barrier layer has been increased in width from 150Å to 200Å.

5.4.1.1 Γ-Valley Transport Only

Figure 5.3 below, displays the Γ conduction band across the active and MQB regions predicted by solution of Poisson's equation using the aforementioned explicit integration technique, also a turn-on voltage of 2V has been dropped across the whole quantum device to simulate lasing conditions of the quantum device.

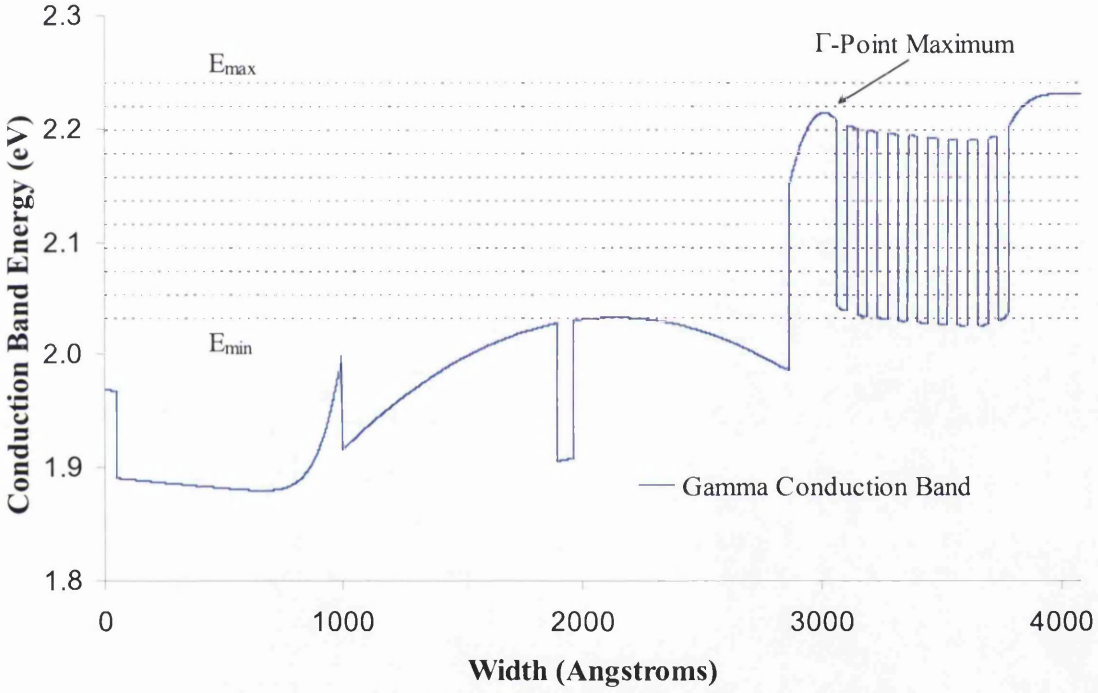

Figure 5.1: Numerically determined Γ (solid blue line) conduction band minimum at a working voltage of 2.6V. The intermittent purple area denotes the energy range of an incident electron, over which the reflectivity spectrum of the MQB was analysed.

In addition to the position of the conduction band minimum in the three regions, Figure 5.3 also illustrates the range of energies an electron incident on the MQB reflector may possess. This energy spectrum is normalised to the Γ-band maximum also highlighted in the Figure. The lower limit of the energy spectrum coincides with the highest energy point across the MQB region, (E_{min}). The upper limit of the energy spectrum is given by the energy of the Γ-band barrier height maximum plus a small energy offset, (E_{max}). Electrons with energy beyond this point have no immediate bearing on the size of the effective enhancement, although

electrons in this range may be reflected back toward the active region by higher lying forbidden minibands (see Figures 5.4 and 5.6).

It is apparent from Figure 5.3, that electrons incident on the MQB with energies less than that of the Γ-point maximum, will be totally reflected back toward the quantum well region, simply because there is no other path available. This is a consequence of the Γ-band maximum being situated in the cladding region of the device, which would in the physical situation extend to a length of approximately 9000Å, which suggests that the likelihood of a tunnelling event occurring is so negligible it may be ignored.

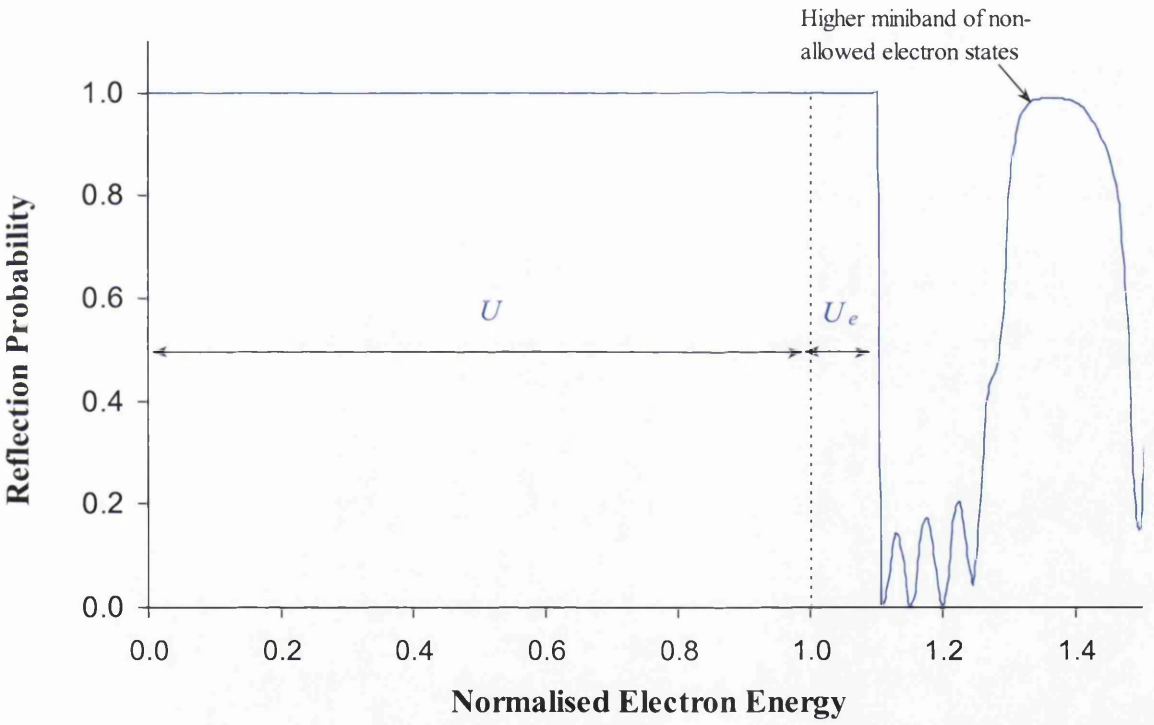

Figure 5.2: Reflectivity plot of the Poisson solved optimised single-band MQB model, where transport modes via the Γ-minimum considered only.

Figure 5.4 above displays the calculated reflectivity profile associated with the single-band MQB structure detailed above. The electron energy on the x-axis of Figure 5.4 has been normalised to the highlighted Γ-point maximum and subsequently predicts a non-trivial effective enhancement, U_e, of approximately 10% with respect to this point.

5.4.1.2 *Inter-Valley Transport*

The optimised structure of the last sub-section is now evaluated using the dual-band Schrödinger solver developed in Section 4.3 of Chapter 4. The position of the calculated X-band relative to the Γ-band is displayed in Figure 5.5 below. In addition to the Γ-point maximum present in Figures 5.3 and 5.5 it is also appropriate to include a corresponding point for the X conduction band when inter-valley transport is considered. The X-point maximum will now be the lower limit on the energy spectrum, as below this energy all electrons will be reflected back toward the active region no matter what minima they reside in.

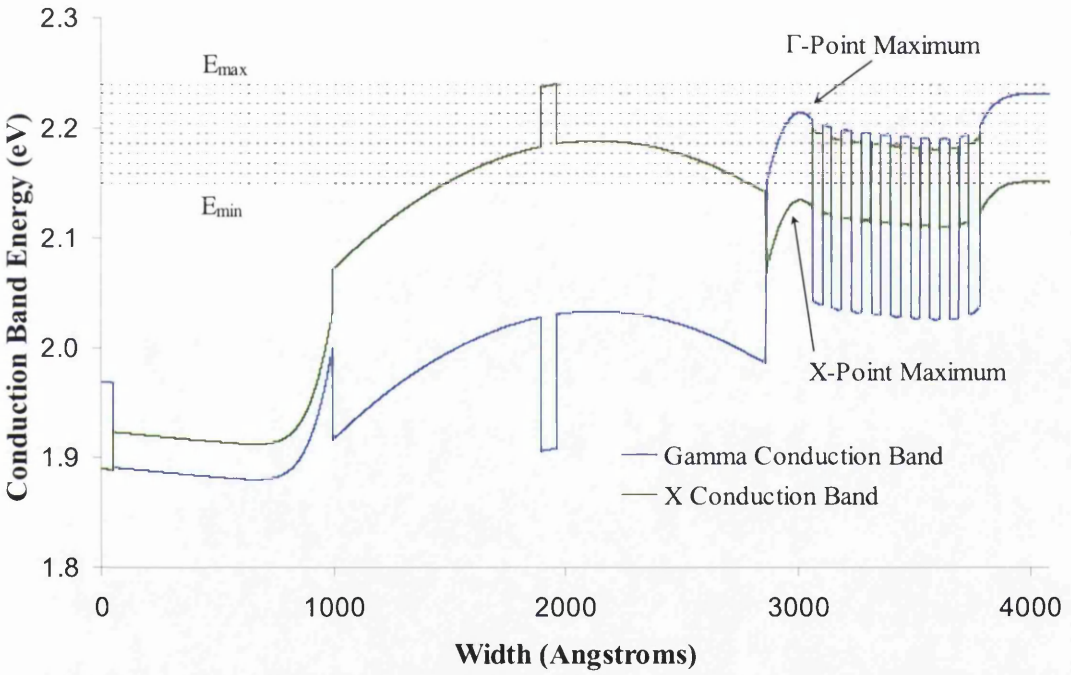

Figure 5.1: Numerically determined Γ and X conduction band minima (solid blue and solid green line respectively) at a working voltage of 2 V. The intermittent purple area denotes the energy range of an incident electron, over which the reflectivity spectrum of the MQB was analysed.

Figure 5.6 predicts the reflection spectra of the same optimised single-band MQB reflector when inter-valley transport is considered over the aforementioned energy range. Examination of the reflectivity in this regime predicts a similar deterioration in the reflection spectra at a comparable energy to that calculated under flatband zero biased conditions seen previously in Chapter 4.

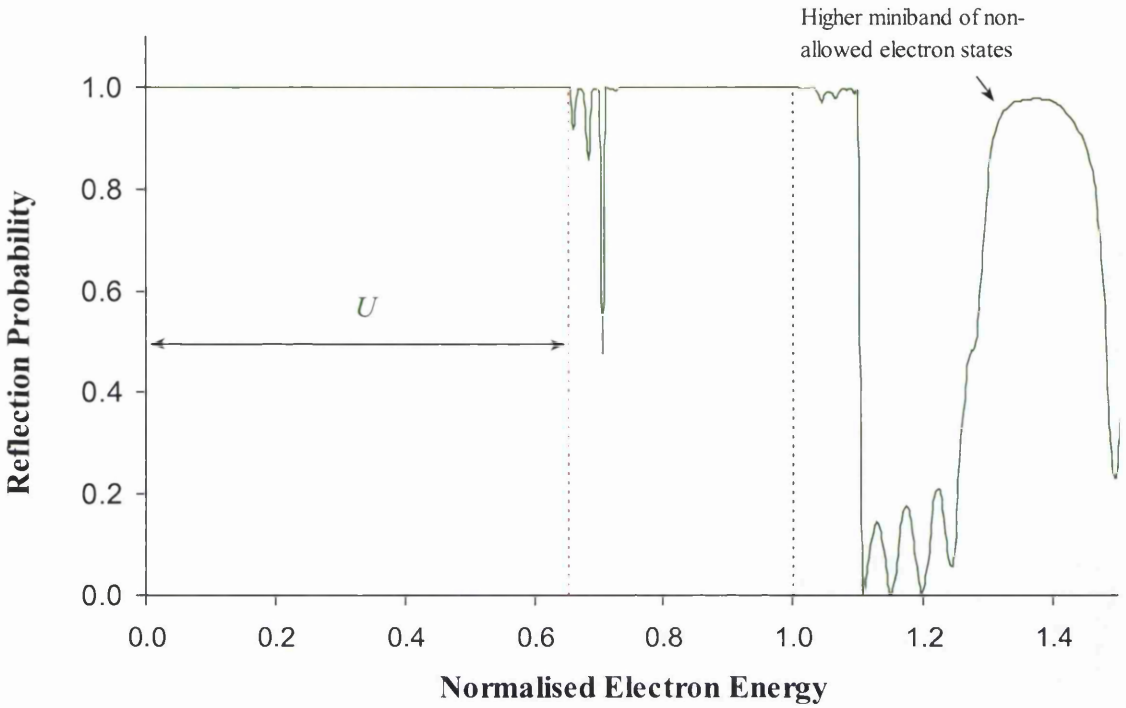

Figure 5.2: Reflectivity plot of the Poisson solved optimised single-band MQB model, where inter-valley transport is considered.

Although, the enlarged forbidden energy peaks, that separate the regions of high reflectivity, are associated with X-band transmission in this case, and not resonant tunnelling modes in the Γ-band as seen previously in Chapter 4. The onset of the X-band leakage current coincides with energies just above the X-band maximum indicated in Figure 5.5, which corresponds to the placement of the X-well in the flatband zero biased case. In both cases, a surge of transmission by either resonant tunnelling modes or via the X-band or indeed a combination of both these processes is apparent whenever it is physically possible to do so. Thus, it seems plausible for structures constructed out of semiconductor materials that experience conduction band crossover, to reference the intrinsic barrier height from highest point (in energy) of the lowest lying conduction band minimum. In this case, this value corresponds to the X-point maximum and unless otherwise stated from herein, all reflection spectra are normalised to this point.

In the following sub-section the previously optimised flatband dual-band MQB structure proposed in Chapter 4, sub-section 4.5.2 to inhibit electron transmission in both the Γ and X bands is placed adjacent to the active region and like

the previous sub-section Poisson solved and biased. The structure is then re-optimised in order to exhibit high reflective properties as that seen in Chapter 4.

5.4.2 Dual-Band Reflector

The individual layer alloy compositions, doping and widths for the dual-band (Γ and X) MQB structure after the re-optimisation process has been completed are shown below in Table 5.2. The optimisation procedure resulted in the dimensions of the two initial low energy electron-stopping layers being increased from 90Å and 60Å, to layers of width 150Å each. Also the number of superlattice periods has been reduced from seven to six.

Material	Layer Type w.r.t. □Γ-band	Doping (cm^{-3})	Layer Width (Å) Optimised Dual-Band Structure
$(Al_{0.7}Ga_{0.3})_{0.5}In_{0.5}P$	cladding	5e17 (*n*+)	50
$(Al_{0.51}Ga_{0.49})_{0.5}In_{0.5}P$	cladding	5e17 (*n*+)	945
$(Al_{0.3}Ga_{0.7})_{0.5}In_{0.5}P$	waveguide	Undoped (*p*+)	900
$Ga_{0.49}In_{0.51}P$	quantum well	Undoped (*p*+)	68
$(Al_{0.3}Ga_{0.7})_{0.5}In_{0.5}P$	Waveguide	Undoped (*p*+)	900
$(Al_{0.7}Ga_{0.3})_{0.5}In_{0.5}P$	barrier	5e17 (*p*+)	150
$(Al_{0.3}Ga_{0.7})_{0.5}In_{0.5}P$	well	5e17 (*p*+)	150
$(Al_{0.7}Ga_{0.3})_{0.5}In_{0.5}P$	barrier	5e17 (*p*+)	96
$(Al_{0.3}Ga_{0.7})_{0.5}In_{0.5}P$	well	5e17 (*p*+)	42
$(Al_{0.7}Ga_{0.3})_{0.5}In_{0.5}P$	barrier	5e17 (*p*+)	42
$(Al_{0.3}Ga_{0.7})_{0.5}In_{0.5}P$	well	5e17 (*p*+)	42
$(Al_{0.7}Ga_{0.3})_{0.5}In_{0.5}P$	barrier	5e17 (*p*+)	42
$(Al_{0.3}Ga_{0.7})_{0.5}In_{0.5}P$	well	5e17 (*p*+)	42
$(Al_{0.7}Ga_{0.3})_{0.5}In_{0.5}P$	barrier	5e17 (*p*+)	42
$(Al_{0.3}Ga_{0.7})_{0.5}In_{0.5}P$	well	5e17 (*p*+)	42
$(Al_{0.7}Ga_{0.3})_{0.5}In_{0.5}P$	barrier	5e17 (*p*+)	42
$(Al_{0.3}Ga_{0.7})_{0.5}In_{0.5}P$	well	5e17 (*p*+)	42
$(Al_{0.7}Ga_{0.3})_{0.5}In_{0.5}P$	barrier	5e17 (*p*+)	42
$(Al_{0.3}Ga_{0.7})_{0.5}In_{0.5}P$	well	5e17 (*p*+)	42
$(Al_{0.7}Ga_{0.3})_{0.5}In_{0.5}P$	barrier	5e17 (*p*+)	42
$(Al_{0.3}Ga_{0.7})_{0.5}In_{0.5}P$	well	5e17 (*p*+)	45
$(Al_{0.7}Ga_{0.3})_{0.5}In_{0.5}P$	cladding	5e17 (*p*+)	200

Table 5.1: List of physical parameters of the dual-band MQB structure.

The relative positions of the re-optimised dual-band MQB reflector and the active region of the visible 630nm laser device can be seen in Figure 5.7. Again for clarity the energy range over which an incident electron is also illustrated where the boundaries of which are located at the X-band maximum and just above the Γ-band maximum.

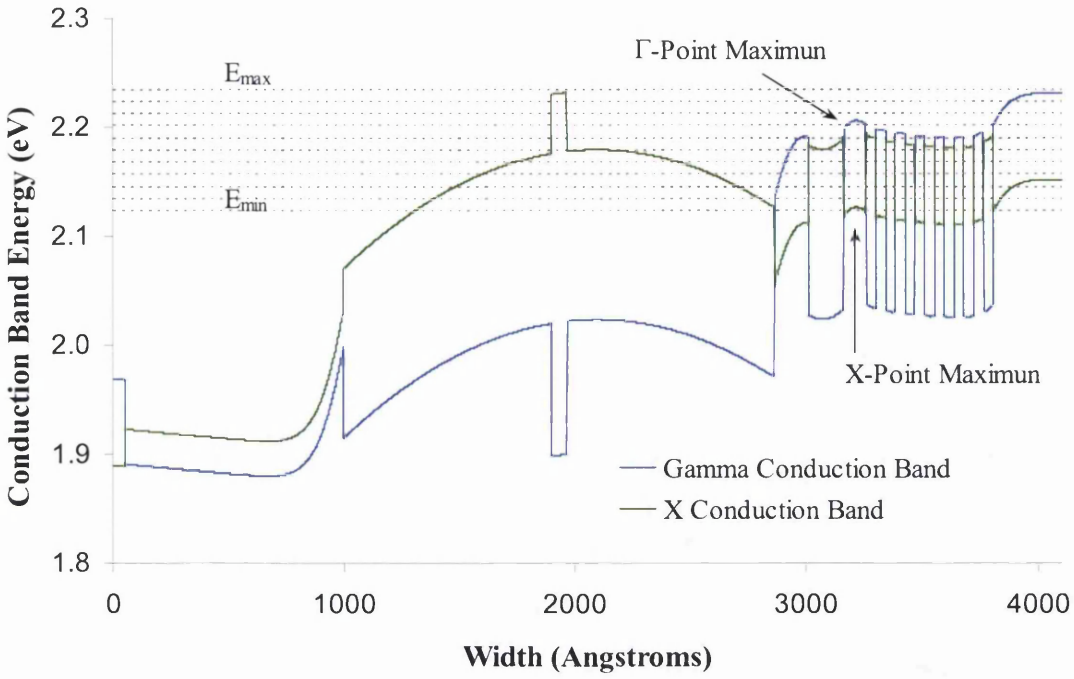

Figure 5.1: Conduction band profiles of both the Γ and X minima, solid blue and green lines respectively, within the active region of a laser diode, biased at a lasing voltage of 2V. The hatched purple area represents the energy interval for which analysis of the reflection probability of the novel MQB structure was taken.

The greater width of the two initial layers can be directly attributed to the band bending effects present across the simulation region. The first two thick materials within the MQB reflector are severely distorted in comparison to their flatband zero biased counterparts (see sub-section 4.5.2) and consequently require a greater width to impart equivalent inhibition of the low energy Γ and X electrons respectively. The number of barrier/well periods within the superlattice is reduced from seven to six in comparison with the optimised dual-band flatband zero biased MQB structure also during the optimisation procedure. This action reduced the extent of the sharp resonant tunnelling modes present due to quasi-bound electron states within the X-band well situated in the Γ-barriers. Thus, reducing the number of superlattice X-band wells/Γ-band barriers reduces the probability of the transmission states occurring. However, if the number of periods was reduced further a surge in X-band transmission was observed. The reflection probability calculated for this novel MQB structure is shown below in Figure 5.8, the incident electron energy has been normalised to the energy of the X-band maximum, also the magnitude of the mixing parameter, α, was set at 0.155eVÅ.

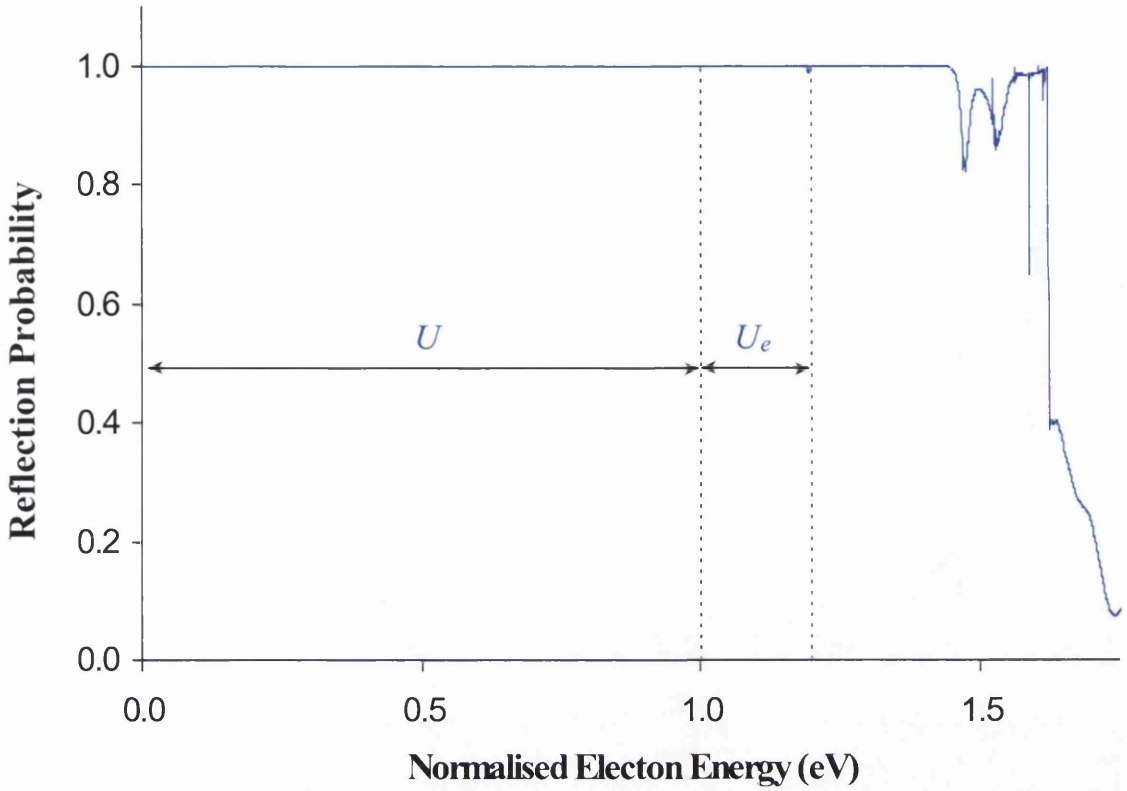

Figure 5.2: Reflectivity plot of the $(Al_{0.3}Ga_{0.7})_{0.5}In_{0.5}P/(Al_{0.7}Ga_{0.3})_{0.5}In_{0.5}P$ proposed novel Γ-X reflector, optimised at a working voltage of 2.0V.

The reflectivity spectra presented in Figure 5.8 reveals an effective enhancement of the order of 20% that of the X-band maximum, which corresponds directly with the position of the Γ-point maximum illustrated in Figure 5.7. Hence, the effective enhancement of above Poisson solved dual-band MQB structure cannot surpass the Γ-point maximum like that of the flatband dual-band MQB presented in Chapter 4. However, this novel MQB design [6] does regain an effective enhancement corresponding to that of intrinsic conduction band offset associated with Γ-band barrier height, as opposed to that of the X-band maximum (shown in Figure 5.7) of the optimised single-band MQB structure when inter-valley transport was initiated.

Figure 5.9 below shows three reflection spectra calculated from the MQB structure developed in this sub-section. Each of the three reflection probabilities corresponds to a particular magnitude of the mixing parameter, α, which are 0.1, 0.155 and 0.2eVÅ. This has been done to investigate what affect the inter-valley mixing parameter α, impacts on the predicted reflection spectra of a particular MQB

design. Each of the above reflection spectra in Figure 5.9 have been normalised with respect to the X-band maximum

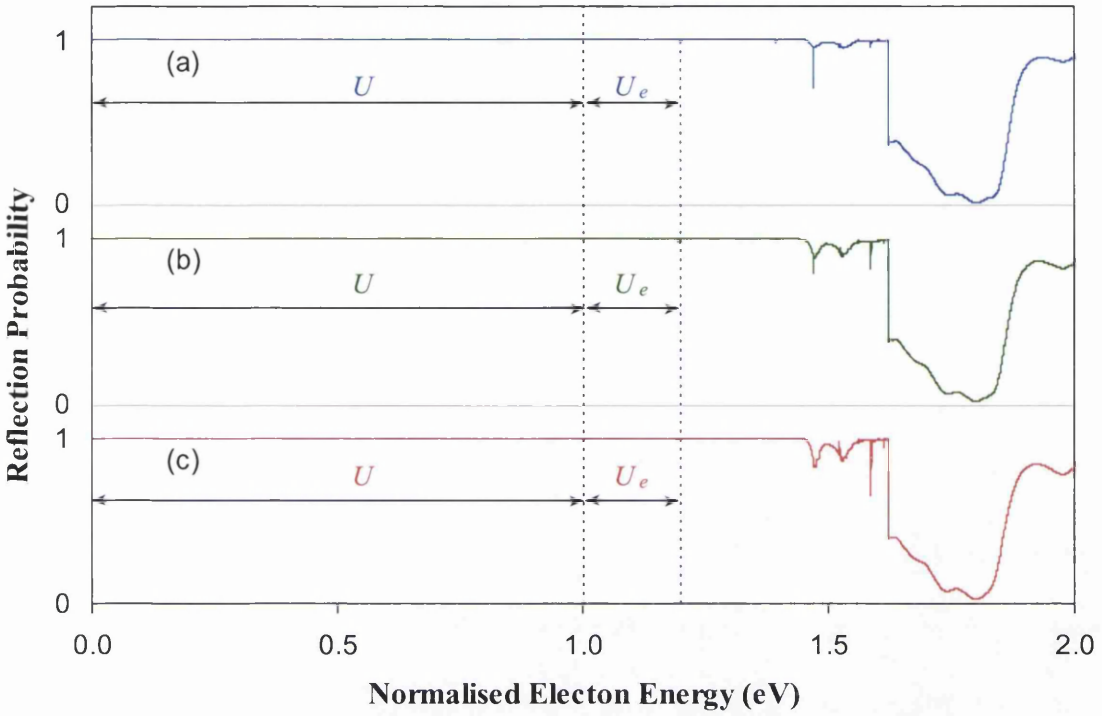

Figure 5.3: Reflectivity profiles of the proposed Γ-X MQB reflector, optimised at a working voltage of 2.0V. Plots (a), (b) and (c) correspond to the magnitudes 0.1, 0.155 and 0.2eVÅ of the inter-valley mixing parameter α.

Comparison of the three reflectivity spectra presented in Figure 5.9, reveals that there is no apparent difference in the reflectivity spectra below the leading edge of the reflection probability. Also, it can be noted that they all fall below a reflection probability of 99% at the same energy (i.e. at an effective enhancement of 20% the height of the X-band maximum). Thus, altering the magnitude of the inter-valley mixing parameter has negligible influence on the calculated reflection spectra; and implies a more physically stable MQB structure has been discovered.

5.5 Summary

The principal objective of this chapter has been to develop and design a simulation package that allows the reflective probabilities of an embedded MQB reflector to be determined under working conditions of the visible 630nm laser diode.

This task has been completed and may be broken down into the following main topic areas

(i) Derivation of Poisson's equation to a form appropriate for numerical analysis of semiconductor devices.

(ii) Development of an explicit integration technique used to solve Poisson's equation.

(iii) Re-emphasis of the inadequateness of single-valley models where the possibility of inter-valley transport is apparent.

(iv) Proposal of a novel dual-band reflector to predict good effective enhancements to the intrinsic conduction band offsets.

The first point in the above list amounts to suitable substitution and rearrangement of Gauss' law to reveal Poisson's equation in a suitable form directly applicable to the numerical simulation of semiconductor materials. The derived form of Poisson's equation detailed in Section 5.2.1 indicates how the electric field across a semiconductor material varies in proportion with the various types of carrier concentration present within the material. To complete the analysis of Poisson's equation in the semiconductor formalism each of its constituent parameters have been detailed.

To solve the derived form of Poisson's equation an explicit integration method has been developed and detailed in Section 5.3.1. This technique in conjunction with a numerical shooting method routine allows simulation of the active and MQB regions of the laser diode, which predict band-bending features due to the non-linearity in charge distribution in these areas. In addition to this a simple dopant and dimension dependent linear biasing technique was introduced in Section 5.3.2 to enable prediction of the conduction band profiles at the operating voltage of the laser device.

By employing the above solution procedure with the previously described dual-band Schrödinger solver described previously in Chapter 4, both the single and dual-band MQB reflectors were re-optimised. The MQB reflector optimised on the premise of single-band transport was shown to further highlight the need to consider inter-valley transport in superlattice structures when the semiconductor material they are constructed from experience switching of conduction band minima. Two reflectivity plots have been calculated and displayed for the single-band reflector, the first indicating approximately 10% enhancement to the Γ-band maximum in single

transport mode, the second depicts total breakdown of the reflectivity spectra to approximately the height of the X-band maximum when inter-valley transport is considered. It was seen that, below the X-band maximum (illustrated in Figure 5.3) transmission through any of the two conduction bands cannot occur and it should be this potential that all reflective spectra should be normalised with respect to. This suggests that the designed single-band reflector have very little impact inhibiting transfer of X-band electrons across the superlattice.

To combat increased X-band tunnelling and the occurrence of additional resonant tunnelling modes present in the Poisson solved single-band reflector and the previously optimised dual-band reflector under flatband zero biased conditions a novel dual-band reflector has been proposed. The re-optimised dual-band model, gives an enhancement corresponding to the height of the maximum Γ-point shown in Figure 5.7, this is analogous to a gain of 20% with reference to the X-point maximum. It has also been shown that a stable enhancement to the intrinsic conduction band offsets has been located due to the fact that variation in magnitude of the inter-mixing parameter had very little effect on the predicted reflection spectra.

When solving Poisson's equation by the explicit integration method outlined above to achieve convergence of the numerical simulation a few physical assumptions had to be made. Firstly, it was supposed that there are flatband conditions across all cladding regions either side of the simulated area. Due to cumulative errors inherent to the solution routine it was only possible to achieve convergence across a small area of the device, namely, the active and MQB regions which account for less than twenty percent of the overall device length. The application of a linear voltage across the simulation region is to a first approximation is adequate, but again physically improbable. To overcome these numerical and physical limitations the following chapter develops a full device simulator using a much more computationally robust and physically rigorous implicit method where the full drift-diffusion equation set is solved. Development of this simulator has been the major focus of my PhD study.

5.6 References

[1] I. S. Grant and W. R. Phillips, 'Electromagnetism 2nd Edition', *Wiley*, (1989).

[2] M. Jaros, 'Physics and Applications of Semiconductor Microstructures', *Oxford*, pp.26, (1989).

[3] L. A. Girifalco, 'Statistical Physics and Materials', *Wiley-Interscience*, New York, (1973).

[4] A.C.Bednarczyk and J.Bednarczyk, 'The Approximation of the Fermi-Dirac Integral $F_{1/2}$', *Phys. Lett.*, **64**A, pp.409 (1978).

[5] D. Kincaid and W. Cheney, 'Numerical Analysis 2nd Edition', *Brooks/Cole*, (1996).

[6] M. R. Brown, K. S. Teng and S. P. Wilks, 'Study of Dual-Valley Transport across a Multiquantum Barrier to Enhance Carrier Confinement', *ICSF-9 Proc.*, Madrid Conf., (2003).

Chapter 6

Quantum Device Simulator

6.1 Introduction

To achieve optimum performance of an embedded MQB reflector within a visible 630nm laser diode it was shown in the previous chapter that it is advantageous to optimise the periodicity of the structure under operating conditions. To a first approximation the method outlined in Chapter 5 to determine the position and the extent of the band-bending features across the active and MQB regions of laser device is satisfactory. However, the underlying idea behind this research is to eventually manufacture these devices commercially, which requires a simulation procedure with more physical and mathematical rigour. Hence, this Chapter focuses solely on the development of a general one-dimensional semiconductor simulation package. Here a step back is taken, in that the following semiconductor device simulator deals solely with the Γ-band. The dual-band simulator is developed in the subsequent Chapter. It was envisaged that simulation in one-dimension was sufficient to accurately model the behaviour of laser diodes as the current flow and electric field in such devices are predominantly unidirectional. Also, to develop a two or three-dimensional simulator with all the added features required to accurately model AlGaInP visible 630nm laser diodes would require more time than the three years dedicated to this thesis.

Therefore the following chapter is structured as follows; in Section 6.2 the semiconductor equations that constitute the drift-diffusion model, which the simulation suite is based upon, are detailed and presented in their residual form i.e. as they appear in the simulator. Also, it is described how these equations are discretised

on a one-dimensional non-uniform mesh, paying particular attention to the numerical stability of the carrier density equations.

The two solution procedures used to determine a solution to the drift-diffusion equation set namely, the Gummel and Newton methods, respectively are detailed in Section 6.3.

To account for the different semiconductor materials and alloys present within a laser device the band parameter model is introduced in Section 6.4. The inclusion of this model allows material parameter variations across abrupt and non-abrupt hetero-junctions and lends itself neatly to the simulation procedure. In addition, the physical models describing the various carrier recombination processes and the dopant dependent mobility model implemented are detailed.

Due to the highly doped cladding layers present within the laser diode it is essential to incorporate effects of degeneracy in the simulation model. Therefore, in Section 6.6, the existing numerical model based on Maxwell-Boltzmann statistics is modified to include the more physically plausible Fermi-Dirac statistics.

In Section 6.5 the capability of the theoretical simulation program is enhanced by adapting the model to take account of two-dimensionally confined electrons present within user defined quantum regions i.e. the quantum well in laser diodes.

Finally, in Sections 6.6 and 6.7 some conclusions on the work carried out in this Chapter are given and all referenced used in the development of this work are displayed respectively.

6.2 Discretisation of the Device Equations

The basic semiconductor equations consist of Poisson's equation (6.1), the continuity equations for electrons (6.2) and holes (6.3) and the current relations for electrons (6.4) and holes (6.5). In the one-dimensional steady-state situation these equations may be written as

$$\frac{\partial}{\partial x}\left(\varepsilon\frac{\partial \psi}{\partial x}\right)=-q\left(p-n+N_D-N_A\right) \tag{6.1}$$

where ε is the material dependent relative permittivity, q is the magnitude of the electron charge, p and n are the hole and electron concentrations, and N_D and N_A are the ionised donor and acceptor concentrations respectively.

$$\frac{1}{q}\frac{\partial J_p}{\partial x} = U \tag{6.2}$$

$$\frac{1}{q}\frac{\partial J_n}{\partial x} = U \tag{6.3}$$

Here, J_p and J_n refer to the hole and electron current densities, and U denotes the sum of the recombination and generation rates (see Section 6.4.2). J_p and J_n are given by

$$J_p = -qD_p\frac{\partial p}{\partial x} - q\mu_p p\frac{\partial \psi}{\partial x} \tag{6.4}$$

$$J_n = qD_n\frac{\partial n}{\partial x} - q\mu_n n\frac{\partial \psi}{\partial x} \tag{6.5}$$

where D_p and D_n are the hole and electron Einstein relations, given by

$$D_p = \frac{k_B T}{q}\mu_p \quad \text{and} \quad D_n = \frac{k_B T}{q}\mu_n \tag{6.6}$$

μ_p and μ_n are the material and dopant dependent hole and electron mobilities (see Section 6.4.3).

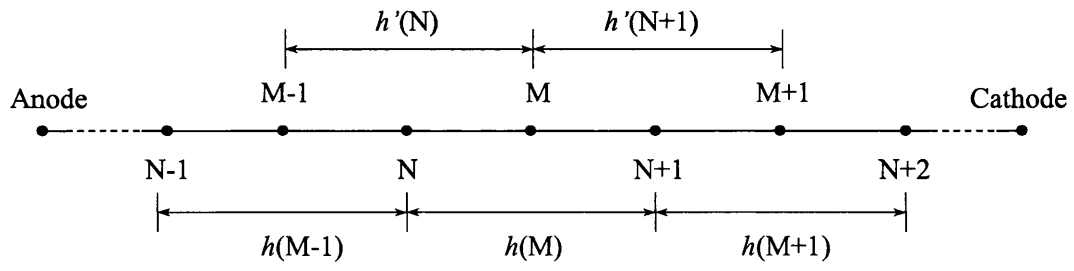

Figure 6.1: Main and auxiliary division points for one-dimensional DC analysis.

In order to execute numerical analysis, these equations must be transformed into difference equations in which the program variables p, n and ψ in this case are defined at a finite number of division points, as illustrated in Figure 6.1. The main nodes in the simulation program are denoted by N, with $N = 1$ and $N = L$ corresponding to the anode and cathode, of the device respectively. In addition, auxiliary points are defined such that the point M is located exactly halfway between the main nodes N and $N + 1$.

The mesh point spacing is defined as a function of the space coordinate x. The main program variables are p, n, and ψ, and are estimated on the main nodes; and the derivatives of these quantities are estimated on the mid-interval auxiliary points. In the following sub-sections, each of the five above equations are analysed and discretised in a form to fit the meshing scheme depicted in Figure 6.1.

6.2.1 Poisson's Equation

In Chapter 5, Poisson's equation was derived from Maxwell's equations to an appropriate form suitable for numerical analysis of semiconductor materials, i.e.

$$\frac{d}{dx}\varepsilon\frac{d\psi}{dx} = -q\left(p - n + N_D - N_A\right) \tag{6.7}$$

By expanding the derivative on the left-hand side, Poisson's equation may be expressed in a more general form appropriate for evaluation of hetero-structures as

$$\frac{d^2\psi}{dx^2} = -\frac{q}{\varepsilon}\left(p - n + N_D - N_A\right) - \frac{1}{\varepsilon}\frac{d\varepsilon}{dx}\frac{d\psi}{dx}. \tag{6.8}$$

It may be noted that the final term in equation (6.8) vanishes for a device fabricated from a homogeneous material, as $d\varepsilon/dx = 0$. Discretisation of equation (6.8) can be achieved directly for evaluation on the above meshing scheme, to yield the following expression

$$\frac{1}{h'(N)}\left[\varepsilon(M)\frac{\psi(N+1)-\psi(N)}{h(M)} - \varepsilon(M-1)\frac{\psi(N)-\psi(N-1)}{h(M-1)}\right] = -q(N_t + p(N) - n(N)) \tag{6.9}$$

where

$$h'(N) = \frac{1}{2}[h(M) + h(M-1)] \tag{6.10}$$

and N_t is the sum of the donor and acceptor concentrations N_D and N_A. Equation (6.9) can be re-written more succinctly in residual form as

$$R_\psi(N) = \gamma_1\psi(N-1) + \gamma_2\psi(N) + \gamma_3\psi(N+1) + q(N_t + p(N) - n(N)) = 0 \tag{6.11}$$

where $R_\psi(N)$ is the residual of the N^{th} node in Poisson's equation and γ_1, γ_2 and γ_3 are given by

$$\gamma_1 = \frac{\varepsilon(M-1)}{h(M-1)h'(N)}$$

$$\gamma_2 = -\frac{1}{h'(N)}\left[\frac{\varepsilon(M)}{h(M)} + \frac{\varepsilon(M-1)}{h(M-1)}\right]. \tag{6.12}$$

$$\gamma_3 = \frac{\varepsilon(M)}{h(M)h'(N)}$$

6.2.2 Current Continuity Equations

In one dimension, under steady-state conditions the hole and electron current continuity equations may be expressed in the following form:

$$\frac{1}{q}\frac{\partial J_p}{\partial x} = -U \tag{6.13}$$

$$\frac{1}{q}\frac{\partial J_n}{\partial x} = U \tag{6.14}$$

Again, these two equations are easily projected on to the aforementioned meshing scheme and in residual form on the N^{th} are given by the following expressions:

$$R_p(N) = \frac{1}{q}\frac{J_p(M) - J_p(M-1)}{h'(N)} + U(N) = 0 \tag{6.15}$$

$$R_n(N) = \frac{1}{q}\frac{J_n(M) - J_n(M-1)}{h'(N)} - U(N) = 0 \tag{6.16}$$

for holes and electrons respectively.

6.2.3 Current Density Equations

Substitution of the corresponding Einstein relations into equations (6.4) and (6.5) yields the following expressions for the hole and electron current densities

$$J_p = -\frac{q\mu_p}{\theta}\frac{\partial p}{\partial x} - q\mu_p p\frac{\partial \psi}{\partial x} \tag{6.17}$$

$$J_n = \frac{q\mu_n}{\theta}\frac{\partial n}{\partial x} - q\mu_n n\frac{\partial \psi}{\partial x} \tag{6.18}$$

where the reciprocal of the thermal voltage $v_T^{-1} = q/k_B T$ is denoted as θ for expediency.

By directly discretising the current density equations in sympathy with the predefined meshing scheme, it is possible to deduce, that to sustain numerical stability requires the potential difference between adjacent nodes be less than twice the thermal voltage, $2k_BT/q$, approximately 0.052eV (A fuller discussion of numerical instability is given in Appendix A). In order to maintain this proviso, an excessive amount of nodal points would be mandatory across most semiconductor devices, which is subsequently very expensive to computation times.

6.2.4 Scharfetter-Gummel Discretisation

In 1969, Scharfetter and Gummel [1] proposed a novel integration scheme that allowed larger potential variation between consecutive nodes due to an exponential interpolation between carrier densities on the corresponding nodes, which in turn

decreases numerical instability, hence, allowing the number of nodes to be reduced, consequentially increasing computation efficiency.

Below the integral form of the electron current density equation is described and then discretised to a form similar to how it appears in the simulator. Considering equation (6.18)

$$J_n = -q\mu_n n\left(\frac{d\psi}{dx} + \frac{d\theta_n}{dx}\right) + \frac{q\mu_n}{\theta}\frac{dn}{dx} \tag{6.19}$$

where $d\psi/dx$ is the electric field $d\theta_n/dx$ is the derivative of the electron band parameter (a more detailed discussion of this quantity is given in Section 6.4.1).

By assuming that electric field, mobility, and current density are constant over the spatial interval N to $N+1$ in the x domain, equation (6.19) may be integrated with the addition of an appropriate integrating factor to yield

$$\frac{J_n}{\alpha}\left[e^{\alpha x}\right]_N^{N+1} = \left[ne^{\alpha x}\right]_N^{N+1} \tag{6.20}$$

where

$$\alpha = -\theta\left(\frac{d\psi}{dx} + \frac{d\theta_n}{dx}\right) \tag{6.21}$$

By evaluating the limits of equation (6.20), and through some simple algebra the following expression for the electron current density may be deduced

$$J_n(M) = \frac{q\mu(M)}{\theta h(M)}\frac{\alpha(M)}{(e^{\alpha(M)}-1)}(n(N+1)e^{\alpha(M)} - n(N)). \tag{6.22}$$

Rearranging this expression in a more convenient form, gives

$$J_n(M) = \frac{q\mu_n(M)}{\theta h(M)}(n(N+1)B(\Delta(M)) - n(N)B(-\Delta(M))), \tag{6.23}$$

where $\Delta(M)$ is the sum of the differences between the potential and the band parameter between nodes $N+1$ and N, i.e.

$$\Delta(M) = (\psi(N+1) - \psi(N)) + (\theta_n(N+1) - \theta_n(N)) \tag{6.24}$$

and $B(\Delta)$ is the Bernoulli function, which is defined as:

$$B(\Delta) = \frac{\Delta}{e^{\Delta} - 1}. \tag{6.25}$$

In order to avoid over and underflows due to floating point arithmetic, it is necessary to pay particular attention to the implementation of the Bernoulli function. In this device simulator the numerical procedure outlined in [2] has been utilised to achieve individual machine floating point accuracy and thus program accuracy on any personnel computer.

By an analogous procedure, the hole current density may be expressed in a similar manner, namely

$$J_p(M) = \frac{q\mu_p(M)}{\theta h(M)}(p(N)B(\Delta(M)) - p(N+1)B(-\Delta(M))) \tag{6.26}$$

Hence, equations (6.23) and (6.26) are the discretised forms of the electron and hole current density relations respectively, used in the simulator when their corresponding continuity equations are evaluated.

6.3 Simulation Procedure

Equations (6.11), (6.15) and (6.16) are all residual equations for a typical node *N*. Upon convergence these residuals will be approximately zero, and the Newton-Raphson iteration process seeks this condition. However, before the fully coupled equation solver is considered, which was found to be the most appropriate solution method and the one employed in the final simulation routine, it is appropriate to

discuss the decoupled (Gummel) procedure initially developed to evaluate the drift-diffusion equation set.

6.3.1 Gummel Iteration

In this numeric routine equations (6.11), (6.15) and (6.16) are solved in a de-coupled manner, whereby each equation is evaluated in turn and the resulting revised variable estimate is used in the assessment of the other program variables in a Gauss-Seidel type iteration until global convergence is attained.

Below the Newton-Raphson technique used to up-date each of the program variables is outlined for all three of the governing equations.

6.3.1.1 Poisson's Equation

As stated above, equation (6.11) represents the residual equation for a single node N of Poisson's equation. If there are N_{max} nodes in the mesh, this can be stated as

$$\boldsymbol{F}^{\psi}(\psi) = 0 \tag{6.27}$$

where ψ is an N_{max} dimensional vector and the N^{th} component of $\boldsymbol{F}^{\psi}$ is represented by equation (6.27). This can then be solved for the vector ψ, using the Newton–Raphson method that at each iterative step requires the solution of the following linear set of equations,

$$\boldsymbol{J}^{\psi\psi}(\psi)\delta\psi = -\boldsymbol{F}^{\psi}(\psi). \tag{6.28}$$

This set can be evaluated by either direct or relaxation methods [3,4,5]. $\boldsymbol{J}^{\psi\psi}$ is the Jacobian matrix defined as

$$\boldsymbol{J}^{\psi\psi}(\psi) = \frac{\partial \boldsymbol{F}^{\psi}(\psi)}{\partial \psi^{T}} \tag{6.29}$$

the vector ψ, is then replaced by

$$\psi^{w+1} = \psi^{w} + \delta\psi \tag{6.30}$$

where

$$\delta\psi = -\left[\boldsymbol{J}^{\psi\psi}(\psi)\right]^{-1} \boldsymbol{F}^{\psi}(\psi) \tag{6.31}$$

by rearranging equation (6.28) and w is the iteration index.

6.3.1.2 The Solution of the Current Continuity Equations

Similarly equation (6.16) represents the residual equation for a single node N of the electron current continuity equation. For an N_{max} nodal mesh discretisation this can be stated as

$$\boldsymbol{F}^{n}(\boldsymbol{n}) = 0\,. \tag{6.32}$$

The equation set given by (6.32) can be solved using an analogous Newton-Raphson scheme to the one used when solving Poisson's equation. Here, at each iterative step, the vector $\boldsymbol{n}$ is updated by

$$\boldsymbol{n}^{w+1} = \boldsymbol{n}^{w} + \delta\boldsymbol{n} \tag{6.33}$$

where

$$\delta\boldsymbol{n} = -\left[\boldsymbol{J}^{nn}(\boldsymbol{n})\right]^{-1} \boldsymbol{F}^{n}(\boldsymbol{n}) \tag{6.34}$$

$\boldsymbol{J}^{nn}$ the Jacobian matrix is defined as

$$\boldsymbol{J}^{nn}(\boldsymbol{n}) = \frac{\partial \boldsymbol{F}^{n}(\boldsymbol{n})}{\partial \boldsymbol{n}^{T}} \tag{6.35}$$

and w is the iteration index.

Thus, the decoupled procedure can now be initiated; firstly Poisson's equation is solved in the manner described above until numeric convergence is achieved. The updated electrostatic potential is then inputted with the initial estimate of the hole and electron concentrations into the hole continuity equation to yield an up-dated estimate. These two revised parameters are then used to produce a similar up-date to the electron concentration from solution of the corresponding continuity equation. This procedure is repeated until global convergence of the three equations is achieved.

6.3.2 Coupled Newton-Raphson Solution

The solution variables p, n and ψ become increasingly coupled as an applied bias is dropped across the laser structure. Therefore, it is much more convenient to solve the drift-diffusion system using a fully coupled solution scheme, which may be written as

$$\begin{bmatrix} \boldsymbol{J}^{pp} & \boldsymbol{J}^{pn} & \boldsymbol{J}^{p\psi} \\ \boldsymbol{J}^{np} & \boldsymbol{J}^{nn} & \boldsymbol{J}^{n\psi} \\ \boldsymbol{J}^{\psi p} & \boldsymbol{J}^{\psi n} & \boldsymbol{J}^{\psi\psi} \end{bmatrix} \begin{bmatrix} \delta \boldsymbol{p} \\ \delta \boldsymbol{n} \\ \delta \boldsymbol{\psi} \end{bmatrix} = - \begin{bmatrix} \boldsymbol{F}_p(\boldsymbol{p},\boldsymbol{n},\boldsymbol{\psi}) \\ \boldsymbol{F}_n(\boldsymbol{p},\boldsymbol{n},\boldsymbol{\psi}) \\ \boldsymbol{F}_\psi(\boldsymbol{p},\boldsymbol{n},\boldsymbol{\psi}) \end{bmatrix} \tag{6.36}$$

using the following notation

$$\boldsymbol{J}^{xy} = \frac{\partial \boldsymbol{F}^x(\boldsymbol{x})}{\partial \boldsymbol{y}^T}. \tag{6.37}$$

Here $\boldsymbol{x}$ and $\boldsymbol{y}$ represent $\boldsymbol{p}$, $\boldsymbol{n}$ or ψ, and the diagonal terms of the Jacobian matrix are given by equation (6.28) and a rearrangement of equation (6.34) respectively. The coupled system has the drawback that off-diagonal terms of the Jacobian matrix of equation (6.36) have to be calculated, but is far faster that the decoupled Gummel scheme [6]. As an initial estimate for the coupled solution however, it is convenient to calculate the diagonal terms by the Gummel method [1,6] described in previous sections.

Upon evaluation of the solution from equation (6.36), if the convergence toleration is attained, the scheme is repeated for the next bias step, otherwise another

Newton iteration is required. This procedure is illustrated in the flow diagram shown in Figure 6.2 below.

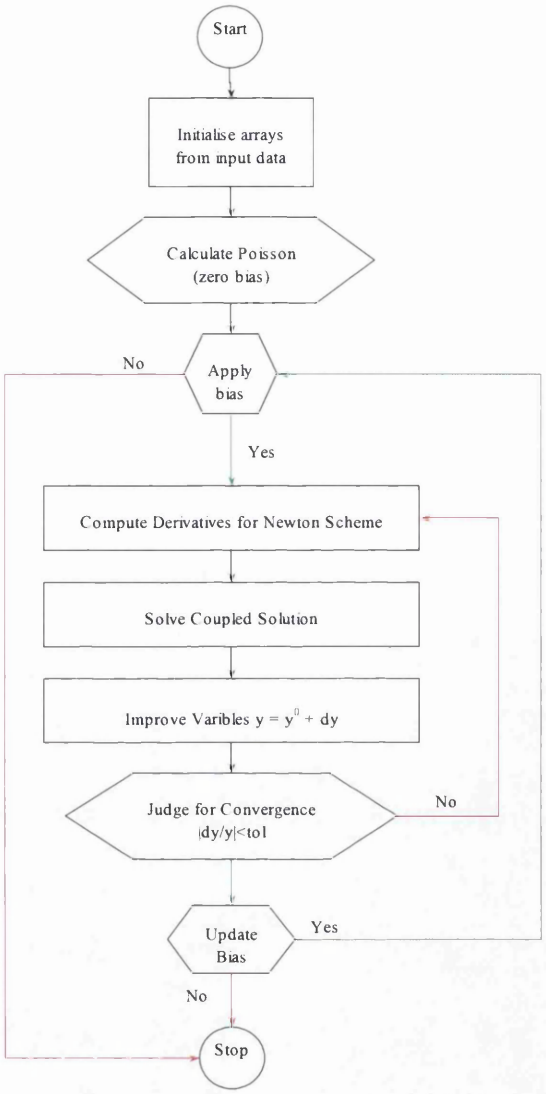

Figure 6.2: Flowchart of the main steps used in the Coupled Drift-Diffusion simulation routine.

The first step of the solution procedure involves initialising array space from user-defined information about the device to solved such as, number of material layers, width and doping of these layers, what recombination mechanism to implement (see sub-section 6.4.2), how many bias points are needed etc. Once all relevant input parameters have been assigned the solution procedure begins. Firstly, Poisson's equation is solved under zero-biased conditions and the relevant variables saved to a user-defined file. A bias is next applied to these initial results and the coupled scheme discussed above is iteratively solved until convergence is met and

again the program variables saved to the designated output file. This process is repeated until all bias points have been evaluated.

6.4 Physical Models

In order to obtain reliable and accurate results from simulation it is necessary to include a comprehensive set of physical models. Of these models only a certain number may need to be included depending on the actual device being simulated.

Thus, the following Section focuses on such physical models. Firstly, the fundamental device equations are adapted to deal with the presence of hetero-materials. Secondly, the recombination processes built into the simulation model are discussed highlighting the processes particularly relevant to laser diodes, and finally, the dopant dependent mobility model used to estimate the electron and hole mobilities within each semiconductor material is outlined.

6.4.1 The Band Parameter Model

This method used to include the effects of non-uniform composition upon electronic band structures is that proposed by Sutherland and Hauser [7], as apposed to the two-thirds approximation [8,9,10] used in Chapters 2, 3 and 4 to determine the conduction band offsets. However, as can be seen in sub-section 7.3.1 of the following Chapter the two models predict almost identical conduction band offsets.

Sutherland and Hauser's model involves using the energy band alignment of Anderson [11] to calculate the band parameters θ_n and θ_p, and uses the vacuum level as the reference for the electrostatic potential, implying that the conduction band discontinuity ΔE_C is given by the difference in the electron affinities of the two materials.

This may not be valid assumption [12] and various alternative schemes have been proposed, such as using the intrinsic level as the potential reference [13] or using a continuous conduction band edge [14]. There is however contradictory and supportive evidence for all models mentioned due to the problems of obtaining reliable consistent data especially in the case of AlGaInP. The Anderson model was

chosen for its simplicity and the ease with which it can be included into this numerical solver [15,16].

Using the notation in Figure 6.3 it is possible to define the conduction and valence band edges (E_C and E_V respectively) in terms of a reference potential ψ_0, the electrostatic potential ψ, the electron affinity χ and the band-gap E_g.

$$E_C = q(\psi_0 - \psi) - \chi \tag{6.38}$$

$$E_V = q(\psi_0 - \psi) - \chi - E_g \tag{6.39}$$

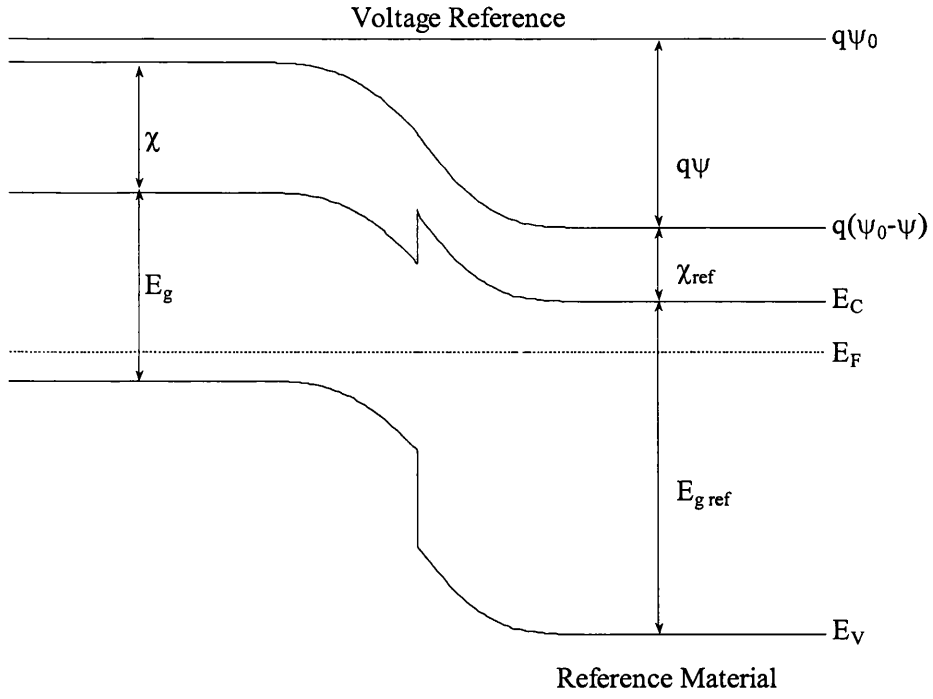

Figure 6.3: Equilibrium energy band diagram for an abrupt heterojunction for the calculation of the band parameters.

The electron and hole concentrations can be related to the conduction and valence band edges and the electron and hole quasi-Fermi levels, and can be recast in terms of voltage to give

$$\phi_n = -\frac{1}{q} E_{Fn} \tag{6.40}$$

$$\phi_p = -\frac{1}{q} E_{Fp} \tag{6.41}$$

N_C and N_V are the effective densities of states and are given by

$$N_C = 2\left(\frac{2\pi k_B T m_e^*}{h^2}\right)^{3/2} \tag{6.42}$$

$$N_V = 2\left(\frac{2\pi k_B T m_h^*}{h^2}\right)^{3/2} \tag{6.43}$$

where m_e^* and m_h^* are the electron and hole effective masses and $\hbar$ is Planck's constant. Using the expressions for the conduction and valence band edges along with the definitions of the quasi-Fermi levels the expressions for the carrier concentrations may be recast to yield

$$n = n_{ir} \exp\left(\theta\left(\psi - \phi_n + \frac{\chi}{q} - \psi_0 + \frac{1}{\theta}\ln\left(\frac{N_C}{n_{ir}}\right)\right)\right) \tag{6.44}$$

$$p = n_{ir} \exp\left(\theta\left(\phi_p - \psi - \frac{\chi}{q} - \frac{E_g}{q} + \psi_0 + \frac{1}{\theta}\ln\left(\frac{N_V}{n_{ir}}\right)\right)\right) \tag{6.45}$$

where $\theta = q/k_B T$ and n_{ir} is the intrinsic carrier concentration of the reference material. The composition dependant terms may then be combined together as band parameters.

$$\theta_n = \frac{\chi}{q} - \psi_0 + \frac{1}{\theta}\ln\left(\frac{N_C}{n_{ir}}\right) \tag{6.46}$$

and

$$\theta_p = \psi_0 - \frac{\chi}{q} - \frac{E_g}{q} + \frac{1}{\theta}\ln\left(\frac{N_V}{n_{ir}}\right) \tag{6.47}$$

The band parameter expressions (6.46) and (6.47) are dependent only on values that are related to the material parameters of the device, and not on the solution variables n, p and ψ. The equations for the carrier concentrations may now be written in a more convenient and recognisable form.

$$n = n_{ir} \exp(\theta(\psi - \phi_n + \theta_n)) \tag{6.48}$$

$$p = n_{ir} \exp(\theta(\phi_p - \psi + \theta_p)) \tag{6.49}$$

6.4.2 Recombination Models

There are three recombination mechanisms incorporated within the numerical model, namely, Direct, Shockley Read Hall (SRH) and Auger recombination. The form of these mechanisms is briefly discussed below.

(i) Direct Recombination

This process involves the direct transition of carriers between the conduction and valence bands. Electrons are excited to the conduction band from the valence band by gaining energy from incident photons. Alternatively electrons lose energy (E_g), which is emitted as a photon and moves from the conduction band to the valence band. This process is significant in narrow bandgap and direct semiconductors such as GaAs and GaInP, hence, should be an integral part when considering simulation of AlGaInP/GaInP laser diodes. The net generation-recombination rate due to photon transition is given by the expression:

$$R_{Dir} = B(n,p)(n_i^2 - pn)\,. \tag{6.50}$$

Here $B(n,p)$ is the carrier dependent radiative recombination coefficient defined as,

$$B(n,p) = B_0 - B_1 \min(p,n) \tag{6.51}$$

where B_0 and B_1 are dependent on doping and temperature [2].

(ii) SRH Recombination

The thermal contribution to the recombination processes is due to phonon transitions occurring as a result of traps, which is usually characterised by the Shockley Read Hall model. This mechanism is termed an indirect process since it involves a trap centre in the energy band gap with associated two-stage capture and emission processes. The net generation-recombination rate for the Shockley Read Hall model is given by,

$$R_{SRH} = \frac{n_i^2 - pn}{\tau_n(p + p_t) + \tau_p(n + n_t)}. \tag{6.52}$$

Where τ_n and τ_p are the non-radiative electron and hole lifetimes and are dependent on doping and temperature [2]. The carrier concentrations p_t and n_t depend on the position and occupancy of the traps. In this numerical model, it is assumed that the trap centres to lie in the middle of the band gap, and these concentrations are replaced with the reference intrinsic concentration n_i.

(iii) Auger Recombination

Auger recombination comprises three particles and involves the recombination of an electron-hole pair and the emission of energy to a third particle. Auger recombination may be considered in terms of direct band gap generation-recombination (i.e. where carriers move across the band gap) and the indirect process involving trap centres. The net Auger recombination rate is given by,

$$R_{Aug} = (C_n n + C_p p)(n_i^2 - pn). \tag{6.53}$$

Where C_n and C_p are the Auger coefficients, and are dependent on temperature and material type [17].

6.4.3 Mobility Model

The hole and electron low field mobilities may be expressed as a function of doping and temperature as given in [17] and [18] as,

$$\mu_n = \frac{\mu_{n0}}{1+\left(\frac{N_D+N_A}{10^{17}}\right)^{1/2}}[cm^{-3}V^{-1}s^{-1}] \tag{6.54}$$

for electrons, and for holes

$$\mu_n = \frac{300}{T}\left[\mu_{p1} + \frac{\mu_{p0}}{1+\left(\frac{N_D+N_A}{10^{17}}\right)^{\alpha}}\right][cm^{-3}V^{-1}s^{-1}] \tag{6.55}$$

where $\mu_{p1} = 50cm^{-3}V^{-1}s^{-1}$, $N_{ref} = 3.232\times10^{17}cm^{-3}$ and $\alpha = 0.4956$. Parameters μ_{n0} and μ_{p0} in equations (6.54) and (6.55) refer to the magnitude of the bulk electron and hole mobilities of the particular material respectively.

Where relevant, the mobilities of the ternary and quaternary materials are reduced as the mole-fraction of aluminium is increased as a result of alloy scattering. This effect is included by the following simple relationship,

$$\mu(x) = m(x)\,\mu(x=0) \tag{6.56}$$

where x is the aluminium mole-fraction and $\mu(x)$ is a linearly decreasing function. This simple relationship is employed because compositionally dependent mobilities for the semiconductor material AlGaInP are not well documented at the present time.

6.5 Fermi-Dirac Statistics

Due to the highly doped cladding regions in the laser diode it is necessary to include the effects of carrier degeneracy. In this Section the band parameter model is adapted to include Fermi-Dirac statistics. Therefore, this Section is organised as follows; Section 6.5.1 discusses the calculation of the carrier densities with reference to both Maxwell-Boltzmann and Fermi-Dirac statistics, section 6.5.2 considers the implementation of Fermi-Dirac statistics within a numerical model. Sections 6.5.3 and 6.5.4 deals with the recalculation of the Jacobians partial derivatives for Poisson's

equation due to the admission of Fermi-Dirac statistics and finally the numerical algorithm used to evaluate the Fermi-Dirac integrals respectively.

6.5.1 Calculation of Carrier Densities

In a semiconductor the carrier densities are calculated by multiplying the density of states function by the carrier distribution function and integrating over the required energy band, i.e.

$$n = \int_{E_C}^{\infty} \rho_c(E) f_n(E) dE \tag{6.57}$$

$$p = \int_{-\infty}^{E_C} \rho_v(E) f_p(E) dE \tag{6.58}$$

where E is the energy, $\rho_c(E)$ and $\rho_v(E)$ are the density of states functions and $f_n(E)$ and $f_p(E)$ are the distribution functions given by

$$f_n(E) = \frac{1}{1+\exp\left(\frac{E-E_{Fn}}{k_B T}\right)} \tag{6.59}$$

$$f_p(E) = \frac{1}{1+\exp\left(\frac{E_{Fp}-E}{k_B T}\right)} \tag{6.60}$$

where k_B is Boltzmann's constant, T is the lattice temperature and E_{Fn} and E_{Fp} are the Fermi levels for electrons and holes respectively. Assuming isotropic parabolic bands $\rho_C(E)$ and $\rho_V(E)$ are given as:

$$\rho_C(E) = \frac{m_n^* \sqrt{2m_n^*(E-E_C)}}{\pi^2 \hbar^3}, \qquad E \geq E_C \tag{6.61}$$

$$\rho_V(E) = \frac{m_p^* \sqrt{2m_p^*(E_V - E)}}{\pi^2 \hbar^3}, \qquad E \leq E_V \tag{6.62}$$

where E_C and E_V are the conduction and valence band edges, m_n^* and m_p^* are the electron and hole density of states effective masses and $\hbar$ is the reduced Planck's constant. The integrals (6.50) and (6.51) above can be evaluated to

$$n = N_C \frac{2}{\sqrt{\pi}} F_{1/2}\left(\frac{E_{Fn} - E_C}{k_B T}\right) \tag{6.63}$$

$$p = N_V \frac{2}{\sqrt{\pi}} F_{1/2}\left(\frac{E_V - E_{Fp}}{k_B T}\right) \tag{6.64}$$

where N_C and N_V denote the effective density of states in the conduction and valence band respectively.

$$N_C = 2\left(\frac{2\pi k_B T m_e^*}{h^2}\right)^{3/2} \tag{6.65}$$

$$N_V = 2\left(\frac{2\pi k_B T m_h^*}{h^2}\right)^{3/2} \tag{6.66}$$

$F_{1/2}(x)$ is the Fermi integral of order ½, which does not have a closed form solution. However, for a large negative argument it can be expressed analytically as

$$F_{1/2}(x) \approx \frac{\sqrt{\pi}}{2}\exp(x), \qquad x << -1 \tag{6.67}$$

equations (6.56), and (6.57) then reduce to

$$n = N_C \exp\left(\frac{E_{Fn} - E_C}{k_B T}\right) \tag{6.68}$$

$$p = N_V \exp\left(\frac{E_V - E_{Fp}}{k_B T}\right) \tag{6.69}$$

Hence, it is only when the Fermi levels are far from the band edge that the Maxwell-Boltzmann approximation is valid. In the existing device simulator a discretisation scheme was used which was formulated upon the Maxwell-Boltzmann approximation thus the expressions for n and p must be recast into a modified Maxwell-Boltzmann expression for use with Fermi-Dirac statistics as follows,

$$n = n_{ir} \exp(\theta(\psi - \phi_n + \theta_n + V_n)) \tag{6.70}$$

$$p = n_{ir} \exp(\theta(\phi_p - \psi + \theta_p + V_p)) \tag{6.71}$$

where n_{ir} is the intrinsic carrier concentration, ψ is the potential, ϕ_n and ϕ_p are the quasi-Fermi potentials and θ_n and θ_p are the corrections for heterogeneous materials as discussed earlier. V_n and V_p are the Fermi-Dirac corrections given by

$$V_n = \frac{1}{\theta} \ln\left(\frac{F_{1/2}(\eta_C)}{e^{\eta_C}}\right) \tag{6.72}$$

$$V_p = \frac{1}{\theta} \ln\left(\frac{F_{1/2}(\eta_V)}{e^{\eta_V}}\right) \tag{6.73}$$

where η_C and η_V are the degeneracy factors

$$\eta_C = \frac{E_{Fn} - E_C}{k_B T} \tag{6.74}$$

$$\eta_V = \frac{E_V - E_{Fp}}{k_B T} \tag{6.75}$$

which maybe recast to a more suitable expressions

$$\eta_C = \theta(\psi - \phi_n + \theta_n) + \ln\left(\frac{n_{ir}}{N_C}\right) \tag{6.76}$$

$$\eta_V = \theta(\phi_p - \psi + \theta_p) + \ln\left(\frac{n_{ir}}{N_V}\right) \tag{6.77}$$

To show that the equations (6.61), (6.62) and equations (6.63), (6.64) are equivalent consider the substitution of V_n into equation (6.63)

$$n = n_{ir}\exp(\theta(\psi - \phi_n + \theta_n))\frac{F_{1/2}(\eta_C)}{e^{\eta_C}} \tag{6.78}$$

Substituting for θ_n

$$\theta_n = \frac{\chi}{q} - \psi_0 + \frac{1}{\theta}\ln\left(\frac{N_C}{n_{ir}}\right) \tag{6.79}$$

$$n = n_{ir}\left(\frac{N_C}{n_{ir}}\right)\exp\left(\theta\left(\psi - \phi_n + \frac{\chi}{q} - \psi_0 + \right)\right)\frac{F_{1/2}(\eta_C)}{e^{\eta_C}} \tag{6.80}$$

Substituting for the degeneracy factor η_c,

$$\eta_C = \frac{E_{Fn} - E_C}{k_B T} \tag{6.81}$$

$$E_C = q(\psi_0 - \psi) - \chi \tag{6.82}$$

$$\phi_n = -\frac{1}{q}E_{Fn} \tag{6.83}$$

gives

$$n = N_C\exp\left(\frac{E_{fn} - E_C}{k_B T}\right) \tag{6.84}$$

Therefore the two formalisms are equivalent. Hole statistics maybe treated in exactly the same manner.

6.5.2 Addition of Fermi-Dirac Statistics

The above method for incorporating Fermi-Dirac statistics within the Maxwell-Boltzmann type formalism is simple to implement for the calculation of carrier densities. First the modification factors are calculated and then introduced into the exponential of the Maxwell-Boltzmann equation. However, problems arise in the Newton-Raphson method, where the partial derivatives of n and p are required with respect to the potential and the quasi-Fermi potentials. This is a major problem as the expressions for V_n and V_p are dependant on the potential and the quasi-Fermi potentials. Therefore, to ensure quadratic convergence the derivatives must also be recalculated to include the effects of Fermi-Dirac statistics. These issues are considered next.

6.5.3 Recalculation of Partial Derivatives

The residuals and Jacobians for all equations must be recalculated to include the dependence of V_n and V_p on the potential and quasi-Fermi potentials. For example the solution to Poisson's equation involves the solution of

$$\boldsymbol{J}_{\psi\psi}(\psi)\delta\psi = -\boldsymbol{F}_{\psi}(\psi) \tag{6.85}$$

where J is the Jacobian matrix

$$\boldsymbol{J}_{\psi\psi}(\psi) = \frac{\partial \boldsymbol{F}_{\psi}(\psi)}{\partial \psi} \tag{6.86}$$

and F_ψ is the residual of the N^{th} component which may be expressed as

$$F_{\psi}(N) = -q\rho(N) - \gamma_1\psi(N-1) - \gamma_2\psi(N) - \gamma_3\psi(N+1) \tag{6.87}$$

when using Fermi-Dirac statistics the residual will be automatically adjusted provided n and p in the charge term $\rho(N)$ have been already adjusted. However, the Jacobian requires the derivative of the charge density with respect to potential.

$$\frac{\partial \rho}{\partial \psi} = \frac{\partial}{\partial \psi}(N_d - N_a + p - n) \tag{6.88}$$

Consider for example the electron concentration

$$\frac{\partial n}{\partial \psi} = n_{ir}\left\{\frac{\partial \exp(\theta(\psi - \phi_n + \theta_n + V_n))}{\partial \psi}\right\} \tag{6.89}$$

$$\frac{\partial n}{\partial \psi} = n_{ir}\left\{\exp(\theta V_n)\frac{\partial \exp(\theta(\psi - \phi_n + \theta_n))}{\partial \psi} + \exp(\theta(\psi - \phi_n + \theta_n))\frac{\partial \exp(\theta V_n)}{\partial \psi}\right\} \tag{6.90}$$

$$\frac{\partial n}{\partial \psi} = n_{ir}\left\{\theta \exp(\theta(\psi - \phi_n + \theta_n + V_n)) + \exp(\theta(\psi - \phi_n + \theta_n))\frac{\partial \exp(\theta V_n)}{\partial \psi}\right\} \tag{6.91}$$

but $$\theta V_n = \ln\left[\frac{F_{1/2}(\eta_C)}{e^{\eta_C}}\right] \quad \text{hence,} \quad e^{\theta V_n} = \left[\frac{F_{1/2}(\eta_C)}{e^{\eta_C}}\right]$$

$$\frac{\partial e^{\theta V_n}}{\partial \psi} = \frac{\partial}{\partial \psi}\left[\frac{F_{1/2}(\eta_C)}{e^{\eta_C}}\right] = \frac{\partial}{\partial \eta_C}\left[\frac{F_{1/2}(\eta_C)}{e^{\eta_C}}\right].\frac{\partial \eta_C}{\partial \psi} \tag{6.92}$$

where

$$\frac{\partial \eta_C}{\partial \psi} = \theta\,. \tag{6.93}$$

If a new variable Y_n is defined, such that

$$Y_n = \frac{\partial}{\partial \eta_C}\left[\frac{F_{1/2}(\eta_C)}{e^{\eta_C}}\right] = e^{-\eta_C}\left[F_{-1/2}(\eta_C) - F_{1/2}(\eta_C)\right] \tag{6.94}$$

Then the derivative of the electron concentration with respect to the potential is then given by

$$\frac{\partial n}{\partial \psi} = \theta n_{ir}\{\exp(\theta(\psi - \phi_n + \theta_n + V_n)) + \exp(\theta(\psi - \phi_n + \theta_n))Y_n\} \tag{6.95}$$

$$\frac{\partial n}{\partial \psi} = \theta n + \theta \exp(\theta(\psi - \phi_n + \theta_n))Y_n \tag{6.96}$$

A similar procedure is used to determine the derivative of the hole concentration with respect to the potential. Thus, the total is then given by

$$\frac{\partial \rho}{\partial \psi} = -\left(\frac{\partial p}{\partial \psi} - \frac{\partial n}{\partial \psi}\right) \tag{6.97}$$

$$\frac{\partial \rho}{\partial \psi} = -\theta p - \theta Y_p n_{ir} \exp(\theta(\phi_p - \psi + \theta_p)) + \theta n + \theta Y_n n_{ir} \exp(\theta(\psi - \phi_n + \theta_n)) \tag{6.98}$$

This can clearly be broken down into the part that comes from Maxwell-Boltzmann statistics and the correction that is derived from Fermi-Dirac statistics.

The recalculation of all other partial derivatives (for example in the coupled scheme there are nine derivatives, which must be calculated corresponding to the nine derivative elements within the Jacobian matrix) may be calculated based on the method described above. The partial derivatives for the continuity equations are considerably more involved than for Poisson's equation due to the complicated discretisation scheme for the current density. For the sake of brevity these derivatives are not shown here nor those for the different recombination mechanisms that must be included, nor those for the recalculated boundary conditions. It is sufficient to say that provided the derivatives of the carrier densities are recalculated (as described with respect to the potential) then the implementation only involves algebra

6.5.4 Calculation of the Fermi-Dirac Integrals

The Fermi-Dirac integral is defined as

$$F_j(\eta) = \frac{1}{\Gamma(j+1)} \int_0^\infty \frac{x^j}{1+\exp(x-\eta_F)} dx \tag{6.99}$$

where the coefficient in front of the integral is a Gamma function.

To solve this integral numerical solutions are used, which have been determined by Bednarczyk and Bednarczyk [19] for $F_{1/2}$ and by Aymerich-Humet [20] for $F_{-1/2}$. These will be considered in turn.

$F_{1/2}$

The approximation is given by

$$F_{1/2}(\eta) = \frac{1}{2}\sqrt{\pi}\left[\frac{3}{4}\sqrt{\pi}a(\eta)^{-3/8} + e^{-\eta}\right]^{-1} \tag{6.100}$$

$$a(\eta) = \eta^4 + 50 + 33.6\eta\left\{1 - 0.68e^{-0.17(\eta+1)^2}\right\} \tag{6.101}$$

The relative error of the above expression is less than 0.4%.

$F_{-1/2}$

Aymerich-Humet used the fitting form

$$F_{-1/2}(\eta) = \left[e^{-\eta} + \xi_{-1/2}(\eta)\right]^{-1} \tag{6.102}$$

$$\xi_{-1/2}(\eta) = \frac{\sqrt{\pi/2}}{\left[\eta + b + (|\eta - b|^c + a)\right]^{1/2}} \tag{6.103}$$

where a = 7.94, a = 1.63 and c = 4.05. This expression gives a maximum error of 0.76 percent.

It is important to consider the accuracy of the approximations. They are of the order of 0.5%, which is not particularly impressive, especially for a numerical model, which requires accuracy in the order of 10^{-15}. The error becomes significant as the solution to the non-linear algebra is approached (very high doping) and quadratic convergence is lost. However, there are approximations available to the Fermi-Dirac integrals in the order of 10^{-30} [21,22,23]. These work on some form of polynomial approximation, notably rational approximations [22,23] for which claim the best accuracies. An additional advantage of the polynomial approximation method is speed. If the area over which the degeneracy is modelled is split into many different intervals (32 in the case of [22,23]) and a polynomial is used for each interval, the calculation time can be greatly reduced. Initially, the polynomial method was not introduced as it was felt that the deterioration in quadratic convergence was not significant enough (in the order of an extra iteration) to necessitate the lengthy coding of all the polynomial coefficients.

In later versions of the code (as discussed in Chapter 7), an additional continuity equation has been added to the coupled set to allow simulation of both the Γ and X conduction band minima. This action results in amplified non-linearity in the Jacobian matrix, to minimise numerical floating-point errors and achieve global convergence, it was necessary to implement the rational approximations given by Antia [23] to evaluate the Fermi-Dirac Integrals. The algorithm describing this function is given in Appendix B.

6.6 Simulation of a Laser Diode

Using the above models it is possible to simulate an entire laser structure, details of which are given in the following table for the single Γ-band only. The structure consists of two heavily doped GaAs outer cladding regions in both the *p* and *n* doped domains. Within the GaAs boundaries various alloys of the AlGaInP semiconductor material are employed, until the active region of the device is reached where there exists GaInP quantum well sandwiched between two undoped waveguide regions. Built in to the *p*-doped cladding layers is a monitor pit; the intention of this layer is to experimentally verify the dominant carrier leaking through this region [24]

by colleagues based at Cardiff University. As hypothesised earlier, this is almost certainly associated with X-band electrons in 630nm visible laser diodes.

Layer Number	Material Composition	Structure Widths (Å)	Doping (cm^{-3})
1	GaAs	6000	5e18 *p*-type
2	$Ga_{0.49}In_{0.51}P$	100	2e18 *p*-type
3	$(Al_{0.7}Ga_{0.3})_{0.5}In_{0.5}P$	5000	5e17 *p*-type
4	$(Al_{0.4}Ga_{0.6})_{0.5}In_{0.5}P$	5000	5e17 *p*-type
5	$(Al_{0.7}Ga_{0.3})_{0.5}In_{0.5}P$	9000	5e17 *p*-type
6	$(Al_{0.51}Ga_{0.49})_{0.5}In_{0.5}P$	945	5e17 *p*-type
7	$(Al_{0.3}Ga_{0.7})_{0.5}In_{0.5}P$	900	Undoped *p*-type
8	$Ga_{0.49}In_{0.51}P$	68	Undoped *p*-type
9	$(Al_{0.3}Ga_{0.7})_{0.5}In_{0.5}P$	900	Undoped *p*-type
10	$(Al_{0.51}Ga_{0.49})_{0.5}In_{0.5}P$	945	5e17 *n* -type
11	$(Al_{0.7}Ga_{0.3})_{0.5}In_{0.5}P$	10000	5e17 *n* -type
12	$Ga_{0.49}In_{0.51}P$	100	2e18 *n*-type
13	GaAs	6000	5e18 *n*-type

Table 6.1: Input parameters for diode laser.

In this simulation example, the multiquantum barrier structure has been excluded; in the following Chapter an improved MQB design is considered.

Figure 6.4(a) below illustrates the zero bias form of the laser structure detailed in Table 6.1. As expected, both the electron and hole quasi-Fermi levels are zero in magnitude across the whole of the structure. Figure 6.4(b) displays the carrier concentrations throughout the laser device; there are fairly abrupt features in the both carrier concentrations stemming from the fact that there are differing alloy compositions along the structure.

Figure 6.5(a) and (b) display similar plots as previous except here an applied forward bias of 2 volts, which is the experimentally determined 'turn-on' voltage, has been dropped across the whole device, to illustrate the position of the energy bands under lasing conditions.

These plots verify that the theoretical simulation model outputs energy band diagrams that were expected. In the next Section, the simulation package is extended to incorporate the contribution to the electron concentration from confined electron states present within the quantum well position in the active region of the device.

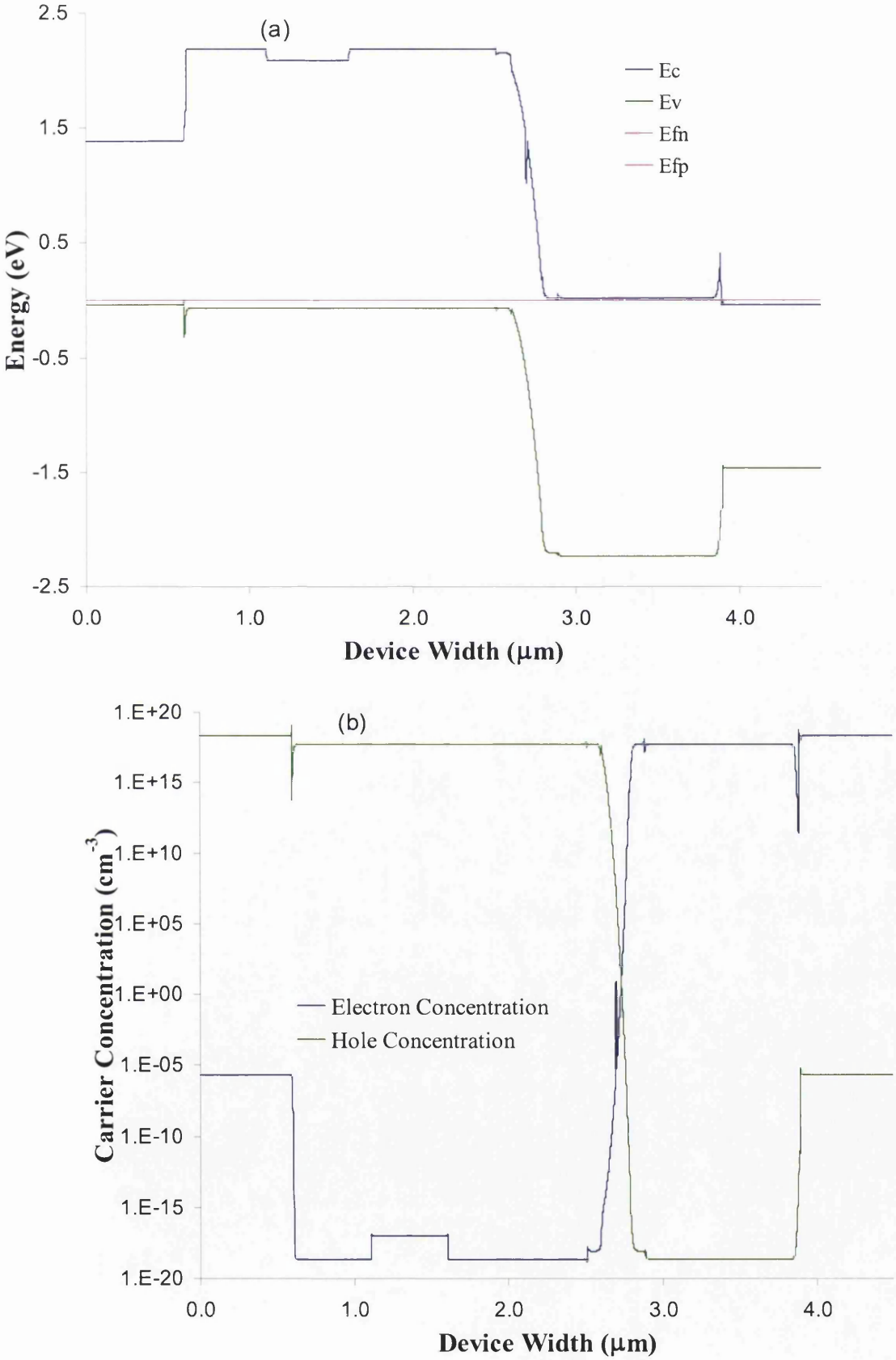

Figure 6.4: (a) Energy band diagram of the control laser sample at zero bias. Plot (b), indicates the magnitudes of the electron and hole concentrations across the structure at zero bias.

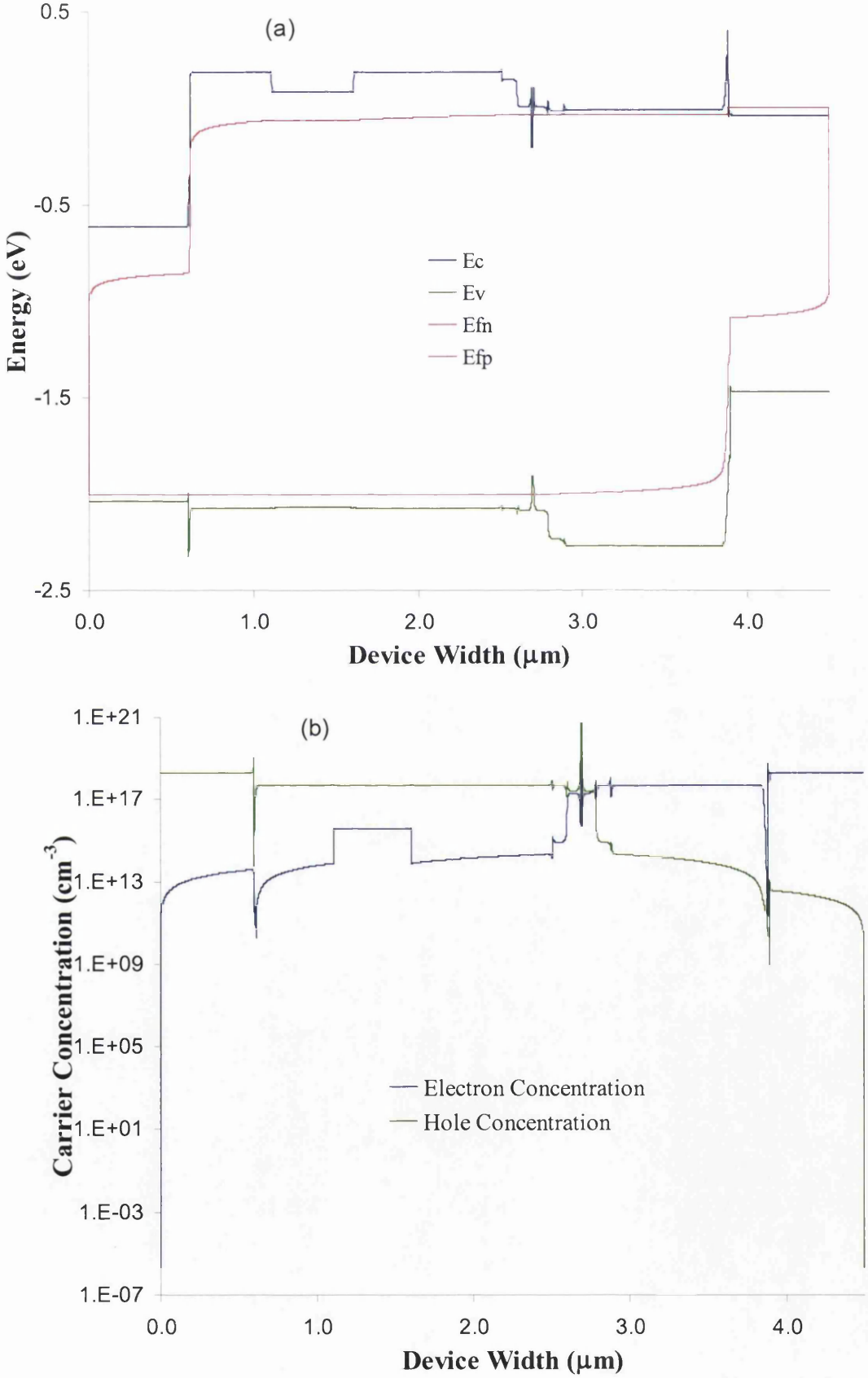

Figure 6.5: (a) Energy band diagram (a), and carrier concentration plot (b), of the control laser sample at a bias of two volts.

6.7 Self-Consistent Solution

A high majority of semiconductor devices have regions where two-dimensionally trapped carrier states are apparent such as quantum wells in laser devices or accumulation layers in resonant tunnelling diodes. The magnitude of the carrier concentration in these layers outweighs the surrounding semiconductor layers and may distort the present band-bending features further. To take account of electrons confined in this way Schrödinger's equation must solved in this region to yield the two-dimensional electron density. The simulation program was modified to iterate in a self-consistent manner between the fundamental drift-diffusion set and Schrödinger's equation until global convergence was acquired. In this Section the numerical methods employed to achieve this task are outlined and then illustrated by considering the effect two-dimensionally confined electrons have on the electron concentration in and around a quantum well embedded in a *pn*-junction as an initial example.

In the following analysis it is assumed that a quantum structure may be computationally split into two distinct segments. A quantum mechanical window [25] separates the conventional part of the device from the area of quantum mechanical operation (i.e. the quantum well within the active region of the device). This enables the parts of the device outside the quantum window to be analysed using conventional carrier statistics as previously described. In this way it acts as a computational tool as it provides a method to consider Schrödinger's equation within a specific region of the device.

6.7.1 Governing Equations

In this investigation, the quantum mechanical effects for electrons are considered only and it is assumed that the effective mass approximation [26,27,28,29,30,31] is valid. Abiding by this conjecture, the electron wave function $\zeta_i(x)$ may be obtained from the following one-dimensional time-independent Schrödinger's equation

$$\left(\frac{\hbar^2}{2}\frac{\partial}{\partial x}\left(\frac{1}{m^*(x)}\frac{\partial}{\partial x}\right)+V(x)+V_{XC}(x)\right)\zeta_i(x)=\lambda_i\zeta_i(x) \qquad (6.104)$$

where x is the one-dimensional coordinate, $\hbar$ is the reduced Plank constant, and m^* is the effective mass of an electron. λ_i is the i^{th} eigen-energy that is the i^{th} eigenvalue of equation (6.97). $V(x)$ is the potential associated with the conduction band minimum. $V_{XC}(x)$ is the local exchange correlation energy due to the many body and correlation effects and its magnitude determined by a local density functional approximation. $\zeta_i(x)$ is the envelope wavefunction of an electron.

The correlation energy, $V_{XC}(x)$, is deduced as a function of the local electron density $n(x)$ only. The following expression reported by Stern *et al.* [32] for $V_{XC}(x)$ is employed in the quantum simulator.

$$V_{XC}(x) = -\left[1 + 0.7734\beta \ln(1+\beta^{-1})\right]\left(\frac{2}{\pi\alpha r_S}\right)R_y \tag{6.105}$$

where

$$\alpha = \left(\frac{4}{9\pi}\right)^{\frac{1}{3}}, \tag{6.106}$$

$$\beta(x) = \frac{r_S}{21} \tag{6.107}$$

$$r_S(x) = \left(\frac{4}{3}\pi a^{*3} n(x)\right)^{-\frac{1}{3}} \tag{6.108}$$

$$a^* = \frac{4\pi\varepsilon_0\varepsilon_r\hbar^2}{m^*(x)q^2} \tag{6.109}$$

where R_y is the effective Rydberg constant, and $a^* = \dfrac{q^2}{8\pi\varepsilon_0\varepsilon_r a^*}$.

If the simulation region is partitioned, the electron wavefunctions must match with each other at the boundaries between sub-regions. The conventional drift-diffusion model (see earlier sections), which is used outside the quantum region,

implicitly assumes that the electron wavefunctions are plane waves in all directions and that the density of states is continuous within the conduction band.

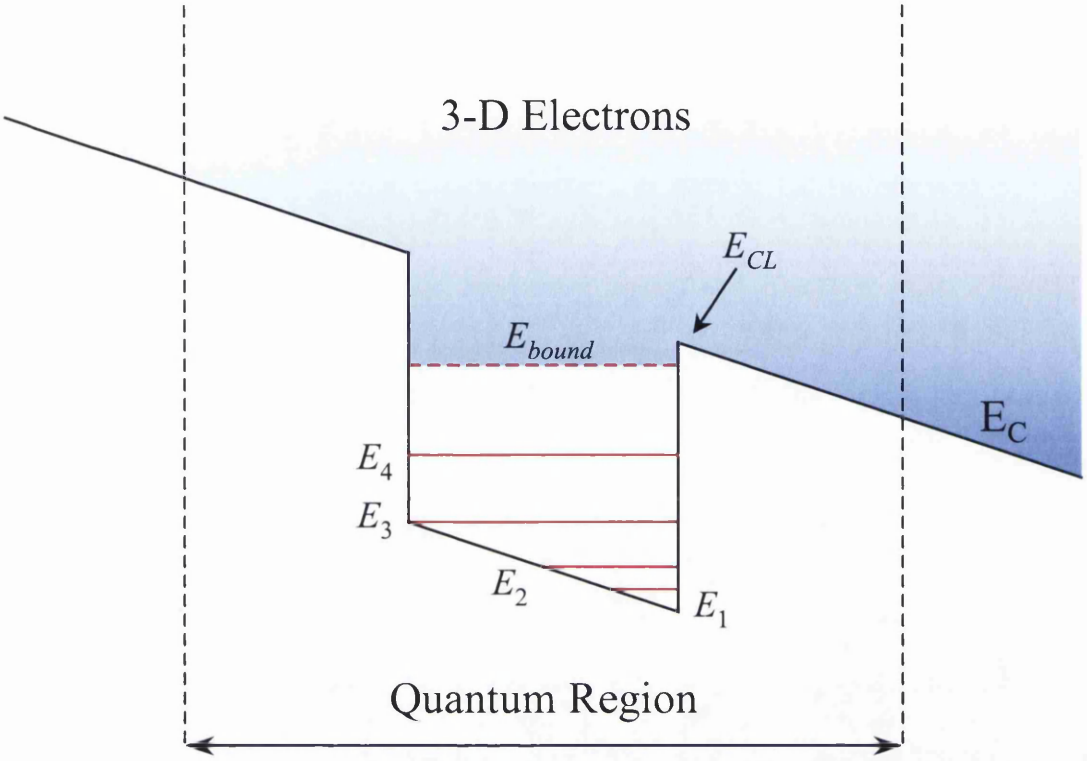

Figure 6.6: Schematic conduction band diagram illustrating a quantum well structure and indicating the quantum region, in which Schrödinger's equation is evaluated. Additionally, the position of E_{bound} the boundary separating the two-dimensionally confined electron states and the three-dimensional electrons is illustrated.

Therefore electrons whose energy in the x-direction is higher than the conduction band edge at one of the boundaries (E_{bound}) (see Figure 6.6) are not confined in the quantum region, because these electron wavefunctions must be connected to plane waves at the boundary and are considered as part of the previous simulation, based solely on the drift-diffusion model.

On the contrary, electrons whose energy in the x-direction is lower than E_{bound} are confined two-dimensionally within the quantum region because there is no density of states outside the well region corresponding to energies lower than E_{bound}. As a result, the two dimensional electrons should have discrete energy levels which are eigenvalues of Schrödinger's equation in the x-direction. The boundary condition for Schrödinger's equation in this case, assumes that the wave function decays exponentially into the adjacent materials.

However, it is not practical for all electrons in all sub-bands of the quantum well to be treated as two-dimensionally confined electrons because summation of

electrons over all sub-bands is needed in order to know the electron concentration at one space location. In this model, it is assumed that electrons in the sub-bands below the highest confined state are two-dimensional in nature, and all other electrons are treated as three-dimensional.

No significant error is expected from the approach because the occupancy probabilities at the sub-bands with higher energy are relatively low due to the Fermi-Dirac statistics. Thus, according to this prescription, the electron concentration within the quantum region may be expressed by the following expression

$$n(x) = n_{2D}(x) + n_{3D}(x), \tag{6.110}$$

where n_{2D} represents the contribution from the two-dimensionally confined electrons, and n_{3D} that from the three- dimensional electrons.

The two-dimensional electron contribution, n_{2D}, can be obtained from the summation of the electron population on each sub-band, which is, in turn, the integral of the product of the distribution function and the wavefunction over the entire k_y-k_z plane; where k_y and k_z are the wave numbers in the y and z directions, respectively:

$$n_{2D}(x) = \sum_i \frac{1}{2\pi^2} \int_{-\infty}^{+\infty} \int \frac{dk_y dk_z}{1 + \exp\left(\frac{E - E_{Fn}}{k_B T}\right)} \left|\zeta_i(x)\right|^2. \tag{6.111}$$

This double integral may be recast in following form

$$n_{2D}(x) = \sum_i \frac{m^* kT}{\pi\hbar^2} \ln\left[1 + \exp\left(\frac{E_{Fn} - E_i}{k_B T}\right)\right] \left|\zeta_i(x)\right|^2 \tag{6.112}$$

with

$$E = E_i + \frac{\hbar^2}{2m^*}(k_y^2 + k_z^2). \tag{6.113}$$

On the other hand, the portion of three-dimensional electrons n_{3D} can be expressed as

$$n_{3D}(x) = \sum_i \frac{1}{2\pi^2} \iiint_{-\infty}^{+\infty} \frac{dk_x dk_y dk_z}{1 + \exp\left(\frac{E - E_{Fn}}{k_B T}\right)} D(k_x) \tag{6.114}$$

with

$$E = E_C + \frac{\hbar^2}{2m^*}(k_x^2 + k_y^2 + k_z^2). \tag{6.115}$$

where $D(k_x)$ is the density of states in the $k = k_x$ momentum plane. Calculation of the density of states may be achieved by solving Schrödinger's equation with respect to the eigenenergies higher than E_{bound}. However, this task is considerably simplified if a constant value of the density of states $D(k_x)$ is assumed, given by

$$D(k_x) = \begin{cases} \frac{1}{2\pi} & \left(\frac{\hbar^2}{2m^*}k_x^2 > E_{bound} - E_C\right) \\ 0 & \left(\frac{\hbar^2}{2m^*}k_x^2 < E_{bound} - E_C\right) \end{cases}. \tag{6.116}$$

Substituting equation (6.116) in equation (6.114) and integrating it in k_y and k_z, yields

$$n_{3D} = \begin{cases} \frac{N_C}{\sqrt{\pi k_B T}} \int_{E_{bound} - E_C}^{+\infty} \ln\left\{1 + \exp\left(\frac{E_{Fn} - E_C - E_x}{k_B T}\right)\right\} \frac{dE_x}{\sqrt{E_x}} \\ \text{(QW)} \\ \frac{N_C}{\sqrt{\pi k_B T}} \int_0^{+\infty} \ln\left\{1 + \exp\left(\frac{E_{Fn} - E_C - E_x}{k_B T}\right)\right\} \frac{dE_x}{\sqrt{E_x}} \\ \text{(Elsewhere)} \end{cases} \tag{6.117}$$

where

$$E_x = \frac{\hbar^2}{2m^*}k_x^2$$

$$N_C \equiv 2\left(\frac{m^* k_B T}{2\pi\hbar^2}\right)^{\frac{3}{2}} \tag{6.118}$$

and where 'QW' refers to the quantum well region where the conduction band minimum is lower than the lowest energy of the three-dimensional electrons (i.e. E_{bound}) (see Figure 6.6). The preceding expressions can be rewritten as equation (6.111) by implementation of the partial integration method:

$$n_{3D} = \begin{cases} \dfrac{2N_C}{\sqrt{\pi}k_B T}\displaystyle\int_{E_{bound}}^{+\infty} \frac{\sqrt{\dfrac{E-E_C}{k_B T}} - \sqrt{\dfrac{E_{bound}-E_C}{k_B T}}}{1+\exp\left(\dfrac{E-E_{Fn}}{k_B T}\right)} dE \\ \text{(QW)} \\ \dfrac{2N_C}{\sqrt{\pi}k_B T}\displaystyle\int_{E_C}^{+\infty} \frac{\sqrt{\dfrac{E-E_C}{k_B T}}}{1+\exp\left(\dfrac{E-E_{Fn}}{k_B T}\right)} dE \\ \text{(Elsewhere)} \end{cases} \tag{6.119}$$

Equation (6.119) satisfies the continuity condition at the boundary of the quantum well ($E_C = E_{bound}$), and also continues outside the quantum region because the formula for $E_C > E_{bound}$ in the equation is exactly the same as the conventional expressions for the carrier concentration.

6.7.2 Solution of Schrödinger's Equation

The first task in the evaluation of Schrödinger's equation in this context is to apply a suitable discretisation scheme to allow its projection on the predefined mesh. It is a simple algebraic task to recast equation (6.104) in the following discretised form

$$-\frac{\hbar^2}{2h'(N)}\left[\frac{\zeta_i(N+1)-\zeta_i(N)}{m^*(M)h(M)}-\frac{\zeta_i(N)-\zeta_i(N-1)}{m^*(M-1)h(M-1)}\right]$$
$$+\left(V(N)+V_{XC}(N)\right)\zeta_i(N)=\lambda_i\zeta_i(N) \tag{6.120}$$

which may be recast in a more succinct form as

$$\hat{\boldsymbol{H}}\boldsymbol{\zeta}_i=\lambda_i\boldsymbol{\zeta}_i \tag{6.121}$$

where $\hat{\boldsymbol{H}}$ is the tri-diagonal Hamiltonian operator comprising of the kinetic and potential energy components (see equation (6.115)), ζ_i is the eigenfunction corresponding to the i^{th} eigenenergy λ_i.

$$\hat{\boldsymbol{H}}=\begin{bmatrix} a_{22} & a_{23} & 0 & \cdots & \cdots & \cdots & 0 \\ a_{32} & a_{33} & a_{34} & & & & \vdots \\ 0 & \ddots & \ddots & \ddots & & & \vdots \\ \vdots & & \ddots & \ddots & \ddots & & \vdots \\ \vdots & & & \ddots & \ddots & \ddots & 0 \\ \vdots & & & & \ddots & \ddots & a_{j-2\,j-1} \\ 0 & \cdots & \cdots & \cdots & 0 & a_{j-1\,j-2} & a_{j-1\,j-1} \end{bmatrix} \tag{6.122}$$

where the index j refers to the node index within the predetermined quantum region, and the elements a_{jj} refer to the coefficients of the wavefunction on that node. To evaluate equation (6.120) requires the calculation of its eigenvalues and eigenvectors. There are many algorithms available for solution of this type of problem. Initially, a numerical routine based around the transfer matrix method (a modified routine to that encountered previously) [29,30,31] was developed [33,34], however, application of this technique proved very computationally expensive. Hence, a more rigorous routine comprising of the union of the QR Algorithm and the Inverse Iteration Method was implemented to determine the eigenvalues and eigenvectors confined in the user-defined quantum windows. These numerical techniques are described briefly in the following sub-sections.

6.7.2.1 *QR Algorithm*

The QR algorithm of Francis [35] is an iterative procedure designed to reveal the eigenvalues of a matrix $\boldsymbol{A}$. This algorithm is often used in the evaluation of eigenvalue problems, due to its high stability [36,37]. The algorithm works by successively transforming the coefficient matrix $\boldsymbol{A}$ according to the following method:

(i) Set $k = 0$

(ii) Decompose $\boldsymbol{A}_k$ into $\boldsymbol{Q}_k$ and $\boldsymbol{R}_k$ such $\boldsymbol{A}_k = \boldsymbol{R}_k\boldsymbol{Q}_k$ where $\boldsymbol{A}_k$ is the Schrödinger tri-diagonal coefficient matrix, $\boldsymbol{R}$ is upper triangular and $\boldsymbol{Q}$ is the unitary matrix.

(iii) Compute $\boldsymbol{A}_{k+1} = \boldsymbol{R}_k\boldsymbol{Q}_k$. The estimates of the eigenvalues equal the leading diagonal of $\boldsymbol{A}_{k+1}$ i.e. diag($\boldsymbol{A}_{k+1}$).

(iv) Check the accuracy of the eigenvalues. If the process has not converged, $k = k+1$; repeat procedure from (ii).

This procedure may be put more concisely in the following expression

$$\boldsymbol{A}_{k+1} = \boldsymbol{R}_k\boldsymbol{Q}_k = (\boldsymbol{Q}_k^T\boldsymbol{A}_k)\boldsymbol{Q}_k = \boldsymbol{Q}_k^T\boldsymbol{A}_k\boldsymbol{Q}_k \tag{6.123}$$

Initially, $\boldsymbol{A}_{k=0} = \boldsymbol{A}$ and provided $\boldsymbol{A}$ is tri-diagonal then $\boldsymbol{A}_k$ is also. The algorithm works because $\boldsymbol{A}_k$ tends to a diagonal matrix with the eigenvalues along its diagonal as the iteration index k increases.

6.7.2.2 *Inverse Iteration*

The By subtracting $\mu\zeta$ from both sides of equation (6.121), the following expression is yielded

$$(\hat{\boldsymbol{H}} - \mu\boldsymbol{I})\zeta = (\lambda - \mu)\zeta \tag{6.124}$$

which may be rearranged to give

$$(\hat{\boldsymbol{H}} - \mu \boldsymbol{I})^{-1}\zeta = \left(\frac{1}{(\lambda - \mu)}\right)\zeta \tag{6.125}$$

Thus, if the following iterative scheme is executed, initiating with the trial vector ζ_i yields

$$(\hat{\boldsymbol{H}} - \mu \boldsymbol{I})^{-1}\zeta_{i+1} = \left(\frac{1}{(\lambda - \mu)}\right)\zeta_i . \tag{6.126}$$

Iteration of this equation will lead to the largest value of $1/(\lambda - \mu)$, i.e. the smallest eigenvalue of $(\lambda - \mu)$. The smallest value of $(\lambda - \mu)$ implies that the value of λ will be closest to μ and ζ_{i+1} will have converged to the eigenvector corresponding to this particular eigenvalue. Thus, by a suitable choice of μ, i.e. using the aforementioned QR algorithm values, a simple procedure for determining the eigenvector for any particular eigenvalue of the system is possible.

Termination of this iterative procedure is commenced when ζ_{i+1} is sufficiently close to ζ_I i.e. when $\|\zeta_{i+1}\|_\infty = 1$. Once this criteria is met i.e.

$$\frac{1}{(\lambda - \mu)} = \|\zeta_{i+1}\|_\infty \tag{6.127}$$

is true. The eigenvalue, λ nearest to μ is given by

$$\lambda = \mu + \frac{1}{\|\zeta_{i+1}\|_\infty} . \tag{6.128}$$

The rate of convergence of this algorithm is extremely fast, due to the fact that the eigenvalues have already been determined. However, equation (6.126) becomes singular if these values are directly inputted into the program, it is necessary to add a small increment to these values to maintain numerical stability.

Figure 6.7 below, displays a flowchart depicting the major steps involved in the above iteration routine used to calculate the eigenenergies and eigenvectors of a potential induced quantum well. Firstly, in the program variables deduced by the drift-

potential induced quantum well. Firstly, in the program variables deduced by the drift-diffusion equation at particular bias point and read in. From the conduction band edge the lowest conduction band point either side of the quantum well (i.e. E_{CL} see Figure 6.6) is determined.

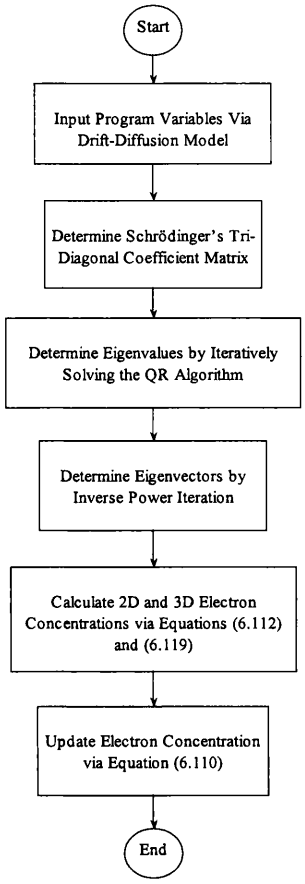

Figure 6.7: Quantum iteration flowchart, showing the major numerical steps involved when finding a solution to Schrödinger's equation.

The elements of the tri-diagonal coefficient matrix are next determined. Utilising the QR algorithm all the eigenvalues of this system are ascertained. The program then discards all eigenenergies greater than E_{CL} (see Figure 6.6). Using the remainder the program calculates their corresponding eigenvectors via the Inverse Iteration routine. Following solution to Schrödinger's equation the program proceeds to evaluate equations (6.112) and (6.119), giving an updated approximation to the electron concentration within the quantum window.

6.7.3 Overall Solution Procedure

The overall self-consistent solution method utilised to evaluated quantum devices is illustrated in Figure 6.8 below. The solution is initially obtained first without considering quantisation effects. An iterative loop is then entered into where Schrödinger's equation is solved across the user-defined quantum region to reveal an up-date to electron concentration by summing the calculated two and three-dimensional electron concentrations.

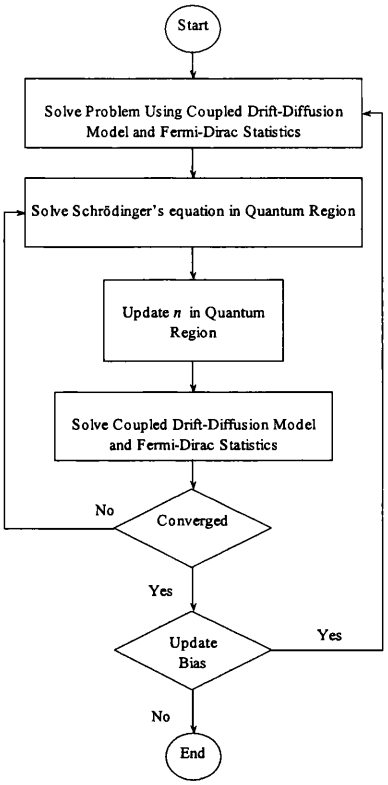

Figure 6.8: Flowchart illustrating the overall solution process.

The revised value of the electron concentration is then re-substituted into Poisson's and the electron current density equation and the coupled drift-diffusion set is again solved until numerical convergence is found. This iteration procedure is repeated until the global convergence criteria are met. The system is then continued at a further bias step, or terminated.

6.7.4 Self-Consistent Solution of a Quantum Well

To illustrate the effect the confined two-dimensional electrons have on the total electron concentration, the case of a simple heterostructure comprising of a

quantum well of width 100Å embedded at the mid-point of a *pn*-junction is considered. The material system used in this example is AlGaAs/GaAs/AlGaAs, and is shown at a forward bias of 0.2V in Figure 6.9. All relevant material parameters for this simulation have been taken from [33,34]. Figure 6.9(a) indicates the relative positions of the conduction and valence bands E_C and E_V, respectively, also shown are the hole, electron, and intrinsic Fermi levels E_{Fn}, E_{Fp} and E_{Fi}. Figure 6.9(b) shows the extent of the quantum region, highlighted in (a), where calculation of the two-dimensional electrons is considered.

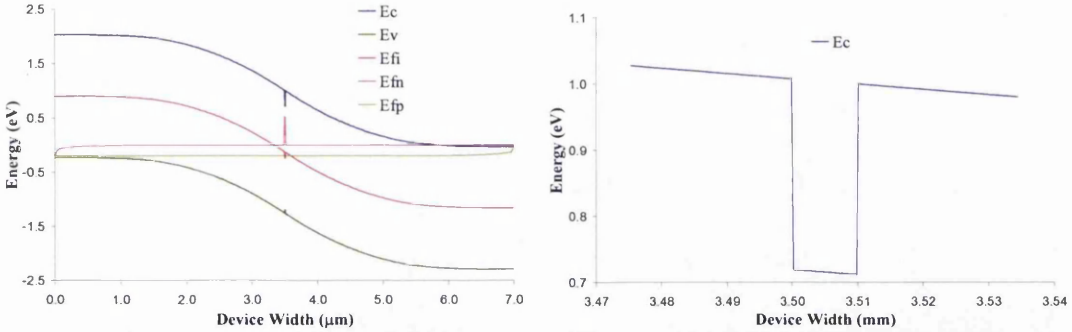

Figure 6.9: Diagram (a) is the calculated energy band profile for the *pn*-junction at zero bias. Plot (b) is an enlargement of the highlighted area in Plot (a), this depicts the position of the quantum well embedded within the *pn*-junction.

Comparison of the electron concentration calculated initially by the drift-diffusion and the self-consistent methods yields a fairly big disparity in magnitude across the quantum well region of the simulation due to the two-dimensionally confined electrons in agreement with separate work of Fukuma *et al.* [33] and Jonsson *et al.* [34].

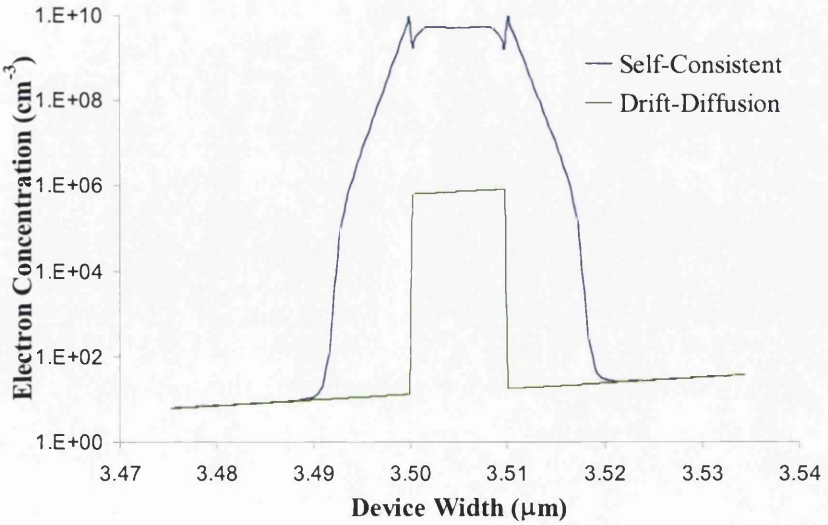

Figure 6.110: Indication of the degree of variance between the electron concentration calculated using the standard drift-diffusion (solid green line) and the self-consistent iteration procedure.

The dissimilarity is shown graphically in Figure 6.10 above. Thus, it is apparent that it is vital to take account of two-dimensionally confined carriers in device structures where quantum structures such as wells are implemented to ensure a more physically realistic picture of the devices nature. In addition to the electron concentration the converged energy eigenvalues and their corresponding eigenvectors with reference to their confining potential are displayed below in Figure 6.11.

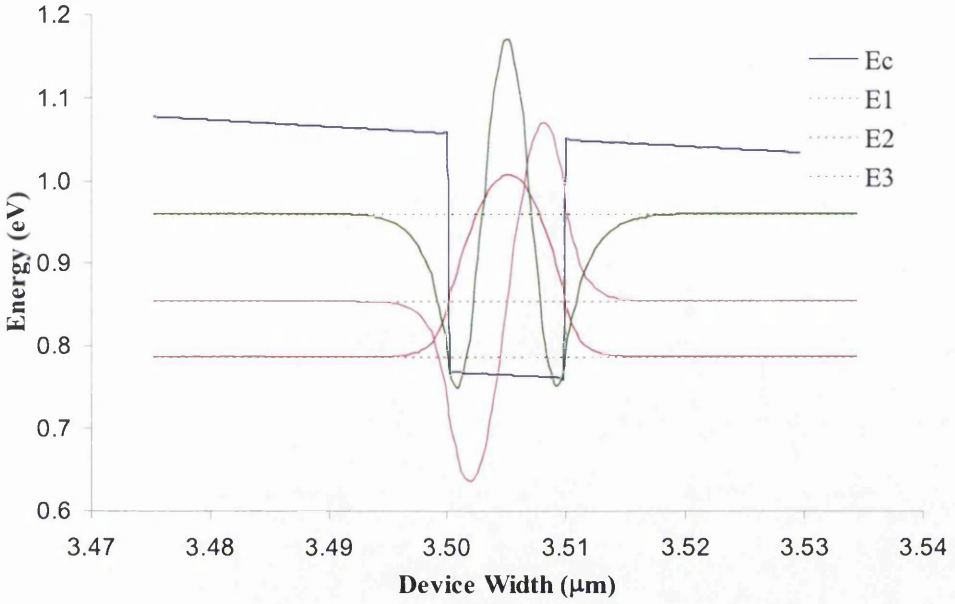

Figure 6.11: The converged position of the three confined two-dimensional eigenvectors superimposed on top of their corresponding eigenvalues (E_1, E_2 and E_3) is shown.

Figure 6.11 shows a magnified view of the quantum well under investigation in this sub-section (blue solid line). The eigenvalues of the three confined electron states present within the well are given by the three intermittent lines, also shown are the corresponding eigenvectors (same coloured solid lines).

6.8 Summary

The major points of discussion within in this chapter have concentrated around the development of a general one-dimensional quantum device simulator. Although, most of the main issues have been implemented with reference to the numerical simulation of laser diodes this simulation package can be applied to a number of other semiconductor devices and each of the above processes may be switched on or off depending on the device of interest.

To lay the foundations of the numerical model the basic equation set to be solved was displayed in their discretised form to allow their projection on a user-defined non-linear mesh in Section 6.2. Particular attention was given to the discretisation of the current density equations to allow greater numerical efficiency.

In Section 6.3, the two solution procedures used to solve the aforementioned equation set were detailed. This comprised of an uncoupled Gummel and the coupled Newton schemes. Also, the Newton-Raphson iteration scheme was given as the method in which Poisson's and the two carrier continuity equations were solved to find an improved up-date to the program variables.

To enhance physical robustness of the model and make the numerical model applicable to heterojunction devices, in Section 6.4, a selection of physical models was introduced. Firstly, the band parameter model was added into the numerical simulation enabling simulation of abrupt or graded material junctions. Also, the recombination processes numerically embedded in the model were given, namely, Spontaneous, Shockley Read Hall and Auger Recombination mechanisms. Finally, this section closed with a brief look at the doping dependent electron and hole mobility models used in the program.

Hitherto this point, the model was founded on the basic assumption of the validity of Maxwell-Boltzmann statistics to all simulated devices. However, due to the highly populated outer cladding regions of a laser diode, the electron and hole Fermi-levels approach and indeed exceed the conduction and valence band edges respectively, severely questioning the validity of Maxwell-Boltzmann statistics. Therefore in Section 6.5, to make the simulation more physically plausible, Fermi-Dirac statistics was incorporated into the model in a formalism that meshed favourably the already written Maxwell-Boltzmann code. This was achieved by the introduction of an additional exponent containing all the information of the Fermi-Dirac corrections in the expression dictating the electron and hole concentrations. Utilising this technique required an extra Newton iteration in the overall solution process to obtain equivalent numerical convergence as that seen under Maxwell-Boltzmann statistics.

The final topic encountered in Section 6.7 of this chapter discusses the onset of perturbations to the electron concentration as a result of two-dimensionally confined electrons in the conduction band.

To permit the simulation of quantised electrons the simulation area was split in to two distinct regions, namely, a region where electron concentration was governed by the normal drift-diffusion equation set and a quantum window in which the program sought a self-consistent solution between the drift-diffusion set and Schrödinger's equation to estimate the electron concentration.

In Section 6.7.2 Schrödinger's equation was discretised in manner that ensured wavefunction continuity across heterointerfaces and allowed non-linear node spacing across the quantum region. In this Section the methods used to evaluate Schrödinger's equation to yield the eigenvalues and eigenvectors of the confined electron states were detailed. Calculation of these values allows estimation of the electron concentration in the quantum window by summing the two and three-dimensional contributions. This updated concentration can then be placed in the drift-diffusion set and the whole process repeated until global convergence is met.

To illustrate the importance of this self-consistent procedure, the method was applied to a simple *pn*-juntion with a 100Å quantum well embedded at the junction. Huge differences in electron concentrations between the standard drift-diffusion and self-consistent models around the quantum well region, which underlines the need for this type of model when two-dimensionally confined electrons, were apparent.

In the following chapter, the simulation package is adapted specifically for simulation 630nm visible laser diodes including a MQB structure. A second conduction band is included in the coupled scheme to allow simulation of both the Γ and X conduction band minima. This model is then used in conjunction with the coupled Schrödinger solver to design a novel dual-band MQB reflector under operating conditions of the laser device.

6.9 References

[1] H. K. Gummel, 'A Self-Consistent Iterative Scheme for One-Dimensional Steady-State Transistor Calculations', *IEEE Trans. Electron. Devices.*, No. **ED-27**, pp. 455-465, (1964).

[2] S. Selberherr, 'Analysis and Simulation of Semiconductor Devices', *Springer-Verlag Wien*, New York, (1984).

[3] R. L. Burden, J. D. Faires and A. C. Reynolds, 'Numerical Analysis 2nd Edition', *Prindle, Weber and Schmit*, (1981).

[4] C. F. Gerald and P. O. Wheatley, 'Applied Numerical Analysis 4th Edition', *Addison-Wesley*, (1989).

[5] D. Kincaid and W. Cheney, 'Numerical Analysis 2nd Edition', *Brooks/Cole*, (1996).

[6] D. L. Scharfetter and H. K. Gummel, 'Large-Signal Analysis of a Silicon Diode Oscillator', *IEEE Trans. Electron. Devices.*, No. **ED-16**, pp. 64-77, (1969).

[7] J. E. Sutherland and J. R. Hauser, 'A computer analysis of heterojunction and graded composition solar cells', *IEEE Trans. Electron. Devices*, Vol. **ED-24**, pp. 363-372, (1977).

[8] H. Tanaka, Y. Kawamura, S. Nojima, K. Wakita, and H. Asahi, 'InGaP/InGaAlP double-heterostructure and multiquantum-well laser diodes grown by molecular-beam epitaxy', *J. Appl. Phys.*, Vol **61**, pp. 1713-1719, (1987).

[9] R. P. Schnieder, Jr., R. P. Bryan, E. D. Jones, and J. A. Lott, 'Excitonic transitions in InGaP/InAlGaP strained quantum wells', *Appl. Phys. Lett.*, Vol **63**, pp. 1240, (1993).

[10] X. H. Zhang, S. J. Chua, and W. J. Fan, 'Band offsets at GaInP/AlGaInP (001) heterostructures Lattice matched to GaAs', *Appl. Phys. Lett.*, **73**(8), pp. 1098-1100, (1998).

[11] R. L. Anderson, 'Experiments of Ge-GaAs heterojunctions', *Solid-State Electron.*, Vol. **30**, p. 341, (1962).

[12] A. G. Milnes, 'Heterojunctions: some knowns and unknowns', *Solid-State Electron.*, Vol. **30**, pp. 1099-1105, (1987).

[13] M. J. Adams and A. Nussbaum, 'A proposal for a new approach to heterojunction theory', *Solid-State Electron.*, Vol. **22**, pp. 783-791, (1979).

[14] O. Ross, 'Theory of extrinsic and intrinsic heterojunctions in thermal equilibrium', *Solid-State Electron.*, Vol. **23**, pp. 1069-1075, (1980).

[15] K. Kokoyama, K. Tomizama, H. Kanbe and T, Sudo, 'A numerical analysis of a heterostructure InP/InGaAs photodiode', *IEEE Trans. Electron. Devices*, **ED-30**, pp. 1283-1288, (1983).

[16] M. S. Lundstrum, 'Numerical analysis of heterostructure semiconductor devices', *IEEE Trans. Electron. Devices*, **ED-30**, pp. 1151-1159, (1983).

[17] C. Snowden, 'Introduction to Semiconductor Device Modelling', *World Scientific*, Singapore, (1986).

[18] C. Hilsum, 'Simple empirical relationship between mobility and carrier concentration', *Elec. Lett.*, Vol **10**(12), pp.259, (1974).

[19] A.C.Bednarczyk and J.Bednarczyk, 'The Approximation of the Fermi-Dirac Integral $F_{1/2}$', *Phys. Lett.* **64**A, pp.409 (1978).

[20] X. Aymerich-Humet, F. Serra-Mestres and J. Millan, 'An analytical approximation for the Fermi-Dirac integral $F_{3/2}$,', *Solid-State Electron.*, **24**, pp. 981-982, (1981).

[21] C. Arpigny, 'Approximate evaluation of the Fermi-Dirac functions', *Astrophys. J.*, **138**, p. 607, (1963).

[22] W. J. Cody and H. C. Thatcher, 'Rational Chebyshev approximations for Fermi-Dirac integrals of order –0.5, 0.5 and 1.5', *Math. Comput.*, **21**, pp.30-40, (1967).

[23] H. M. Antia, 'Rational Function Approximations for Fermi-Dirac Integrals', *Astrophys. Supp. Series*, **84**, pp. 101-108, (1993).

[24] S. A. Wood, C. H. Molloy, P. M. Smowton, P. Blood and C. C. Button, 'Minority Carrier Effects in GaInP Laser Diodes', *IEEE J. Quantum. Electron.*, **36**, pp. 742-750, (2000).

[25] C. Takano, Z. Yu and R. W. Dutton, 'A non-equlibrium one-dimensional quantum mechanical simulation for AlGaAs/GaAs HEMT structures', *IEEE Trans. CAD.*, Vol **9**, pp.1217-1224, (1990).

[26] S. Datta, 'Quantum Phenomena', Chapter 1, 6, Reading, MA: *Addison-Wesley*, (1989).

[27] Chapter 2, Section 2.4.3, this thesis.

[28] Y. Seko, S. Fukatsu and Y. Shiraki, 'Optical transition energies of GaInP quantum wells with GaInP/AlInP superlattice barriers', *J. Appl. Phys.* **72**, pp. 1355-1357, (1994).

[29] R. Tsu, and L. Esaki, 'Tunnelling in a finite superlattice', *Appl. Phys. Lett.*, **22**, pp. 562-564, (1973).

[30] K.Iga, H. Uenohara, and F. Koyama, 'Electron Reflectance of Multiquantum Barrier (MQB)', *Electron. Lett.*, **22**, pp. 1008, (1986).

[31] H. Uenohara, K.Iga, and F. Koyama, 'Analysis of electron reflectivity and leakage current of multiquantum barrier, (MQB)', *Trans. IEICE Japan*, **J70-C**, pp. 851-857, (1987).

[32] F. Stern and S. D. Sarma, 'Electron energy levels in GaAs-AlAs heterojunctions', *Phys. Rev. B*, Vol **30**, pp.840-848, (1984).

[33] W. W. Lui and M. Fukuma, 'Exact solution of the Schrödinger's equation across an arbitrary one-dimensional piecewise-linear potential barrier', *J. Appl. Phys.*, **60**(5), pp 1555-1559, (1986).

[34] B. Jonsson and S. T. Eng, 'Solving Schrödinger's Equation in Arbitrary Quantum Well Potential Profiles Using the Transfer Matrix Method', *IEEE J. Quantum. Electron.*, **26**, pp. 2025-2035, (1990).

[35] J. G. F.Francis, 'The QR transformation: A unitary analogue to the LR transformation', *Parts 1 and 2 Computing Journal*, **4**, (1961).

[36] J. H. Wilkinson and C. Reinsch, 'Linear Algebra', *Springer Verlag*, Berlin, (1971).

[37] J. H. Wilkinson, 'The Algebraic Eigenvalue Problem', *Clarendon Press*, Oxford, (1965).

Chapter 7

Coupled Dual-Band Model and Final Results

7.1 Introduction

Within the following chapter, the general device simulator developed previously in Chapter 6 is extended specifically for numerical analysis of visible 630nm laser diodes. The major obstacles that need to be overcome to achieve this goal are integration of a supplementary continuity equation into the coupled scheme and population of the two conduction band minima in a physically viable manner. Addressing these issues allows simulation of the relative positions of both the Γ and X conduction band minima across the whole laser device.

Subsequently, the discussion topics in this chapter are primarily two-fold; firstly, the necessary changes to the previous coupled iteration procedure to allow a second conduction band are detailed in Section 7.2. In addition, this Section also considers the numerical refinements needed to instigate the dual-band recombination mechanisms needed when considering two conduction band minima. Furthermore, this Section details the initial and final procedures used to populate the Γ and X minima.

Secondly, in Section 7.3, the coupled dual-band simulation program is used in conjunction with the dual-band transfer matrix Schrödinger solver detailed in Chapter 4, to investigate the reflective nature of the MQB structures previously displayed, i.e.:

(i) The flatband dual-band MQB reflector developed in Section 4.5.2 of Chapter 4.

(ii) The Poisson solved dual-band MQB reflector presented in Chapter 5, sub-section 5.4.2.

Taking the calculated reflectivity profiles of the aforementioned dual-band MQB structures, the optimisation procedure detailed in Section 4.4 of Chapter 4, is again utilised to design novel MQB structure. Here the dual-band Schrödinger solver (Section 4.3) is used in conjunction with the coupled dual-band simulator presented in Section 7.2 to predict high stable effective enhancement to the intrinsic conduction band offset.

This chapter closes with Sections 7.4 and 7.5, where conclusions on the main issues discussed are given, and referenced articles are listed respectively.

7.2 Development of Dual-Band Drift-Diffusion Model

The first topic addressed in this Section is the inclusion of an additional electron continuity equation and its corresponding current density equation into the existing coupled equation set introduced previously in Section 6.3. Within this modified equation set the recombination mechanisms used previously for the single-band simulator have to be slightly modified to account for transfers between the two conduction bands and the valence band. It is assumed in the steady-state regime employed in this study, that there is no transfer of electrons between Γ and X minima in the bulk regions of the laser device. Processes of this type are only assumed to be present across the thin material layers within the MQB region, where inter-valley transport is mediated by the mixing parameter, α, introduced in Chapter 4.

Sub-section 7.2.2 tackles the issue of conduction band population. To apply the solution procedure in the steady-state regime, it is necessary to populate each conduction band minimum as a fraction of the total user defined electron concentration entered at the initialisation stage of the program. This problem was initially tackled by calculating the electron temperature across the device. From this, it is possible to deduce what percentage of electrons have sufficient energy to reach and exist in the higher lying minimum, which subsequently makes it possible to populate the bands accordingly. However, due unforeseen device dynamics this method could

not be realised, hence, an alternative mechanism was used in the final simulation model is also detailed in sub-section 7.2.2.

7.2.1 Second Electron Continuity Equation

Under steady-state conditions, the electron continuity equation and corresponding electron current density equation were originally given by the equations

$$\frac{1}{q}\frac{\partial J_n}{\partial x} = U_n \tag{7.1}$$

and

$$J_n = qD_n\frac{\partial n}{\partial x} - q\mu_n n\left(\frac{\partial \psi}{\partial x} + \frac{\partial \theta_n}{\partial x}\right) \tag{7.2}$$

By indexing equations (7.1) and (7.2) the pair of electron continuity equations utilised within the simulation, may be given by

$$\frac{1}{q}\frac{\partial J_n^{\sigma}}{\partial x} = U_n^{\sigma} \tag{7.3}$$

and the corresponding current densities given by

$$J_n^{\sigma} = qD_n^{\sigma}\frac{\partial n^{\sigma}}{\partial x} - q\mu_n^{\sigma}\left(\frac{\partial \psi}{\partial x} + \frac{\partial \theta_n^{\sigma}}{\partial x}\right). \tag{7.4}$$

In both cases (equations (7.3) and (7.4)) the superscript index σ refers to the upper and lowest conduction band minima (U or L respectively).

Instead of perhaps the more conventional Γ-X band formalism, the simulator calculates the position of the two conduction band minima by evaluating the lower and upper conduction band minima, which are both combinations of the Γ and X minima. This convention is illustrated below in Figure 7.1(a). The basis for this preference is predominantly due to numerical idiosyncrasies. Utilising the upper and

lower band formalism it was found numerically a much easier task to populate the two conduction bands (see following section), secondly, the global convergence of the overall solution procedure was greatly improved, due to the reduced non-linearity in elements of the extended Jacobian matrix. Once convergence is achieved, it is a simple process to revert the calculated program variables (i.e. electron concentrations) to a form that depicts the position of the Γ-X bands (see Figure 7.1(b)).

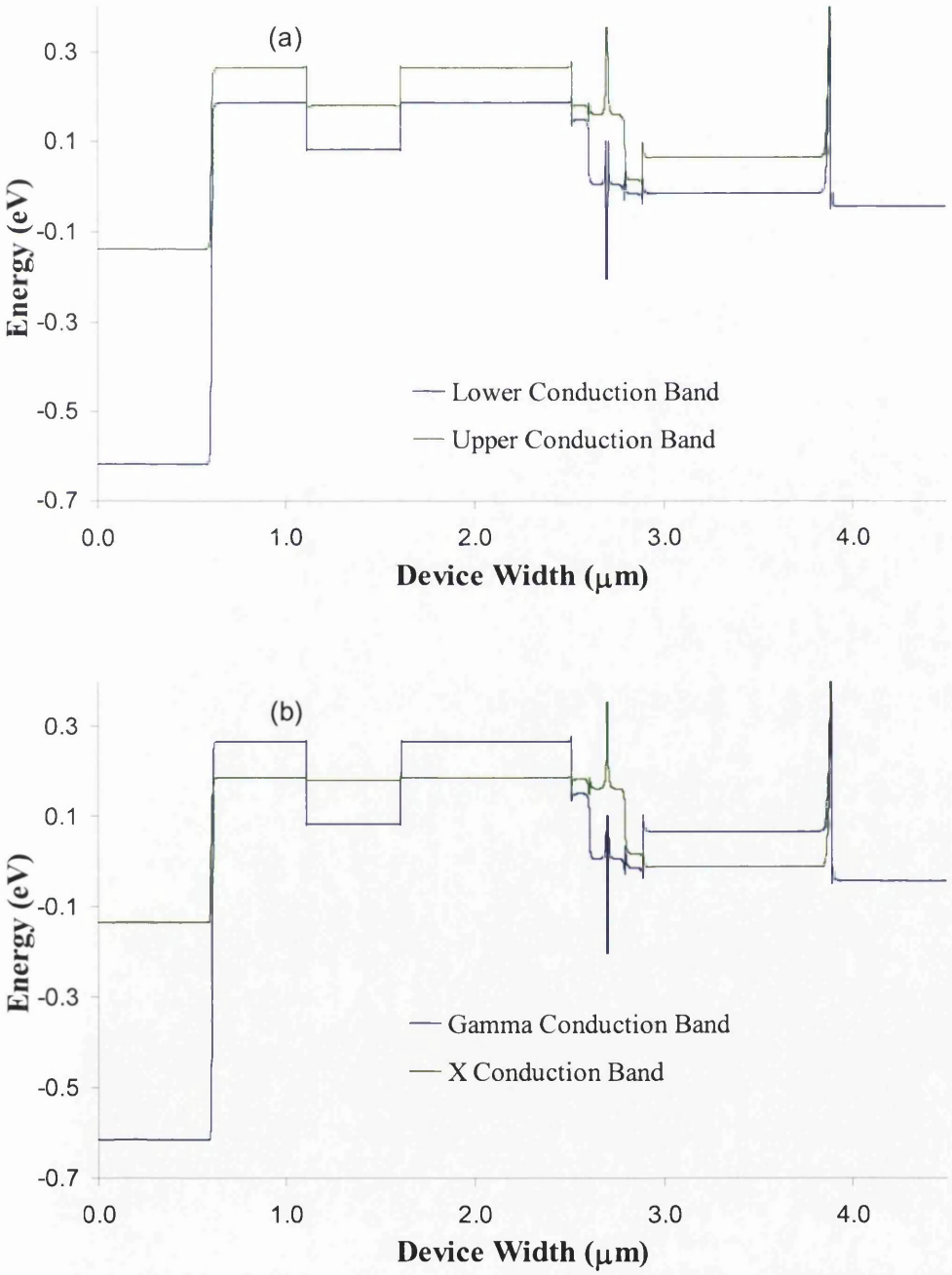

Figure 7.1: Diagrams displaying the calculated position of the conduction band edges of a laser diode under a forward bias of two volts. Plot (a) indicates the position of the upper and lower conduction bands as outputted from the solver, and plot (b) displays the conduction band edges of the Γ and X minima deduced from the upper and lower bands.

The recombination-generation terms present in equation (7.3) now have attached superscripts because they now take different forms depending on which electron-valley is being considered. This adjustment is true for all the recombination mechanisms given previously in Chapter 6. However, for the sake of brevity, the adapted Shockley Read Hall (SRH) mechanism employed is detailed only. Here, recombination terms are given by

$$R_n^{\sigma} = \frac{n_i^2 - n^{\sigma} p}{\tau_p (n^{\sigma} + n_i) + \tau_n (p + n_i)} \quad \sigma = U \text{ or } L \tag{7.5}$$

for electrons in either band and

$$R_p = \sum_{\sigma} \frac{n_i^2 - n^{\sigma} p}{\tau_p (n^{\sigma} + n_i) + \tau_n (p + n_i)}. \tag{7.6}$$

for holes. The other recombination mechanisms, namely, optical and Auger, are treated in an analogous manner to that described above.

The above equation modifications throws out an additional primary variable, namely, the upper conduction band electron concentration n_U. The necessary changes to the coupled non-linear equation set, are succinctly given by the following matrix expression:

$$\begin{bmatrix} J^{pp} & J^{pn_L} & J^{pn_U} & J^{p\psi} \\ J^{n_L p} & J^{n_L n_L} & J^{n_L n_U} & J^{n_L \psi} \\ J^{n_U p} & J^{n_U n_L} & J^{n_U n_U} & J^{n_U \psi} \\ J^{\psi p} & J^{\psi n_L} & J^{\psi n_U} & J^{\psi\psi} \end{bmatrix} \begin{bmatrix} \delta p \\ \delta n_L \\ \delta n_U \\ \delta \psi \end{bmatrix} = - \begin{bmatrix} F_p(p, n_L, n_U, \psi) \\ F_{n_L}(p, n_L, n_U, \psi) \\ F_{n_U}(p, n_L, n_U, \psi) \\ F_{\psi}(p, n_L, n_U, \psi) \end{bmatrix}. \tag{7.7}$$

The main differences to the previous equation set are the additional Jacobian entries, detailing the extra derivatives with respect to the new variable n_U, on the left-hand side of equation (7.7), and the corresponding residual form of equation (7.3) on the right-hand side. The chief problem when evaluating equation (7.7) from a computational point of view is the inclusion and calculation of the extra derivatives associated with the additional continuity equation, and coding in an efficient manner

the increased complexity of the recombination processes. Both these issues have a substantial effect on the simulation time. Thus, to reduce time congestion the total node point number was kept to a minimum. However, this was not an easy task, as it was necessary to specify a node spacing of 1Å across the quantum sectors of the device, which encompassed both the quantum well and MQB regions, where self-consistent calculation of the electron concentration and evaluation of the reflectivity probabilities are respectively initiated. Elsewhere, the node spacing across the device varied non-linearly as a function of material layer width, where each individual layer was initially allocated 20 nodal points. However, as one of the quantum regions in the device is approached the program alters the nodal positioning such that, the 1Å spacing apparent in the quantum region stretches into each of the adjoining cladding layers for at least 150Å. Thus, at least 1300 nodal points are typically required to evaluate the laser device as a whole. Hence, using this nodal number as an example, and excluding all zero elements form the total matrix, approximately 62304 scalar elements for each bias point need to be evaluated, which is non-trivial. Also, it was noted that the existing matrix inverting routine, based on Sylvester's algorithm [1] did not cope effectively or efficiently with the increased non-linearity of the matrix elements. To combat this numerical issue, a more efficient and much more complex matrix inverting routine based on the complete scaled pivoting method given in [2] was implemented.

7.2.2 Electron Dual-Band Population

In this sub-section, the procedure employed to populate the two electron conduction bands and maintain particle conservation is described. However, prior to the final method used to perform this task, the initial course of action to address this issue is briefly detailed.

Originally, the energy transport equation (equation (7.8)) was solved iteratively in union with the coupled single band model.

$$\frac{dS_n}{dx} = J_n E - \frac{W - W_0}{\tau(\xi)} \tag{7.8}$$

where ξ is the position dependent average electron energy, $W = n\xi$, $\tau(\xi)$ is the energy-dependent relaxation time, taken from data obtained through Monte-Carlo simulations [3], and

$$S_n = -\mu_n(\xi)WE - \left(\frac{k_B}{q}\frac{d(\mu_n(\xi)WT_n)}{dx}\right) \tag{7.9}$$

is the energy flux. This equation calls for energy dependent mobilities [3,4], in addition to the previous material and dopant dependent model detailed earlier Chapter 6. The electron energy is given by,

$$\xi = \frac{3}{2}k_B T_n \tag{7.10}$$

in this work [3]. To complete this procedure, an additional term is needed within the electron current density to account for temperature flux, (i.e. last term in the following expression)

$$J_n = -qn\mu_n\left(\frac{\partial\psi}{\partial x} - \frac{\partial\theta_n}{\partial x}\right) + k_B T_n \mu_n \frac{dn}{dx} + k_B n\mu_n \frac{dT_n}{dx} \tag{7.11}$$

From this solution procedure it was envisaged that a variation in the electron temperature with that of the lattice would be evident. If any such deviation occurred, the following expression proposed by Bozler and Alley [5] to populate the two bands:

$$\frac{3}{2}k_B T_n = \xi_T - G_U(\xi)\Delta\xi_{UL} \tag{7.12}$$

may be utilized. Here k_B is the Boltzmann constant T_n is the electron temperature, $\Delta\xi_{UL}$ is the separation between the lower and upper valley's (0.36eV in GaAs), $G_U(\xi)$ is the proportion of electrons in the upper valley and ξ_T is the total energy.

In this study, an attempt to analyse the reflective nature of an embedded multiquantum barrier in a laser diode, when the device is operational is the main

objective. As detailed previously, in this mode of operation the laser diode is forward biased to an extent such that approximate flatband conditions are observed across the active region of the device. This regime is adhered to, to maximise the amount of injected carriers into the active region of the device. As a consequence of the approximate flatband condition, the electric field across the active region is at its minimum. Thus, using the equation set outlined above it was found that this field minimum is insufficient to accelerate the electrons and subsequently raise the electron temperature from that of the lattice anywhere across the device. Therefore, to evaluate this problem an alternative approach has been adopted, which is detailed presently.

The premise of the final method employed to populate the two conduction band minima was thus, firstly, as mentioned above the Γ and X bands are split in to upper and lower lying bands. For each minimum a position dependent band parameter θ_n^L or θ_n^U is deduced from the input parameters in a similar manner to that described in Section 6.4 of Chapter 6. For the lowest lying band the electron concentration is deduced in a similar fashion to that of the single band model i.e.

$$n_L = n_{iref} e^{\theta(\psi - \phi_n^L + \theta_n^L + V_n^L)}. \tag{7.13}$$

Whereas to calculate the population of the upper band, a similar principle to that given in equation (7.12) is adopted, that is, inclusion of an extra term in the exponent corresponding to the material dependent energy-gap difference $\Delta\xi_{UL}$, between the lower and upper bands. This modification yields the following expression

$$n_U = n_{iref} e^{\theta(\psi - \phi_n^U + \theta_n^U + V_n^U - \Delta\xi_{UL})}. \tag{7.14}$$

To uphold particle conservation, the sum of electron concentrations are normalised with respect to the user defined value, such that

$$n = n_L + n_U \tag{7.15}$$

in zero bias conditions. Here, n is the user defined electron doping concentration in each material region. This procedure may not be maintained at applied bias due to loss of carriers through the various recombination mechanisms.

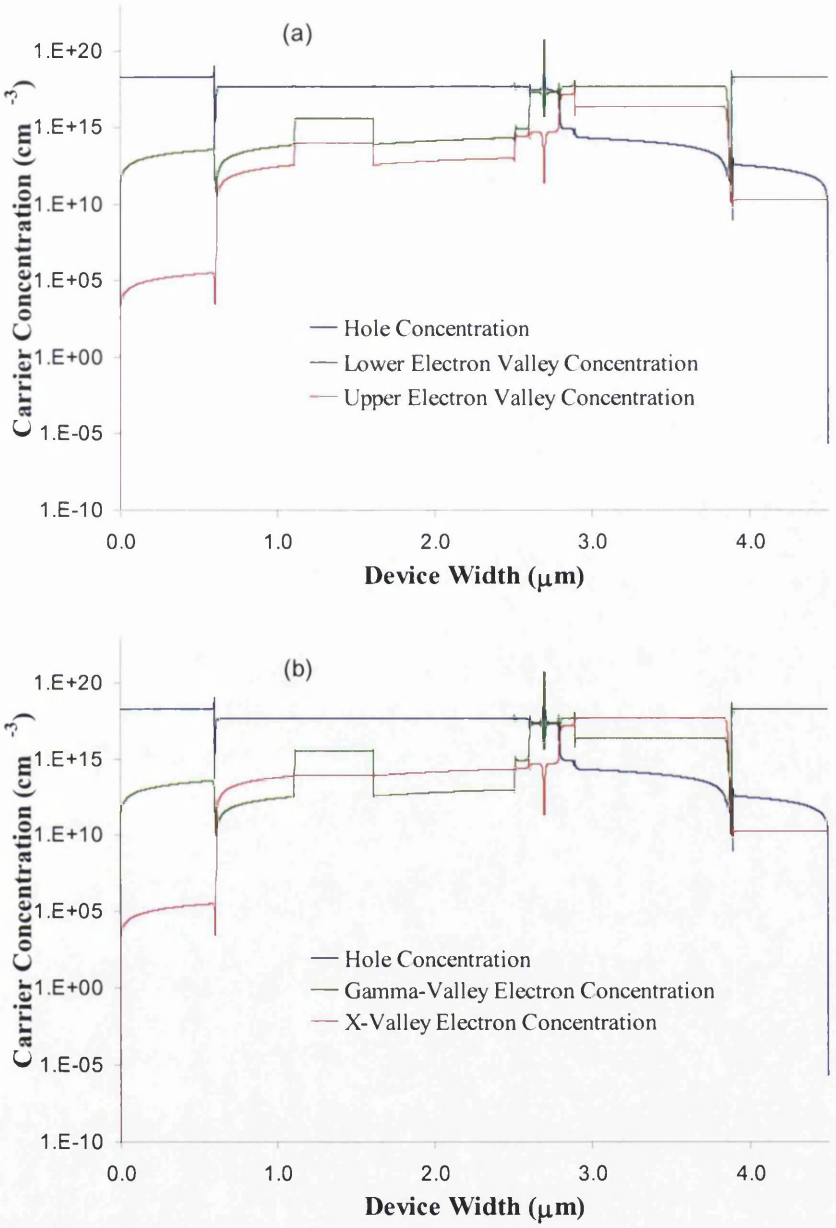

Figure 7.2: Plots showing the magnitude of the carrier concentrations across the laser device under forward bias conditions of two volts. Plot (a) indicates concentrations in the upper and lower band formalism and plot (b), in the Γ and X band representation.

It has been shown by [6] that ordinarily a very high percentage of electrons would occupy the lowest lying conduction band n_L. This postulate is upheld as indicated in Figure 7.2(a) where the laser diode is forward biased to the lasing voltage of two volts. Stark difference between the electron concentrations in the upper and lower conduction bands is observed, in fact, if the sum of the magnitudes is deduced

and expressed as a fraction of the whole, it is found on average, the population percentage is of a ratio 99:1 in favour of the lower band. This figure is in agreement with that proposed by [6]. However, at low biases in the self-consistent scheme this behaviour is not always true locally as it is globally. In the self-consistent regime the two-dimensional electron contribution to the overall electron concentration is only evaluated for the lowest lying conduction band minimum only, as the upper conduction band has no quantised states in the quantum well region (see Figure 7.1(a)).

However, as a result of the conversion from the upper and lower conduction band formalism to the more conventional Γ-X form, the X-band electron concentration is exaggerated in magnitude either side the quantum well giving rise to an unphysical discontinuity in the electron concentration. This is attributed to the fact that the wave guide regions either side of the quantum well were part of the lowest lying conduction band in the self-consistent simulation, this inconsistency is most evident at forward biases less than half a volt. This phenomenon is not physically probable, and is a numerical artefact of the steady-state approximation used in the numerical routine. The discrepancy may be removed if a transient solution to this problem is supposed, whereby, carriers evolve in time as well as spatially. In this regime it would be possible to implement a bulk scattering mechanism, which would permit inter-valley transitions between the upper and lower conduction band minima. Thus, enabling the top-heavy conduction band population to scatter back to the more energetically favourable lowest lying conduction band minimum. However, at the working bias of two volts, the contribution from the confined carriers is overwhelmed by the injection of minority carriers across the intrinsic region of the device, consequentially, no significant discontinuities in the carrier concentrations are evident.

7.3 Final Results

The final result of this thesis will be an optimised multiquantum barrier structure designed using the above coupled dual-band self-consistent solver, detailed above in Section 7. 2. However, prior to this result, a study comparing the reflectivity profiles of the previous proposed dual-band MQB structures is presented.

To initiate this investigation, the optimised flatband and Poisson solved dual-band MQBs presented in sub-sections 4.5.2 and 5.4 of this thesis respectively, are implemented within the *p*-doped region of the laser device. Their corresponding energy band diagrams are then determined via the coupled dual-band drift-diffusion solved outlined above. Finally, from these results their corresponding reflectivity spectra are determined and compared in sub-section 7.3.1. A novel MQB structure is then proposed in sub-section 7.3.2. This structure was determined via the optimisation procedure detailed in Section 4.4, using the dual-band drift-diffusion model in conjunction with the dual-band Schrödinger solver to locate a suitable MQB structure that predicts high, stable effective enhancements.

7.3.1 Reflection Spectra of Previous Dual-Band MQB's

The calculated conduction band profiles, corresponding to the previously proposed optimised flatband and Poisson solved dual-band MQB structures using the above dual-band drift-diffusion model are displayed below in Figures 7.3 and 7.4 respectively.

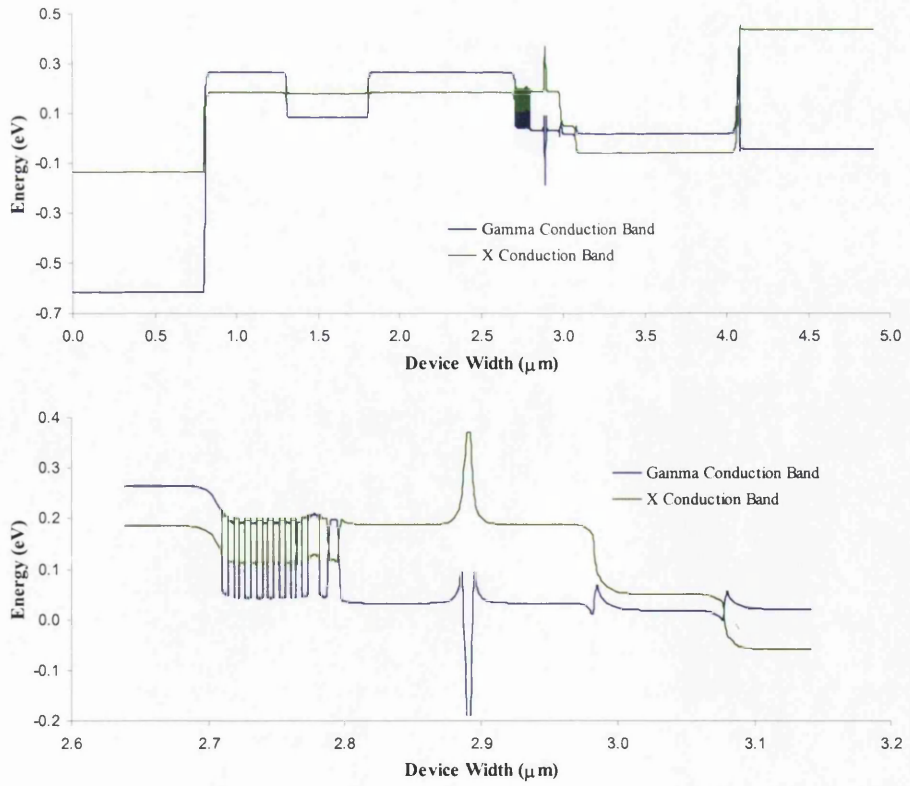

Figure 7.3: Energy band profiles of the previously optimised flatband MQB structure embedded within a laser device (see Chapter 4). Figures (a) indicates the position of the conduction bands across the device and (b) a zoomed in view across the active region.

Figures 7.3 and 7.4 indicate the relative positions of both the Γ and X conduction band minima across the laser diode. Each of these Figures contains two plots (a) and (b). Plot (a) indicates the position of the Γ and X minima across the whole of the laser device and plot (b) which shows an enlargement of the active region and the immediately surrounding *p* and *n*-doped cladding regions, of which the former contains the dual-band MQB structures. Each energy band diagram is shown under a forward bias of two volts, corresponding to the turn-on voltage of the laser device.

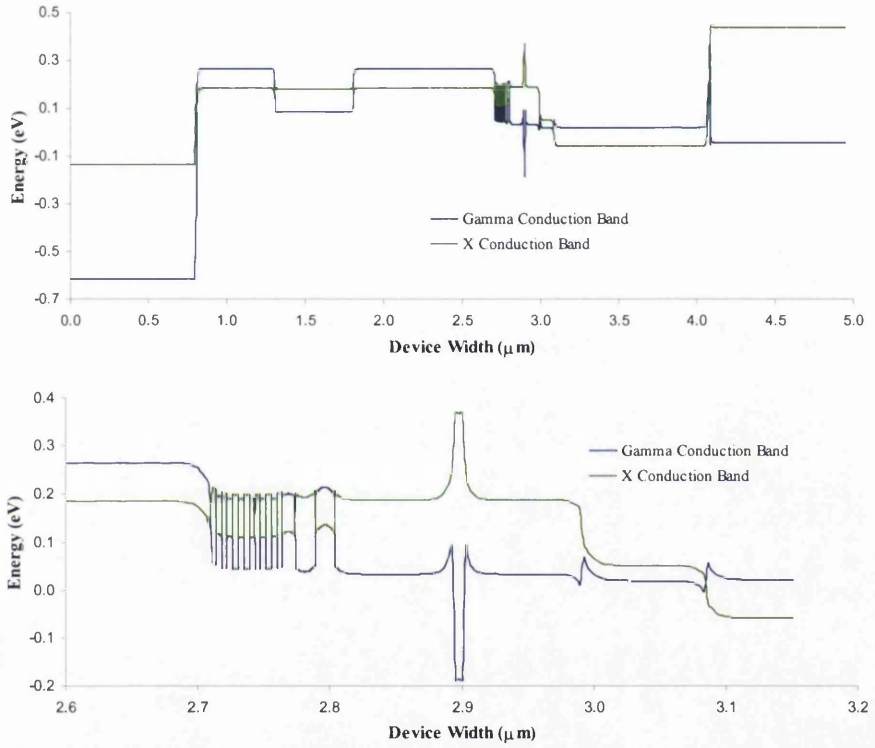

Figure 7.4: Energy band profiles of the previously optimised Poisson solved MQB embedded within a laser device. Figures (a) and (b) refer to the positions conduction bands across the device and a zoomed in view across the active region respectively.

From the both Figures 7.3(b) and 7.4(b), it can be observed that the relative positions of the Γ and X conduction band minima calculated using the Anderson electron affinity rule [7], differs slightly to that of the two-thirds approximation suggested by [8,9,10] and used previously in Chapters 4 and 5. The potential barrier height with respect to the Γ-band and the X-band well within the Γ barrier remains fixed at approximately 0.16eV and 0.08eV respectively, however, the position of the X-band barrier height is located at a higher position of 0.175eV compared to the two-thirds model of 0.156eV. The discrepancy between these two values occurs as a direct result of the electron affinity rule, as the same equations predicting the magnitude of

the Γ and X energy band gaps were consistently used throughout all the investigation. The magnitude of the electron affinity employed was obtained through the experimental work conducted by Krijn [11]. However, the two-thirds approximation suggested by [9,10,11] is given for the single Γ-band only. The position of the X-band with respect to the Γ-band is calculated by determining the difference in band gap between each of these bands in every individual material layer. This suggests the electron affinity model at present is a more physically accurate model where prediction of the relative position of the X-band minima is concerned, simply because all factors in this calculation i.e. the energy band gaps have been acquired experimentally. Whereas, previously in Chapters 4 and 5 the assumption that the position of the X-band relative to the Γ-band is explicitly the band gap difference between the two in each material layer, has no scientific grounding. Nevertheless, the two-thirds approximation seems to be a very good first approximation when predicting the relative positions of the Γ and X minima in both the flatband and Poisson solved MQB structures. To gain further insight into the 'true' positioning of the bands, would require either a full psuedo-potential model like that of Marsh [12,13,14], for the AlGaInP material system, or the development of more sophisticated experimental techniques to deduce these values.

The principal discrepancy of this behaviour amounts to a shift in the energy where the onset of transmission or reflection through the X-minimum occurs. To re-iterate, it was stated that the X-band barrier height resides at a relative position of 0.175eV in the electron affinity model as opposed to 0.156eV in the two-thirds approximation, corresponding to a upwards energy shift of 19meV. From a designing standpoint this energy shift is a welcome one; an incident electron has to acquire a further 19meV to exist in the X-band minimum, hence transmission and reflection through the X-minimum will be reduced to that previously seen in Chapters 4 and 5. However, the most destructive transport mechanism in this context still remains, i.e. the quasi-bound transmission states that may be evident for energies greater than the 0.08eV. The reflectivity spectra of these two structures are displayed overleaf in Figure 7.5, where both plots have been normalised with respect to the X-band maximum, a procedure illustrated previously in Chapter 5. Investigation of these two reflection spectra reveals good enhancements with respect to the X-band maximum, both of which are more than double the normalised energy. It is interesting to note that the optimised Poisson structure (Figure 7.5(b)) predicts a greater enhancement

with respect to the X-maximum, than that of the flatband optimised structure (Figure 7.5(a)). This result is not surprising result considering the extent of the band bending occurring across the active regions of the two laser structures. In both cases, the band bending features appear very similar to that predicted by the simplistic Poisson routine detailed in Chapter 5. The Poisson solved MQB structure is designed to cope with the band-bending features, whereas the flatband structure is not. Thus, it is expected that the Poisson solved MQB reports a superior compared to that of the flatband structure.

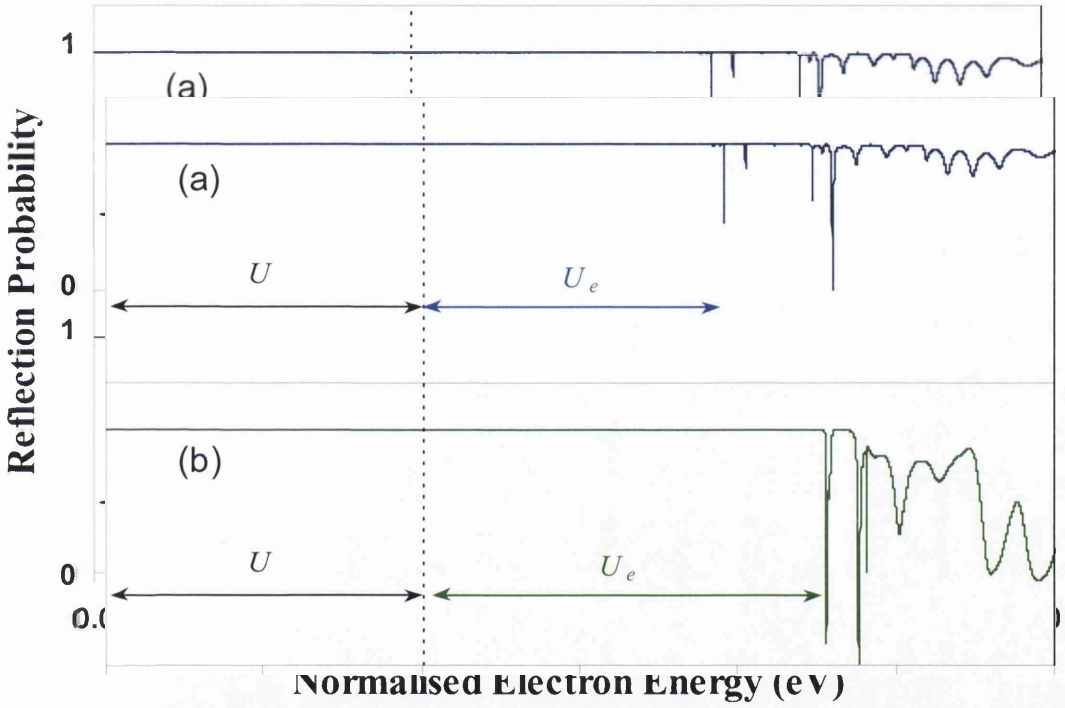

Figure 7.5: Normalised reflectivity plots of (a) the optimised flatband MQB structure and, (b) the optimised Poisson solved MQB superlattice when determined via the dual-band drift-diffusion model and the dual-band Schrödinger solver.

In both the above reflectivity plots, the existence of the aforementioned quasi-bound states present within the X-band well may be observed and are suppressed more efficiently as expected by the optimised Poisson MQB structure. Thus, this section has highlighted the importance of relative band alignment when designing such MQB structures, and emphasised the validity of the Poisson approximation with respect to the dual-band model. In the following sub-section, the dimensions of the Poisson solved MQB structures are re-optimised to gain maximum reflectivity when the energy band profile is deduced via the coupled dual-band model.

7.3.2 Re-Optimisation of Dual-Band MQB Structure

In this sub-section, a novel MQB structure is proposed by re-optimising the Poisson solved dual-band MQB structure presented previously in Chapter 5. To obtain this re-optimised structure, the above coupled dual-band drift-diffusion model and the dual-band Schrödinger solver were used in unison within the optimisation procedure.

Thus, sub-section 7.3.2.1 presents the optimised structure and its associated reflectivity profile and sub-section 7.3.2.2 illustrates the effect on the aforementioned reflectivity plot when the inter-valley mixing parameter, α, is varied.

7.3.2.1 Novel Dual-Band MQB structure

From the information acquired from the reflectivity profiles presented in sub-section 7.3.1, it was apparent that the flatband MQB structure detailed in Chapter 4 gave the best enhancement. Thus, the optimisation procedure initially began with this structure. After many iterations around the optimisation procedure a MQB stucture which predicted a high stable effective enhancement was uncovered. The material alloy, doping and widths of each individual layers that comprise this MQB structure are shown below in Table 7.1.

Material	Layer Type w.r.t. the Γ-band	Doping (cm^{-3})	Structure Widths (Å)
			Optimised Dual band
$(Al_{0.7}Ga_{0.3})_{0.5}In_{0.5}P$	barrier	5e17 *p*-type	159
$(Al_{0.3}Ga_{0.7})_{0.5}In_{0.5}P$	well	5e17 *p*-type	129
$(Al_{0.7}Ga_{0.3})_{0.5}In_{0.5}P$	barrier	5e17 *p*-type	120
$(Al_{0.3}Ga_{0.7})_{0.5}In_{0.5}P$	well	5e17 *p*-type	42
$(Al_{0.7}Ga_{0.3})_{0.5}In_{0.5}P$	barrier	5e17 *p*-type	42
$(Al_{0.3}Ga_{0.7})_{0.5}In_{0.5}P$	well	5e17 *p*-type	42
$(Al_{0.7}Ga_{0.3})_{0.5}In_{0.5}P$	barrier	5e17 *p*-type	42
$(Al_{0.3}Ga_{0.7})_{0.5}In_{0.5}P$	well	5e17 *p*-type	42
$(Al_{0.7}Ga_{0.3})_{0.5}In_{0.5}P$	barrier	5e17 *p*-type	42
$(Al_{0.3}Ga_{0.7})_{0.5}In_{0.5}P$	well	5e17 *p*-type	42
$(Al_{0.7}Ga_{0.3})_{0.5}In_{0.5}P$	barrier	5e17 *p*-type	42
$(Al_{0.3}Ga_{0.7})_{0.5}In_{0.5}P$	well	5e17 *p*–type	42
$(Al_{0.7}Ga_{0.3})_{0.5}In_{0.5}P$	barrier	5e17 *p*–type	42
$(Al_{0.3}Ga_{0.7})_{0.5}In_{0.5}P$	well	5e17 *p*–type	42
$(Al_{0.7}Ga_{0.3})_{0.5}In_{0.5}P$	barrier	5e17 *p*–type	42
$(Al_{0.3}Ga_{0.7})_{0.5}In_{0.5}P$	well	5e17 *p*-type	45

Table 7.1: Optimised MQB structure obtained from analysis of the coupled dual-band model.

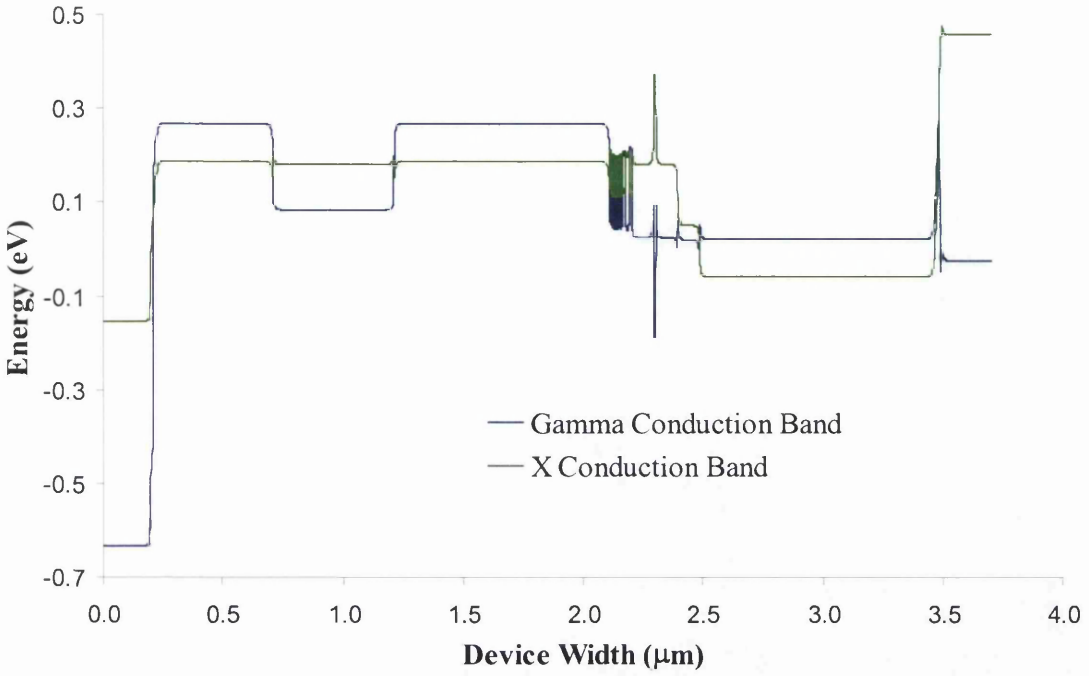

Figure 7.6: Full energy band structure of laser device under forward bias conditions of two volts. Embedded within the device, is the optimised MQB structure devised via the coupled dual-band model.

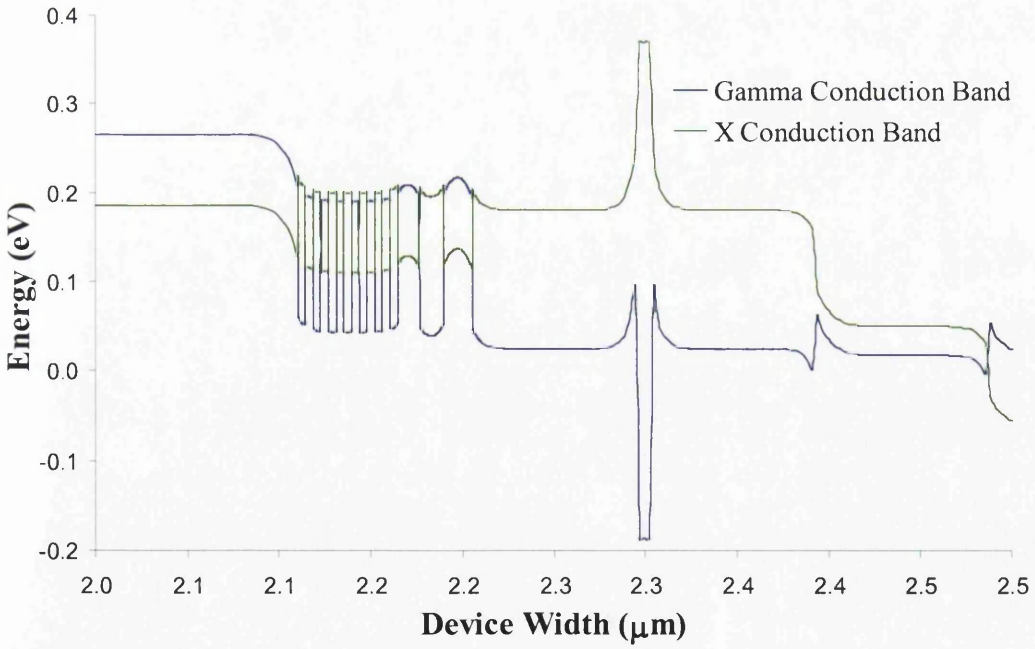

Figure 7.7: Magnification of the active region of the laser device, indicating the relative positions of the two conduction band minima.

The re-optimised MQB structure tabulated above, has retained the main features of the Poisson solved structure, i.e. thick initial stopping layers designed to reduce low electron tunnelling in both the Γ and X bands. The only difference being

that the two initial Γ-barriers have been increased further and the X-barrier (Γ–well) has been reduced slightly. The two to Γ-barriers were increased to lessen the influence of band-bending across the superlattice and the X-barrier reduced inhibit sharp resonant tunnelling spikes associated with quasi-bound electron states. These layers were refined from 150-150-96Å to 159-129-120Å. The whole energy band structure and an enlargement focusing on the active region are displayed above in Figure 7.6 and above in Figure 7.7 respectively.

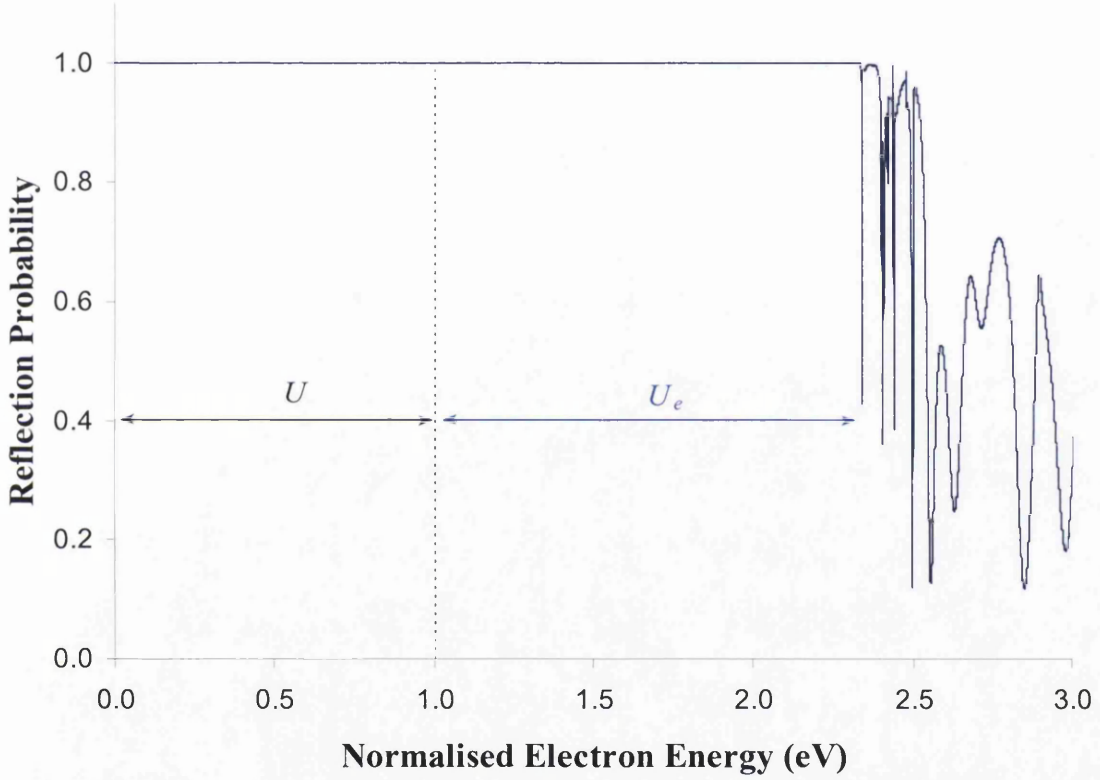

Figure 7.8: Reflectivity profile associated with the optimised MQB structure given in Table 7.1.

Figure 7.8 above shows the calculated reflectivity spectra gained from examination of the MQB structure displayed in Figures 7.6 and 7.7 and given in Table 7.1. This structure predicts the ideal reflectivity characteristics outlined in Chapter 4 i.e. high effective enhancements, no low energy transmission, no occurrence of transmission spikes due to quasi-bound electron states and no electron leakage via the X-band minimum. In fact, it can be observed that the reflectivity profile produces a reflectivity profile that exceeds the X-band maximum by some margin.

7.3.2.2 *Variation of Inter-Valley Mixing Parameter*

The reflectivity probabilities associated with the above MQB structure are displayed below for various magnitudes of the interface mixing parameter α.

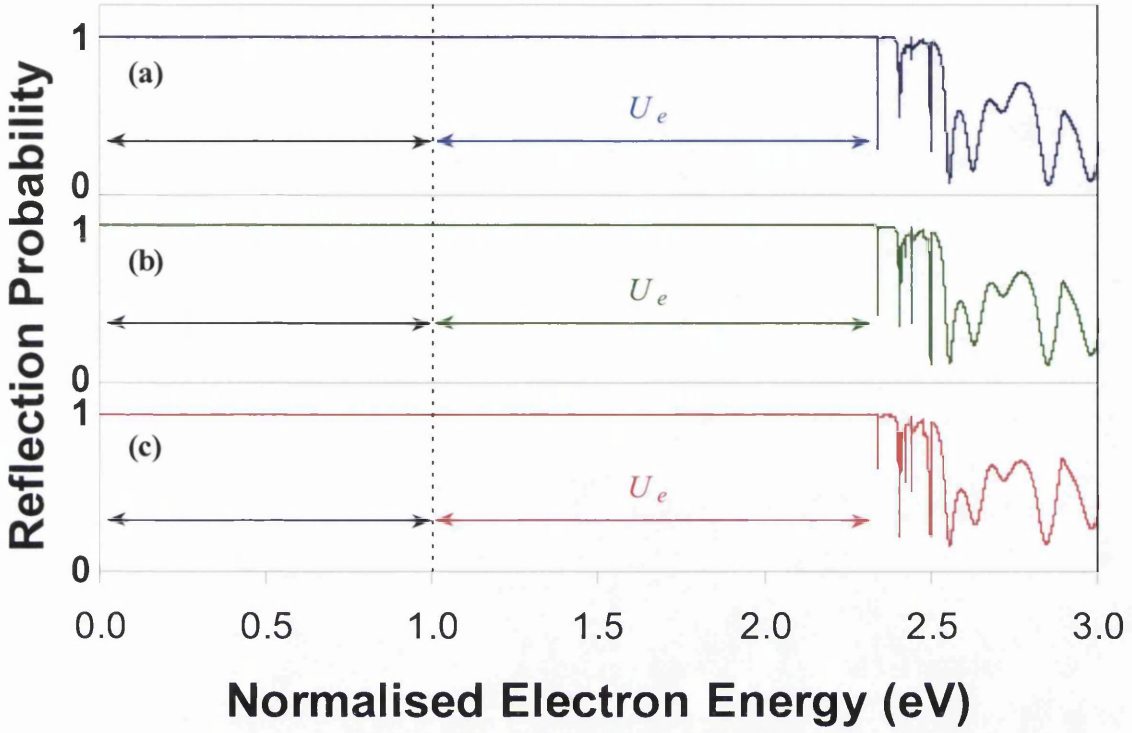

Figure 7.9: Reflectivity spectra of the proposed coupled dual-band MQB structure under lasing conditions, where plots (a), (b) and (c) correspond to the magnitudes 0.1, 0.155 and 0.2eVÅ of the inter-valley mixing parameter α.

Figure 7.9 above indicates the calculated reflectivity profiles of the newly proposed coupled dual-band MQB structure, for magnitudes of the inter-valley mixing parameter of 0.1, 0.155 and 0.2eVÅ. Each plot produces a reflectivity profile that exceeds the X-band maximum by approximately 60% in all cases. As mentioned in the previous sub-section this also corresponds to an effective potential barrier enhancement with respect to the Γ-maximum of 2% [15].

The magnitude of the mixing parameter has been varied to investigate any additional amplification or reduction in the transmission associated with quasi-bound electron states. However, no significant supplementary features are observed in the enhanced area. This implies a theoretically stable MQB structure has been found; in that variation in amount of inter-valley transport predict enhancements that deviate with no effect to the theoretically predicted reflection spectra.

7.4 Conclusion

The main issues covered in this chapter were the development of a simulation program to incorporate a second conduction band, and the re-evaluation of previously designed MQB structures using the improved numerical procedure.

To integrate a supplementary conduction band into the existing program required the addition of a second electron continuity equation into the coupled solver. The main difficulties to overcome this task were the evaluation of an additional set of derivatives in the global Jacobian, which become quite time congestive as the problem is also treated utilising Fermi-Dirac statistics. In addition, the recombination mechanisms have to be coded in a more complex manner than that of the previous coupled single-band model, due to possible recombination processes from either conduction band minimum.

A lot of time was spent developing the energy transport model, whereby; temperature characteristics of the electrons were to be deduced, in order to populate the conduction bands in a physically viable manner. However, this part of the study proved fruitless in the sense that ultimately it was not feasible to populate the two minima due to inadequate electric field strength at applied bias, to initiate sufficient acceleration of the electrons to achieve a higher velocity, and hence gain energy. This setback was overcome by splitting the Γ and X conduction bands into two composites, an upper and lower band. The lower band was then populated using the usual Fermi-Dirac equations, and the upper similarly but with additional exponent, which comprised of the energy difference between the upper and lower bands in each particular material region. Both these electron concentrations were then normalised to the user defined electron concentration inputted for each individual layer.

The population fraction at an applied working voltage across the laser device was next investigated. At a lasing bias of two volts, approximately 99% of electrons was found to exist in the lower conduction band, which agreed faithfully to previous theoretical work proposed by Bøltekjær [6].

An issue that became evident when approaching the problem this way was the possibility of discontinuities and over or under estimations of the electron concentrations in the Γ and X conduction bands arising from the coupled dual-band procedure. These discrepancies arose from the fact that in the coupled dual-band routine deduced a solution for two-dimensionally confined electron states in the lower

conduction band only. When reverting back to the Γ and X regime, some regions that where previously in the lower band with high a population density, are transform to the higher lying X-band which should be considerably less populated than the lower Γ conduction band. This problem occurred for applied biases up to half a volt, thereafter, the contribution of the two-dimensional carriers was overwhelmed by the injection of the minority carriers across the active region of the device. This inconsistency would disappear if the problem were to be solved in a transient manner. In this scenario a bulk scattering mechanism could be implemented to allow a transfer of electrons between conduction bands in a time dependent manner, this would allow the over-estimated electron concentration present in the upper bands to scatter to the more energy favourable lower bands.

The second main topic of this chapter, revolved around the simulation of the previously optimised MQB structures, solved numerically utilising the coupled dual-band model. Subsequently, these results were evaluated by the dual-band Schrödinger solver, allowing any differeces to the previously predicted reflectivity probabilities to be stressed.

In both cases deviations from previously achieved results were observed. It was found that at a bias that mimics the 'turn-on' voltage of the laser device, that approximate flatband conditions are generated. However, there is residual band-bending features across the MQB layers due to doping, and thus, to no surprise the Poisson solved MQB structure produced a superior reflectivity enhancement to that of the flatband MQB structure. However, both cases yielded high reflectivity probabilities with respect to the X-band.

In each of the two structures, some disparity in the relative positions of the Γ and X conduction band minima calculated via Anderson's electron affinity rule [7], to that predicted earlier using the two-thirds approximation [8,9,10], is evident. Here, it was found that the X-band barrier within the superlattice was at a higher energy position than previously deduced, consequently, transmission or reflection through the X-band minimum is reduced, as an incident electron needs a higher energy to access the X-band states for this type of transport to occur. However, the more destructive resonant transmission features that emanate from quasi-bound states within the X-well regions of the superlattice still persist.

In the final section of this chapter, the development of a novel MQB structure is the main focus. Here again, the coupled dual-band model is used in conjunction

with the dual-band Schrödinger solver to first mimic the position of the energy bands under lasing conditions and then calculate the corresponding reflectivity profile of the MQB structure. From the optimisation procedure a stable MQB structure was arrived at, which predicted large enhancements with respect to the X-band maximum and also surpasses the height of the intrinsic Γ-point maximum by 2%. This structure was tested with varying magnitudes of the inter-valley mixing parameter and yielded a consistent stable enhancement for all values.

7.5 References

[1] M. Kurata, 'Numerical Analysis for Semiconductor Devices', *Lexington Books*, Toronto, Canada, (1982).

[2] D. Kincaid and W. Cheney, 'Numerical Analysis 2nd Edition', *Brooks/Cole*, (1996).

[3] E, A, Cole, C. M. Smowton and S. Hussain, 'Hot Electron Modelling of HEMTs', *VLSI design*, **13**, Nos. 1-4, pp. 287-293, (2001).

[4] Chapter 6, Section 6.4.3, this thesis.

[5] C. O. Bozler and G. D. Alley, 'Fabrication and Numerical Simulation of the Permeable Base Transistor', *IEEE Trans. Electron. Devices*, **ED-27**, pp.1128-1141, (1980).

[6] K. Bøltekjær, 'Transport Equations for Electrons in Two-Valley Semiconductors', *IEEE Trans. Electron. Devices*, **Ed-17**(1), pp. 38-47, (1970).

[7] R. L. Anderson, 'Experiments of Ge-GaAs heterojunctions', *Solid-State Electron.*, Vol. **30**, p. 341, (1962).

[8] H. Tanaka, Y. Kawamura, S. Nojima, K. Wakita, and H. Asahi, 'InGaP/InGaAlP double-heterostructure and multiquantum-well laser diodes grown by molecular-beam epitaxy', *J. Appl. Phys.*, Vol **61**, pp. 1713-1719, (1987).

[9] R. P. Schnieder, Jr., R. P. Bryan, E. D. Jones, and J. A. Lott, 'Excitonic transitions in InGaP/InAlGaP strained quantum wells', *Appl. Phys. Lett.*, Vol **63**, pp. 1240, (1993).

[10] X. H. Zhang, S. J. Chua, and W. J. Fan, 'Band offsets at GaInP/AlGaInP (001) heterostructures Lattice matched to GaAs', *Appl. Phys. Lett.*, **73**(8), pp. 1098-1100, (1998).

[11] M. P. C. M. Krijn, 'Heterojunction band offsets and effective masses in III-V quarternary alloys', *Semicond. Sci. Tech.*, Vol 6, pp. 27-31, (1991).

[12] A. C. Marsh, 'Indirect bandgap tunnelling through a (100) GaAs/AlAs/GaAs heterostructure', *Semicond. Sci. Technol.*, **1**, pp. 320-326, (1986).

[13] A. C. Marsh, 'Electron tunnelling in GaAs/A/GaAs heterostructures' *IEEE J. Quantum. Electron.*, **23**, pp. 371-375, (1987).

[14] A. C. Marsh and J. C. Inkson, 'An empirical pseudopotential analysis of (100) and (110) GaAs-$Al_xGa_{1-x}As$ heterostructures' *J. Phys.C: Solid-State Phys.*, **17**, pp. 6561-6571, (1984).

[15] M. R. Brown, K. S. Teng, and S. P. Wilks, 'AlGaInP Multiquantum Barriers Designed and Optimised Using a Novel Dual-Band Drift-Diffusion Simulator', Submitted to *Journal of Quantum Electonics* June (2004).

Chapter 8

Conclusions and Future Work

8.1 General

The underlying purpose of this research project has been to develop a theoretical model capable of calculating the potential confining capabilities of a multiquantum barrier (MQB) placed within a 630nm laser diode under operating conditions. To achieve this goal the project as a whole has been split into six main topic areas, each of which concern the development of a numeric routine. These may be categorised as follows:

(i) A single-band Schrödinger solver and an optimisation routine that allows the best arrangement of superlattice material widths to be determined to achieve large and stable theoretical effective enhancements to the intrinsic barrier height.

(ii) A coupled dual-band Schrödinger solver able to take account of elastic inter-valley scattering between the Γ and X conduction band minima evident in AlGaInP MQBs across a user-defined structure. This numerical routine was subsequently used in conjunction with the aforementioned optimisation procedure to locate dual-band MQB structures that predicted high and stable effective enhancements of the same order as was found by analysing single-band MQB structures.

(iii) An explicit integration routine to solve Poisson's equation, in order to give an indication of how band bending features arising from non-linear charge distribution across the active region of the device effect the reflectivity spectra of a user-defined MQB. This process was performed on both the single and dual-band cases, and using the optimisation process, a novel dual-band MQB structure was proposed that showed stable effective enhancements.

(iv) A general coupled and uncoupled single conduction band drift-diffusion device simulator. This numerical simulator allows the energy band diagram of the whole laser device to be determined under forward and reverse bias conditions. This routine has inbuilt recombination and mobility mechanisms that can be used at the users discretion. Also, the user has the ability to alter the input parameters to simulate their choice of semiconductor device.

(v) A self-consistent solution procedure to take account of two-dimensionally confined electrons present within the quantum well region of the laser device. This scheme iterates in a self-consistent manner between the fundamental device equations of the drift-diffusion model and Schrödinger's equation. Again, this routine was designed to be as general as possible, whereby, the area in which self-consistency is attained may be controlled by the user.

(vi) A coupled dual-band device simulator, whereby, the coupled single band model was extended to incorporate a supplementary electron continuity equation to allow simulation of the X conduction band minimum and hence take account of the intrinsic switching of the lowest conduction band minima evident in a laser diodes fabricated from the AlGaInP semiconductor alloy. This routine was then used in union with the dual-band Schrödinger solver and the optimisation procedure to determine a more physically accurate novel dual-band MQB structure that theoretically predicted a high and stable effective enhancement.

The numerical results attained from this thesis may in a similar manner be broken down into four main sections. Firstly, comparison of the predicted reflection spectra obtained from evaluation of a GaAs/AlAs/GaAs potential barrier of various widths by the dual-band Schrödinger solver based on a model presented by Lui [1], with work published by Marsh *et al.* [2,3,4]. The psuedo-potential method presented

by Marsh *et al.* is extremely complex and very computationally expensive, and subsequently, not really suitable for the kind of application required in this thesis. The reflection spectra gained from both these numerical models was presented in Figure 4.7 of Chapter 4, analysis of which reveals very good quantitative agreement in the predicted reflection spectra across a single-layer GaAs/AlAs hetero-structure.

Secondly, the dual-band Schrödinger solver was applied to a flatband MQB structure that was optimised on the premise that electron transport across the hetero-structure occurred via the direct Γ-point minimum only. Using the single-band Schrödinger solver this MQB predicted high stable enhancements approximately 5% of the intrinsic barrier height. However, the reflection probability fell to almost two-thirds the intrinsic barrier height when solved using the dual-band Schrödinger solver. At this energy the previously high reflection probability was drastically reduced by resonant tunnelling modes situated in the X-band well regions across the structure. To combat these transmission modes the MQB structure was re-optimised by repeatedly iterating between the optimisation process detailed in Chapter 4 Section 4.4 and the dual-band Schrödinger solver until a MQB structure was found that predicted a high stable enhancement [5]. This dual-band MQB structure regained approximately the same effective enhancement as that predicted by the single-band model when electron transport was considered via the Γ-minimum only.

The next set of results concerned the design and optimisation of the novel dual-band MQB structure under working conditions of the laser diode. From experimental analysis it was found that the laser diode reached lasing conditions at a forward bias of approximately two volts. To mimic the band bending effects across the active and surrounding cladding regions emanating from charge transfer due to differently doped material layers Poisson's equation was solved numerically across the active region of the device. In addition, the turn-on voltage was dropped linearly across the device to yield an improved depiction of the relative positions of the two conduction bands as opposed to the flatband approximation used previously. Here again, the optimised dual-band structure was compared with an optimised single-band model to re-emphasise the importance of accounting for transmission states via the X-band minimum. The optimised dual-band MQB structure indicated good stable enhancements as the magnitude of the mixing parameter was varied [6].

In the final result section, a novel MQB structure was again proposed [7], in this case the more physically rigorous coupled dual-band simulator developed in

Chapter 7 was utilised to predict the energy band diagrams across the whole device at the working bias. This model was used in conjunction with the optimisation process and the dual-band Schrödinger solver to locate a MQB structure that predicts stable and high effective enhancements. Before optimisation of this structure was established, the reflectivity of the previously optimised dual-band MQB structures was calculated using this model. It transpired that both MQB structures predicted good enhancement with respect to the lowest X-point, with the Poisson solved structure yielding a slightly greater enhancement.

8.2 Future Work

There are many possible avenues open for improved simulation ability, which due to time constraints have been unable to be addressed in this research project. The most obvious of these is to investigate what effect inclusion of the MQB structure has on hole transport under flatband and lasing conditions. This may be achieved by employing a separate Schrödinger solver able to determine the reflection and transmission probabilities across the MQB in the valence band. This solver could be used also in conjunction with the dual-band drift-diffusion model to attain more accurate valence band profiles.

By solving the gain equations at each bias point in the dual-band solver the optimum lasing conditions could be deduced and subsequently a MQB structure could be designed and optimised at this point instead of at the turn-on voltage of the device, which has hitherto been used.

Another welcome addition would be to include into the existing framework the effects of strain on conduction and valence band alignment. Such effects could be easily fitted into the pre-processing routine at the start of the program.

As pointed out in Chapter 2, all values of effective mass used in this thesis have been independent of electron energy. From the analysis shown Section 2.4 of Chapter 2, this is to a first approximation adequate as the energy ranges used to deduce the reflectivity profiles are not very large. But to achieve a better approximation the energy dependence of the effective masses should be taken into account.

For the area of study presented in this thesis it has been sufficient to model the laser diodes in one-dimension only due to the unidirectional movement of the carriers. However, to make the simulation package more general and applicable to a different range of semiconductor devices, the numeric code could be extended to two-dimensions. However, this upgrade would constitute a whole PhD thesis in itself.

8.3 References

[1] H. C. Lui, 'Resonant tunnelling through single layer heterostructures', *Appl. Phys. Lett.* Vol.51, No.13, (1987).

[2] A. C. Marsh, 'Indirect bandgap tunnelling through a (100) GaAs/AlAs/GaAs heterostructure', *Semicond. Sci. Technol.*, **1**, pp. 320-326, (1986).

[3] A. C. Marsh, 'Electron tunnelling in GaAs/A/GaAs heterostructures' *IEEE J. Quantum. Electron.*, **23**, pp. 371-375, (1987).

[4] A. C. Marsh and J. C. Inkson, 'An empirical pseudopotential analysis of (100) and (110) GaAs-$Al_xGa_{1-x}As$ heterostructures' *J. Phys.C: Solid-State Phys.*, **17**, pp. 6561-6571, (1984).

[5] M. R. Brown, K. S. Teng, A.Kestle, and S. P. Wilks, 'Theoretical investigation of the role of inter-valley transport in AlGaInP MQB structures', Submitted to *Applied Surface Science* June (2004).

[6] M. R. Brown, K. S. Teng and S. P. Wilks, 'Study of Dual-Valley Transport across a Multiquantum Barrier to Enhance Carrier Confinement', *ICSF-9 Proc.*, Madrid Conf., (2003).

[7] M. R. Brown, K. S. Teng, and S. P. Wilks, 'AlGaInP Multiquantum Barriers Designed and Optimised Using a Novel Dual-Band Drift-Diffusion Simulator', Submitted to *Journal of Quantum Electonics* June (2004).

Appendix A

Matrix Non-Singularity Considerations Related to Current Density Equations

The implicit method always involves a solution procedure for the matrix-vector equation of the form $AX = B$, where it is required that the matrix A is non-singular. In general, the non-singularity is guaranteed by the condition,

$$|a_{ij}| > \sum_{k=1,l}^{k\neq i} |a_{ik}| \qquad \text{for } 1 \leq i \leq l, \tag{A.1}$$

where a_{ij} denote elements of the matrix A. This matrix property, in mathematical terms, refers to the matrix A being strictly diagonally dominant. In order to investigate the condition with respect to the matrix appearing in the device analysis, the electron current density equation encountered in Chapter 6 may be transformed to a difference form in a natural manner, to field the following expression

$$\begin{aligned} j_n = -\frac{q\mu_n}{2h(M)}[\psi(N+1)-\psi(N)]\times[n(N)+n(N+1)] \\ +\frac{q\mu_n}{\theta h(M)}[n(N+1)-n(N)] \end{aligned} \tag{A.2}$$

The continuity equation for electrons is given as before, by,

$$\frac{1}{q}\frac{j_n(M)-j_n(M-1)}{h'(N)} = R(N)\,. \tag{A.3}$$

If equation (A.2) is substituted into equation (A.3), and for simplicity, mobility and node spacing is taken to be constant, and additionally, the potential between nodes $N-1$, N and $N+1$ varies linearly and their difference denoted by V_D, the following expression can be obtained:

$$\psi(N-1)-\psi(N)=\psi(N)-\psi(N+1)=V_D, \tag{A.4}$$

Following this, it is possible to express equation (A.3) as:

$$\frac{\mu_n}{2h}\left[\left(\frac{2}{\theta}-V_D\right)n(N-1)-\frac{4}{\theta}n(N)+\left(\frac{2}{\theta}+V_D\right)n(N+1)\right]=R(N)h \tag{A.5}$$

Thus, unless the generation-recombination terms on the right-hand side of equation (A.5) are of great enough magnitude to deform the matrix coefficients on the left, the diagonal dominant condition is approximately satisfied, provided that $|V_D| << 2/\theta$. On the contrary, if $|V_D| \geq 2/\theta$ is true, then the diagonal dominance is lost. The only possibility of satisfying the condition in this case is to reduce the spacing between consecutive nodes, *h*, so much that V_D becomes sufficiently small. However, this will often cause the total point number to increase excessively, ultimately reducing computation efficiency. However, as shown in Chapter 6, this defect may be removed by employing an integral form of the current density equations, as proposed by Schafetter and Gummel [1].

Utilizing the aforementioned integral method and employing the same conditions used to deduced equation (A.5), the following form of the electron continuity equation may be acquired

$$\begin{aligned} &V_D\left(\frac{-1}{1-e^{V_D\theta}}\right)n(N-1)+V_D\left(\frac{1}{1-e^{V_D\theta}}+\frac{1}{1-e^{-V_D\theta}}\right)n(N) \\ &+V_D\left(\frac{1}{1-e^{-V_D\theta}}\right)n(N+1)=R(N)h^2\mu_n \end{aligned} \tag{A.6}$$

Here, in the case where $V_D >> 1/\theta$, the ratio of the three coefficients is equal too $-e^{-\beta}:1-e^{-\beta}:1$. Also. If V_D is negative and $|V_D| >> 1/\theta$, the ratio is $-1:(e^{\beta}+1):-e^{\beta}$, so that in both cases, deviation from the diagonal dominant condition is non-essential. Hence, employment of the Schafetter-Gummel integral discretisation scheme for the current equations substantially improves the matrix property, in that the non-singularity condition is at least approximately satisfied even for very high potential differences between consecutive nodes.

Appendix B

Rational Function Approximations for Fermi-Dirac integrals

The complete Fermi-Dirac integrals are usually defined by

$$F_n(x) = \int_0^\infty \frac{t^n dt}{e^{t-x}+1}, \quad n > -1. \tag{B.1}$$

These integrals appear in various applications of Fermi-Dirac statistics in the non-relativistic limit, the most frequently employed values being –½ , ½ and 1½ in semiconductor device analysis. For example, in Chapter 5, 6 and 7, the number density of electrons in a degenerate electron gas is given by

$$n = \frac{4\pi}{h^3}(2m_e k_b T)^{3/2} F_{1/2}(\eta) \tag{B.2}$$

where n is the number density of electrons, h is Plank's constant, m^* is the effective electron mass multiplied by the free electron mass, k_B is the Boltzmann constant, T is the temperature, and η is the degeneracy parameter.

In Chapter 7, there are three variables to be determined like that shown in equation B.1. Hence, it is essential to incorporate a temporally efficient and numerically accurate scheme to evaluate these equation and the various associated derivatives at each nodal point. The procedure utilised employs the rational function approximation proposed by Antia [2].

The Fermi-Dirac integral in this numerical scheme is divided into two distinct ranges i.e.

$$F_n(x) \approx \begin{cases} e^x R^1_{m_1 k_1}(e^x) & (x < 2) \\ x^{n+1} R2^1_{m_2 k_2}(x^{-2}) & (x \geq 2) \end{cases} \tag{B.3}$$

where

$$R^1_{m_1 k_1}(e^x) = \frac{a_0 + a_1 x + \cdots a_{m_1} x^{m_1}}{b_0 + b_1 x + \cdots b_{k_1} x^{k_1}} \tag{B.4}$$

$$R^2_{m_2 k_2}(e^x) = \frac{c_0 + c_1 x + \cdots c_{m_2} x^{m_2}}{d_0 + d_1 x + \cdots d_{k_2} x^{k_2}} \tag{B.5}$$

i	a_i	b_i	c_i	d_i
0	5.57834152995465e06	6.49759261942269e06	4.85378381173415e-14	7.28067571760518e-14
1	1.30964880355883e07	1.70750501625775e07	1.64429113030738e-11	2.45745452167585e-11
2	1.07608632249013e07	1.69288134856160e07	3.76794942277806e-09	5.62152894375277e-09
3	3.93536421893014e06	7.95192647756086e06	4.69233883900644e-07	6.96888634549649e-07
4	6.42493233715640e05	1.83167424554505e06	3.40679845803144e-05	5.02360015186394e-05
5	4.16031909245777e4	1.95155948326832e05	1.32212995937796e-03	1.92040136756592e-03
6	7.77238678539648e02	8.17922106644547e03	2.60768398973913e-02	3.66887808002874e-02
7	1.00000000000000e00	9.02129136642157e01	2.48653216266227e-01	3.24095226486468e-01
8	...	...	1.08037861921488e00	1.16434871200131e00
9	...	...	1.91247528779676e00	1.34981244060549e00
10	...	...	1.00000000000000e00	2.01311836975930e-01
11	...	...	...	-2.14562434782759e-02

Table B.1: Coefficients of the Rational Function Approximation for $F_{1/2}(x)$.

Thus, utilising the coefficients given in Table B.1 together with equations B.4 and B.5 to evaluate equation B.3 approximation to the Fermi-Dirac integral can be achieved to an accuracy 10^{-15} for the entire range of the degeneracy factor.

The MATLAB function used to implement this procedure is given below,

```
function f = fphalf(x)
m1=7;
k1=7;
m2=10;
k2=11;
a1 = column 1 of Table B.1
b1 = column 2 of Table B.1
a2 = column 3 of Table B.1
b2 = column 4 of Table B.1

if x<2
   xx = exp(x);
   rn = xx+a1(m1);
   for i = m1:-1:1
      rn = rn*xx+a1(i);
```

```
   end
   den = b1(k1+1);
   for i = k1:-1:1
      den = den*xx+b1(i);
   end
   fermi = xx*rn/den;
else
   xx =1/x^2;
   rn=xx+a2(m2);
   for i = m2:-1:1
      rn = rn*xx+a2(i);
   end
   den = b2(k2+1);
   for i = k2:-1:1
      den = den*xx+b2(i);
   end
   fermi = (xx^(an+1))*rn/den;
end
f = fermi;
```

References

[1] D. L. Schafetter and H. K. Gummel, '*Large-Signal Analysis of a Silicon Diode Oscillator*', IEEE Trans. Electron. Devices., No. ED-16, pp. 64-77, (1969).

[2] H. M. Antia, '*Rational Function Approximations for Fermi-Dirac Integrals*', Astrophys. Supp. Series, **84**, pp. 101-108, (1993).